Dynamic Finite Element Analysis of A Flexible Pavement System with Geosynthetic Reinforcement

Bassam Saad

A Thesis

in

The Department

of

Building, Civil and Environmental Engineering

Presented in Partial Fulfillment of the Requirements
for the Degree of Master of Applied Science at
Concordia University
Montreal, Quebec, Canada

March 2003

ABSTRACT

Dynamic Finite Element Analysis of A Flexible Pavement System with Geosynthetic Reinforcement

Bassam Saad

Nonlinear three-dimensional (3-D)dynamic finite element (FE) analyses are carried out to examine the structural performance of a pavement foundation system with and without the presence of geosynthetic reinforcement. Preliminary analyses are aimed at constructing a realistic finite element model representing a conventional pavement system in terms of geometry, loading system, boundary conditions and materials mechanical behavior. The dynamic implicit mode is used to handle dynamic equilibrium equations of the pavement system under traffic triangular wave load. Different strategies and provisions are made for considering the domain dimensions, choice of mesh and the constraints. In these preliminary analyses, the asphalt concrete (AC) viscoelastic behavior, the elastoplastic and elastoplastic strain hardening behavior of the base and subgrade, in addition to the linear elastic material of each layer are all covered in details and tested for the suggested finite element mesh. As a result of such analyses, a linear elastic asphalt concrete layer resting on a Drucker-Parger granular base underlined by a Cam Clay subgrade are adopted for conducting the parametric studies for reinforced and unreinforced conventional pavement systems. The parametric study is achieved through a series of analyses in which several models are built to test the influences of the subgrade quality and the base quality and thickness on the fatigue of the pavement system reflected by the maximum tensile strain at the bottom of asphalt concrete layer, and the rutting of the pavement system reflected by the maximum compressive strain transmitted to the subgrade .For the unreinforced systems, the results show that the subgrade strength has a significant effect on the pavement system rutting and little effect on its fatigue For the geosynthetic reinforced pavement system analyses, it is found that the geosynthetic placed at the bottom of AC leads to the highest fatigue resistance. On the other hand, the resistance to rutting tends to increase with an increase in the maximum compressive strain transmitted to the subgrade and it is mainly dependent on the base depth and the geosynthetic location.

Key words:, Finite element, dynamic analysis, pavement foundation, geosynthetic

ACKNOWLEDGMENTS

I wish to express my sincere gratitude for the encouragement and critical research advices provided by my two supervisors. Professor H.B. Poorooshasb and Professor H.S.Mitri

The supervision of Professor H.B Poorooshasb, the distinguished scholar of soil mechanics and geotechnical engineering, has been an exceptional rewarding privilege. His continued encouragement and guidance are greatly appreciated. I wish him very good health in continuing his enduring research legacy begun in 1960 at Cambridge.

I wish that I were able to put into words an adequate description of the scientific generosity and courtesy of Professor H.S.Mitri who has given me numerical keys and logical engineering steps to more successfully assess and approach the problems of continuum mechanics. I am deeply indebted for his dedicated support.

TABLES OF CONTENTS

Chapter 4
CONSTITUTIVE MODELS FOR GEOGRID-REINFORCED FLEXIBLE PAVEMENT SYSTEM LAYERS

Chapter 5
FINITE ELEMENT MODELLING CONSIDERATIONS

Chapter 6
MODEL SELECTION AND PARAMETRIC STUDY

LIST OF FIGURES

LIST OF TABLES

LIST OF SYMBOLS

$E, G,$ and ν	refer to the elastic modulus, shear modulus and Poission's ratio respectively
ε_t	maximum tensile strain at the bottom of asphalt layer
ε_c	maximum vertical compressive strain transmitted to the top of subgrade
N_f	allowable number of load repetitions before a specific fatigue cracking occurs,
N_d	allowable number of load repetitions before a specific rutting occurs, rutting
F_{max}	strength of the geogrid rib or junction (breaking load),
ε_{max}	strain at breaking load
τ	frictional shear stress
σ_n	normal stress
ϕ	angle of friction
c	cohesion
B_g	minimum width of geogrid aperture,
d_{50}	average particle size in which the geogrid is embedded
F1	ultimate frictional resistance of the longitudinal ribs $= 2 \times A_l \sigma_n tg\phi$
F2	ultimate passive bearing resistance against the front of the transverse ribs $= 2 \times A_t \sigma_n tg\phi$
F3	frictional resistance of the transverse ribs $= A_B \sigma_n N_B$
A_l	area covered by longitudinal ribs,
A_t	area covered by transverse ribs.
A_B	bearing area of transverse ribs
J(t)	creep compliance (material property)
E(t)	relaxation modulus (material property)
ζ	variable of integration or superposition variable integration(dummy variable)
ξ	modified time scale for plotting the master curve of E(t) for a thermological AC
a_T	shift factor $= t_T / t_{T_0}$
t_T	time at temperature T
t_{T_0}	time at the reference temperature To
$D(t)$	creep compliance for generalized Burger model
T_i	retardation time for generalized Burger model
T_x	relaxation time for generalized Burger model

G_i	a constant of the generalized Burger model expressed as a series obtained from
ε_{ij}	strain tensor= $e_{ij} + 1/3\varepsilon_{kk}\delta_{ij}$
e_{ij}	deviatoric strain tensor = $\varepsilon_{ij} - 1/3\varepsilon_{kk}\delta_{ij}$
	volumetric strain tensor = $1/3\varepsilon_{kk}\delta_{ij}$
	for the principal stress situation i=j
	$1/3\varepsilon_{kk}\delta_{ij} = \varepsilon_{kk} = (\varepsilon_{11} + \varepsilon_{22} + \varepsilon_{33})$: The volumetric strain that is the volume change per unit volume
I_1	first invariant of the strain tensor = $\varepsilon_{11} + \varepsilon_{22} + \varepsilon_{33}$
I_2	second invariant of the strain tensor = $1/2\,\varepsilon_{ij}\varepsilon_{ji}$
I_3	third invarient of the strain tensor = $1/3\varepsilon_{ik}\varepsilon_{km}\varepsilon_{mi}$
I_{1D}	first invariant of the deviatoric strain tensor = 0
I_{2D}	second invariant of the deviatoric strain tensor = $1/2\,e_{ij}e_{ji}$
I_{3D}	third invarient of the deviatoric strain tensor = $1/3e_{ik}e_{km}e_{mi}$
σ_{ij}	strain tensor= $S_{ij} + 1/3\sigma_{nn}\delta_{ij}$
S_{ij}	deviatoric stress tensor = $\sigma_{ij} - 1/3\sigma_{nn}\delta_{ij} = \sigma_{ij} - p\delta_{ij}$
	volumetric stress tensor = $1/3\sigma_{nn}\delta_{ij}$
σ_{nn}	hydrostatic stress = $\sigma_{11} + \sigma_{22} + \sigma_{33}$
p	mean stress in triaxil test = $\dfrac{\sigma_{11} + \sigma_{22} + \sigma_{33}}{3} = \dfrac{J_1}{3}$
	In the triaxial test, where axisymmetry exists, the
p	mean stress in triaxial test = $\dfrac{\sigma_1 + 2\sigma_3}{3} = \dfrac{J_1}{3}$
q	deviatoric stress in the triaxial test = $\sigma_1 - \sigma_2 = \sqrt{3J_{2D}}$
J_1	First invariant of the stress tensor = $\sigma_{11} + \sigma_{22} + \sigma_{33}$
J_2	second invariant of the stress tensor = $1/2\,\sigma_{ij}\sigma_{ji}$
J_3	third invarient of the stress tensor = $1/3\sigma_{ik}\sigma_{km}\sigma_{mi}$
J_{1D}	first invariant of the deviatoric stress tensor = 0
J_{2D}	second invariant of the deviatoric stress tensor = $1/2\,S_{ij}S_{ji}$
	In the case of principal stress
	$J_{2D} = 1/6\{(\sigma_1 - \sigma_2)^2 + (\sigma_2 - \sigma_3)^2 + (\sigma_1 - \sigma_3)^2\}$
J_{3D}	third invarient of the deviatoric stresss tensor = $1/3S_{ik}S_{km}S_{mi}$
$S_{ij}(t)$	deviatroic shear stress at time t, $S_{ij}(t) = \sigma_{ij}(t) - \dfrac{1}{3}\delta_{ij}\sigma_{kk}(t)$,
$e_{ij}(t)$	deviatoric strain tensor at time t, $e_{ij}(t) = \varepsilon_{ij}(t) - \dfrac{1}{3}\delta_{ij}\varepsilon_{kk}(t)$
G(t)	relaxation shear modulus

K(t)	relaxation bulk modulus
χ	dummy variable for conducting the superposition integral for the new axis of ξ
α(t)	temperature-dependent coefficient of thermal expansion.
A,B	Ferry-William-Landel constants for shift factor of a viscoelastic thermological material
G_∞ , K_∞	long term shear modulus and bulk modulus, respectively
β_i , γ_i	decay constants for the shear modulus and bulk modulus, respectively
η_G , η_K	Viscosities of the dashpots existing in the rehological model representing AC in creep (pure shear test), and in creep pressure test, respectively. E^* the complex modulus of AC layer = E1+i E2
E1	$=(\frac{\sigma_0}{\varepsilon_0})\cos\delta$ is a measure of the elastic stiffness.
E2	$=(\frac{\sigma_0}{\varepsilon_0})\sin\delta$ characterizes the internal damping and measures the viscous behavior. σ_0 is the stress amplitude for sine wave stress pulse, ε_0 Amplitude of the recoverable sine wave strain, δ is the phase angle by which the strain lags the stress .
|E*|	$=(\frac{\sigma_0}{\varepsilon_0})$ = dynamic modulus which measures the elasticity of AC .
E_s	flexural stiffness at applied stress σ ,
ω	angular velocity ,
M_R	resilient modulus or the stress dependency elastic modulus $M_R = K\times\sigma_\theta^{\ n}$ or $M_R = K_A(\frac{\sigma_\theta}{P_0})^{K_B}(\frac{\sigma_d}{P_0})^{K_C}$
K, n	elastic nonlinearity materials properties. σ_θ is the sum of the principal stresses (bulk stress)
σ_d	$=\sigma_1-\sigma_3$ (deviator stress)
P_0	unit reference pressure (1KPa or 1psi)
K_A, K_B, K_C	material constants obtained from repeated load triaxial test performed on granular material
dλ	a positive scalar factor (loading parameter) usually not constant
Y	stress yielding value obtained from pure tension or compression
Π	plane passing from origin and perpendicular to the hydrostatic line
K_t	Tresca material constant
φ	dilation angle
Q	plastic potential function
α, K_m	failure envelope constants for yield function Mohr- Coulomb or Drucker-Parger drawn in $J_1, \sqrt{J_{2D}}$ space

k	hardening parameter in the strain hardening Cap model
D, W	constants of the material modeled by the strain hardening Cap material model
n	soil porosity
R	ratio of the major to minor axis of the elliptical cap
e	void ratio
de^P	plastic component of the incremental void ratio
de^P	elastic component of the incremental void ratio,
M	slope of the critical state line
λ	slope of isotropic consolidation
κ	slope of over consolidation line
C_c	slope of virgin loading line on $e - \log_{10} p$
C_s	slope of unloading-reloading curves on the same previous plot
v	specific volume =1+e,
Γ	specific volume at isotropic consolidation state when the pressure = $\frac{J_1}{3} = P$ equals to1
μ	coefficient of friction in Taylor's equation $\frac{\tau}{\sigma} = \mu + \frac{dy}{dx}$ Strength = Friction + Interlocking dy expresses the increase in sample thickness and a separation of the two halves of the shearing box., dx expresses the horizontal relative displacement of the two halves of the shearing box
$\{r\}$	displacements and rotations vector according to the specified degree of freedome
$\{\dot{r}\}$	velocity vector according to the specified DOF
$\{\ddot{r}\}$	accerelation vector according to the specified DOF
$\{R^{int}\}$	internal force vector and it is =[K][r] in linear analsis
$\{R^{ext}\}$	external force vector
[C]	damping matrix
[K]	stiffness matrix
[M]	mass matrix
$(v_{st})_0$	static deformation due to P0. $(v_{st})_0 = \frac{P_0}{K_v}$

ξ damping ratio or fraction of the critical damping $\frac{c}{c_c}$ where

$$\delta = \ln(\frac{v_2}{v_1}) = -2\pi\xi$$

c_c critical damping corresponding to a specific DOF =2m w.

w_D damped vibration frequency, given by $w_D = w\sqrt{1-\xi^2}$

w natural frequency of this DOF=$\sqrt{\frac{K_v}{m}}$.

K_v stiffness according to considered DOF

α, β proportional damping factors

c_E compression wave speed $= \sqrt{\frac{E}{\rho}}$

c_G shearing wave speed $= \sqrt{\frac{G}{\rho}}$

w_{max} largest natural frequency of the system .

w_{min} smallest natural frequency of the system

Chapter 1
INTRODUCTION

1.1 General

The unprecedented increase in the speed and power of personal computers in the last decades has made numerical methods ,like the finite element method, attractive for analyzing and understanding the behavior of many sophisticated structures under the effect of any complex loads.

The necessity of adopting the finite element method to predict the structural performance of a pavement system arises from the following points:

- The empirical methods derived to investigate the structural behavior of pavement systems do not fully account for the mechanism or the stress-strain state to which these systems have been subjected. Because of the cost, field or laboratory test programs cannot cover all the important variables involved in controlling the structural performance of the pavement systems that makes their results product-specific and test-dependent.
- The analytical methods represented mainly by the classical elasticity theory cannot adequately handle the complex behavior of the pavement materials under dynamic traffic loading

This necessity becomes more justified when an additional layer of different characteristics, like a high modulus geosynthetic or geogrid membrane is involved as a reinforcing material ,which is the case in this study. In such a case, more detailed

computations and analyses are required to understand the behavior of the pavement system, which is not conventional any more, under different circumstances.

1.2 Scope and objectives

In this study, the finite element method will be employed for analyzing the structural performance of a pavement system under different conditions of its components, Moreover, it will be used for investigating the potential of high modulus geosynthetic or geogrid in improving such performance. The structural performance of the pavement system is evaluated mainly through the strains which are usually adopted in pavement design practices. They are shown in Figure (1.1) :

- The maximum tensile strain transmitted to the bottom of the asphalt concrete layer, ε_t, which is the traditional criterion for judging the fatigue life of the pavement
- The maximum compression strain transmitted to the subgrade, ε_c, which is normally used for evaluating the rutting life of the pavement

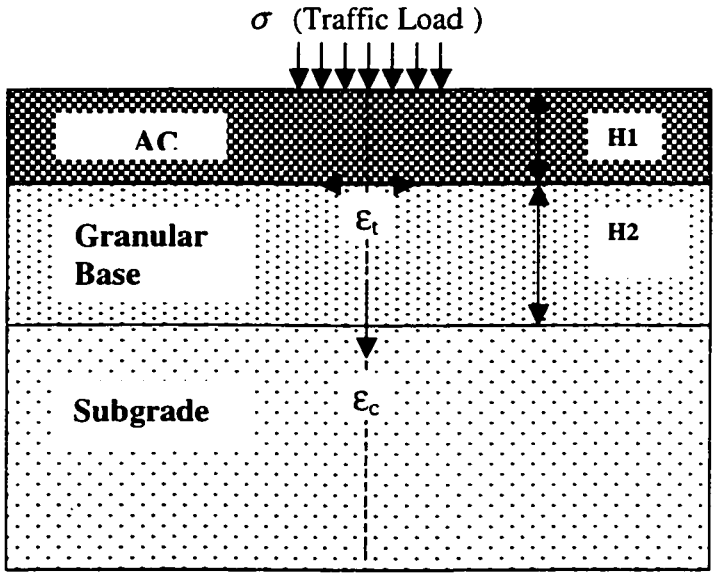

Figure (1.1) A conventional pavement system scheme

In the unreinforced finite element models emphasis is given to the mechanical behavior of the pavement system and its dynamic response under the traffic loading. The focus in the geogrid reinforced pavements analyses is to determine the conditions under which the geogrid ,operated by its membrane, is more beneficial to the pavement performance. The different objectives of the models are :

- Varying location of geosynthetic reinforcement within the base with no slippage assumed.
- Investigating two types of subgrade namely, clay soil, silty sand soil.
- Testing the strength of the base by modeling two types of base
- Varying the thicknesse of the base from 30.48 cm (12 in), and 15.24 cm (6 in).

The data of the materials used is taken from previously published literature.

1.3 Thesis outline

Chapter two discusses the basic information related to a conventional pavement system, geosynthetic reinforcement and its mechanism in supporting the pavement system, in addition to some reported analytical solutions concerning the geosynthetic reinforcement of unpaved road systems.

Chapter three includes brief review of the empirical methods and numerical simulations related to the performance of geosynthetic pavement systems

Chapter four presents in detail the constitutive behavior of the pavement materials and the corresponding constitutive laws which could represent each layer in the geosynthetically reinforced pavement system.

Chapter five presents the finite element modeling considerations and issues in modeling of pavement systems in terms of geometry, meshing strategy, and dynamic analysis. The pavement dynamic response under the traffic loading wave is emphasized..

In chapter six, several models are first constructed and implemented in preliminary finite element analyses to derive a convenient model that is able to represent as accurately as possible the pavement system under the given load. Computation time and computer storage are also considered as judgment factors in the model selection.

Having selected the model, a detailed parametric study is conducted on a pavement system with and without the presence of the geosynthetic reinforcement. The effects of the subgrade quality, base quality and its thickness on the fatigue performance and rutting of a pavement system, are studied in the parametric study.

The variation of surface deflection and the horizontal strain at the bottom of asphalt concrete layer at the peak wave load, in addition to envelopes of surface deflection and the horizontal strain at the bottom of asphalt concrete layer through the duration time of the traffic load are also presented in this chapter .

The variation of vertical plastic strain across the base depth are shown for some analyses.

At the end of this chapter, some simulations are carried out to test the grid lateral restraining effect, which is idealize to give the maximum effect, and to determine if elastic behavior of the pavement system layer adopted will have a significant effect on the performance of the geosynthetic. Such simulations are conducted for a specific pavement system.

Chapter seven reports the conclusions drown from this study . Also, recommendations for further research topics are made.

Chapter 2

THEORETICAL BACKGROUND AND ANALYTICAL LITERATURE

2.1 Conventional flexible pavement system

A conventional flexible pavement system is a layered system, consisting of the surface asphalt concrete (AC) layer, the granular base course, and the subgrade layer which is the soil immediately below the granular base layer, as shown in Figure (1.1) . The stresses transmitted from traffic loads to a point within a layer depend on the stiffness and thickness of each layer. The main function of the pavement layers is to decrease such stresses so that each point remains within an allowable deformation throughout the designated service life of the system.

2.1.1 Subgrade

The desired characteristics of the subgrade include strength, ease of compaction, and good drainage. The California Bearing Ratio (CBR), an empirical index used to indicate the soil shear strength, has been a decisive design parameter of a pavement system for a long time. In the ASSHTO report prepared by (Berg et al, 2000), the subgrade strength in the context of (i) normal highway truck traffic, or (ii) typical highway construction equipment is defined as follows:

firmer subgrade: CBR>8; shear strength>240 kPa; E>80MPa

moderate subgrade: 3≤CBR≤ 8; 90kPa ≤shear strength 240KPa; 30 MPa≤E≤ 80 MPa

low subgrade: CBR<3; shear strength≤90 kPa; E≤30 MPa.

Today, the resilient modulus method (Yang,1993) proves to give more conservative results, as the soil should operate at a stress level within the elastic range.

2.1.2 Granular base layer

It is the layer that lies immediately below the wearing course of the pavement. Sometimes another layer of a different material separates the base from the subgrade, this course is called subbase layer. The base and subbase courses may be constructed from stone fragments, slag, soil-aggregate mixture, cement-treated granular materials or bituminous-aggregate mixtures.

The base provides added stiffness and resistance to fatigue, and decreases the stress transmitted to the subgrade, it may also form a drainage layer and resist the frost.

Grading, size, soundness, and permeability of the materials are important properties for evaluating the suitability of the base.

2.1.3 Bituminous layer (asphalt concrete layer)

Ideal wearing course layer is usually divided into a binder course and a surface course built separately with a tack coat at the interface. The uppermost layer, surface course, is thinner, has smaller aggregates and includes more bitumen than the binder course, which lies immediately on the prime-coated base layer. Many flexible pavements have been built in practice, consisting of only one uniform bituminous course above the base layer. Bituminous materials can be asphalt or tars. Asphalt may be natural or manufactured. Tars are manufactured in coke or gas ovens. The design of the stabilized asphalt-aggregate mix is based on the Marshall test, which gives, for the selected aggregate

materials, the optimum binder ratio leading to the highest strength of the AC mixture. Hveem criterion is also widely used to specify the optimum binder ratio.

The surface must provide safe, smooth riding quality, adequate skid resistance, non load-associated fracture, and good resistance effects to permanent deformation resistance.

2.2 Environmental influences

Temperature and moisture affects are usually incorporated in many design methods of the pavement design, the stiffness of the AC layer is dependent on the temperature which should be also considered when designing the asphaltic mix, while the subgrade and base moduli vary according to the moisture content. The effect of water and air on the deterioration of asphalt mix is called durability. Durability and frost heave should be accommodated when characterizing the materials of the system.

2.3 Traffic loading

The traffic loads are converted to an equivalent number of standard axle reference load, 80 or 100 kN axle load. An equivalent single wheel load (ESWL) is defined as the load on a single tire bringing about the same stress or strain at a given location within a specific pavement system to that resulting from a multiple-wheel load at the same location.

Modeling of the different wheel loads and their dynamic effects on the distress design criteria is considered by many of design methods particularly Asphalt Institute and Shell methods, as will be shown in Chapter Five.

2.4 Design criteria

Damage analysis or failure modes of the pavement system are normally represented by fatigue cracking of the AC layer and surface permanent deformation.

The tensile strains at the bottom of asphalt layer have been used as a design criterion to prevent fatigue cracking. The failure criterion for fatigue cracking is expressed as (Yang,1993)

$$N_f = f_1 \times \varepsilon_t^{-f_2} \times E_1^{-f_3} \qquad (2.1)$$

Where :

N_f is the allowable number of load repetitions before fatigue cracking occurs, :

ε_t is the tensile strain at the bottom of asphalt layer

E_1 is the elastic modulus of the AC layer

f_1, f_2, f_3 are constants determined from fatigue tests; their values for the standard mix are assigned by Asphalt Institute after considering that 20% of area cracked as 0.0796, 3.291, and 0.854 for f_1, f_2, f_3, respectively.

The corresponding values adopted by Shell for f_1, f_2, f_3 are 0.0685, 5.671, 2.363, respectively.

Because the exponent f_2 is much greater than f_3 its effect of ε_t on N_f is much greater than that of E_1 and the Equation (2.1) becomes

$$N_f = f_1 \times \varepsilon_t^{-f_2} \qquad (2.2)$$

Equation (2.2) has been used by several agencies as listed below (Yang,1993):

Illinois Department of Transportation:

$$N_f = 5\times10^{-6}\times(\varepsilon_t)^{-3.0}$$

Transport and Road Research Laboratory of U.K:

$$N_f = 1.66\times10^{-10}\times(\varepsilon_t)^{-4.32}$$

Belgian Road Research Center:

$$N_f = 4.92\times10^{-14}(\varepsilon_t)^{-4.76}$$

It can be seen that the exponent f_2 of the fatigue varies from 3.0 to 5.671, but the coefficient f_1 varies over several orders of magnitude from 5×10^{-6} to 4.92×10^{-14}.

The exponents f_1 and f_2 are usually determined from fatigue tests or laboratory specimens however, f_1 must shift from laboratory to field values by calibration (Pell,1987)

The permanent vertical deformation of the wheel path, which is called the pavement rutting, can be evaluated through the vertical compressive strain on the top of the subgrade. In this case, the allowable number of road repetitions to limit rutting is

$$N_d = f_4\times\varepsilon_c^{-f_5} \qquad (2\text{-}3)$$

Where : ε_c the vertical compressive strain at the top of subgrade.

f_4, f_5 are constants. Their values are tabulated by different agencies, according to the allowable value of the rut depth. as shown in Table (2.1).

As can be seen from the Table (2-1), the exponent f_5 falls within a narrow range, but the coefficient f_4 varies a great deal. Both constants should be calibrated by comparing the predicted performance with field observation.

Considering the permanent vertical deformation of the AC layer is negligible, the total accumulated permanent deformation based on the permanent deformation properties of the base and subgrade layer which leads to the total surface deflection is a more accurate design criterion for permanent deformation than the subgrade strain.

Given the surface deflection, the vertical strain transmitted to the subgrade can be calculated after conducting back analysis through elasticity theory using for example KENLAYER or BISAR software. However, the finite element analysis is more appropriate for more complicated representations of the pavement layers and traffic load.

Table (2.1) Subgrade vertical strain criterion used by various agencies (afterYang,1993)

Agency	f_4	f_5	**Allowable rut depth, in(cm)**
Asphalt Institute	1.365×10^{-9}	4.477	0.5 (1.27)
Shell : (95% reliability)	1.05×10^{-7}	4	
(85% reliability)	1.94×10^{-7}	4	
(50% reliability)	6.15×10^{-7}	4	
U.K.Transport and Research Record : Laboratory (85% reliability)	6.18×10^{-8}	3.95	0.4 (1.02)
Belgian Road Research	3.05×10^{-9}	4.35	

2.5 Design methods of a conventional pavement system

Defining the thickness and the strength coefficient of each layer after considering the existing factors of soil strength and type, load and traffic characteristics, environmental conditions and economics of design, are implemented in the design procedure. Pavement design was first approached by purely empirical methods like the CBR and the AASHTO methods, which are based on extensive tests results. The various mechanistic-empirical design methodologies are the subsequent step in pavement design. That was mainly done by the Asphalt Institute using the mechanistic multilayer theory in conjunction with the empirical failure criteria to determine the pavement layer thicknesses. Theoretical methods are based on the elasticity theory which is at best, an approximation of the real situation-one layer (Odemark-Boussinesq equations), two layers (Burmister theory), the three layers (Jones and Peattie Graphs). All are considered theoretical analyses of the pavement Apart from its limitations, it is worthwhile to mention that Odemark-Boussinesq method illustrated in Figure (2-1) has been found to be the simplest method for predicting actual stresses, strains and deflections and in handling the non-linearity in the real pavement (Per Ullidtz, 1987).

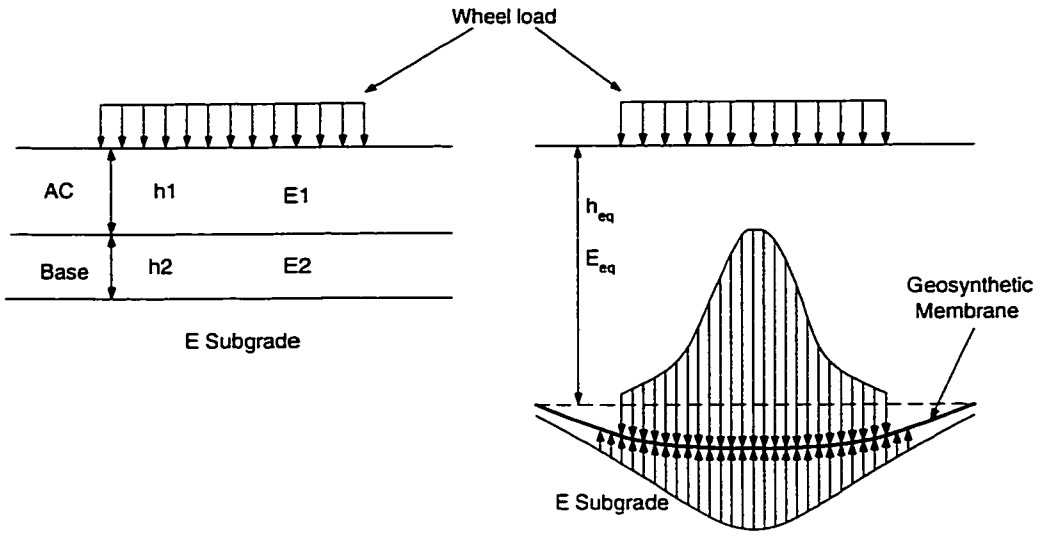

Figure (2.1) Odemark theory illustration which is based on the assumption that any layer can be replaced by another layer with different elastic coefficients and the same flexural rigidity, provided that the layers strengths are decreasing in the downward direction

2.5.1 The finite element method

The versatility of the method allows for the modeling of any number of layers which may have variations in the structural properties and mechanical behavior with area and depth subjected to complex non-uniform loading patterns.

The principle of the method is that the region of interest, i.e., the pavement, base and subgrade, is discretized or divided into a number of elements. At the top center of the region of interest is a single wheel load. The elements are extended in three dimensions from the wheel to include the area within the influence of the wheel. The analysis of the pavement could be almost invariably axisymmetric and the loading is assumed to be applied by a single load. The interrelationship between multiple wheels and axles is readily considered by summation. The elements interconnect at nodes. Increasingly more

sophisticated element types have been introduced. A particularly stable and successful element is the eight-noded isoparametric element with reduced integration rule. The section through the pavement is divided into quadrilaterals (the majority of which are rectangles). For a typical wheel loading, it is adequate to extend the mesh to a radius of the order of 3.5 m and to a depth of 2.5 m. The boundaries of the mesh are vertical and horizontal and are assumed to be constrained by rollers in the direction perpendicular to each side face of the mesh. The wheel loading is applied as a pressure acting on the upper surface.

The output from the finite-element program consists of the following:

1-Displacements at each node

2-Strain tensor and principal strains and directions at a number of points within each element

3-Stress tensor and principal stresses and directions at the same points as the strains

The validity of the computations depends critically on the selected constitutive laws representing the mechanical behavior of the system layers

2.6 Geosynthetic reinforcement

Geosynthetic reinforcement materials have been introduced in recent years as a means to help improve the structural performance of pavement system. One of the more commonly used reinforcing geosynthetic materials is the polymeric geogrid

A geogrid is defined by the ASTM Committee D-35 as follows: "a geosynthetic used for reinforcement which is formed by a regular network of tensile elements with apertures of

sufficient size to allow strike through of surrounding soil, rock or other geotechnical material".

It is clear that geogrid differs from geotextile as it is composed of either stiff or flexible high-tensile strength grids with apertures of specifically larger size used mainly for reinforcing purpose.

Geogrid can be either uniaxial or biaxial, Figure (2.2). Uniaxial geogrid resists the applied loads in one direction only, its ribs tend to be thicker and the apertures are long narrow slits.

The leading geogrid suppliers are Tensar Corp and Tenax Corp. According to the material manufacturing method of connecting the ribs, a geogrid can be divided into extruded, knitted, or woven and welded geogrid,

The geogrid has many possible uses, it can be used as a reinforcement for paved, unpaved roads and railroad construction, embankment fills and earth dams, sheet anchors and facing panels for retaining wall, reinforcing disjointed rock sections, cement or concrete

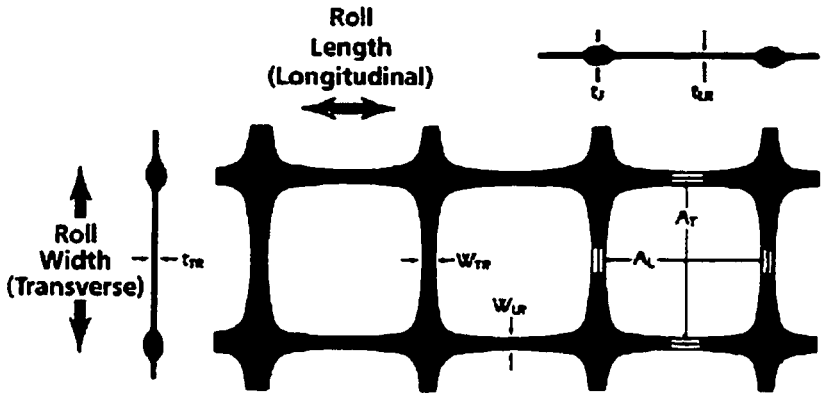

(b) Biaxial geogrid

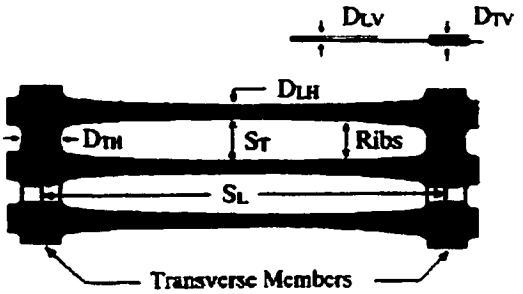

(a) Uniaxial geogrid

Figure(2.2) Sample illustration of geogrid (Tensar Corp production)

reinforcement in wide variety of applications, gabions for wall construction and bridge abutments, and it is widely also used for repairing slope failures and landslides.

According to an AASHTO report prepared by Berg et al (2000), the benefits added to pavements as a result of geosynthetic reinforcement are measured by one of the following:

TBR (Traffic Benefits Ratio): A ratio of load cycles on a reinforced section to reach a defined failure state to the number of load cycles on unreinforced section, with the same geometry and material constituents, to reach the same defined failure state.

BCR (Base Course Reduction): The percent reduction in the reinforced base, thickness from the unreinforced thickness, with the same material constituents, to reach the same defined failure state.

LCR (Layer Coefficient Ratio): A modifier applied to the layer coefficient of the aggregate. This value is back-calculated, based upon the number of load cycles on a reinforced section to reach a defined failure state to the number of load cycles on the unreinforced section, with the same geometry, to reach the same defined failure state.

2.6.1 Physical properties

Mass per unit area, specific gravity, thickness, percent open area of geogrid sheet are important indicators of the manufacturing materials and physical body of the inclusion, these properties can be measured directly.

Flexural stiffness is a defining characteristic of the grid measuring the ease of the geogrid sheet to deform and bend under its own weight. Flexural rigidity test ASTM D1388 is adopted to quantify the stiffness or flexibility of geogrid which is diminished by weight-length unit.

2.6.2 Mechanical properties

As the cross section of the geogrid can not be defined easily, the tensile strength is measured in units of force per unit width. The in-isolation single junction strength test is conducted by pulling; i.e., applying a tension force only on a longitudinal rib from its transverse rib junction until failure (Koerner, 1994). The strength of a single rib is measured by a separate tensile test, then the geogrid junction strength efficiency is calculated by taking the ratio of the aforementioned strength results.

The stress-strain characteristics for the single rib or junction can be fully explored from the tensile test, and the following characteristics are obtained:

(i) F_{max} is the strength of the rib or junction (breaking load), ε_{max} is the strain at breaking load

(ii)E (modulus of elasticity): The tensile stiffness, which can be one of the following: The tangent stiffness (initial stiffness), the slope of the straight first part of the stress-strain curve, or the secant modulus: the slope of the line connecting two particular points on the stress strain curve.

2.6.3 Friction characteristics

The interaction of the geogrid with the surrounding media is dependent on its mechanical and physical properties, and it can be analyzed by two tests, the direct shear and pullout tests.

The shear strength test is conducted using the normal geotechnical shearing box at which geogrid is placed and fixed. The geogrid- soil friction relation can be found using the equation:

$$\tau = \sigma_n \tan\phi + c \qquad (2.4)$$

τ is the frictional shear between the geogrid and the upper medium, σ_n is the normal stress at failure, ϕ is the angle of friction between the geogrid and the soil.

c is the adhesion between the geogrid and the upper medium (it is considered negligible)

The aperture and the soil particle size have a strong influence on the shearing resistance Sarsby (1985) reported that the optimum transfer of shear stress occurs when

$$B_g \geq 3.5 d_{50} \qquad (2.5)$$

Where: B_g is the minimum width of geogrid aperture, and d_{50} is the average particle size .The pullout strength is different from direct shear in that the geogrid is sandwiched between the upper and lower soil layers, and one of its ends is left out and clamped in jaws; the box is fixed and the geogrid is pulled by the jaws at a constant rate of displacement. The relative movement between the embedded geogrid and the embedding media mobilizes frictional forces on both sides of the geogrid which resists the pull out force. After tensioning the geogrid, a non-uniformly distributed strain along the sheet of geogrid develops and the relative movement between the geogrid and the particles will not be the same. The average shear stress is calculated as :

$\tau = F/A$, where A is the contact area. This is not the case in pull out test in which the stress is localized and has high value at the loaded end. Such stress decreases along the geogrid from the pulled end until it disappears at the free unloaded end

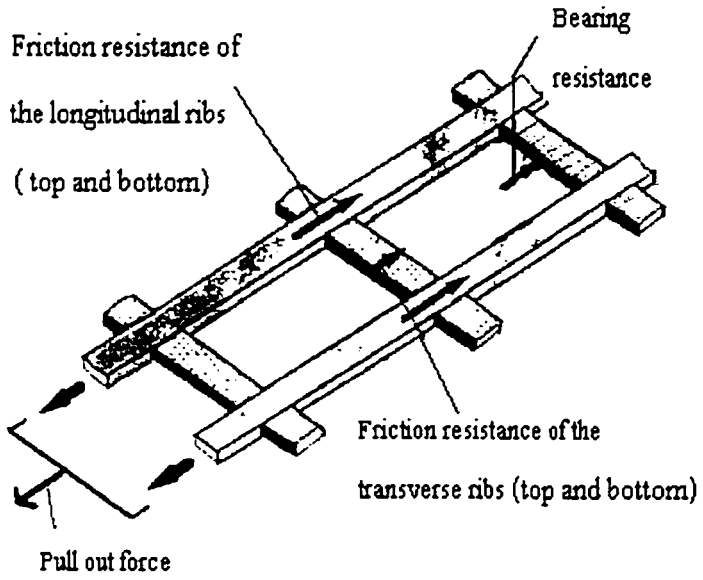

Figure (2.3)The components of pullout resistance after (Keorner, 1994)

The pull out resistance is dependent on the extensibility of the geogrid mesh. The pull out resistance, as explained by (Koerner, 1994), is a result of three components (i)the frictional resistance of the longitudinal ribs(ii) the passive (bearing) resistance against the front of the transverse ribs(iii) and the frictional resistance of the transverse ribs [Figure (2.3)].

The ultimate pull out resistance is F=F1+F2+F3 where:

F1 (ultimate frictional resistance of the longitudinal ribs)

$= 2 \times A_l \sigma_n \tan \phi$

F2 (ultimate passive (bearing) resistance against the front of the transverse ribs

$= 2 \times A_t \sigma_n \tan \phi$

F3 (frictional resistance of the transverse ribs)

$= A_B \sigma_n N_B$

A_l is the area covered by longitudinal ribs,

A_t is the area covered by transverse ribs.

A_B is bearing area of transverse ribs

ϕ is the interface angle of friction.

F1 should be less than the ultimate strength of the geogrid

As the force taken by transverse ribs will be transmitted through the junctions, (F2+F3), the force carried by any transverse rib, should be less than ultimate force carried by transverse rib which is governed by the strength of the junction

In addition, F should be less than the tensile strength of geogrid.

For different types of geogrid, Koerner et al.(1989) assumed different coefficients of friction and bearing resistance depending on the strain level mobilized in the geogrid. Koerner concluded that the pull out resistance is highly dependent on the flexibility of geogrid, especially at low pull out loads.

2.6.4 Reinforcement mechanisms

The geogrid placed at the bottom of, or within the aggregate base is considered to reinforce the pavement system by two mechanisms:

(1) membrane tensioned and (2)lateral restraint; see Figures (2.4) and (2.5)

The membrane tension appears to be predominant when the soil is soft allowing for a vertical deformation, hence for surface rutting.

When the geogrid deforms, it improves the stress distribution in the lower media (soil or granular), as the normal stress at the bottom of the geogrid becomes less than that on the top (membrane behavior); [Figure (2.5)]. With increasing rut depth, the difference increases and the added benefits to the subgrade bearing capacity increase considerably more until an equilibrium is reached and the subrgade can bear the distributed load without further plastic deformation.

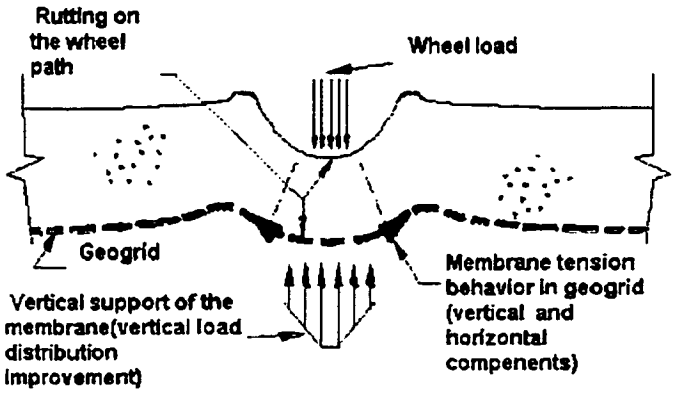

Figure (2.4) The geogrid membrane support of the system (Berg et al 2000)

Geogrid of high modulus is expected to give greater support because larger tensile forces are induced with much smaller elongation. Quantifying the magnitude of membrane tension and its influence on the subgrade strength (bearing capacity factor) and the bearing capacity of granular-soil system as a whole (unpaved roads) was investigated by David (1994), Chandan and Madhav (1994) and Giroud and Noiray (1981)

Membrane effect can be also explained physically as follows. When successive wheel loads are applied, a relatively large rut depth occurs because subgrade experiences an impending shear failure; i.e., vertical permanent deformation exceeds its bearing capacity, as a result the geogrid deformation, upward reaction in the areas immediately under the wheel path and a vertical downward confinement of the subgrade is created, [Figure (2.5)].

The deeper is the rut becomes, the higher are the values of the horizontal and vertical membrane reactions. Following this mechanism, Nishigata and Yamaoka (1990) calculated the bearing capacity of an unpaved road reinforced by geosynthetic membrane. Related structural and mathematical calculations for cables and membranes are detailed by Borg (1990).

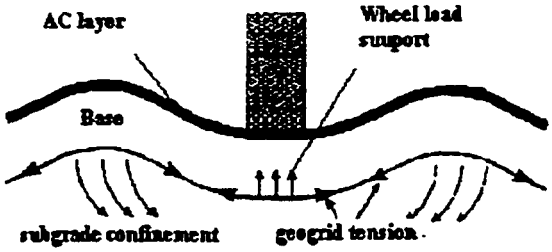

Figure (2.5) Physical illustration of the membrane support (Berg et al, 2000)

The lateral restraint mechanism would be manifested with a small rut depth or when the subgrade foundation is not weak.

As the vehicular load is applied on the surface, the particles of the granular base tend to laterally spread [Figure (2.6)] leading to a decreasing thickness of the base proportional to the rut depth; this horizontal motion creates tensile lateral stress in the unbound granular base which in turn leads to undesired stress-strain state helping the failure strains to take place in the system. The frictional components are represented by interlocking of the granular with the georgrid apertures and the inward shear stresses induced at the top and bottom geogrid interfaces with the surrounding media resist lateral motion of the granular base.

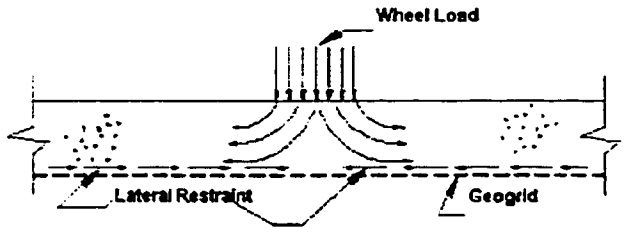

Figure (2.6) Lateral restraint effect of the geogrid on the surrounding medium(Berg et al, 2000)

Another analysis for lateral restraint mechanism can be interpreted by the following empirically confirmed observations. Reinforcing the base by the geogrid mesh will result in a stiffer base, and a smaller vertical stress will develop in the granular base and the subgrade as a consequence beneath the wheel path. In addition, the shear stress expected to develop in the underlying media (soil or base) will be also reduced. The base stiffness

increase is dependent on the depth of the geogrid and the strength parameters of base and subgrade The large scale laboratory experiments show that geogrid with large apertures performed as well as a continuous woven fabric having a stiffness of 2 to 2.5 times that of the grids as a result of interlocking. The horizontal confinement was analyzed and quantified by Chandan and Madhav (1994) who found that by using stiffer base in shearing, the confinement support becomes more pronounced.. Giroud and Bonaparte (1984) showed that the bearing capacity factor improves from π to π+2 by the lateral restraint of the geogrid placed at base-subgrade interface. They concluded after conducting elastic analysis on an unpaved system, that for a geogrid with a specific stiffness, the horizontal effect decreases when using a thicker base layer.

Houlsby and Richard (1990) used limit analysis theory to quantify the bearing capacity increase of an unpaved system as a result of using the geosynthetic.

Figure (2.7) shows how the bearing capacity of the soil is improved as a consequence of geogrid reinforcement

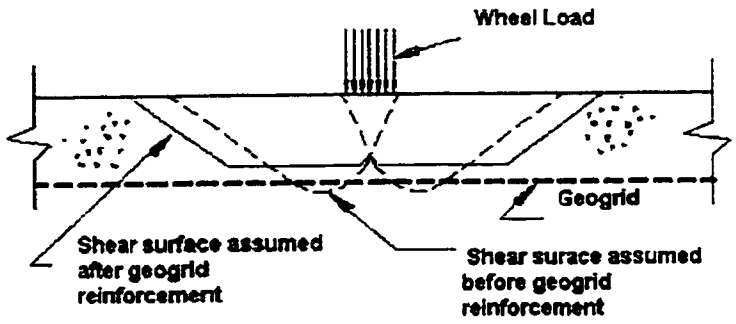

Figure (2.7) Subgrade bearing capacity increase as a result of geogrid reinforcement (Berg et al.2000)

Studying the effect of geogrid stiffness on the bearing capacity of an unpaved system was carried out separately by Burd and Brocklehurst (1990).Roughness, initial stiffness modulus, physical shape, strength and the aperture sizes of the reinforcement geogrid are controlling factors of the lateral restraint mechanism. A geogrid must have a high stiffness in order to keep operating as a lateral restraint.

In summery, the lateral restraint includes the following functions

1-Restraining the lateral movement of base aggregate.

2-Increasing the modulus of base aggregate due to confinement.

3-Improving the vertical stress distribution.

4-Reducing the shear stress transmitted to the top of the subgrade.

Chapter 3

LITERATURE REVIEW OF EXPERIMENTAL AND NUMERICAL STUDIES

3.1 Experimental studies

Several laboratory investigations have been undertaken to demonstrate the role of geogrid as an effective reinforcing layer in pavement systems.

Haas (1984) placed a polymeric grid at the bottom of the AC layers of different thicknesses. In each loop the AC layer was placed on (i) a weak subgrade and (ii) a strong subgrade. The comparison between the reinforced section and unreinforced section was based on a failure criterion of 30 mm of permanent deformation and development of extensive cracks at the bottom of the AC layer. The tests showed reduction of 30% in the maximum tensile strain transmitted to the bottom of the AC layer (ε_t) and 20-40 % of maximum vertical compressive stress at the top of subgrade. It was concluded from this study that a thickness saving ranging from 50mm to 100mm in asphalt thickness could result from geogrid placement at the lowest part of the AC layer.

Haas did not include geogrid stiffness and granular base thickness influences in the study.

Haas et al (1988) conducted intensive test programs to justify the importance of geogrid and its location within the base. For 0.8 in (2.03 cm) of surface deflection taken as a failure criterion, Haas, et al. showed that the base thickness could be reduced about 25 to 50 % .

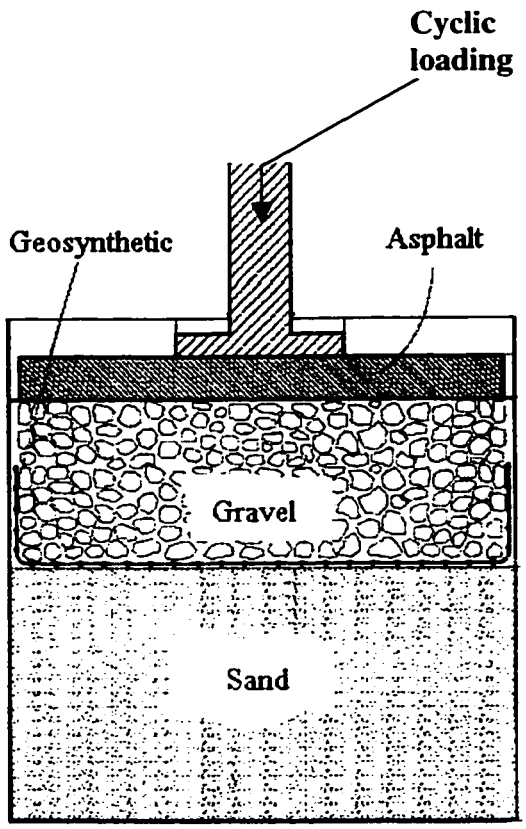

Figure (3.1) A typical conventional reinforced section under test

The optimum depth was found to be dependent on the granular base layer and the subgrade strength. After the first 10,000 load cycles (when a membrane effect has not been developed significantly, and the interlocking mechanism is predominant), the rut depth decreases from 0.8in (2.03 cm) for unreinforced system to 0.46in (1.16 cm) for the reinforced system. That reduction was higher for weaker subgrade. This conclusion occurs when initial strain beneath the load center is less than 0.2 percent for geogrid located at base-subgrade interface, the geogrid provides higher support because of its interlocking function. Checking the strength against pull out is not required in this case.

The best location can be chosen by using stress-strain analysis such that the radial strain under the load center at the proposed grid location should be within some limiting range between 0.05-0.2 %. In addition, grid placed at the midpoint of a 12in (30.48 cm) in base layer thick does not show any benefits until large deformation are attained.

Haas et.al, (1988) did not consider the effects of AC layer and base moduli on the performance of a geogrid-reinforced pavement system in their study. Moreover, the location influence on the fatigue of AC layer was also not considered in their investigations.

Miura et al.(1988) carried out a comprehensive laboratory investigations on the role of the geosynthetic reinforcement in pavements. The surface settlement was taken as a comparison criterion . They concluded that :

1-When placing the grid at the base-subgrade interface, the magnitude of the tensile strain in the geogrid is maximum at the center of loading test plate. The induced tensile force in a grid with a higher modulus is higher than that of a grid with a lower modulus, and the geogrid contributes more effectively to suppress the surface rutting.

2-If the grid is placed at the bottom of the AC layer, the performance of the asphalt pavement improves if strong bonding is maintained between the AC layer and the geogrid. Further improvement is obtained in the case of dynamic loading.

Miura et al stated that interlocking function was not considered in deformation analysis and further research work was necessary.

Special laboratory tests were conducted by Dave et al. (1988) to evaluate the resistance of geogrid reinforced asphalt-concrete (AC) beam to fatigue cracks.

The geogrid was laid at 1/3 of the thickness of the specimen from bottom surface. The failure criterion was defined when the crack grew throughout the entire cross section of the beam which was placed on a rubber mat idealizing the subgrade. The number of cycles to failure for the reinforced was much greater than for the unrinforced beam under different levels of loading. In addition, the surface settlement was also reduced compared to the reference unreinforced system.

Barksdale et al (1989) found that for the stronger pavement, the stiff geogrid at the bottom of the granular base did not produce any significant improvement. Their results indicated that the geogrid at the middle and bottom, despite its lower stiffness, resulted in a better performance against permanent deformation than the geotextile. This fact was highly pronounced for the first 10^5 load cycles. Permanent vertical deformation of the pavement was taken as a parameter to characterize the performance of a reinforced system compared to the unreinforced one. Permanent vertical strain, vertical resilient strain, transient stresses were also analyzed.

The geogrid positioned at the middle of granular layer may lead to a smaller increase rate in the horizontal stress at the top of this layer. For a relatively thicker base, the interlocking function did not play a significant role until large deformations occurred and the membrane affect became more effective.

Moghaddas and Small (1996) investigated the rule of a geogrid in a conventional pavement system and concluded that a remarkable reduction in the vertical surface deformation resulted from the interlocking function particularly in the vicinity of the reinforcement. In both single and multiple track tests performed, the smallest surface deformation was obtained with geogrid at the center of base layer.

Hoe and Liu (2001) attached the geogrid to the bottom of the asphalt concrete layer which was prepared separately and placed on Ottawa sand. Such installation of geogrid at the interface makes the field construction easier. Their program included monotonic and cyclic load tests and for two types of geogrid-polyester and polypropylene-which is able to achieve better interlocking with the surrounding medium. The loading was terminated when the loading actuator had reached its maximum capacity. The load-displacement relationship was approximately linear. obtained prior to failure for both the reinforced and unreinforced sections and the stiffness of the reinforced was 60% of the unreinforced in the linear range of load displacement curve. Hoe and Liu also measured strains induced along the geogrid. Polypropylene resisted a higher load and showed higher strains than polyester, because of its interlocking. For cyclic loading, the system reinforced with polypropylene showed three times higher strength than the unrinforced system strength and no debonding was noticed between the geogrid and AC layer when the system failed. This situation did not exist for the Polyester -reinforced AC layer. In the unrinforced system, failure first occurred in the asphalt along the edges of the footing, and then a shear failure was induced in the sand was induced. In their final remarks Hoe and Liu (2001) stated" to improve the rigidity of asphalt concrete layer.....

The geogrid is included as a tensile reinforcement. Pavement is improved if an effective bonding is maintained between the asphalt concrete and the geogrid. The reinforced asphalt pavement may also be designed by extending the layered theory (Burmister). Meanwhile the finite element procedure may be adopted with a more realistic representations of the soil, geogrid, and the AC layer".

Dondi (1996) also showed the beneficial effect of geogrid on a bituminous mix layer without including any supporting layer at the bottom. Dondi used a bending test beam to evaluate the added stiffness obtained from reinforcing a sample of bituminous mix with dimensions of 100*100*600 mm by a polyester woven geogrid with tensile strength 160 kN/m and placed at height of 35mm starting from the bottom.

The initial stiffness increased from 80N/mm to150 N/mm as a result of the reinforcing.

The ultimate strength of the reinforced beam was 60% higher than that of unreinforced beam, which means that after the initiation of failure or reflective cracking, bearing capacity of geogrid reinforced AC layer is still higher than the unreinforced one. Noticing that the cracks never reached the surface of the reinforced specimen and the main failure was represented by the sliding of that specimen confirmed the last observation.

Perkins (2001) tested three different locations of the geogrid, while varying its stiffness, base thickness and the subgrade strength

The impact of the reinforcement placed 40 mm above the base- strong subgrade interface was found to be very small.

For a weak subgrade, the surface deflection was reduced by 50% at 10000 cycles when it was placed at the middle of the base; this reduction was noticed to continue with increasing the number of cycles. The geogrid with a higher stiffness gave better Traffic Benefits Ratio (TBR). The increase in TBR when the geogrid placed at the middle was higher than the value obtained when the same geogrid was placed at base-subgrade interface.

When the rut depth becomes more than 10mm the geogrid in the system with a thicker base produced a higher TBR than the system with a thinner base. In Perkins program, the geogrid showed much better results than the geotextile toward improving the TBR and decreasing the rut depth. The effect of the geogrid and its location on the fatigue life of the pavement, the quality of the base and AC layers were not included in the study.

Table(3.1) lists the experimental test facility and the loading condition adopted for each of the experimental studies reviewed . Furthermore, the information regarding the range of layer thickness and the mechanical properties for each of the above-mentioned experimental studies are presented in Table(3.2) . Physical and mechanical properties of the geogrid used in these studies are also shown, as reported by manufacturing company in Table (3.3)

Table(3.1) Test facilities and load data used in the references reported in the literature

Reference	Facility test information	Load information
Haas et al. (1988)	Laboratory tank 4.5*1.8*0.9 m	Stationary circular steel plate Pressure=550 kPa Diameter =300mm Frequency=8 cycles/sec or 8 Hz
Miura et al. (1988)	Laboratory tank 1.5*1.5*1.0 m	Circular plate Pressure=200 kPa Diameter =200 mm Frequency=0.18 Hz (4 sec load and 2 sec unload)
Barksdale et al. (1989)	Indoor large track test 1.4*0.5*0.8 m	Multi-track test, random and transversely applied cycles Pressure=460-500 kPa Radius =68-76 mm Frequency=3.2-4.8 km/h
Small and Nejad. (1996)	Indoor large track test 1.4*0.5*0.8 m	Moving single wheel, and multiple wheel Pressure=210 kPa Radius =230mm Frequency=0.18 m/sec
Perkins. (1999)	Indoor large track test 2*2*1.5 m	Circular steel plate, Moving single wheel Pressure=550 kPa Diameter =305 mm Frequency=0.67 m/sec

Table (3.2) Layers and geogrid data used in the references reported in the literature

Reference	Layer thickness			Mechanical properties			Geogrid type and location
	AC (mm)	Base (mm)	Subgrade (mm)	AC	Base	Subgrade*	
Hass et al (1988)	75, 100	100,150, 200,250, 300	Not Reported	Only mix specific-ation were given	Gw, A-1-b	SP,A-3 CBR=8, 3.5, 1 %, Saturated	Geogrid A at Bottom, middle, Top of base
Miura et al (1988)	50	150 200	600	E=500 Kg/cm^2 ν=0.43	E=250K g/cm^2 ν=0.43	E=20K g/cm^2 ν=0.47	Geogrid B(top of subgrade, top of subbase) Geogrid C (top of subgrade)
Barksdale et al (1989)	32	208	425 1000	E=2874 (KPa) ν=0.43	E=211 (KPa) ν=0.43	CBR=2.6 % CBR=15 %	Geogrid A At the bottom of Base. Prestressed geogrid A at the middle
Small and Nejad (1996)	20	40	Not Reported	Mix specificati -on Only given	SP A-1-a	SP A-3	Geogrid B at base-subgrade interface,At the middle of base
Perkins (1999)	75	200 300 375	1045 1128 970	3400 3920 1710	A-1-a or GW with friction angle of 48 degree	CBR=15, 1.5 %	Geogrid A at base-subgrade interface and 40mm above interface. Geogrid A at the middle of base. Geogrid B at base-subgrade interface

Table (3.3) Properties of the geogrids used by references reported in the literature

Geogrid	Company, Product name	Structure	Polymer type	Mass/ unit area g/cm^2	Apera -ture size (mm)	Secant modulus at 5% strain (kN/M)	Flexural rigidity (g-cm)
A	Tensar,BX1100	PSDB	PP	203	25/36	120/260	250
B	Tensar,BX1200	PSDB	PP	306	25/33	220/400	750
C	Tensar,BX1300	PSDB	PP	247	46/64	220/340	450

PSDB= Punched, sheet drawn biaxial
PP= Polypropylene
*The modulus of subgrade can be calculated from the CBR of the subgrade using the equation developed by Shell:
$E_{subgrade}=10*CBR$ (MPa).
Experiments carried out by The National Danish Road Laboratory gave more accurate relation as follows:
$E_{subgrade}=10*CBR^{0.73}$ (MPa)

3.2 Finite element studies

All numerical analyses studies reviewed in this section use the finite element method as the analysis tool. Barksdale et al (1982) presented a detailed study on modeling soil-aggregate system reinforced at the interface by a geotextile fabric. They used eight nodes-isoparametric plane element for a nonlinear large displacement analysis for the base which considered the nonlinear geometric and material nonlinearties. By changing the geometry, as the body undergoes large displacement, stresses-strains and displacements for each configuration can be obtained. The granular base is modeled by Drucker-Prager material model, the portion of the granular material placed immediately above the geosynthetic fabric had special attention, because of the tensile state of strain existence in this area.. Slippage between the fabric and adjacent material was represented by interface elements, and the maximum allowable shear at interface was given by dynamic direct shear test giving the interface properties Linear, two- dimensional, axisymmetric, and

plane strain fabric element, as an extension of a one-dimensional pinned bar element, was used to simulate the geotextile behavior. For a moderate rut depth their model gave a good agreement with the measured data.

Miura et al (1988) modeled the geosynthetic fabric as a truss and assumed the stiffness of the joint elements. They did not consider the interlocking function, hence their prediction model did not agree with the realistic behavior of the reinforced system.

Barksdale et al (1989) used axisymmetric representation for the pavement system. They suggested two models for the base, the first was a non-linear isotropic elastic-plastic model, and the second was a cross anisotropic model. The geogrid was modeled by a membrane element. Their model underestimated the vertical strain at the top of subgrade and overestimated the strain induced in the geosynthetic located at the bottom of the bases by 33%

De Bondt (1995) and X-Liu et al (1998) established average values of the bonding stiffness representing adhesion and bearing mechanisms of the grid when surrounded by granular materials

Six-noded interface elements were utilized for bond between the reinforcement and the granular materials. They also specified anisotropic constitutive law for modeling the granular base and they used the results of Sweere (1990) to obtain the parameters of different unbound materials. The tensile strain at the bottom of the AC layer and the surface deflection, were not considered as comparison criteria in their study. Instead they used the propagating speed of reflective cracking as the comparison criteria which was analyzed through the Paris law (they assumed that the crack was already initiated) and the

enhancement of the bearing capacity added to the base when reinforced .Their study did not consider the significance of the geogrid location in the system.

In his FE simulation study, Perkins (2001) used a three dimensional model to simulate the pavement system placed in the test box. Perkins's first model represented the unreinforced system, the second model was called a perfectly reinforced FE model in which the lateral displacement of the base at the interface with geogrid was prevented completely. This was achieved by modifying the previous model by prescribing boundary conditions at the nodes at the bottom of the base. In this model, the reinforcement was assigned an infinitely stiff contact with interface.

The third model assumed the sheet of the geogrid as part of the pavement cross-section. In this situation, the material model for the geosynthetic reinforcement was formulated to include components of elasticity, plasticity, creep, and direction dependency. The parameters of these modes of behavior were defined from laboratory tests (Perkins, 1999) and incorporated in the constitutive laws of elasticity and plasticity. The geogrid was effectively modeled by a membrane type (4-node quadratic) two dimensional element, and it was formulated to have in-plane strain and shear stiffness and strength without taking any bending or compression with a thickness of 1mm and Poisson's ratio of 0.5.

The Coulomb friction model was used to describe the interaction between the geosynthetic reinforcement and the base aggregate layer. The model provided reasonable prediction of the pull out test conducted by Perkins .Two steps were followed to simulate the interactions:

Firstly, the boundary conditions were assumed to obtain the interaction parameters. This was done separately through a special numerical solution which assumed that surrounding soil is a rigid body such that absolute movement of the geogrid was equivalent to a relative movement between the geogrid and the surrounding media. This simplified model considered that the shear stress and the displacement between the geogrid and surrounding medium are functions of the initial interface modulus, the peak and residual friction angles for the interface, and the normal stress on the interface. These material parameters were varied until a reasonable match was achieved between the experiments of pull out test data and the model test predictions.

Secondly, calibration of the material parameters contained in the geogrid-aggregate interaction Mohr- Coulomb model was accomplished by creating a finite element model for pull out box, and the initial values of the material parameters used in the Coulomb model were assumed from the previous simplified numerical model.

The AC was modeled by anisotropic elastic-perfectly plastic model .

The plasticity implementation in the model allowed the pavement layer to deform permanently with the underlying base. The anisotropy allowed for the reduction of the flexural stiffness of the AC layer, preventing it from acting completely as an elastic slab, while maintaining the vertical stiffness in compression.

A boundary surface plasticity model was used for both the subgrade and the aggregate materials. This mode uses a yield surface formulation extended from the critical state of soil . The model showed elastic-plastic behavior with isotropic hardening. This model has the ability to describe the accumulation of permanent strain under repeated load and

requires assigning many materials constants (Kaliakin et al, 1987) Such a model is discussed in detail by Dafalias and Hermann (1982)

The models prescribed above employed one contact interface, namely the one between the geogrid and the bottom of the base, The FE results reported by Perkins indicated the importance of the shear stress transmitted to the subgrade. The many models suggested by Perkins which included another set of interface elements at the down interface, contact interface between the geogrid and underlying subgrade, did not give the anticipated results. The same difficulties were encountered when the geogrid was placed within the base. Perkins stated that these cases required improvements in the base aggregate model to account for the effects of the reinforcement. He pointed out that further examination of the contact interface model on a reinforced system should be performed. The tensile strain at the bottom of the AC layer, and the effect of geogrid placement at the bottom of AC layer on the performance of the system were not treated in that study.

Table (3.4) summarizes the FE studies conducted by different researchers to model the layers of the reinforced pavement system

Table (3.4) Finite element studies (after Perkins, 2001)

Author	Burd &. Houlsby (1986)	Barksdale et al. (1989)	Burd & Brocklebutst (1990)	Burd & Brocklehurst (1992)	Dondi (1994)	Miura et al (1990)	Wathugala el al,. (1996)
Analysis Type	Plane strain	Axi-symmetric	Plane strain	plane strain	Three-dimensional	Axi-symmetric	Axi-symmetric
AC Constitutive Model	None	Isotropic. non-linear elastic	None	None	Isotropic. Linear elastic	Isotropic, linear elastic	Isotropic elastoplastic, D-P
AC Thickness (mm)	None	Variable	None	None	120	50	89
Base constitutive Model	Isotropic elastoplastic, Matusoka	Anisotropic. Linear elastic	Isotropic elastoplastic, Matusoka	Isotropic, elastoplastic, Matusoka	Isotropic, elastoplastic, D-P	Isotropic linear elastic	Isotropic, elastoplastic, D-P
Base Thickness (mm)	75	Variable	300	300	300	I50	140
Geosynthetic Constitutive model	Isotropic, linear elastic	Isotropic, linear elastic	Isotropic, linear elastic	Isotropic, linear elastic	Isotropic, linear elastic	Isotropic, linear elastic	Isotropic, elastoplastic, Von Mises
Geosynthetic Element	Membrane	Membrane	Membrane	Membrane	Membrane	Truss	Solid continuum
Goosynthetic Thickness (rnm)	None	None	None	None	None	None	2
Interface element and interface model	None	Linear elastic-perfectly plastic	None	Elastoplastic, Mohr-Coulomb	Elastoplastic, Mohr-Coulomb	Linear elastic Joint element	None
Subbase Constitutive Model	None	None	None	None	None	Isotropic, linear elastic	Isotropic, elastoplastic, Hiss
Subbase Thickness mm	None	None	None	None	None	200	165
Subgrade Constitutive Model	Isotropic, elastoplastic, Von Mises	Isotropic, non-linear elastic	Isotropic, elastoplastic,Von Mises	Isotropic, elastoplastic. Von Mises	Isotropic, elastoplastic, Cam Clay	Isotropic, linear elastic	Isotropic, elastoplastic, Hiss
Load Application	Monotonic, footing width 75 mm	Monotonic	Monotonic, footing width 500 mm	Monotonic, footing width ~ 500 rnm	Monotonic, two rectangular areas 240 mm x 180 mm	Monotonic, 200 mm diameter plate	Single cycle,peak pressure = 725 kPa on a 180 nun diameter plate
Remarks, on Observed Improvement	improvement seen after a penetration of 4 min. Model over predicted improvement beyond a 4 mm displacement	Base layer could be reduced in thickness bv 4-18 %. Greater improvement seen for sections with weak subgrade	Improvement seen after a penetration of 12 mm. Improvement increased with increasing geosynthetic stiffness	Improvement seen after a penetration of 25 mm	15-20 % reduction in vertical displacement, fatigue life of section increased bv a factor of 2--2-5	5 reduction in vertical displacement Improvement level did not match experimental result	20 % Reduction in Permanent Displacement

Chapter 4

CONSTITUTIVE MODELS FOR GEOGRID-REINFORCED FLEXIBLE PAVEMENT SYSTEM LAYERS

Mathematical modeling of the mechanical behavior of the engineering materials of a pavement system requires the definition of the constitutive relations, which are then implemented in the modern numerical techniques to obtain solutions for the analyzed pavement systems. The accuracy of the numerical solution depends on the constitutive law assigned for each layer, which is usually considered to be continuum, in the pavement.

The purpose of this chapter is to discuss the "realistic" mechanical behavior of each layer in the pavement system and the associated constitutive laws that could reflect, as much as possible, such behavior. At the end, the most suitable constitutive laws related are selected for the finite element simulations.

4.1 Asphalt concrete layer

The mechanical behavior of AC layer is very complex behavior. Its bituminous mix exhibits viscoelastic behavior at low temperature and visco-elasto-plastic response at high temperatures (Harold, 1994). Visco-elasto-plastic analysis of asphalt mixture is considered tedious and requires considerable amount of empirical work to decide the model parameters. This can be seen in the works of (Lu and Wright, 1997; Mordechai et al, 1983). Figure(4.1) illustrates the elasto-viscoplastic response of AC material to a single load cycle

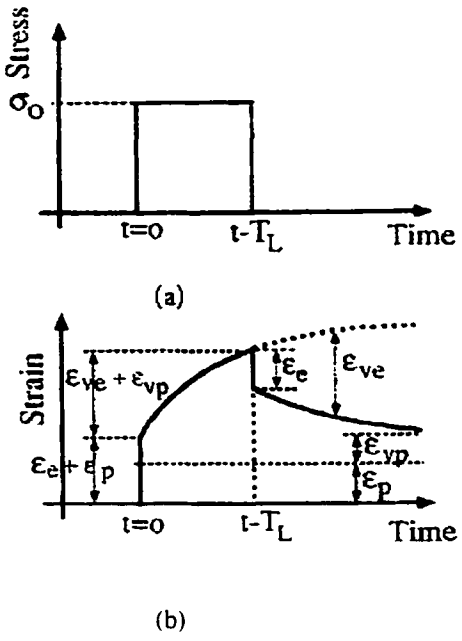

Figure (4.1) Visco-elasto-plastic behavior of (AC) during one loading cycle (a)dynamic load (b) response (Harold, 1994).

The viscoelastic model is considered to be more practical and flexible for describing the behavior of AC and implementing such behavior in FE (Finite Element) simulations is simpler than the visco-elasto-plastic model. In addition, the contribution of AC to the plastic permanent deformation is considered insignificant compared to those of granular base and subgrade materials. These reasons have encouraged researchers (Collopet et al, 1995; Papagiannakisct et al, 1996; White et al, 1995; Sameh and Thomas, 1997; Dong et al, 2002) to use this model.

In the subsequent section, the important basics of the linear viscoelastic behavior of the (AC) layer with the associated mathematical laws and physical concepts are presented.

4.1.1 Viscoelastic mechanical behavior of (AC)

The viscoelastic mechanical behavior of AC can be empirically defined by one of the following moduli:

-Creep modulus

-Complex modulus

4.1.1.1Creep modulus:

According to the viscoelastic behavior, the strain-stress curve is affected by loading time and temperature. In a relaxation test, a step of constant strain is applied and the stress $\sigma(t)$ is measured. If the material behaves linearly, the stress can be given by:

$$\sigma(t) = \varepsilon_0 E(t) \tag{4.1}$$

The function E(t) is called the relaxation modulus (material property)

On the other hand, the creep test requires a step of constant stress and the strain is calculated from:

$$\varepsilon(t) = \sigma_0 J(t) \tag{4.2}$$

The function J(t) is called the creep compliance (material property)

Using the integral representation, the linear viscoelastic material can be prescribed through strain history or stress history given by the superposition integral (Hereditary or Boltsman's integral):

$$\sigma(t) = \int_0^t E(t-\zeta)\frac{d\varepsilon(\zeta)}{d\zeta}d\zeta \tag{4.3}$$

$\sigma(t)$ gives the stress history for a linear elastic non-aging material, $E(t-\zeta)$ is the uniaxial relaxation model, $\varepsilon(t)$ is the strain at the dummy variable ζ, and ζ is the variable of integration (dummy variable). Superposition integral is used efficiently to calculate the strain history resulting from a dynamic or cyclic load. For studying the thermal effects, the pavement can be considered a thermological simple material, which means that there exists a function of temperature f(T) directly related to the temperature dependency on the viscosity of the AC layer, such that the time axis may be mapped into the ξ axis according to the general equation

$$\xi(xi,t) = t / f[T(xi)] \qquad (4.4)$$

Where $\xi(xi,t)$ is the modified time scale (reduced time)

Accordingly a new system of axes, $[E(\xi), \xi]$, is created for which all the curves of E(t) at various temperatures can be coalesced into a single curve (master curve) corresponding to a reference temperature when plotted versus ξ.

Practically, if the creep compliances under a reference temperature (T_0) are known for specific time intervals, then those under any given temperature T can be obtained for the same time intervals by using the temperature shift factor (a_T)

$$a_T = t_T / t_{T_0} \qquad (4.5)$$

Laboratory tests on asphalt mixes have shown that a plot of log (a_T) versus temperature results in a straight line of slope

$$\beta = \log (t_T / t_{T_0}) / (T - T_0) \qquad (4.6)$$

β may vary from 0.061 to 0.170 with an average value, given by Federal Highway Administration (FHWA), of about 0.113. If the creep compliance based on reference temperature To is given through generalized Burger rheological model, which is originally given as (Yang,1993)

$$D(t) = \frac{1}{E_0} \times (1 + \frac{t}{T_x}) + \sum_{i=1}^{N} \frac{1}{E_i} (\exp(\frac{-t_{T_0}}{T_i})) \qquad (4.7.a)$$

where T_i is retardation time, T_x is relaxation time.

Figure (4.2) below shows the basic rehological models for viscoelastic materials

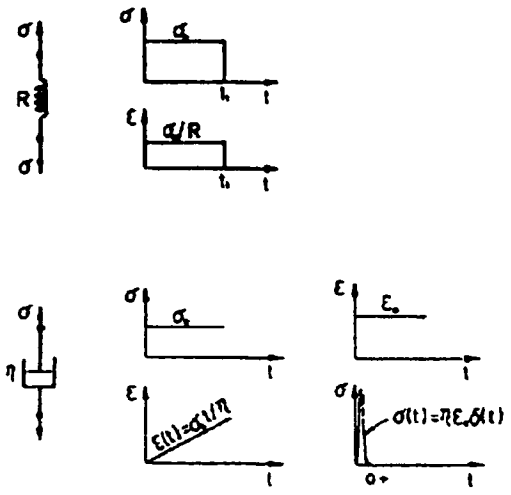

(a) Basic linear elastic and viscous models

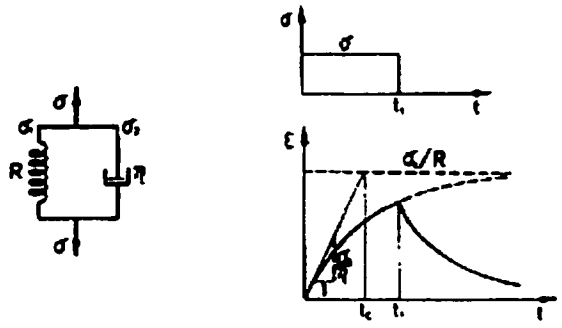

(b) Kelvin model

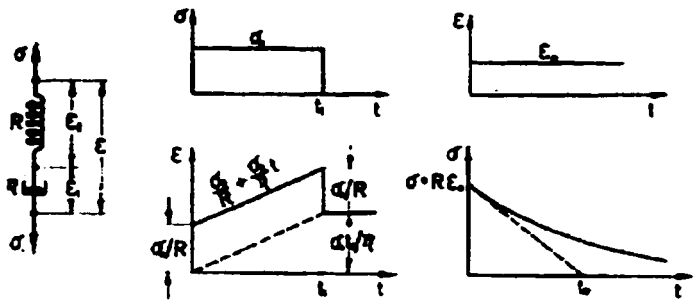

(c) Maxwell model

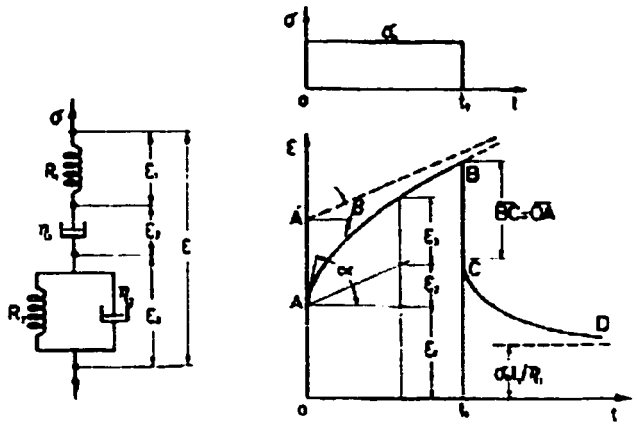

(d) Burger model

Figure (4.2) Simple rheological models for viscoelastic materials (William et al.1976)

As the creep compliance D(t) caused by the viscous strain resulting from the short duration of the moving load is negligible, the creep compliance based on the reference temperature To becomes (Yang,1993):

$$D(t) = \sum_{i=1}^{N} G_i \exp(\frac{-t_{T_0}}{T_i}) \qquad (4.7.b)$$

The creep compliance based on reference temperature T is

$$D(t) = \sum_{i=1}^{N} G_i \exp(\frac{-t_T}{T_i}) \qquad (4.8)$$

Where G_i are constants obtained from regression. The relationship between t_T and t_{T0} is given in Equation (4.5)

Table (4.1) Basic and simple rheological models implemented in more generalized rheological models to reflect the realistic behavior of viscoelastic AC, with the corresponding constitutive laws

Model		Constitutive relation
Spring (linear)		$\sigma = R\varepsilon$
Dashpot (linear)		$\sigma = \eta \dot{\varepsilon}$
Maxwell	Under constant stress	$\varepsilon(t) = \sigma_0 / R + (\sigma_0 / \eta)t$
	Under constant strain	$\sigma(t) = R\varepsilon_0 e^{\frac{-Rt}{\eta}}$
Kelvin (Under constant stress)		$\varepsilon(t) = \sigma_0 / R(1 - e^{\frac{-Rt}{\eta}})$
Burger		$\sigma + (\frac{\eta_1}{R_1} + \frac{\eta_1}{R_2} + \frac{\eta_2}{R_2})\dot{\sigma} + \frac{\eta_1\eta_2}{R_1R_2}\ddot{\sigma} = \eta_1 \dot{\varepsilon} + \frac{\eta_1\eta_2}{R_2}\ddot{\varepsilon}$

*The Kelvin model does not show a time-dependent relaxation. Owing to the presence of the viscous element, an abrupt change in strain ε_0 can be accomplished only by an infinite stress.

Generalized Maxwell model could also be a suitable rheological simulation of (AC) layer for obtaining a suitable realistic relaxation modulus, or creep compliance being able to reflect the actual response of (AC)

$$E(\xi) = \sum_{i=1}^{N+1} E_i e^{\xi/\lambda i} \qquad (4.9)$$

Where E(t) is the relaxation modulus at reduced time, E_i, λ_i are the Prony series parameters for master relaxation modulus curve.

The creep test is easier, more practical and controllable to be conducted than the relaxation test. After conducting the creep test at different temperature, relaxation modulus is obtained after transforming the following equation

$$D(\xi)=D(0)+\sum_{i=1}^{N} D_i(1-e^{-\xi/\lambda i})+\xi/\eta_v \tag{4.10}$$

Where D (ξ) is the creep compliance at reduced time ξ; ξ is reduced time; D (0), D_i, λ_i, η_v are Prony series parameters.

Linear viscoelastic constitutive laws and formulas based on relaxation and creep moduli data:

The constitutive laws of the linear viscoelastic, isotropic (AC) layer which are traditionally employed in the finite element analyses are (ADINA,2001)

$$S_{ij}(t) = 2G(0)e_{ij}(t) + 2\int_0^t e_{ij}(t-\zeta)\frac{dG(\zeta)}{d\zeta}d\zeta \tag{4.11}$$

$$\sigma_{kk}(t) = 3K(0)\varepsilon_{kk}(t) + 3\int_0^t \varepsilon_{kk}(t-\zeta)\frac{dK(\zeta)}{d\zeta}d\zeta \tag{4.12}$$

Where ζ is the dummy variable for conducting superposition integral, t is the real time

Accounting for temperature variations with time T(t)

$$S_{ij}(t) = 2G(0)e_{ij}(t) + 2\int_0^t e_{ij}(\xi-\chi)\frac{dG(\chi)}{d\chi}d\chi \tag{4.13}$$

$$\sigma_{kk}(t) = 3K(0)[\varepsilon_{kk}(t) - 3\alpha_0\theta(t)] + 3\int_0^{\xi}[\varepsilon_{kk}(\xi-\chi) - 3\alpha_0\theta(\chi)]\frac{dK(\chi)}{d\chi}d\chi \tag{4.14}$$

Where $S_{ij}(t) = \sigma_{ij} - \frac{1}{3}\delta_{ij}\sigma_{kk}$ is the deviatroic shear strain at time t, and

$e_{ij}(t) = \varepsilon_{ij} - \frac{1}{3}\delta_{ij}\varepsilon_{kk}$ is the deviatoric strain G(t) is the shear modulus, K(t) is the bulk modulus, $\varepsilon_{kk} = (\varepsilon_{11} + \varepsilon_{22} + \varepsilon_{33})$ is the volumetric strain that is the volume change per unit volume

$\sigma_{kk} = (\sigma_{11} + \sigma_{22} + \sigma_{33})$ is the first invariant of stress tensor

ξ is the reduced time, χ is the dummy variable for conducting the superposition integral for the new axis of ξ reduced time

The relation between the reduced time ξ and the real time is established through the shift function $\phi[A, B, T_0, T(\zeta)]$ as follows (ADINA,1999)

$$\xi = \int_0^t \phi \, d\zeta \tag{4.15}$$

$$\phi(T=T_0)=1,\ \phi(T)>0,\ \frac{d\phi}{dT}>0 \tag{4.16}$$

and the dummy variable χ for the reduced time is

$$\chi = \int_0^{\zeta} \phi[T(\eta)]d\eta \tag{4.17}$$

$$\theta(t) = 1/\alpha_0 \int_{T0}^{Tt} \alpha(T')\ dT' \qquad , \alpha_0 = \alpha(T_0) \tag{4.18}$$

$\alpha(t)$ is the temperature-dependent coefficient of thermal expansion.

The shift time factor is given according to Ferry-William-Landel equation as

$$\log \phi = \frac{A(T - T_0)}{B + (T - T_0)} \tag{4.19}$$

A sample of a master curve for AC is shown below in Figure (4.3)

If the temperature is constant one obtains equations (4.11) and (4.12).

The material properties required for viscoelastic modeling of the AC is data of

G(t) and K(t), in addition to the shift time factor constants.

Using of Prony series the integral forms giving G(t) and K(t) can be transformed to

$$G(t) = G_{\infty} + \sum_{i=1}^{\eta_G} G_i \, e^{(-\beta_i t)} \tag{4-20}$$

$$K(t) = K_{\infty} + \sum_{i=1}^{\eta_k} K_i \, e^{(-\gamma_i t)} \tag{4-21}$$

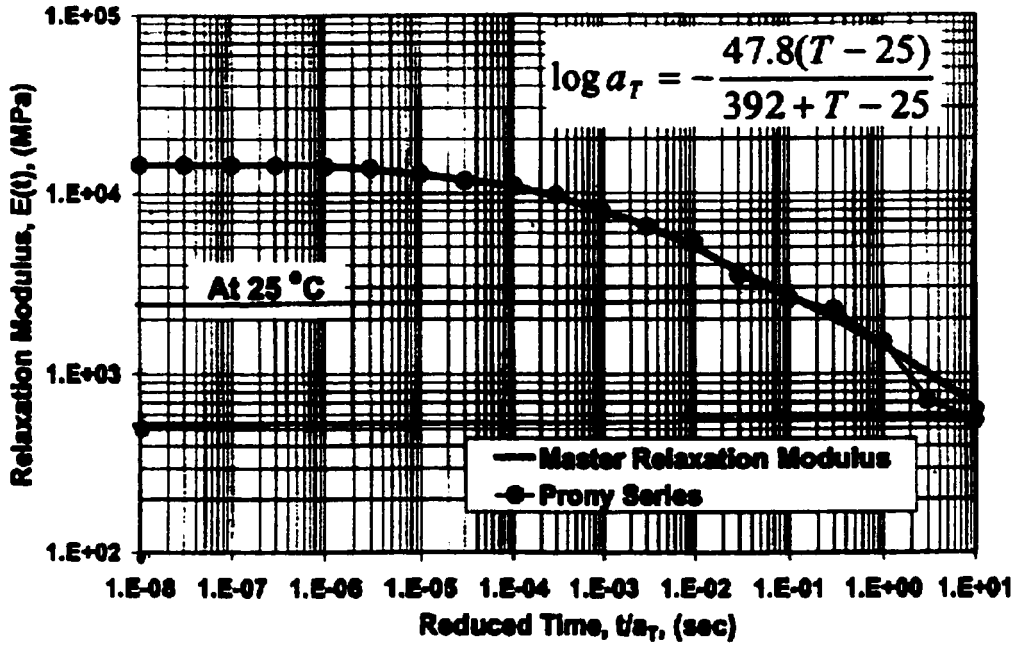

Figure (4.3) Sample of master curve and shift time factor used in the simulation of Dong (2002).

Where:

G_{∞}, K_{∞} are the long term shear modulus and bulk modulus, respectively

β_i , γ_i are the decay constants for the shear modulus and bulk modulus, respectively

$\beta_i = \frac{E_{G_i}}{\eta_{G_i}}$, $\gamma i = \frac{E_{k_i}}{\eta_{k_i}}$ are the inverse relaxation times when generalized Maxwell model is adopted for representing the AC to get its G(t) value from shear creep test or its K(t) from pressure creep test , and the inverses of the retardation times when generalized The Burger model is adopted for representing the AC to get its G(t) from the shear creep test or its K(t) value from pressure creep test , and the retardation η_G , η_K are the number of time-dependent terms or, in other words they are the viscosities of the dashpots existing in the rehological model representing AC in pure creep shear test , and in creep pressure test, respectively.

These two properties are obtained after adopting a suitable rheological model for AC (generalized Maxwell or Burger) and conducting the creep pressure test to get K (t) and the creep shear test G(t).

Usually a 1000-s creep test with the stresses measured at time intervals varying according to the number of parameters in the suggested rehological model is conducted to get the creep data. If it is required to include temperature-dependency, then the nodal point temperatures at all solution steps must be defined. Numerically, the nodal temperature for all solution steps can be defined via direct input, in which case the time variations of the temperature are specified by time function. Figure (4.4) shows the variation of temperature, which is assumed to change with depth only (Dong, 2001) .

The viscoelastic behavior of (AC) can be assumed incompressible. Sam et al (1998) investigated the AC dependency on the stress history (speed or frequency), and they used the following constitutive laws:

$$\begin{Bmatrix} G(t) = G_R + (G_G - G_R)\, e^{-\beta t} \\ \left\{ \frac{\partial S_{ij}}{\partial t} = 2 \int G(t-\zeta)\left(\frac{\partial e_{ij}}{\partial \zeta}\right) d\zeta \right\} \\ P = -K\varepsilon_v \end{Bmatrix} \tag{4.22}$$

In this case only, G_G (instantaneous or initial shear modulus), G_R (long term shear modulus), β (relaxation time) and the elastic bulk modulus are needed for FE simulation The initial shear modulus is the elastic G =E/2(1+v), and G_R is assumed according to the suggested rheological model and relaxation time. They assumed it to be $G_R = G_G/2$

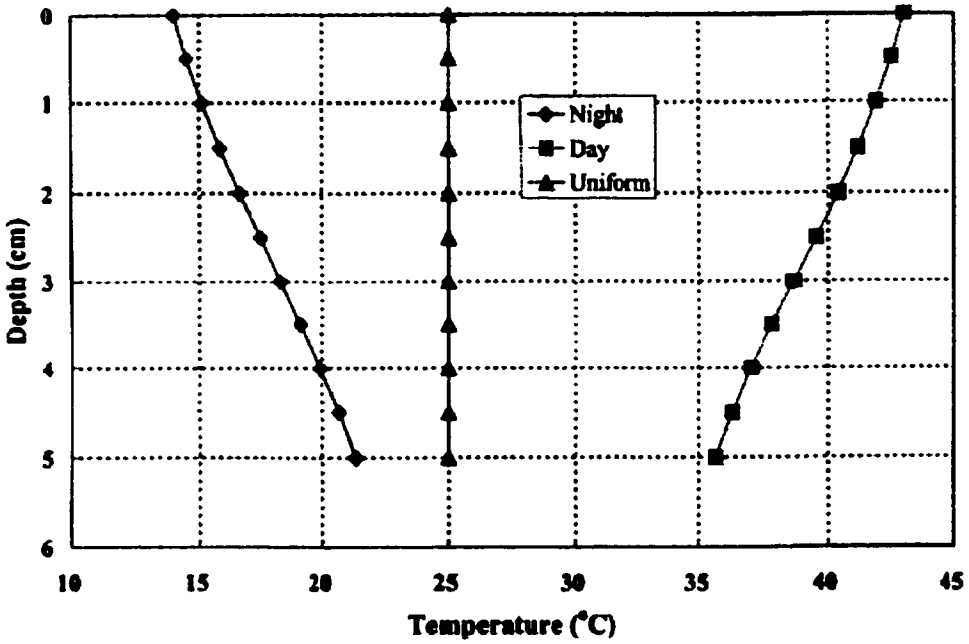

Figure (4.4) Assumption of temperature change with depth only and three suggested distributions of temperature through AC layer (after Dong et al, 2002).

4.1.1.2 Complex modulus

The complex modulus is used to characterize the damped viscoelastic material. It requires haversine or sinusoidal loading with no rest period (frequency domain analysis).

$$E^* = E1 + i\,E2 \tag{4.23}$$

where: $E1=(\frac{\sigma_0}{\varepsilon_0})\cos\delta$ is a measure of the elastic stiffness. It is associated with the energy storage and release during periodic deformation.

$E2=(\frac{\sigma_0}{\varepsilon_0})\sin\delta$. characterizes the internal damping and measures the viscous behavior. It is associated with dissipation of energy and transforming it into heat.

σ_0 is the stress amplitude, ε_0 is amplitude of the recoverable strain , δ is the phase angle by which strain lags stress . δ is determined from the test and it is dependent on temperature and frequency. It is a measure of the viscous response.. The complex modulus can also be written as

$$E^* = |E^*| e^{i\delta} \tag{4.24}$$

$|E^*| = (\frac{\sigma_0}{\varepsilon_0})$ is the dynamic modulus which measures the elasticity of AC . It is a function of temperature.

Witczak and Root (1974) showed the dynamic modulus and angle phase for different AC mixes at variant temperatures and frequencies. They concluded that the elastic part of the complex modulus $|E^*|$ may be predicted at any load frequency from the results of flexural stiffness values obtained by flexural fatigue beam test according to the formulas:

$$E_s = E_0 A_1^{\sigma} \tag{4.25}$$

$$|E^*| = A_2 f^a E_0^{\left(\frac{b}{f^c} - d\right)} \tag{4.26}$$

where:

E_s is flexural stiffness at applied stress σ, A1= regression constant depends on temperature, A_2=0.1808, a=2.1456, b=14.6918, c=0.01,d=13.5739

f= test frequency in Hz

Saraf and Majidzadeh (1974) related the dynamic modulus to the viscosity of the binder as follows:

$$\left|E^*\right| = 3.12\times10^{4}\ (\text{viscosity of binder})^{0.1607} \tag{4.27}$$

Analytically, the complex modulus can be obtained using the differential constitutive equations of the viscoelastic material

$$P\sigma = Q\varepsilon \quad \text{Where} \tag{4.28}$$

$$\left\{\begin{array}{l} P = \sum_{J=0}^{J=m} p_j \dfrac{\partial^j}{\partial t^j} \\ Q = \sum_{J=0}^{J=m} q_j \dfrac{\partial^j}{\partial t^j} \end{array}\right\} \tag{4.29}$$

$$\sigma = \sigma_0 e^{i w t} \tag{4.30.a}$$

$$\varepsilon = \varepsilon_0 e^{i(wt-\delta)} \tag{4.30.b}$$

w is the angular velocity , and σ_0 is the stress amplitude, ε_0 is the strain amplitude

δ is the phase angle by which strain lags stress . As

$$E^* = \frac{\sigma}{\varepsilon} \tag{4.30.c}$$

After substituting equations (4.28), (4.29) in equation (4.30) equations and applying Fourier transformation to both sides of equation (4.30) to remove the time dependency (as one usually does when using the Laplace transformation to mathematically transform the material from viscoelastic ; i.e, remove the time variable, to an elastic one) then one

takes the inversion of Fourier transformation to reach the complex modulus as given in equation (4.23)

$$E^* = f1(w) + if2(w) \tag{4.31}$$

Alternatively, a complex modulus can be obtained from creep or relaxation modulus data which was described in the previous section .

It is assumed that $\zeta' = t - \zeta$ and substitute in (4-30) then one gets the following equations after applying Fourier transformation

$$E1(w) = \int_0^\infty E(\zeta') \sin w\zeta' \, d\zeta' \tag{4.32}$$

$$E2(w) = \int_0^\infty E(\zeta') \cos w\zeta' \, d\zeta' \tag{4.33}$$

The results of the complex test have been compared to the results of creep test quite successfully (Pagan, 1965).

The thermological concept is also applied when dealing with the complex modulus (Terrel et al, 1974) conducted condensed tests and obtained very useful graphs for time shift factor at different temperatures and binder content ratios.

Curves of Master complex modulus $|E^*|$ versus reduced frequency for many AC mixes at reference temperature =70° F were also established in details by Terrel et al (1974).

Terrel at el (1974) found that the value of complex modulus is equivalent to the stiffness of the free elastic parameter in the four-element model computed from creep test.

4.2 Granular materials and soil

4.2.1 Nonlinear elastic and orthotropic elastic response

The elastic response for the granular materials and soil may be considered to depend on the stress levels. Such dependency has been mathematically optimized and modeled by Hicks and Monismith (1971) and Uzan (1985). Demonstration of granular base and soil non linearity can be also obtained from in-situ measurements by back analysis procedure using the Weight Deflectometer test or from using the repeated load triaxial equipment which is usually used to get resilient moduli of grained soils, ,granular materials and asphalt mix materials. The nonlinearity of the granular material has been frequently represented by the relation (Uzan,1985; Yang, 1993):

$$M_R = K \times \sigma_\theta^{\,n}, \qquad (4.34)$$

where :

M_R is resilient modulus

K, n are materials properties. They are given for many types of the granular materials by Yang (1993)

σ_θ is bulk stress: the sum of the principal stresses or (first stress invariant)

The K-σ_θ model, however, can give inaccurate results since it neglects the important effect of the shear stress on the resilient modulus. That is concluded by Uzan (1985). The Uzan's model considers the shear stress effects in the granular materials as the following relation shows;

$$M_R = K_A \left(\frac{\sigma_\theta}{P_0}\right)^{K_B} \left(\frac{\sigma_d}{P_0}\right)^{K_C} \qquad (4.35)$$

σ_θ bulk stress

$\sigma_d = \sigma_1 - \sigma_3$ (deviator stress)

P_0 unit reference pressure (1kPa or 1psi)

K_A, K_B, K_C material constants obtained from repeated load triaxial test performed on granular material

Erol and Marshall (1997) adopted the orthotropic behavior as a remarkable response of unbound material, particularly for the granular base medium where the moduli in compression and tension are different. The stress strain relationship for a linear orthogonal response is:

$$\begin{bmatrix} \varepsilon_x \\ \varepsilon_y \\ \varepsilon_z \\ \gamma_{xy} \\ \gamma_{xz} \\ \gamma_{yz} \end{bmatrix} = \begin{bmatrix} \frac{1}{E_x} & \frac{-\nu_{yx}}{E_y} & \frac{-\nu_{zx}}{E_z} & 0 & 0 & 0 \\ \frac{-\nu_{xy}}{E_x} & \frac{1}{E_y} & \frac{-\nu_{zy}}{E_z} & 0 & 0 & 0 \\ \frac{-\nu_{xz}}{E_x} & \frac{-\nu_{yz}}{E_y} & \frac{1}{E_z} & 0 & 0 & 0 \\ 0 & 0 & 0 & \frac{1}{G_{xy}} & 0 & 0 \\ 0 & 0 & 0 & 0 & \frac{1}{G_{xz}} & 0 \\ 0 & 0 & 0 & 0 & 0 & \frac{1}{G_{yz}} \end{bmatrix} \begin{bmatrix} \sigma_x \\ \sigma_y \\ \sigma_z \\ \tau_{xy} \\ \tau_{xz} \\ \tau_{yz} \end{bmatrix} \tag{4.36}$$

where $E, G,$ and ν refer to the elastic modulus, shearing modulus, and Poission ratio, respectively, where the subscripts x ,y denote the in-plane horizontal directions, and z denotes the vertical direction .

Five material properties are needed to define cross anisotropic elastic material under ax-symmetric case(Zienkiewicz and Taylor, 1989) they are

E_h is the anisotropic material elastic modulus in the horizontal direction

E_v is the anisotropic material elastic modulus in the vertical direction

ν_v is the Poisson ratio in the vertical direction

ν_h is the Poisson ratio in the horizontal direction

G is the shearing modulus

The Poisson's ratios for the different layers has a relatively small effect on pavement responses. Therefore it is customary to assume reasonable values in designing the layers (Yang 1993). For pure linear elastic material, elasticity modulus and thickness effects of each layer on the stress- strain state induced in each layer was investigated in detail by Yang (1993) .

4.2.2 Elastoplastic mechanical behavior

The elastoplastic behavior of soil and granular materials; i.e, the recoverable response at low stress levels and irrecoverable response at higher stress levels, is well documented (Desai and Siriwardane, 1984; Baladi and Chen, 1985). The unwanted pavement situation with excessive surface deflection and pavement fatigue is mainly a consequence of the elastoplastic behavior of subgrade and granular base.

Implementing the plasticity theory in a pavement system analysis toward a suitable finite element simulations for these materials requires clear understanding of many concepts, principles, and models related to the plastic behavior of such materials. In the concept of plasticity the development of incremental stress-strain relation is based on the following essentials

(i) The existence of initial and subsequent yield surfaces

(ii) The formulation of an appropriate loading rule that describes the evolution of subsequent loading surfaces (perfect plasticity, isotropic hardening, kinematic hardening and so on)

(iii) A flow rule specifies the general form of the stress-strain relationship.

The following subsection will treat the concepts associated with ideal plastic material.

For an elastoplastic material the total incremental strain

$$d\varepsilon_{ij} = d\varepsilon_{ij}^{P} + d\varepsilon_{ij}^{e} \tag{4.37}$$

$d\varepsilon_{ij}^{P}$ is the plastic strain increment)

$d\varepsilon_{ij}^{e}$ is the elastic strain increment)

The elastic-perfectly plastic (elastoplastic) assumption is a special case of the general plasticity theory. The Drucker's postulates for ideal elastoplastic material are

(i) Yield surface should be convex in stress space.

(ii) Yield surface and plastic potential should coincide which leads to an associated flow rule.

(iii) The material must not collapse during yielding, or its strength must not decrease during failure under increasing loads; i,e, the material is not softening.

(iiii) The material is non-hardening.

Those postulates are given by the following formulas:

$$d\sigma_{ij} \times d\varepsilon_{ij}^{P} \geq 0 \tag{4.38}$$

$$d\varepsilon_{ij}^{P} = d\lambda \frac{\partial f}{\partial \sigma_{ij}} \text{ or } \dot{\varepsilon}_{ij}^{P} = \dot{\lambda} \frac{\partial f}{\partial \sigma_{ij}} \tag{4.39}$$

$$d\varepsilon_{ij}^{P} = \left\{ \begin{array}{ll} d\lambda \dfrac{\partial f}{\partial \sigma_{ij}} & \text{if } f = 0, \text{and } df = 0 \quad \text{(plastic state)} \\ 0 & \text{if } f < 0, \text{and } df < 0 \quad \text{(elastic state)} \end{array} \right\} \tag{4.40}$$

$d\lambda$ is a positive scalar factor (loading parameter) usually not constant

$d\lambda$ for an elastoplastic material is obtained explicitly by Desai and Siriwardane(1984) as :

$$d\lambda = \frac{\dfrac{\partial f}{\partial \sigma_{ij}} d\varepsilon_{ij} + \dfrac{3K - 2G}{6G} dI_1 \times \dfrac{\partial f}{\partial \sigma_{ij}} \delta_{ij}}{\dfrac{\partial f}{\partial \sigma_{ij}} \left(\dfrac{\partial f}{\partial \sigma_{ij}}\right) + \dfrac{3K - 2G}{6G} \left(\dfrac{\partial f}{\partial \sigma_{ij}} \delta_{ij}\right)} \tag{4.41}$$

where f is the yield function ,K is the bulk modulus, I_1 is the first invariant of the strain tensor. σ_{ij} is the stress tensor $d\sigma_{ij}$ is the stress increment

Flow rule with hydrostatic stress independence, Prandtl-Reuss constitutive equations, and the empirical Von Mises and Tresca yield criteria:

If there is independence of the hydrostatic stress then yield surface is a function of the second and third stress invariants only. That can be expressed as $f(J_2, J_3) = 0$ (Tresca) and $f(J_2) = 0$ (Von Mises: where independence of both J_3 and J_1 exists)

In general:

$$\frac{\partial f}{\partial \sigma_{ij}} = \left(\frac{\partial f}{\partial J_{2D}} S_{ij} + \frac{\partial f}{\partial J_{3D}} R_{ij}\right) \tag{4.42}$$

$\sqrt{J_{2D}}$ is the second invariant of the deviatoric stress tensor

$\sqrt{J_{3D}}$ is the third invariant of the deviatoric stress tensor

$$R_{ij} = \frac{\partial J_{3D}}{\partial \sigma_{ij}} , \tag{4.43}$$

$$S_{ij} = \frac{\partial J_{2D}}{\partial \sigma_{ij}} \tag{4.44}$$

$$d\varepsilon_{ij}^{\ e} = \frac{dS_{ij}}{2G} + \frac{d\sigma_{kk}}{3K}\delta_{ij} \quad \text{(elastic strain increment)} \tag{4.45}$$

Substituting equations (4-41), (4-42), (4-43), (4-44), (4-45) into equation (4-37), one gets the total strain increment of an elastic- incompressible plastic material.

The relation between the incremental stress and incremental strain can be given in a matrix notation as follows:

$$\{d\sigma\} = \{[C^e] - [C^p]\} * \{d\varepsilon\} \tag{4.46}$$

where $[C^e]$ and $[C^p]$ are the elastic and plastic stress-strain matrices, respectively. Equation (4.46) is the practical stress-strain plasticity relationship to be implemented in finite element analysis.

The constitutive equations, for a linear elastic, perfectly incompressible plastic (also called elastoplastic) can be written according to **Prandtl-Reuss** assumption of $\frac{\partial f}{\partial \sigma_{ij}} = S_{ij}$

$$e_{ij} = d\lambda S_{ij} + \frac{S_{ij}}{2G} \tag{4.47}$$

$$\varepsilon_{kk} = \frac{\sigma_{kk}}{3K} \tag{4.48}$$

e_{ij} is the deviatoric strain, S_{ij} is the deviatoric stress, G is the shearing modulus, ε_{kk} is the bulk strain, δ_{ij} is the Kronecker delta, σ_{kk} is the bulk stress.

Prandtl-Reuss material shows no hysteresis during loading and unloading, and the strength of such material depends on the mean normal stress.

According to the **Von Mises** yield criterion, the yield surface can be specified in three dimensions by the equation

$$J_{2D} = \frac{1}{2} S_{ij} S_{ij} = K_m^{\,2} \quad \text{(at the onset of yielding)} \tag{4.49.a}$$

K_m is the material constant =k (the yielding of the pure shear) (4.49.b)

However, when the yielding of the pure tension, or compression (because the material is considered isotropic) is adopted then

$$K_m = Y/\sqrt{3} \tag{4.49.c}$$

Y is the yield stress value obtained from pure tension or compression test).

Projecting the Von Mises equation drawn in the space of $(\sigma_1, \sigma_2, \sigma_3)$ on the Π plane (the plane passing from origin and normal to the hydrostatic line) one gets the circle of diameter dependent on the value of K_m ,Figure (4.6).

The **Tresca** flow rule states that a material begins yielding when the maximum shear stress reaches a certain value related to the material property. This definition can be interpreted by the following equation:

$$K_t = 1/2(\sigma_{max} - \sigma_{min}) \tag{4.50.a}$$

The left side of (4.50) represents the maximum shear stress where σ_{max}, σ_{min} are the maximum and minimum principal stress, respectively and the right side represents the material property .

K_t =k (the shear yield stress) (4.50.b)

Equation (4.50.a) is considered when testing the material yielding is decided to be obtained by the pure shear test

$$K_t = Y/2 \qquad (4.50.c)$$

Equation (4.50.c) is used when testing the material yielding is decided to be obtained by the simple tension or compression test. Considering all possible maximum shearing stress values in three dimensions, it can be shown that the yield surface is a surface of an infinitely long regular hexagonal cylinder and its axis is the hydrostatic line, Figure (4.5). Physically, the assumption of insensitive hydrostatic independent yield surface means that the internal friction resistance of the material particles is negligible when this material is subjected to external forces. This assumption is somewhat empirically verified for metals. However the geological materials do show a frictional resistance; i,e, dependency on the hydrostatic (mean stress) as we will see in the following section.

Yield surface dependence on the hydrostatic stress (Mohr-Coulomb and Drucker-Parger yield criteria):

In case one considers that the material is a hydrostattic-sensetive one, then the general equation of yield surface is given as

$$f(\sigma_1, \sigma_2, \sigma_3) = 0 \qquad (4.51.a)$$

$$f(\sigma_{ij}) = 0 \qquad (4.51.b)$$

$$f(J_1, J_2, J_3) = 0 \qquad (4.51.c)$$

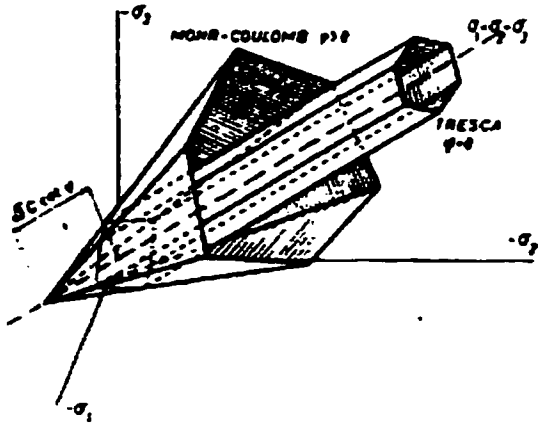

Figure (4.5) Tresca hydrostatic stress-independent yield function and Mohr-Coulomb yield functions in the principal stress space (Majed, 1991)

The material sensitive to mean stress can be modeled by Mohr-Coulomb or Drucker-Parger yield criteria.The Coulomb frictional failure law is defined by:

$$\tau = \sigma_n \tan\phi + c \qquad (4.52)$$

τ is the shearing stress.; σ_n is the normal stress ϕ : is the angle of internal friction. c : is the cohesion. The graphical representation of equation (4.52) in terms of the principal stresses is implemented through Mohr circle, then equation (4.52) can be written as follows

$$\frac{\sigma_1 - \sigma_2}{2} = \frac{\sigma_1 + \sigma_2}{2}\sin\phi + c\cos\phi \qquad \{\text{corresponding to equation (4.51.a)}\} \qquad (4.53.a)$$

The Mohr-Coulomb equation (4.52) can be shown in the tensor of the second order space (σij space) as:

$$\sqrt{\frac{(\sigma_{11} - \sigma_{33})^2}{4} + {\sigma_{12}}^2} = \frac{\sigma_{11} + \sigma_{33}}{2}\sin\phi + c\cos\phi \quad \{\text{corresponding to equation (4.51.b)}\}$$

(4.53.b)

In the space of $(\sigma_1, \sigma_2, \sigma_3)$, equation (4.51.a) is presented considering all possible states of the principal stresses. The resultant shape is a conical giving irregular hexagon when projected on Π plane Figure (4.5). When $\sigma_1 = \sigma_2 = \sigma_3 = 0$ we have σ_m = -c cotϕ and the apex of the hexagonal conic, its 0, lies along the space diagonal at a point. Then,

$\sigma_1 = \sigma_2 = \sigma_3 = \sigma_m$=-c cot$\phi$.

According to the Mohr-Coulomb criterion the yield strength in tension is less than that of compression.

Writing the Mohr –Coulomb in terms of stress invariants and considering the associated flow rule the following is obtained (ADINA,2001)

$$\left\{\begin{array}{l} f = \alpha_m J_1 + \sqrt{J_{2D}} - K_m \quad \text{or} \\ f = J_1 \sin\phi + \frac{1}{2}[3(1-\sin\phi)\sin\theta + \sqrt{3}(3+\sin\phi)\cos\theta)\sqrt{J_{2D}} - 3c = 0 \\ \theta = \frac{1}{3}\cos^{-1}[\frac{3\sqrt{3}}{2}\frac{J_3}{J_2^{1..5}}] \end{array}\right\} \qquad (4-54-a)$$

If the non-associated flow rule is considered

(potential plastic function Q is not the yield function f) then Mohr-Coulomb is written as

$$\left\{\begin{array}{l} Q = J_1 \sin\varphi + \frac{1}{2}[3(1-\sin\varphi)\sin\theta + \sqrt{3}(3+\sin\varphi)\cos\theta)\sqrt{J_{2D}} - 3c = 0 \\ \theta = \frac{1}{3}\cos^{-1}[\frac{3\sqrt{3}}{2}\frac{J_3}{J_2^{1..5}}] \end{array}\right\} \qquad (4-54-b)$$

ϕ is the friction angle, c is the cohesion, φ is the dilatation angle J_1, J_3 the first and third stress invariants J_{2D} the second invariant of the deviatoric stress, α_m, K_m the Mohr Coloumb material constants

Knowing the yield surface represented by equations (4.54.a), or the potential yield surface by (4.54.b), one applies the general flow rule discussed above to get the total incremental strain written in matrices notations.

In the ADINA finite element code (ADINA, 2001) it is assumed that the material follows a non associated flow rule with a yield function and its corresponding potential function given in equations (4.54.a), and (4.54.b) respectively.

(ADINA, 2001) considered the following considerations in constructing Mohr-Coulomb material model :

(I)The material is a an elastic perfectly plastic without any strain hardening

(II)The volume dilatation due to shearing is only governed by the dilatation angle, and in order to reduce the pathologically large material dilatation (which does not agree with the empirical observation, the specified dilatation angle should be smaller than the friction angle.

(III) In the case of vertex yielding, the plastic strain increments are obtained by applying a flow rule to the Drucker-Parger equation.

(VI) The stress states beyond the tension cut-off value are not possible. When this limit is reached or exceeded, the maximum tensile stress criterion (Rankine) is applied by shifting the hydrostatic stress component to the hydrostatic pressure corresponding to the tension cut-off

Conventional triaxial tests of dynamic loading are used to get the parameters of Mohr-Coulomb. The **Drucker-Prager** failure criterion is based on modifying the Von Mises yield criterion. That modification concerns the dependency on the hydrostatic stress as follows:

$f(J_1, J_2)=0$ The Drucker-Prager yield equation is (4.55)

$$\alpha_{DP} J_1 + \sqrt{J_{2D}} = K_{DP} \quad (4.56)$$

α_{DP}, K_{DP} are the Drucker-Parger material constants. Drawing this surface in $(\sigma_1, \sigma_2, \sigma_3)$ space one gets a circular cone Figure(4.6).

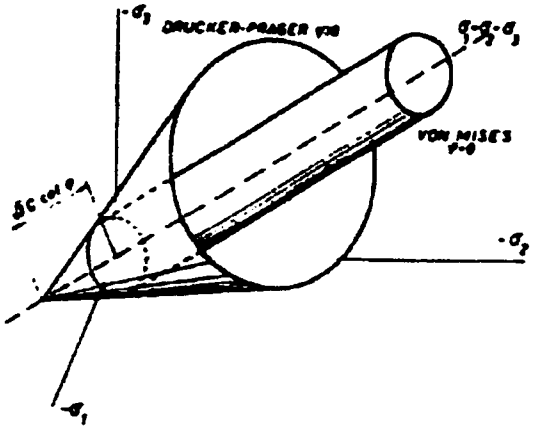

Figure (4.6)Von Mises hydrostatic stress-independent yield function and Drucker-Parger yield function in the principal stresses space (Majed,1991)

The Drucker-Prager parameters values could be extracted from Mohr-Coulomb parameters values. The interrelationships between the two sets of parameters is the result of the coincidence of circle with the outer or inner apices of the Mohr-Coulomb hexagon. When one has outer coincidence and the Mohr-Coulomb parameters obtained from conventional triaxial compression test (cylindrical specimen) , they are α_m, K_m

$$\alpha_m = \frac{2\sin\phi}{\sqrt{3(3-\sin\phi)}} \tag{4.57.a}$$

$$K_m = \frac{6c\cos\phi}{\sqrt{3}(3-\sin\phi)} \tag{4.57.b}$$

When the Mohr-Coulomb parameters are obtained from the plane strain condition there are different relationships.

$$\alpha_m = \frac{\tan\phi}{(9+12\tan^2\phi)^{0.5}} \tag{4.58.a}$$

$$K_m = \frac{3c}{(9+12\tan^2\phi)^{0.5}} \tag{4.58.b}$$

Inner coincidence gives new sets of relationships (Owen and Hinton, 1980).

$$\alpha_m = \frac{2\sin\phi}{\sqrt{3(3+\sin\phi)}} \tag{4.59.a}$$

$$K_m = \frac{6c\cos\phi}{\sqrt{3}(3+\sin\phi)} \tag{4.59.b}$$

Knowing the yield surface (f) equation, one can apply the general flow rule discussed above to get the total incremental strain written in matrices notations. The Drucker-Prager and Mohr-Coulomb are the simplest models, which could represent the elastoplastic soil and granular material behavior. Such models reflect some of the important characteristics of the soil and the granular material behaviors such as: elastic response at lower loads, small material stiffness near failure, failure condition, and elastic unloading after yielding (Baladi and Chen, 1985). The empirical parameters needed for

finite element simulation are usually the cohesion c, and angle of internal friction ϕ in addition to two elastic parameters

4.2.3 Elastoplastic work hardening (softening) behavior:

Concept of work hardening, the general flow rule and constitutive law

The perfectly plastic model assumes that the yield surface is fixed in stress space, which means that the perfectly plastic material does not change its yielding limit according to the suggested plastic model. However, experiments have shown that after the granular or soil reaches the initial yielding, the stress level at which further plastic strain occurs is remarkably dependent on the current degree of plastic strain. Thus granular material and soil are considered work hardening materials (Desai and Siriwardane,1984; Owen and Hinton, 1980; Chen and Baladi, 1985). In other words, with successive loading and unloading the stress points defining the yield surface move beyond the current yield surface, and a new yield surface (loading surface) is created. The new surfaces describing the hardening behavior are called hardening caps (Desai and Siriwardane, 1984)

The suggested strain hardening or softening rule controls the change which the yield surface experiences and transforms to many successive new ones before failure occurs. Isotropic strain hardening arises if the subsequent surfaces preserve their shape by uniform expansion or contraction (strain softening) without translation.

The kinematic hardening takes place if the subsequent surfaces translate only, i,e, change their locations without changing in size or shape. The concept of a nested yield surface is an application of the kinematics hardening

Figure(4.7)shows stress-strain relationship for elastoplastic strain hardening material. The simple cases of uniaxial stress and the strain hardening curve as straight line are presented for simplicity only.

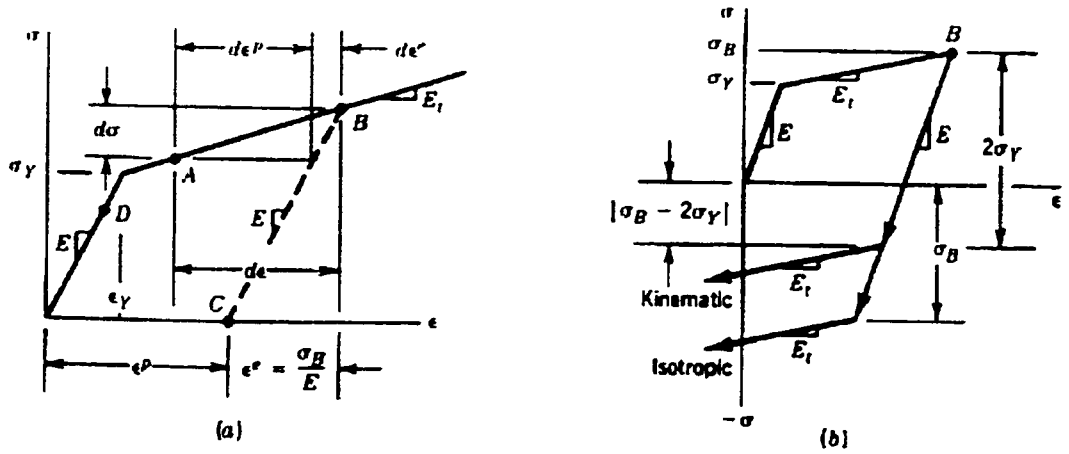

Figure (4.7):Strain hardening material response under uniaxial condition (*a*) Stress-strain plot in uniaxial stress, idealized as two straight lines, where σ_Y is the stress at the first onset of yielding. (*b*) Kinematic and isotropic hardening rules. (Cook et al,1989)

A combination of isotropic and kinematic hardening models leads to a general hardening rule. The bounding surface model is an example of this mix type of hardening

The strain hardening behavior of the geological material is also pronounced during the hydrostatic loading and since the behavior is plastic under the hydrostatic loading the successive yield surface should intersect the J_1 axis when representing the yield surface in $(\sqrt{J_{2D}}, J_1)$ plane . Drucker's stability postulates for a work-hardening material are summarized as follows:

(i) Yield surface should be convex in stress space.

(ii) Yield surface and plastic potential should coincide which leads to an associated flow rule

(iii) Work softening must not occur.

The equations which usually define the work hardening plastic material :

$$d\sigma_{ij} d\varepsilon_{ij} > 0 \tag{4.60}$$

$$d\sigma_{ij} d\varepsilon_{ij}^{P} \geq 0 \tag{4.61}$$

$$d\varepsilon_{ij}^{P} = d\lambda \frac{\partial f}{\partial \sigma_{ij}} \quad \text{or} \quad \dot{\varepsilon}_{ij}^{P} = \dot{\lambda} \frac{\partial f}{\partial \sigma_{ij}} \tag{4.62}$$

$$d\varepsilon_{ij}^{P} = \begin{cases} d\lambda \dfrac{\partial f}{\partial \sigma_{ij}} & \text{if } f = 0, \text{and } \dfrac{\partial f}{\partial \sigma_{ij}} d\sigma_{ij} > 0 \quad \text{(pastic state)} \\ 0 & \text{if } f < 0, \text{or } f = 0 \text{ and } \dfrac{\partial f}{\partial \sigma_{ij}} d\sigma_{ij} \leq 0 \quad \text{(elastic state)} \end{cases} \tag{4.63}$$

As $df = \dfrac{\partial f}{\partial \sigma_{ij}} d\sigma_{ij}$, then the plastic strain will occur only if df>0 and f=0

During unloading (df<0)or neutral loading (df=0), the material behaves elastically.

An isotropic work hardening material: The Generalized Cap Model and Cam Clay Model

For isotropic hardening material, $d\lambda$ is given by (Chen and Baladi, 1985):

$$d\lambda = \frac{\dfrac{\partial f}{\partial J_1} d\varepsilon_{kk} + \dfrac{G}{\sqrt{J_{2D}}} \dfrac{\partial f}{\partial \sqrt{J_{2D}}} S_{ij} de_{ij}}{9K\left(\dfrac{\partial f}{\partial J_1}\right)^2 + G\left(\dfrac{\partial f}{\partial \sqrt{J_{2D}}}\right)^2 - 3\dfrac{\partial f}{\partial J_1}\dfrac{\partial f}{\partial k}\dfrac{\partial k}{\partial \varepsilon_{kk}^{P}}} \tag{4.64}$$

Equation (4.64) is reduced to equation (4.41) when the loading function is independent of the plastic volumetric strain.

The cap model can describe the behavior of materials under all significant conditions and stress paths. The cap model in this work is assumed to be isotropic and consists of two parts, an ultimate failure envelope (surface) which services to limit the maximum shear stresses in the material and a strain-hardening surface (cap) that produces plastic volumetric and shear strain as it moves.

Generally, the loading function of an isotropic-work hardening material is given by

$f(J_1, \sqrt{J_{2D}}, k) = 0$ where k is a hardening parameter which may be taken as

$$k = k(\varepsilon_{ij}^{P}) \tag{4.65}$$

For the cap model, the failure envelope portion of the loading function is considered fixed denoted by

$f_{fe} = f_{fe}(J_1, \sqrt{J_{2D}}) = \sqrt{J_{2D}} - F1(J_1)$ (the failure envelope portion of the loading function)

While the moving part of the yield surface (cap) is given by :

$f_{cap} = f_{cap}(J_1, \sqrt{J_{2D}}, k) = \sqrt{J_{2D}} - F1(J_1, k)$ (the strain hardening surface portion , cap portion)

Assuming f_{fe} as a linear one can write

$$f_{fe} = \alpha J_1 + \sqrt{J_{2D}} - K \tag{4.66}$$

Equation (4.66) could be Mohr-Coulomb, Drucker-Prager, Mises, or any other yield function. It also could be a combination of two yield surface

Figure(4.8) shows the strain hardening cap portion which is given as:

$$f_{cap} = \sqrt{J_{2D}} - F1(J_1, k) = \sqrt{J_{2D}} - \frac{1}{R}\{[X(k) - l(k)]^2 - [J_1 - l(k)]^2\}^{0.5} \tag{4.67}$$

where α, Km are the material constants associated with friction and cohesive strengths

R is the ratio of the major to minor axis of the elliptical cap and *k* is hardening parameter

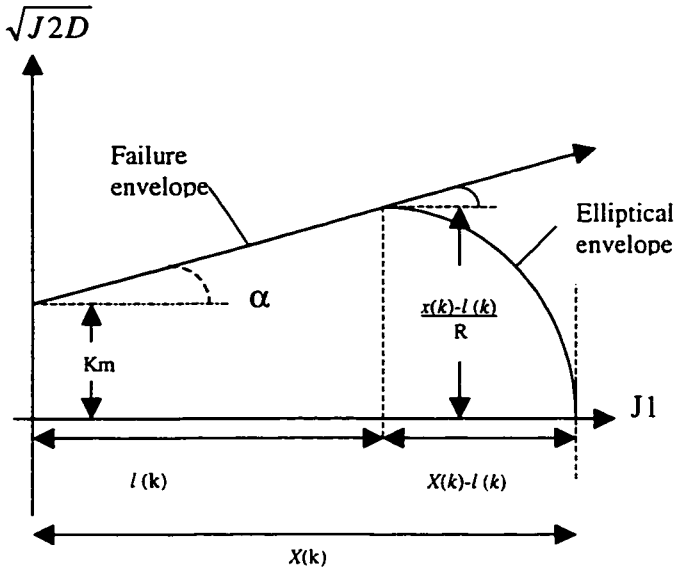

Figure(4.8)Yield function according to the cap model (Chen and Baladi, 1985).

The hardening surface is chosen so that the tangent at its intersection with the failure envelope is horizontal. This is equivalent to

$$X(k)=L(k)+R[\alpha L(k)+K] \tag{4.68}$$

where $l(k)= L(k)$ if $L(k)>0$, $l(k) = 0$ if $0 \geq L(k)$ (4.69)

The hardening function is assumed to be

$$k= \varepsilon_{kk}^{P} = W(1-e^{\{-D X(k)\}}) \text{ or} \tag{4.70}$$

$$X(k)= -\frac{1}{D}\ln(1-\frac{\varepsilon_{kk}^{P}}{W}) = -\frac{1}{D}\ln(1-\frac{k}{W}) \tag{4.71}$$

$$W= n\,(1-s) \tag{4.72}$$

Where *D, W* are the material constants which can be found from the hydrostatic test results, n is the porosity, s is the degree of saturation

The complete procedure for evaluating the cap model parameters can be found in (Desai and Siriwardane, 1984).

The above model requires seven material constants to be determined, namely, the cohesion, the angle of internal friction, two elastic parameters, D, W, and R

(ADINA, 2001) considered the Drucker-Prager model as the fixed part of the cap model of the ADINA finite element code

The Drucker-Prager model in ADINA (which is actually a cap model) is based on:

(I) An associated flow rule (normality) using Drucker-Prager and cap yield function..

(II) A perfectly plastic Drucker-Prager yield behavior.

(III) Tension cut-off

(IV) Cap hardening. In other words, the yield function used consisted of a perfectly plastic (failure portion) fitted to a strain hardening elliptical or straight cap. The movement of the cap is controlled by the increase or decrease of the plastic volumetric strain. Strain hardening in this model can therefore be reversed. Such mechanism leads to an effective control of dilatancy .

ADINA model eliminates the pure Drucker-Prager misrepresentation of soil and granular material which assumes that these materials can bear unlimited hydrostatic pressure and it dilates excessively as a consequence of an associated flow rule assumption.

Moreover, by including the tension cut-off, the Drucker-Prager ADINA model avoids the overestimation of the tensile strength resulted from pure Drucker-Prager criterion.

ADINA implemented the following analytical development in ADINA code for the cap model:

$$\alpha_{DP} J_1 + \sqrt{J_{2D}} = K_{DP} \quad \text{or} \quad f_{fe} = \alpha_{DP} J_1 + \sqrt{J_{2D}} - K_{DP}$$

The cap yield function depends on the shape of the cap, for a plane cap:

$f_C = -J_1 + J_1^{\,a}$ where $J_1^{\,a}$ is a function of volumetric plastic strain

Where $J_1^{\,a} = -\frac{1}{D}\ln(1-\frac{e_v^{\,p}}{w}) + {}^0J_1^{\,a}$

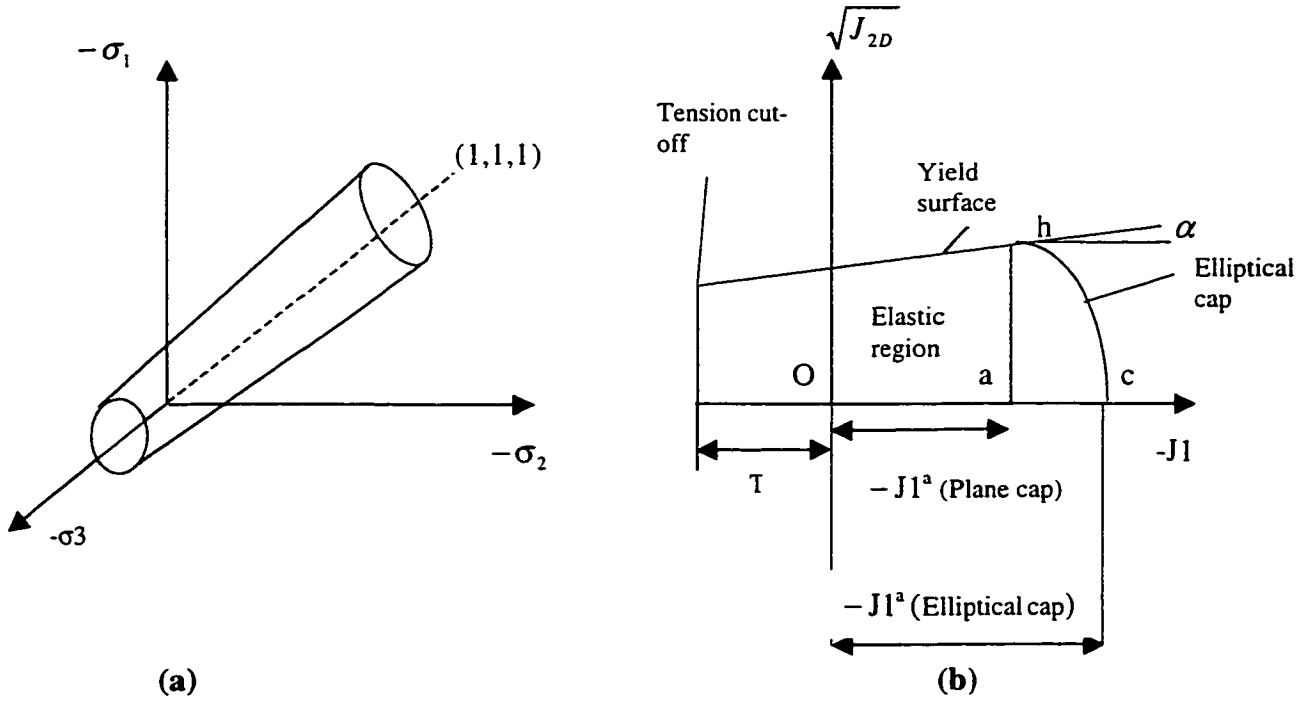

Figure (4.9) Drucker Prager- Cap model (ADINA, 2001), (a) Drucker-Parger yield surface $(\sigma_1, \sigma_2, \sigma_3)$ space (b) Drucker-Parger model in $(J_1, \sqrt{J_{2D}})$ space.

In the case of tension cut-off ,T is the maximum value that Ji^a can take

If α_{DP} approaches zero, then the initial position of the cap is moved far to the right and Ji[a] is not reached in the analysis, and the position of the tension cut-off T is moved far to the left and is also not reached in this analysis, then the Drucker-Prager yield condition approaches the von Mises yield condition α_{DP}=0 and no dilatency exists).

The volume expansion of the material resulted from shear is governed by α_{DP}.

Including the cap yielding leads to an increase of compressive plastic volumetric strain. If the plane cap is used, there is no change of the deviatoric plastic strains while if elliptical cap is used the deviatoric components of the plastic strain change during the cap yielding. The vertex yielding represented by point h corresponds to the Drucker-Parger and cap yielding .Figure(4.9) above illustrates the Drucker-Prager yield locus combined with Cap strain hardening yield locus.

Cam clay model

Cam clay model is based on the critical state concept. which can be understood through explaining the consolidation and dilation as follows:

According to its bulk density and its state of the stress, the soil undergoes consolidation or dilatation, Figure(4.12).

For high density, small void ratio, and/or low normal stress , the shear stress will induce and increase at the beginning without any noticeable plastic shear deformation, until it reaches the critical shear $\tau_{critical}$ yield state which is dependent on its void ratio and the applied normal stress. To maintain the shear deformation after passing the $\tau_{critical}$, the $\tau_{critical}$ would decrease to a constant value $\tau_{constant}$ as shown in Figure (4.10.b), independent of the void ratio and only a function of the normal stress. Physically, the

decrease from $\tau_{critical}$ to $\tau_{constant}$ is associated with weakening of the soil during the initiation of the plastic deformation; i.e., a smaller shear force is needed for deforming the material. This behavior is called failure or dilation which arises from the need of a densely packed granular soil to spread in order to make enough room for allowing grains to move. In the dilation case the shear strain occurs in a very thin layer, for each specific void ratio or bulk density, resulting in a convex τ,σ yield curve of. As shown in Figure(4.10.a) the higher is the normal stress σ, the higher is the shear stress τ required for reaching failure. For a given normal stress, the higher is the bulk density, the higher is $\tau_{critical}$ required for reaching yield. Once values of τ tends asymptotically to $\tau_{constant}$ the material tends to a constant density which means that the material will continue to undergo shear deformation without any further volumetric deformation dilatation or increase in the volume [Figure (4.12)] . At this stage, the critical state is reached. Dry and overcosolidated soil exhibit this behavior.

On the other hand, when having a small initial bulk density, i.e., large void ratio, and/or large normal stress, a different situation exists. After reaching the critical value of shear (shear at yield), which causes plastic deformation (volumetric deformation or decrease in the volume and shear deformation together), this critical shear needs to be increased in order to maintain the plastic deformation, until a constant value of shear is reached for which the soil keeps it plastic deformation (plastic shear deformation only) without any further volume change as shown in Figure (4.11.b) and consolidation ceases and the soil reached a critical state.

For each specific void ratio or bulk density, there exists a convex yield curve of τ,σ. The higher is the normal stress σ, the less is the shear stress needed to initiate consolidation, Figure (4.11.a) illustrates this relationship.

For a given normal stress the less void ratio, the higher the shear stress for reaching yield The curves of τ,σ are called the consolidation loci. Consolidation can occur as a result of normal stress only τ =0.

Note: The previous discussion could also be based on the relationship between p(isotropic stress) and q(deviatoric stress) in case one is dealing with triaxial stress condition instead of σ_n (normal stress) and τ (shearing stress), respectively, which are used in the simple shear case. For the different bulk densities or void ratios, the dilation curves and consolidation curves are connected at points representing the critical states of the soil for such different bulk densities or void ratios. Such points form a curve called critical state locus which is mostly a straight line ,as shown in Figure (4.13). The material will consolidate or expand according to whether (τ,σ) lies to the right or left side of this line. Therefore when

$\frac{\partial\tau}{\partial\sigma} > 0$ (left side of the critical state locus) there is dilatation

$\frac{\partial\tau}{\partial\sigma} < 0$ (right side of the critical state locus) there is consolidation.

The critical state line on the (τ,σ) plane is similar to the idea of the fixed failure envelopes in the generalized cap model.

Some researchers define the critical state by the following equations:

$$\frac{\partial\tau(\sigma,e)}{\partial(\sigma)} = 0 \qquad (4.73)$$

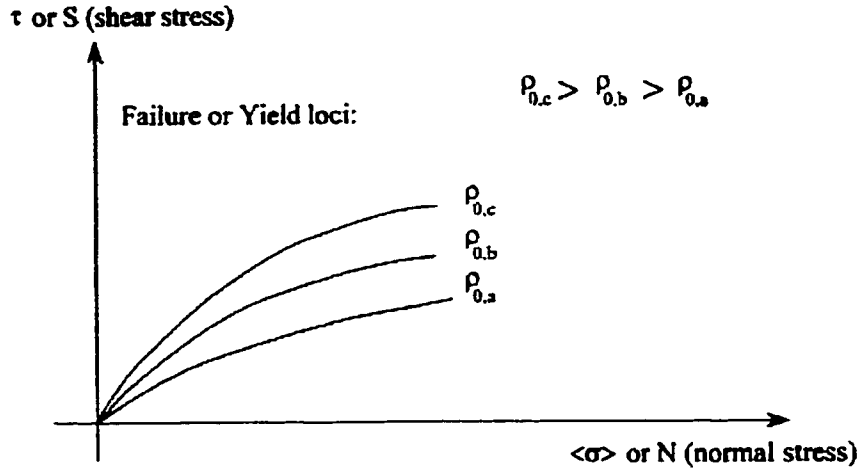

(a)

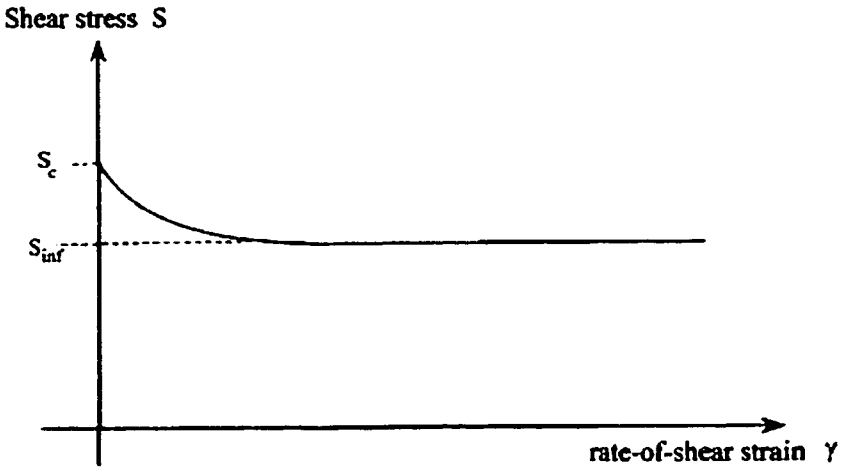

(b)

Figure (4.10) Critical state for dilative soils and failure loci (a) yield loci in terms of the relationship between the normal stress and the shearing stress of soils of different densities under dilation (b)Shearing stress- rate of shear strain relationship for soil failing under dilation

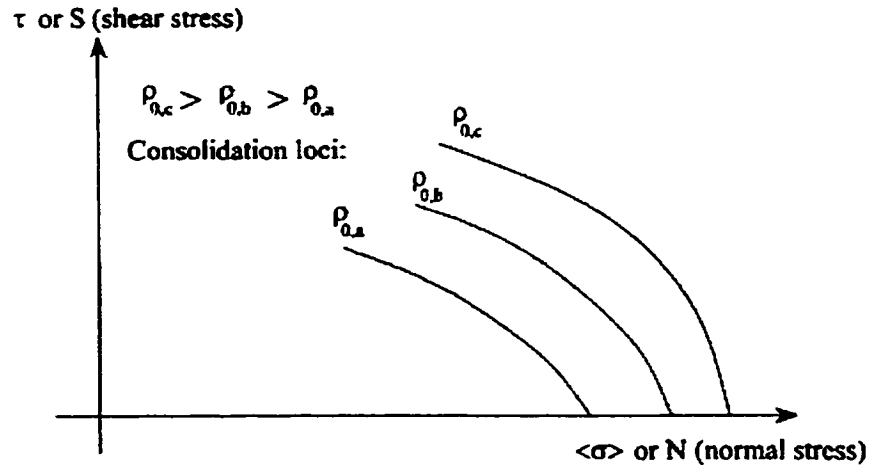

(a)

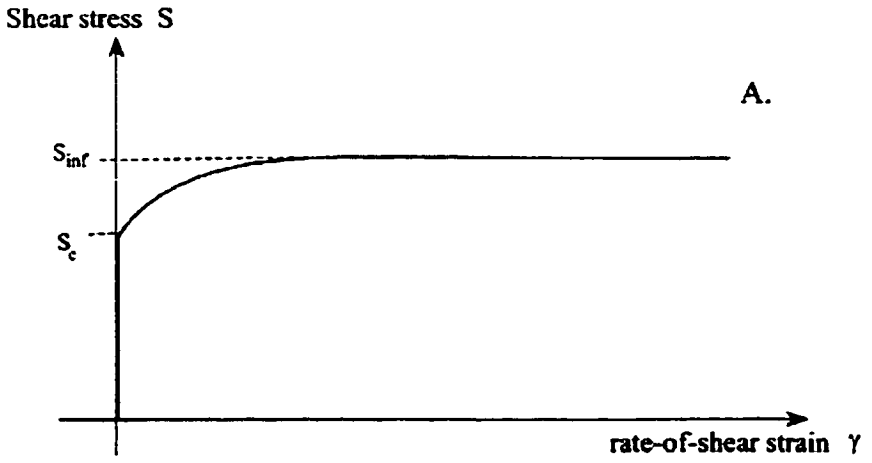

(b)

Figure (4.11) Critical state for contractive soils and consolidation curves (a) consolidation curves in terms of the relationship between the normal stress and shearing stress of soils with different densities. (b)Shearing stress-rate of shear strain relationship for soil reaching the critical state through consolidation

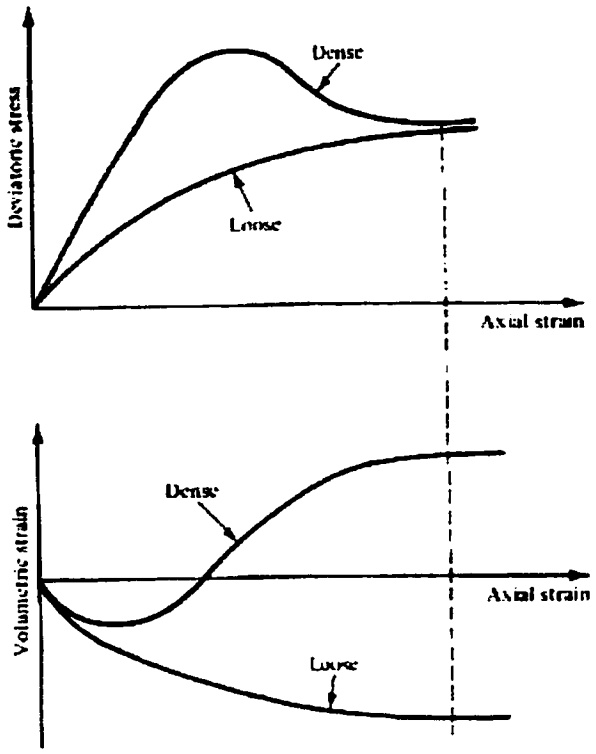

Figure (4.12) Schematic of deviatoric and volumetric stress-strain behavior for loose and dense soil (Desai and Siriwardane,1984)

As the yield locus (failure and consolidation locus) is a function of the void ratio or the specific volume v. The material is considered elastic if $\tau < \tau(\sigma, e_0)$,and it deemed a plastic if this condition is not met. Figure (4.14) shows the yield loci space (τ, σ ,v) for positive deviatoric stress. For a specific initial yield density and state of applied stress, the material will change this density at yield because it deforms (dilates if the normal stress is less than that at the critical state or consolidates if normal stress is higher than that at the critical state), which means that the material will move to new successive yield loci until reaching the yield locus for which the applied normal stress represents the stress of the critical state.

For such a yield locus the material will have constant void ratio or bulk density with continuous plastic shear deformation.

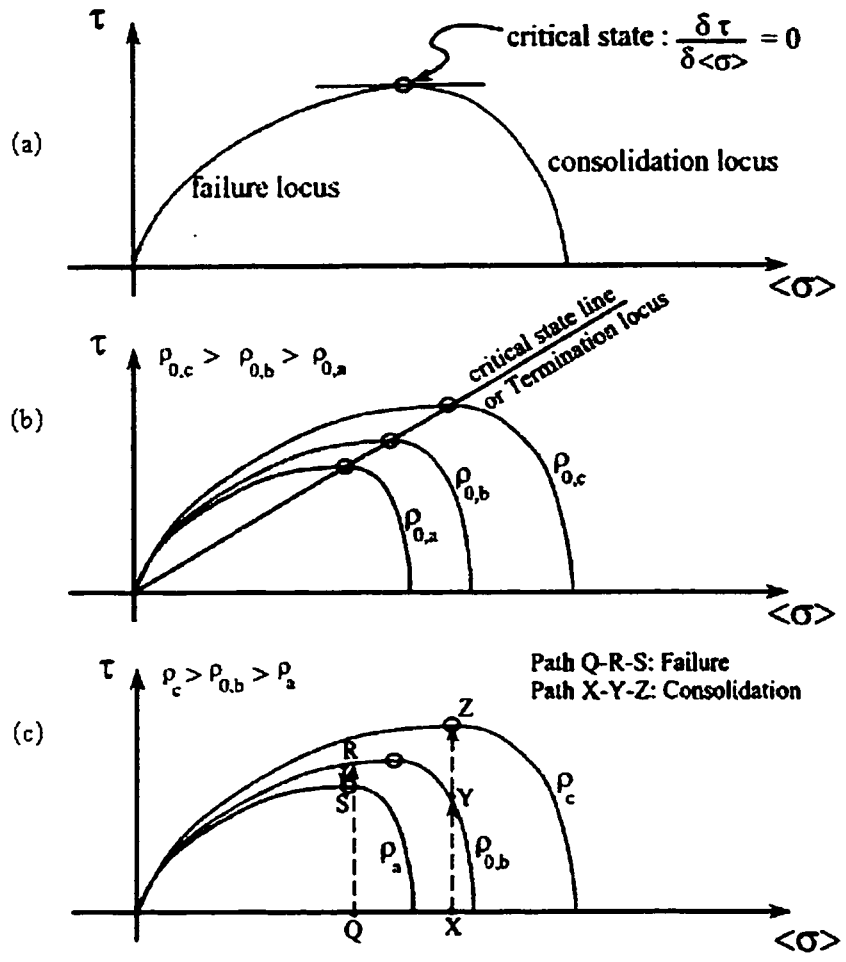

Figure (4.13) Critical state for yield locus curve, which is a combination of a failure locus curve and a consolidation locus curve, in the(σ, τ) coordinate system (a)for a specific bulk density(b)Yield loci curves for different bulk densities with critical state line are shown,(c)Examples of failure and consolidation paths

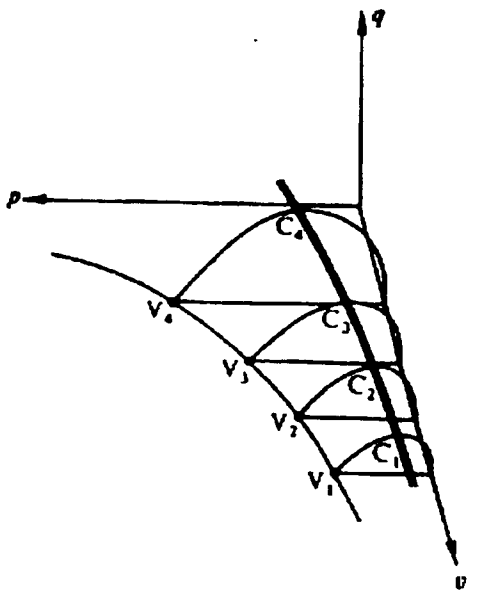

Figure (4.14) Upper half of state boundary surface in the space(p, q, v) (Schofield and Worth, 1968)

For the axisymmetric conditions of wet soil (right side of the critical state line)

For a sample placed in the triaxial test box, the following relationships hold

$$p = \frac{\sigma_1 + 2\sigma_3}{3} = \frac{J_1}{3} \tag{4.73}$$

$$d\varepsilon_2 = d\varepsilon_3$$

$$q = \sigma_1 - \sigma_2 = \sqrt{3J_{2D}} \tag{4.74}$$

$$d\varepsilon_v = d\varepsilon_1 + 2d\varepsilon_3 \quad (4\text{-}73)$$

$$d\varepsilon_s = \frac{2}{3}(d\varepsilon_1 - d\varepsilon_3)$$

$$d\varepsilon_1 = \frac{dH}{H}$$

The work done on the test specimen per unit volume,

$$dW = \sigma_1 d\varepsilon_1 + 2\sigma_3 d\varepsilon_3 \tag{4.75.a}$$

$$dW = pd\varepsilon_1 + qd\varepsilon_3 \tag{4.75.b}$$

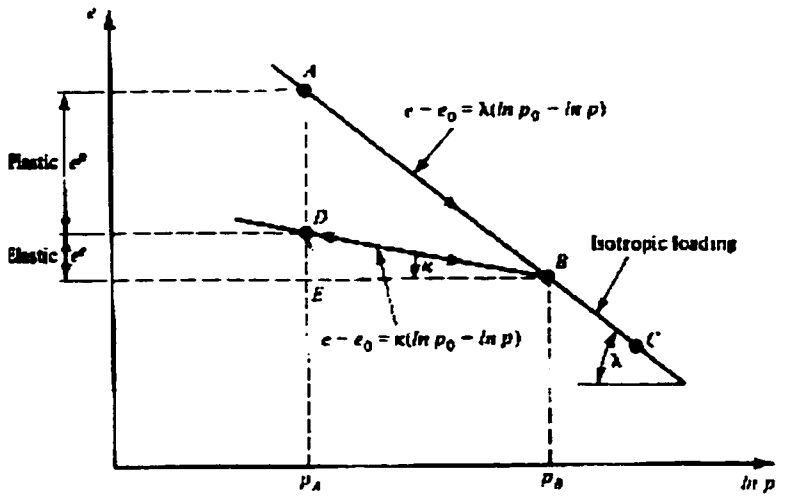

Figure (4.15) The relation between the isotropic loading on the logarithmic axis and the void ratio for loading(A-B), unloading (B-D), and reloading(D-B) cases (Desai and Siriwardane,1984)

As shown in Figure (4.15) if the material is normally consolidated at A, the isotropic loading will follow the path AB, if we unload the sample is unloaded to the mean pressure p_A, because of the elastoplastic behavior the material will follow the path BD upon unloading, if the material is reloaded from pressure p_A to p_B, it will usually follow the same path as the unloading path DB.

The total change in void ratio (e) during the loading and unloading cycle is

$$e = e_A - e_B = \lambda(\ln p_B - \ln_A) \tag{4.76}$$

$$e^e = e_D - e_E = k(\ln p_B - \ln_A) \tag{4.77}$$

Differentating with respect to e and rearranging gives:

$$de = -\lambda \frac{dp}{p} \tag{4.78}$$

$$de^e = -k \frac{dp}{p} \tag{4.79}$$

$$de^p = de - de^e = -(\lambda - k)\frac{dp}{p} \tag{4.80}$$

$$d\varepsilon_v = -\frac{de}{1+e_0} = \frac{\lambda}{1+e_0}\frac{dp}{p} \tag{4.81}$$

$$d\varepsilon_v^e = -\frac{de}{1+e_0} = \frac{k}{1+e}\frac{dp}{p} \tag{4.82}$$

where e is the void ratio; λ is the slope of loading path; k is the slope of unloading or reloading path; de^p is the plastic component of the incremental void ratio; de^e is the elastic component of the incremental void ratio; $d\varepsilon_v$ is the compressive volumetric strain

In the critical state concept, it is assumed that there is no recoverable energy associated with shear distortion, which means that

$$d\varepsilon_s^e = 0 \Rightarrow d\varepsilon_s = d\varepsilon_s^p \tag{4.83}$$

According to the normality condition, the incremental plastic strain vector is normal to the yield surface an any point as illustrated in Figure(4.16) that leads to :

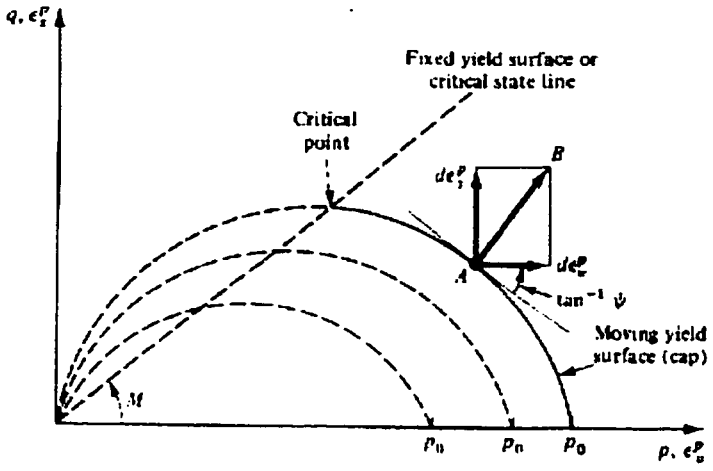

Figure (4.16 Normality rule for yield locus of the critical state case, in terms of (p,q) (Rosco and Burland,1968)

$$\frac{d\varepsilon_s^p}{d\varepsilon_v^p} = -\frac{dp}{dq} \tag{4.84}$$

Assuming that:

$$\frac{q}{p} = \eta \tag{4.85}$$

$$\frac{dq}{dp} = -\varphi \text{ gives:} \tag{4.86}$$

$$\left\{ \begin{array}{l} dq = pd\eta + \eta dp \text{ or} \\ pd\eta + \eta dp = -\varphi\, dp \text{ or} \end{array} \right\} \tag{4.87}$$

$$\frac{dp}{dq} + \frac{d\eta}{\eta + \varphi} = 0 \tag{4.88}$$

The equation defines a yield locus $p = f(q, \varphi = \frac{dq}{dp})$. Because we are considering the isotropic hardening is being considered, the successive yield loci (hardening cap) are geometrically similar and independent of the $\frac{dq}{dp}$. Therefore any yield locus passing from a known point $(p_0, 0)$ will be obtained through integrating equation that gives the following

$$\ln p - \ln p_0 + \int_0^{\eta} \frac{d\eta}{\eta + \varphi} = 0 \tag{4.89}$$

p_0 is treated as a variable having a unique value for each yield surface. This is called hardening parameter. When the soil changes its state; e, i., moves from one yield surface to another, the change in the hardening parameter p_0 is the same irrespective of the stress path followed. The ratio $\frac{dq}{dp} = -\varphi$ can be obtained by considering the dissipated energy

while undergoing deformation on the state boundary surface. Various assumptions can be made to define the magnitude of the dissipated energy

Schofield (1962) derived a theoretical yield locus for an ideal soil (wetter than the critical). Based on this assumption, when the soil deforms, there exists some combination of volume change and shear distortion, and it is the shear strain that determines the dissipation rate. The dilation or volume change is a geometrical consequence of interlocking, and does not need to appear explicitly in the dissipation function. According to Schofield's assumption the dissipated energy

$$\left[\begin{array}{l} dW = pd\varepsilon_v^p + qd\varepsilon_s^p = Mpd\varepsilon_s^p \\ \dfrac{d\varepsilon_v^p}{d\varepsilon_s^p} + \dfrac{q}{p} = M \Rightarrow \dfrac{d\varepsilon_v^p}{d\varepsilon_s^p} + \eta = M \end{array}\right] \tag{4.90}$$

The incremental strain vector is normal to the yield surface, consequently the ratio is

$$\frac{d\varepsilon_v^p}{d\varepsilon_s^p} = -\varphi$$

$$\left[\begin{array}{l} \dfrac{dq}{dp} + \eta = M \\ \dfrac{d\eta}{dp} = \dfrac{1}{p}\left(\dfrac{dq}{dp} - \dfrac{q}{p}\right) = -\dfrac{M}{p} \Rightarrow \\ \dfrac{d\eta}{M} + \dfrac{dp}{p} = 0 \text{ hence} \\ \dfrac{\eta}{M} = \dfrac{q}{Mp} = 1 - \ln\dfrac{p}{p_0} \end{array}\right] \tag{4.91}$$

where M is the slope of the critical line or as explained by Schofield (1962) is the generalized coefficient of friction μ which is used in Taylor's equation stating that the strength of soil results from contribution of both friction and interlocking

$$\frac{\tau}{\sigma} = \mu + \frac{dy}{dx}$$

Strength = Friction + Interlocking

where dy expresses the increase in the sample thickness and a separation of the two halves of the shearing box.. At peak strength, dx expresses the horizontal relative displacement of the two halves of the shearing box of the

For the modified Cam Clay, the dissipated energy is given by:

$$\left[\begin{array}{l} dW = p\sqrt{(d\varepsilon_v^p)^2 + M^2(d\varepsilon_s^p)^2} \Rightarrow \\ \frac{d\varepsilon_s^p}{d\varepsilon_s^p} = \frac{2\eta}{M^2 - \eta^2} \Rightarrow \\ \varphi_{cm} = \frac{M^2 - \eta^2}{2\eta} \end{array}\right] \qquad (4.92)$$

Substituting in the equation (4.87) and integrating gives the equation of yield locus as:

$$\frac{M^2 + \eta^2}{M^2} = \frac{P_0}{p} \qquad (4.93)$$

M can be calculated from the internal friction angle as

$$M = \frac{6\sin\phi}{3 - \sin\phi} \qquad \text{(If triaxial compression tests are performed)} \qquad (4.95)$$

$$M = \frac{6\sin\phi}{3 + \sin\phi} \qquad \text{(If triaxial extension tests are performed)} \qquad (4.96)$$

The parameters required for Cam Clay model are (M, λ, k) where

To determine the value of M, one needs the value of the mean pressure (p) and deviatoric stress (q) at ultimate conditions. The parameters λ, k can be related to compression index C_c and swelling index C_s

where C_c is the slope of virgin loading line on $e-\log_{10} p$, and C_s is the slope of unloading-reloading curves on the same previous plot

The $e-\log_{10} p$ plot for any constant stress ratio test $\frac{q}{p}$(constant) is parallel to that obtained from the hydrostatic test. The one dimensional consolidation test is a special case of the constant $\frac{q}{p}$ test .The $e-\ln p$ curve obtained a in hydrostatic test is parallel to that obtained under critical state condition. This leads to :

$$e-e_0 = C_c \log_{10}(\frac{p}{p_0}) = \lambda \ln(\frac{p}{p_0}) \Rightarrow \lambda = \frac{C_c}{\ln 10} \tag{4.94}$$

$$e-e_0 = C_s \log_{10}(\frac{p}{p_0}) = k \ln(\frac{p}{p_0}) \Rightarrow k = \frac{C_s}{\ln 10} \tag{4.95}$$

The hardening rule in (ADINA,2001) is written in terms of the specific volume, which is defined as the total volume of a quantity of soil containing a unit volume of soil grains v =1+e, at a specified time (t) as :

$${}^t v = N - \lambda \ln {}^t P_0 + k \ln \frac{{}^t p_0}{{}^t p}$$

$$N = \Gamma + (\lambda - k)\ln 2$$

The effective bulk modulus at time t can be expressed as:

$${}^t K = \frac{{}^t v \, {}^t P}{k}$$

The corresponding shear modulus at time t is obtained as:

$${}^t G = \frac{3(1-2\nu)}{2(1+\nu)} {}^t K$$

4.3 High modulus geosynthetic reinforcement (Geogrid)

The behavior of the geogrid under the repeated traffic loads is not completely understood Flexibility, stiffness, and tensile strength are the important characteristics defining the mechanical behavior of the geogrid as reinforcement. The stiffness of the geogrid is the most important reinforcing characteristic. A model including components of elasticity, plasticity, creep, and directional dependency. of the polymeric geogrid might be reasonably realistic (Perkins ,1999). However such a model is considered over-simplified and not practical for use in the numerical simulations, because it needs many parameters which are not defined in the existing manuals, produced by the manufacturers.

In this study, the geogrid is assumed to act as either elastic material or as a frictionless perfectly plastic (Von Mises or Tresca) which can capture the irrecoverable strains occurring in the geogrid as a result of the repeated loads. More details about geogrid stiffness and its effect on the performance of the pavement system was discussed in details in Chapters Two and Three.

As can be seen from the work of Perkins (2001), Table (3.4) , the geosynthetic reinforcement is recognized by many researchers as an isotropic elastic material. In the elastic analysis, the behavior of geogrid is also assumed to be isotropic, i,e, the longitudinal ribs, transverse ribs, and the junctions have the same stress-strain curve.

The mechanical properties of the geogrid needed in the elastic analysis are the stiffness (Sg) and Poisson's ratio (ν) .

The geogrid stiffness, as defined and used by Barksdale (1989), is equivalent to the modulus of elasticity of the geogrid times its average thickness. The geogrid stiffness (Sg) should be used because the modulus of elasticity of a thin

geosynthetic has relatively little meaning unless its thickness is taken into consideration. The wide width tension test specified by ASTM test method D-4595 is used to determine the (Sg). As the load-displacement behavior of geogrid shows non-linearity, the stiffness is selected at a standard defined level of the strain, which is usually 5%.

The Poisson's ratio was found to have moderate effect on the force taken by the geogrid Barksdale (1989) reported the following impact of the geogrid's Poisson ratio on the performance of the reinforced pavement " As the value of the Poisson's ratio increases, the force developed in the geosynthetic also becomes larger, and hence the effectiveness of the reinforcement increases. For light pavement sections on a weak subgrade, increasing Poisson's ratio from 0.2 to 0.4 results in a 29 % increase in the force developed in the geosynthetic. The corresponding reductions in tensile strain in the asphalt surfacing and vertical compressive strain on the subgrade are less than 0.2 and 1 percent, respectively"

In his analysis, Barksdale (1989) chose the Poisson's ratio to be 0.3 for the geogrid A in Table (3.4)

Perkins (2000) used a Poisson's ratio (ν) of 0.5 for the geogrid A,B shown in Table(3.4) which means that the membrane thickness decreases in all cases when the uniaxial force is applied. However, the Poisson ratio was assumed to be zero for the polymeric geosynthetic in Wathugala et al (1996) simulations meaning that the membrane deforms only in the direction of the load application.

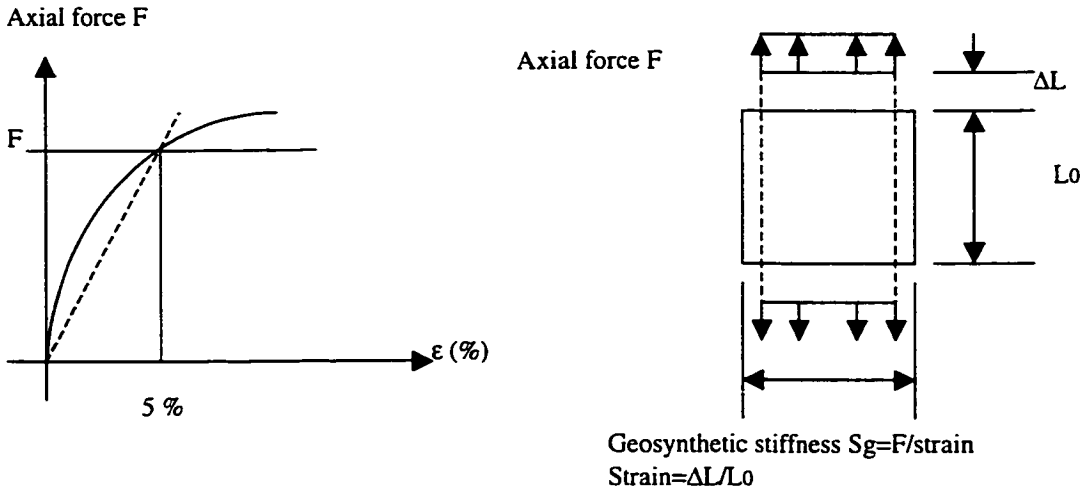

Figure (4.17) Geosynthetic stiffness selection at a standard axial strain

As the geogrid Poisson's ratio has a small effect on its reinforcing performance, its value can be assumed, if it is not reported in literature. For the frictionless perfectly plastic geogrid, one needs its strength in addition to E . Like all the geomembranes, the geogrid is usually modeled by a membrane element which has in-plane tensile and shear stiffness and strength without containing any bending and compression resistance.

The geometry of the modeling membrane is also determined from the manufacturing company. When the thickness is not included in the geometry description, one can assume an average value for it. Wathugala et al (1996) assumed the thickness of 0.1in to be fixed for the geogrid structure. Perkins (2000) suggested a thickness of 1 mm for the geogrid A,B existing in the Table(3.4).

Geogrid interface with the surrounding media:

The possibility of slippage occurrence along the interface between the geosynthetic and the surrounding materials is related to the shear strength and the level of shear stress developed along the interface developed at the interface which is associated with the resilient and permanent deformation in the pavements. Studying such possibility requires analyzing the behavior of the geogrid interface with the surrounding medium that is usually investigated by shearing or pull out test and numerically simulated through the interface, contact, element.

Barksdale et al (1989) concluded that the shear stresses developed at the geosynthetic interface become larger and, hence, a greater tendency to slip occurs as the total deflection of the geosynthetic increases. If the full friction in the geosynthetic is not mobilized, problem with slip can occur at deformation less than 0.25in (6.35 mm). The laboratory shear tests showed that a relative movement of up to 2in (50.8mm) between a geosynthetic and a soft cohesive soil is required to mobilize full friction. Barksdale et al's non linear finite element analysis indicated that the slip is not likely to occur for sections of moderate strength with CBR$\geq$3%.

An elastoplastic hydrostatic-dependence material model (friction interface), Mohr-Coulomb or Drucker-Prager, can accurately simulate the behavior of the geogrid interface with the surrounding soil and granular materials. It can capture the interface strength dependence on the normal stress and estimates reasonably the elastic stress level induced at interface .

As discussed in the previous section, the parameters required for Mohr-Coulomb model are the shear and normal stiffnesses, friction angle, and adhesion. Many experiments

were conducted to investigate the interface parameters of the geotextile-soil and granular materials systems (Saxena and Budiman, 1985; Koerner, 1994; Milligan, 1984).

On the other hand, fewer test results describing the frictional parameters and characteristics of geogrid with the surrounding media have been reported. Jewell et al (1984) discussed the components of interaction force components between the geogrid and surrounding soil materials in details. They gave the friction angles of the geogrid with several types of aggregates. Bearden and Labuz (1998) carried out a condensed laboratory program to test the interface shearing strength of geogrid with surrounding granular materials and concluded that the frictional resistance of the geogrid-base interface is approximately equal to the frictional resistance of the base alone. Additionally, the Federal Highway Administration (FHWA manual provided by Minnesota Local Road Research Board in1998 states that the interface friction angle approaches that of the soil itself (Hans and Andrew, 2000). Moreover, Hans and Andrew (2000) reported that the friction angle of the interface is usually assumed equal to the surrounding material's friction angle since the open apertures of the geogrid allow particle interlock.

Little information concerning adhesion was found in the literature. Hans and Andrew (2000) relied on a numerical study to investigate the adhesion between the geogrid and the surrounding granular materials. As the base material was assumed cohesionless, only adhesion of the geogrid with the surrounding subgrade was investigated. It was concluded from Hans and Andrew's study that adhesion has insignificant effect on system response.

Evaluation of the geogrid-AC interface parameters is more complicated than that of geogrid-soil materials interface parameters, since the behavior of geogrid-AC interface depends on additional variables, namely, temperature of the pavement, the type and rate of tack coat placed on the grid laid on the granular base, and other factors related to construction process and technology.

The bonding behavior between the geogrid and AC has been reported to be quite poor, since the geogrid's placement at the bottom of (AC) or within the AC (at the lower part of AC) was not a topic of interest to pavement researchers except for a few cases as reported in Chapter Two.

4.4 Suggested constitutive models for the FE simulations and required parameters

AC layer

(i) Linear elastic: Two elastic parameters

(ii) Linear viscoelastic thermological material with consideration of temperature change with time and throughout the depth. The required parameters are:

- Shear modulus curve with time at reference temperature G(t)
- Bulk modulus curve with time at reference temperature K(t)

If the material is incompressible, one needs only the G (t) and K is obtained from the elastic relations

- The constants of shift factor A,B .
- The temperature change with time, T(t)
- The temperature distribution function throughout the AC thickness T(Z)

- The thermal expansion coefficient of AC

(iii) Linear viscoelastic material without temperature consideration. The required parameters are:

- Shear modulus curve with time at reference temperature, G(t)
- Bulk modulus curve with time at reference temperature, K(t)

Granular materials (Base)

(i)Linear elastic: Two elastic parameters

(ii) Linear elastic- cross anisotropic. The constants required are:

- The elastic modulus in the horizontal directions(x,y), E_h
- The elastic modulus in the vertical direction (z), E_v
- Poisson's ratio in the horizontal directions(x,y), ν_h
- Poisson's ratio in the vertical direction (z), ν_v
- Shearing modulus

(iii)Elastoplastic and hydrostatic- dependent body (Mohr-Coloumb associated) or Drucker- Prager:

- The elastic modulus, E
- Poisson's ratio ,ν
- Friction angle, ϕ

(iiii) Elastoplastic, hydrostatic dependence and strain hardening material (generalized cap model)

- The elastic modulus, E
- Poisson's ratio, ν

- Friction angle, ϕ
- The ratio of the major to minor axis of the elliptical cap, R
- The Cap model material constants (D and W) which can be found from the hydrostatic test results.

Subgrade

(i)Linear elastic: Two elastic parameters

(ii)Elastoplastic and hydrostatic- dependent body (Mohr-Coloumb associated) or Drucker- Prager:

- Two elastic parameters
- Friction angle, ϕ

(iii) Cam Clay

- The specific volume at isotropic consolidation state when the pressure = $\frac{J_1}{3} = P$ equals to1
- Two elastic parameters
- The slope of the critical state line, M
- Is the slope of isotropic consolidation line, λ
- The slope of over consolidation line, κ

Geogrid

(i)Linear elastic material: Two elastic parameters

(ii)Elastoplastic material (Von Mises or Tresca)

- *Two elastic parameters*
- Shear strength

Geogrid –surrounding materials

(i) Complete bonding, no slippage in other words at the interface element with infinite stiffness

(ii)Linear elastic in the normal and shearing directions

- Interface element stiffness in the normal direction, K_n
- Interface element stiffness in the shearing direction, K_s

(ii)Elastoplastic frictional dependent elements (Mohr-Coloumb) in the normal and shearing direction

- Interface element stiffness in the normal direction, K_n
- Interface element stiffness in the shearing direction, K_s
- Shearing strength

Chapter 5

FINITE ELEMENT MODELLING CONSIDERATIONS

This chapter covers the numerical modeling considerations in the related literature and texts including the system geometry, boundary conditions, mesh procedure and traffic load application .

5.1 Geometry

Despite the huge computational time and computer memory, the three dimensional (3D) analysis is considered to be superior to the two dimensional (2D) analysis of the by many pavement analysts (Sam et al, 1998; Hjelmeted et al, 1997; Jiwon and William, 2002). The necessity for adopting the 3D(three dimension) arises from

(i) Geometric characteristics of the pavement system including the multiple layers having different thicknesses which can be fully simulated by 3D analysis which could substitute the test facility in a better manner than the 2D analysis

(ii) The mechanical behavior of pavement layers and the interfaces under moving loads are complex and need advanced constitutive models requiring space considerations

(iii) Simulating the pavement response to the dynamic load and thermal excitation cannot be controlled by 2D analysis. This is because the 3D analysis is capable of simulating the best shape representing the wheel load, the rectangular shape. (Witczak and Yoder,1973). In other words, when dealing with 2D analysis, the load shape should be restricted to a circular (axisymmetric condition) or infinite strip load (plane strain condition).

Moreover, the isotropic thermal effect in the plane deformation cannot be captured by the 2D analysis.

5.2 Kinematic boundary conditions

Domain truncation is examined with two different artificial boundary conditions, namely the roller and fixed conditions that are applied along the truncated domain. The roller support at the side edges of the pavement and the infinite stiffness (fixed) at the bottom of the of element have been used efficiently as displacements boundary conditions (Chen et al, 1995; Uddin et al, 1994; Zaghloul and White, 1993)

5.3 Mesh development procedures

The assumed domain size has a remarkable influence on the accuracy of the results. Assuming the system as a half space is only appropriate for axisymmetric representation and elastic analysis. According to the conventional boundary truncation method, the domain is truncated at a large but finite distance from the zone of influence and it is considered as if nothing exists beyond that distance. Imposition of artificial boundaries and prescription of their positions is assumed in this analysis.

Adopting a specific mesh size is dependent on the available memory, desired computational time and the type of load configuration analysis, i.e., single axle with single tire, single axle with tandem tire, and so on. In all cases the symmetry should be considered and only a half or quarter of the system should be analyzed, if possible. The mesh dimension in the vertical direction is assigned according to the pavement layer thicknesses. Zaghloul and White (1993) used subgrade depth of 4ft (1.22m) . Zaghloul

and White also investigated the effect on the deep foundation type (type of the layer under the adopted 4ft (1.22m) of the sandy silt subgrade in the pavement design evaluation), and they concluded that the soft to medium clay foundation results in a higher deflection than that of the bed rock and stiff clay. Uddin et al (1994) found that 40 ft (12.20m) is the optimum subgrade depth, which simulates a semi-infinite subgrade. Dondi (1996) used subgrade thickness of 2.5 m under the base layer.

In terms of the section length, adequate length of the pavement section should be considered to reduce any edge effect error. However the length should be increased with care in order to decrease the problem size and the analysis time. An evaluation of the section length was conducted by Zaghloul and White (1993). After using lengths ranging from 5.08 m to 35.56 m, they found that for sections longer than 10.16m no significant effect on the pavement response was pronounced, Zaghloul and White adopted length of 15.24m in their analysis. Uddin et al (1994) determined the optimum pavement length by testing lengths from 12.2m to 73.2m. They found that the optimum length is 18.3m which is close to the length of 15.24m adopted by (Zaghloul and White, 1993).Dondi (1996) used length of 2.79m. The width of the analyzed section is controlled by the number of lanes in the road, widths of these lanes, the shoulders widths (if any).

Uddin et al (1994) investigated the optimum subgrade width extension by studying the lateral extent of the subgrade below the pavement. A total width of subgrade was found to be 26.6m (87.3ft). Such extension was not considered by other pavement finite element analysts (Dondi, 1996; Sam et al, 1997; Chen et al, 1995; Yoon et al, 1996; Zaghloul and White, 1993)

The effect of pavement shoulders width on the system performance is not included in this study. A special parametric study including the effects of shoulder width and pavement-shoulder joint was conducted by Zaghloul and White (1993) showing that the sections without shoulders have higher values of the surface deflection than the shoulder-supported sections.

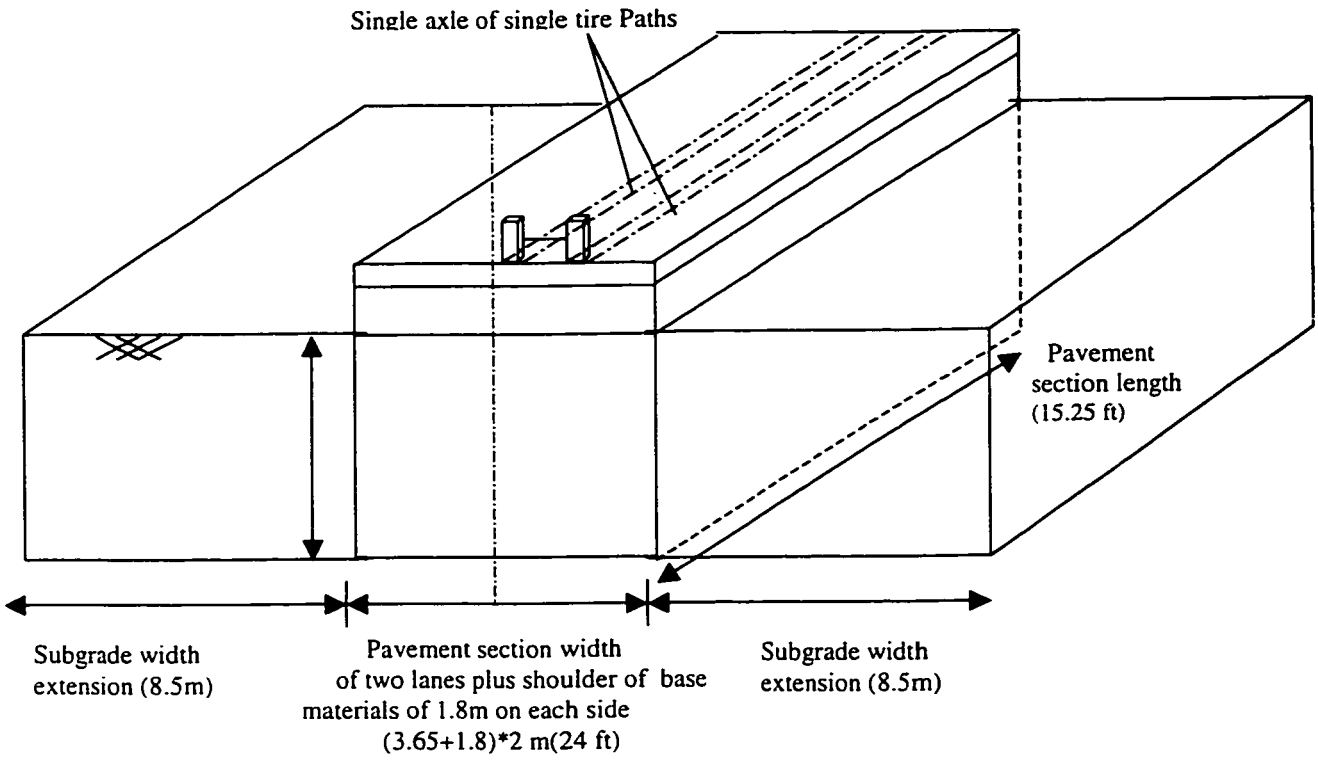

Figure(5.1) Selected FE domain dimensions of a flexible pavement system Uddin et al. (1994)

Refining and the grading mesh, element type ,aspect ratio and other issues

As the loading on the pavement surface is highly localized, the finest mesh is required near the load to capture the step stress and strain gradient in these areas. The finer the mesh, the faster the convergence but the longer the computing time and much larger memory requirement. The mesh of Sameh and Thomas (1993) consisted of two equally

spaced meshes in the horizontal (xy) plane. A coarse mesh with 22.2" (56.4 cm) spacing was used in both the transverse (x) and longitudinal (y) directions, and in the region of load path, finer mesh with a 11.28 cm× 56.4 cm spacing in x and y directions.

Yoon et al (1996) used for mesh spacing of 13.97 cm×26.67 cm in the x - y plane one layer of elements having thickness of 10.16 cm was used to represent AC and three layers of 10.16 cm thickness were used to represent the concrete slap under the AC layer. On the other hand, thicker layer of elements having thickness of 25.4 cm was used to represent the subgrade. According to Chen et al (1995), quadratic elements perform well even with a coarse mesh. A reduced integration element is advised for reducing the computational time. Yoon et al (1996) reported using two element types, full integration solid and reduced integration rule were used. Both linear and quadratic elements with different configurations were used. It was concluded from their elastic finite element study that quadratic element with infinite elements at the borders gives matched results with the elasticity theory analysis. A particularly stable and successful element is the eight-noded isoparametric element with reduced integration rule (David and Paul,1991)

The accuracy of the solution is affected by the element aspect ratios. The aspect ratio of 1:1:1 is the optimum for good accuracy. As discussed earlier, small size elements should be used in the areas of step strain and stress gradient .Achieving this will lead to a non-uniform mesh and non-uniform optimum aspect ratio throughout the system. Hence, moving to larger elements in the domain of load localization should be done carefully in order to keep the desired aspect ratio optimum as much as possible.

A radially graded mesh affords the best compromise between the problem size and accuracy for pavement problems, because element aspect ratios are relatively uniform

In addition, ill conditioning associated with having adjacent elements of vastly different sizes is minimized, and smooth transitions from one element size to another is achieved. These conclusions about the smooth element transitions were reported by Hjelmstad et al. (1997). In 3D analysis it is impossible to have a perfectly smooth transition of both element size and aspect ratio in the whole domain modeled. However, the priority should be given to the areas close to the applied load. On the other hand, the traditional mesh grading strategy may lead to a slower convergence, but its advantage of having better regularity of the modeling element shape makes it acceptable for use in pavement modeling, provided that efficient grading is preferred to keep the aspect ratio as small as possible, (e.g. less than 4 in the areas of interest)

Sam et al (1997); Chen et al (1995); Yoon et al (1996); Zaghloul and White (1993); Uddin (1994) applied the traditional grading strategy in their analyses

For developing an effective mesh toward numerical stability, good rate of convergence with accurate results, least computational time and computer memory the following guidelines should be followed:

-Particular attention should be given to the areas of interest such as, wheel pass, localized loading area, and the areas where high distresses are expected. Moreover, the subdivision is performed such that the distributed load is carried by an integer number of elements.

-Trying to keep the aspect ratio close to one where the strain and stress gradients are high and in the areas of interest to achieve faster convergence

-Large stiffness discrepancies between elements, poor choice of quadrature rule, extremely thin solid elements and Poisson's ratio of 0.5 for these elements may lead to ill-conditioning, locking, or instability. These aspects can seriously degrade results rather

than making them so peculiar that it becomes obvious that some thing is wrong (Cook et al, 1989) .

-The same guidelines followed in the descritizaion for the static load case can also be followed in the dynamic loading conditions. However, a dynamic analysis may require more elements than the analogous quasistatic problem to capture the essential features of the dynamic response and to calculate accurate natural frequencies and mode shapes.

-The mass matrix will be a poor discrete representation of the actual continuous mass distribution of the structure, and consequently artificial wave reflection and additional numerical noise arise, if the element sizes do not change smoothly

-If the refinement does little to change the results, then there is an evidence that results are satisfactory. Analogously, in a response history analysis, one might examine if the results are significantly changed by a change in the number of modes used in a modal method or by a change in the time step of the direct integration method (Cook et al,1989).

-In a linear analysis, the extra energy produced by the numerical instability, which leads to a blow up in the response is easy to detect . On the other hand, in nonlinear analysis with elastic-plastic (energy dissipation) material behavior, or other energy dissipating materials, the extra energy introduced in the system by numerical instability may be dissipated by plastic work or some other irreversible mechanism so that it is possible for the instability to be arrested. An arrested stability is often difficult to detect because the solution, although in error by 10% to 100% may appear reasonable (Cook et al, 1989).

-When analyzing nonlinear problem by explicit methods, it is usually advisable to perform an energy balance check to help assure stable and accurate computation.

5.4 Dynamic Load application

5.4.1 Wheel load configuration and contact area

Types of the truck-wheel arrangements can be divided into several basic categories

(1)single and dual wheel.

(2)single and tandem axles

(3) nose wheel.

Truck wheels may be arranged in several combinations of these listed above.

The legal axle load in most states ranges from 18,000 pounds (80 kN) and 20,000 pounds (90 kN), which implies that a load on one set of dual tires will be 9,000 pounds (40 kN) to 10,000 pounds (45kN). Thus if greater loads are required, it is common to add a tandem axle (Yoder and Witczak,1975)

For most problems, the contact pressure between the tire and the pavement must be equal to the tire pressure, and the contact pressure is assumed to be uniform over the imprint area .

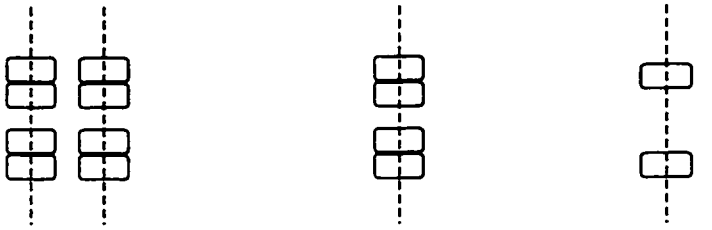

(a)Tandem axle with dual tires

(b)Single axle with dual tires

(c)Single axle with single tire

Figure(5.2) Basic types of truck wheel configurations (Yoder and Witczak, 1975)

The thickness of AC dictates whether the stresses caused by the dual tires have some overlapping or not. It also dictates if overlapping is equivalent to the stress caused by

one is equivalent to the stress caused by one tire whose load is the sum of the overlapped wheel loads. As the effect of load value, configuration and shape is not considered in this study, only a single tire of the single axle of load (10,000 Ib=45 kN) is considered which is on tire pressure of 550 kPa

In the 3D analysis, the shape of the contact area could be a combination of a central rectangle with semi circles at the ends (Yoder and Witczak, 1975) with length calculated as

$$L=\left(\frac{A}{0.5226}\right)^{1/2} \tag{5.1}$$

where A is the contact area in square inches.

The Center of Transportation Research investigated tire contact area versus wheel loading. The average contact area under 40 kN wheel load was reported to be between 100 inch square (645.20 centimeter square) and 110 inch square (709.72 centimeter square). For a single wheel load of 45 kN Sam et al (1997) assumed the contact area 125 inch square (806.50 centimeter square)

If Equation (5.1) is applicable to a pure rectangular area, then for A =125 inch square (806.50 centimeter square) , the dimensions of the contact area are: L=15in (38.1 cm), and B=8.33in (21.16 cm).

5.4.2 Time duration and the wave shape of traffic loading

As traffic moves on a highway, the axial and the radial stresses change over a short period of time of each wheel pass can be considered as a stress pulse . The magnitude, shape, and duration of these pulses vary with the wheel load, its speed, and the depth in the pavement at which the stress is considered (Terrel et al, 1974).When the load is

directly above the given point, the stress at the point is maximum, and when the wheel load is at a considerable distance from that point in the pavement the stress at the point is zero. It is therefore reasonable to assume the stress pulse to be a haversine or triangular loading the duration of which depends on the vehicle speed and the depth of the studied point

Terrel et al (1974), Terrel and Awad (1972), and Yang (1993) presented detailed literature, graphs, and discussed the interactions between the assumed wave shapes (triangular, rectangular haversine), the various depths through the pavement system, and the corresponding pulses times. The graphs given by Barksdale (1971); Mclean (1974) [Figure(5-3) and Figure (5-4)] are very valuable in deciding the pulse shape and duration time for a specific depth according to a given speed. Because the lower speed leads to higher strains and deflections than the higher speed (Sam et al, 1998). A relatively low speed (15-30 mph) will be adopted for this study shape. The duration from such speeds are obtained from the graphs given by Barksdale (1971) and McLean (1974).

The average of the time lagging between two successive axles is reflected in the repeated load test by considering a short rest period .The effect of the speed is usually reflected in the load duration which is dependent on the contact area and the depth of the point under study. In the view of the fact that the vehicle speed varies a great deal and the depth of the material may not be known during the design stage, it is recommended that haversine load with duration of 0.1s and a rest period of 0.9s be used. However Terrel et al (1974) concluded after intensive test program that there is no significant difference in the magnitude of the total or resilient strains between the triangular and sinusoidal stress pulses.

Coffman (1967) investigated the relation between these factors for a circular contact area, and concluded that the traffic load has particularly no effect at a point when its center is located at distance of 6a from this point where a=vD/12 or when the duration time, D = 12 a / v, where: 12a (in) is the assumed to be the influence length of the circular tire contact pressure. From this study, Coffman (1967) concluded that the speed of vehicle in field is related to the frequency of the dynamic load in the laboratory and that the vehicle acts as a cyclic load with a wavelength of 6 ft (182.88 cm). Barksdale (1971) arrived at the same conclusion

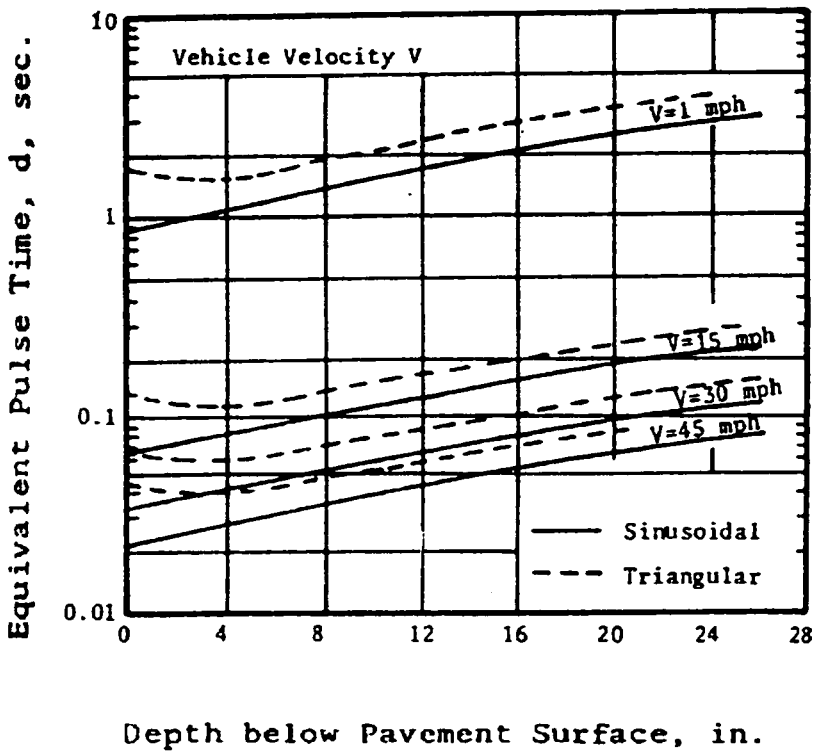

Figure(5.3) Vertical stress pulse time under haversine or triangular loading (after Barksdale,1971)

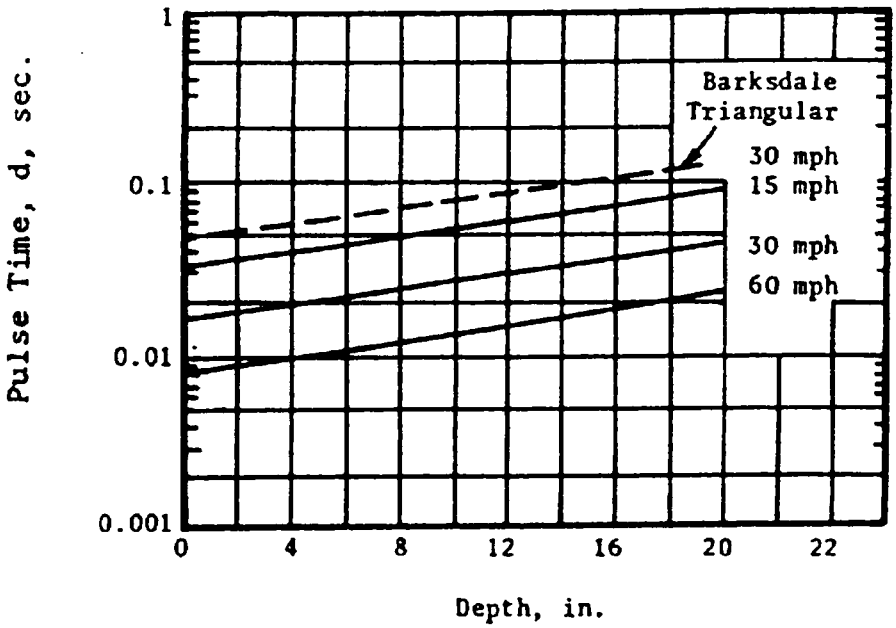

Figure(5.4) Vertical stress pulse time under square wave form loading (after Mclean,1974)

5.5 Dynamic analysis

5.5.1 Basic equations and concepts

The dynamic equilibrium equation of a structure is (Cook,1989)

$$[M]\left(\ddot{r}\right)+[C]\left(\dot{r}\right)+\left(R^{int}\right)=\left(R^{ext}\right) \qquad (5-2)$$

(r) is the displacements and rotations vector

$\left(\dot{r}\right)$ is the velocity vector

$\left(\ddot{r}\right)$ is the accerelation vector

$\left(R^{int}\right)$ is the internal force vector and it is =[K][r] in linear analsis where [K] is the stiffness matrix

$\left(R^{ext}\right)$ is the external force applied (function of time)

[C] is the damping matrix

[M] is the mass matrix

Considering a system of a single degree of freedom (SDOF) with a mass m, the response due to a pulse load Po is given, after considering viscous damping *c* against this motion, as

$$V(t)=(V_{st})_0\{1-e^{-\xi w t}[\cos w_D\, t+\frac{\xi}{\sqrt{1-\xi^2}}\sin w_D t]\} \qquad (5.3)$$

Where :

$(v_{st})_0$ is the static deformation due to Po. $(v_{st})_0=\frac{Po}{K_v}$

K_v is the stiffness of the SDOF system

ξ is the damping ratio or fraction of the critical damping $\frac{c}{c_c}$

c_c is the critical damping of the system

$$c_c = 2m\,w. \tag{5.4}$$

w_D is the damped vibration frequency and is given by

$$w_D = w\sqrt{1-\xi^2} \tag{5.5}$$

w is the natural frequency of this system where $w = \sqrt{\frac{k_v}{m}}$. The natural frequencies of a system are independent of the amplitude if conditions remain linearly elastic, gaps do not open or close, and amplitudes are small in comparison with structural dimensions so that any geometric nonlinearity does not appear

If damping $c > c_c$, the motion decays without oscillation

If damping $c < c_c$, the motion is oscillatory and it decays gradually or slowly with time.

For small damping, ξ, is obtained after assigning the ratio of any two consecutive displacement peaks as :

$$\delta = \ln(\frac{v_2}{v_1}) = -2\pi\xi \tag{5.6}$$

5.5.2 Damping

Damping can be treated by (1) phenomenological damping methods, in which the actual physical dissipative mechanisms such as elastic-plastic hysteresis loss, structural joint friction, material microcracking are modeled. (2) spectral damping methods, in which the viscous damping is introduced by means of specified friction of the critical damping (Critical damping, for which the damping ratio ξ=1, marks the transition between the

oscillatory and non-oscillatory response). The first method requires detailed models for dissipative mechanisms and almost results in nonlinear analysis

On the other hand, in spectral methods, for each frequency experimental observations of the vibratory response of a structure are used to assign the critical damping as a function of the frequency or more commonly as a single damping fraction for the entire structure at that specific frequency.

A popular spectral damping scheme is Rayleigh or proportional damping giving [C] as

$$[C]=\alpha[M]+\beta[K] \tag{5.7}$$

For multiple degree of freedom system, the critical damping ratio at any frequency of mode is given as

$$\xi_i=\frac{1}{2}\left(\frac{\alpha}{w_i}+\beta w_i\right) \tag{5.8}$$

The variation of the normalized critical damping ratio with the angular frequency is shown in Figure (5.5). The mass proportional damping is dominant at lower angular frequency ranges, while stiffness-proportional damping dominates at higher angular frequencies. In other words, damping attributes to the stiffness side of equation increases with increasing frequency, whereas damping attributes to the mass side increase with a decreasing frequency. Usually the two frequencies and their corresponding critical damping friction used to determine α and β , namely, w_{lowest}, which is taken as the lowest natural frequency of the structure with its corresponding ξ_1 and $w_{highest}$ is taken as the maximum frequency of interest in the loading, or response with its corresponding ξ_2.

However, damping in the geological media is commonly hysteretic, frequency independent, and obtaining Rayleigh damping requires special consideration.

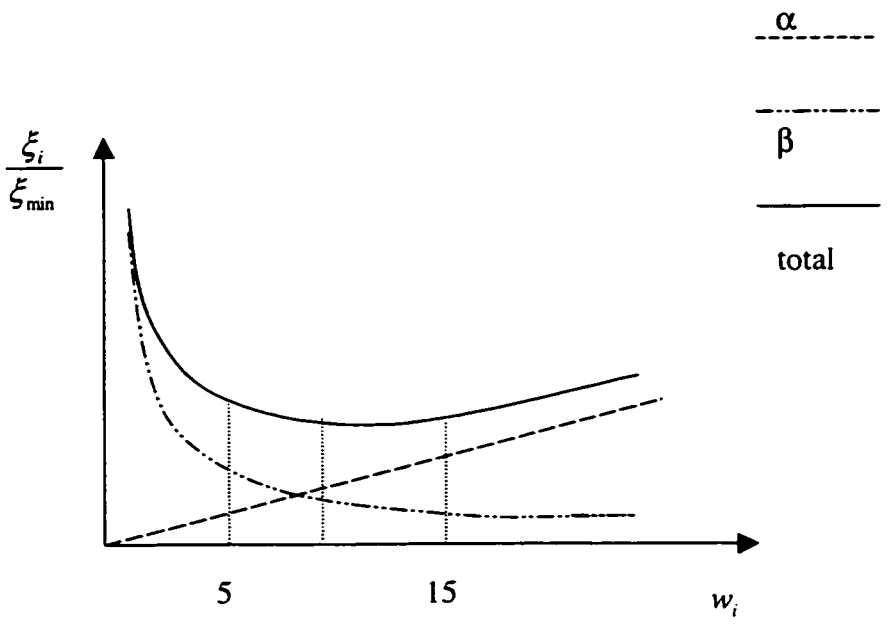

Figure (5.5) Variation of normalized critical damping ratio with angular frequency (FLAC manual, 2001)

As shown in Figure (5.5), there is a predominant value of frequency for which the damping coefficient becomes frequency independent. If the predominant frequency starts at a specific value then it is noticed that the damping ratio is almost constant over at least three times this specific value, frequency range (say for, example from 5 to 15), which may reflect approximately hysteretic that damping coefficient is minimal

$\xi = \xi_{min}$ and for this situation can be calculated with a corresponding w_{min} as:

$$\left\{ \begin{array}{l} \xi_{\min} = (\alpha\beta)^{0.5} \\ w_{\min} = (\frac{\alpha}{\beta})^{0.5} \end{array} \right\}$$

$$\alpha = \xi_{\min} w_{\min} \tag{5.9}$$

$$\beta = \frac{\xi_{\min}}{w_{\min}} \tag{5.10}$$

and the center frequency is then defined as

$$f_{\min} = \frac{w_{\min}}{2\pi} \tag{5.11}$$

It is noted that at only the frequency $w_{\min}$ mass damping and stiffness damping each supply half of the total damping force . $w_{\min}$ is usually chosen to lie in the center of the range of frequencies present in the numerical simulation-either natural frequencies of the model or predominant input frequencies . The plastic flow dissipates considerable energy at high excitation levels, hence the selection of the damping parameters is less critical to the outcome of the analysis than if an elastic response otherwise used. A center frequency or $w_{\min}$ must be specified to reflect the frequencies associated with both the system and input wave. The frequency of the input wave (loading frequency)is acceptably used as $w_{\min}$ (FLAC, 2001).

Alternatively, the natural frequency of the free oscillation of the undamped system excited by a single pulse (Applying and removing the load quickly and then observing the frequencies recorded after removing the load, is the physical implementation of the eigenvalue problem) .

In some cases, the fundamental vibration frequency may be estimated by reducing the problem of to a single DOF, then calculating $w_1 = \sqrt{\frac{k}{m}}$ (Cook et al, 1989)

To find the stiffness it is assumed that the fundamental vibration mode resembles static deflection resulting from applying a unit vertical (let us say the direction of interest) load on the surface of the system which is elastic.

For geologic materials critical damping coefficient falls in the range of 2 to 5% , If the plasticity constitutive law such as Mohr-Coulomb is involved, then a considerable amount of energy dissipation occurs during plastic flow. Thus a minimum percentage of damping may be assigned to the Cam Clay soil, further, dissipation will increase with amplitude for stress/strain cycles that involve plastic flow.

In summary, the following guidelines are followed when assigning the Rayleigh damping constants , in case it is considered to represent the damping of the system :

1- The frequencies which are not important physically should be damped. The important frequencies can be considered as those frequencies whose values are close to the loading frequency value and the most important frequency is that whose value equals to the load frequency value, because here the dynamic effect will reach its maximum; i.e, dynamic magnification factor is maximum and the resonance case appears.

2- As one has a highly plastic material (weak soil modeled by Cam Clay),a lot of energy is dissipated (plastic work) throughout the response, and here one should look for decreasing the damping which also results in energy dissipated if we want to avoid difficulty in obtaining convergence [(External work-Internal work)=allowed error].

3-As damping in the geologic materials tends to be hysteretic(frequency-independent) or what is called local damping which only needs the damping coefficient as an input. and as ADINA is ill equipped with feature therefore one should select the best α and β which reflect as much as possible this hysteretic behavior.

5.5.3 Selection of the dynamic method to handle the system equilibrium equation

Basically problems of dynamics are considered to be as either structural dynamics (SD) or wave propagation (WP) problems. In these problems, the focus may be on natural frequencies or vibration and corresponding mode shapes to compare them with the frequency of excitation, or on how the structure moves under a prescribed load, i,e, a time history analysis. The methods used to treat time history analyses are modal methods and direct integration methods. The direct integration method includes implicit and explicit modes When the frequency of excitation is high, impact load or blast load, and hence the structure responses are rich in high frequencies, therefore high frequency natural modes must be represented in the analyses, and the number of the significant modes should be large, may be 2/3 of the DOF if accelerations are required as a function of time. In WP problems, the analysis spans short period of time and it is typically of the order of a wave traversel time across the structure .On the other hand , in SD problems, the frequency of excitation is usually of the same order as the structure's lowest natural frequencies of vibration, i,e, the loads vary more slowly with time, the response is dominated by the lower modes and high modes may be insignificant in application.

In addition ,the inertial force is very important in structural dynamics problems

If the rise time and duration of the load exceeds a small multiple of the time required for a sound wave to travel through the structure, the problem is probably of the structural dynamic type (Cook et al, 2002). Adopting either explicit or implicit method is strongly problem-dependent. Discussing the positive and negative attributes of each of these method is helpful to define and classify the dynamic situation of the pavement system and accordingly choose an effective solution procedure

(i) Implicit method

Strong points of the implicit method

-The implicit method is suited to structural dynamics problems; it competes with modal superposition, and it may be cheaper where many modes would be needed in the modal analysis.

-It is conditionally stable and the size of Δt ,in contrast with explicit method, is limited only by consideration of the accuracy rather than the numerical stability.

-Non-linearity can be accommodated without great trouble. However for severe non-linearity the convergence may be difficult

Weak points of implicit method

-The dynamic equation is a system of coupled linear algebraic equations even if [C] and [M] are diagonal matrices

-An additional loading function constitutes a new problem, without cost-saving carryover from the preceding problem other than reuse of the previously computed effective stiffness in its forward –reduced form for equation-solving

-Cost per time step is expensive and needs more time compared to the explicit method

-Mass matrix should be consistent

-Time step and accuracy: Cook et al (1989) states that the time step which will provide accurate results in the implicit method should equal about

$$\Delta t \leq \frac{1}{20} T_{co} \qquad (5.12)$$

where:

$$T_{co} = \frac{2\pi}{w_{co}} \qquad (5.13)$$

$$w_{co} = 3w_u \qquad (5.14)$$

where w_{co} is called frequency cut off, w_u is the highest frequency of interest in the loading, which may be represented by Fourier series in case it is complicated, or response of a structure. This could be the frequency of the wave load in this work

w_u is multiplied by three because in a system having large number of excited frequencies, high w_{co} will give adequate solution accuracy with a more likely consideration as a problem of wave propagation (Bathe, 1996)

Note :A smaller time step is occasionally required in nonlinear analysis to avoid convergence difficulties

(ii) Explicit method:

Strong points of the explicit method

The advantages of using the explicit method (central difference) method are justified by:

-The dynamic equation of the system is a set of linear algebraic equations and if the mass and damping matrices are diagonal , then these equations become uncoupled (no need to solve simultaneous equations). In this case the stability condition is:

$$\Delta t \leq \frac{2}{w_{max}} . \qquad (5.15)$$

where w_{max} is the highest natural frequency of the $[K]-w^2[M]=[0]$

-The uncoupled equations are obtained even when [C] is not diagonal, in other words when the stiffness contribution to the damping is operational. However, the time step achieving stability should become smaller as:

$$\Delta t \leq \frac{2}{w_{max}}(\sqrt{1+\xi^2}-\xi) \qquad (5.16)$$

where the corresponding fraction of the critical damping at the highest undamped natural frequency is w_{max}.

- Because the element stiffness [k] need not be formed when getting the internal force at each time interval $\{R^{int}\}_n = [K]\{q\}_n$, explicit method can treat large three dimensional models with comparatively modest computer storage requirements

-Computing the displacement, D_{n+1}, requires, $[R^{int}]_n$, for non linear materials. The constitutive laws are functions of strain (not strain rate) $[R^{int}]_n$ and it is easy to evaluate because D_n and hence the strain at the step n Δt, is known. For this reason the explicit method is suited for nonlinear analysis

- A feature of the dynamic equilibrium equation formed according to the explicit method is that the stability is not affected by damping, therefore, the central difference method should have both the damping matrix and mass matrix diagonal in order to be economically competitive with the implicit method. According to Rayleigh or proportional damping, the diagonal damping matrix means that the contribution of the stiffness to damping is zero

Weak points of the explicit method

The shortcomings of using the explicit method (central difference method) are

- It is conditionally stable, which means that the response of the system will not stabilize at certain values or will not decay, and it will blow up giving unbounded time-history response, unless the time step meets the conditions of stability as explained above.

The numerical instability is very hard to detect because the solution, although in error by 10%100% or more, may appear to be reasonable.

-It is difficult to model damping by spectral methods (Raleigh damping) if [C] is intended to be diagonal

Some remarks about using the explicit method

-Lumped mass matrix should be used

-Element order and integration rule:

-As the internal element force $\int [B]^T \{\sigma\}_n dV$ requires the same order of quadrature as used for the element stiffness matrix, $\int [B]^T [E][B] dV$ at each time step , hence there is considerable motivation to use the reduced quadrature to evaluate the internal forces particularly in three dimensions. However, when reduced energy integration is used, additional precautions are needed to prevent mesh instabilities. In general, the lower-order displacement element are more adept at modeling the discontinuities of the strain propagating thought the model in wave propagation problem

-Damping and the critical time step : in the explicit method assigning the right time step is essential, as this method is conditionally stable . If stiffness proportional damping is not used then the time step condition used for dynamic runs is given by equation (5.15) .

If the stiffness proportional is in operation, then the time step condition is given by equation (5.16)

$$\Delta t \leq \frac{2}{w_{max}}(\sqrt{1+\xi^2}-\xi) \tag{5.16}$$

where w_{max} is the highest natural frequency of the $[K]-w^2[M]=[0]$

The highest frequency is found as follows

If one considers the undamped free system undergoing harmonic motion, say under initial condition $\{D\}=\{\overline{D}\}\sin wt$,in which each DOF moves in phase with all other DOFs substituting in the main dynamic equilibrium equations gives

$$([K]-w^2[M])\{\overline{D}\}=[0] \tag{5.17}$$

Premultiplying by $\{\overline{D}\}^T$ and solving for w^2 gives the Rayleigh quotient

$$w^2=\frac{\{\overline{D}\}^T[K]\{D\}}{\{\overline{D}\}^T[M]\{\overline{D}\}} \tag{5.18}$$

The Rayleigh quotient is, in fact an extreme value when the $\{\overline{D}\}$ varies in the neighborhood of an exact eigenvector, accordingly the extraction of eigenvalue can be approached as an optimization problem. The values of the Rayleigh proportional damping factors are bounded by the largest and smallest eigenvalues. That is ,for any vector $\{v\}$

$$w^2_{min} \leq \frac{\{v\}^T[K]\{v\}}{\{v\}^T[M]\{v\}} \leq w^2_{max} \tag{5.19}$$

where w_{max} and w_{min} are, respectively, the largest and the smallest frequencies of the system. It is proved that un upper bound to w_{max} can be obtained by considering the eigenproblem for a single, unsupported element as:

$$\det([k]-{}^{e}w^{2}[m])=0$$

If ${}^{e}w_{max}$ then $w_{max} \leq {}^{e}w_{max}$ (5.20)

The same argument can be applied for obtaining the minimum frequency of the system ,and it can be shown that

for ${}^{e}w_{min}$, $w_{min} \geq {}^{e}w_{min}$ (5.21)

Applying this method to unsupported bar element with mass density ρ , and considering the lumped mass matrix (Bathe, 1996 ; Cook et al,1989), the highest natural frequency of the element can be found by hand calculation as

$${}^{e}w_{max} = \frac{2c}{L} \tag{5.22}$$

where

$c_E = \sqrt{\frac{E}{\rho}}$ is the compression wave speed, or (5.23.a)

$c_G = \sqrt{\frac{G}{\rho}}$ is the shearing wave speed (5.23.b)

The results obtained for the bar can be generalized to a solid or plane element after replacing L by an effective element length L_e which is chosen depending on whether implicit or explicit solution is employed. In the explicit (central difference method) and when using lumped mass matrix and lower order element (8 nodes for 3D analyses). If a relatively uniform mesh is used, then L_e is equal to the smallest distance between any two of the nodes of the mesh employed.

Chapter 6

MODEL SELECTION AND PARAMETRIC STUDY

6.1 Introduction

The first part of this chapter describes the finite element model selected for the pavement system in terms of the geometry dimensions, mesh configuration, materials constitutive models loading configuration, and dynamic load representation.

Preliminary analyses are conducted at first. Such analyses are made to investigate the following objectives :

1- Determine the best level of mesh refinement and number of elements which give small aspect ratio where the strain gradients are high with good rate of convergence and accuracy with less time computations and computer memory. This objective is achieved using the linear system.

2- Determine the dynamic response of the mesh using the implicit method. This, at the same time , allows for testing the capacity of this method to handle the vibration response of linear and non linear pavement systems.

3-Investigate the effect of AC viscoelastic response, base elastoplastic behavior, base linear elastic cross anisotropic behavior, the elastoplastic and strain hardening behavior of the subgrade on the fatigue and rutting lives of the pavement system.

The second part of this chapter presents the model parametric study. The analyses for this part have the following objectives :

(i) Determine the influences of the base quality, base thickness, subgrade quality on fatigue and rutting of a non linear pavement system under dynamic traffic load

(ii) Investigate the performance of a conventional pavement system reinforced by geosynthetic and determine the best location of the geosynthetic in such system and how the quality of base, its thickness, and quality of the subgrade may affect such location

As mentioned earlier the following criteria will be considered in evaluating the results

- ε_t, the maximum tensile strain occurring at the bottom of AC at element B shown in Figure (6.1) which is calculated for evaluating the fatigue life of AC.

- Δ_z, the maximum vertical deflection of the surface at node 1 shown in Figure (6.1),

and / or

- ε_c, the maximum vertical strain transmitted to the top of sub grade at element C shown in Figure (6.1)which is calculated for evaluating the rutting life of the whole system.

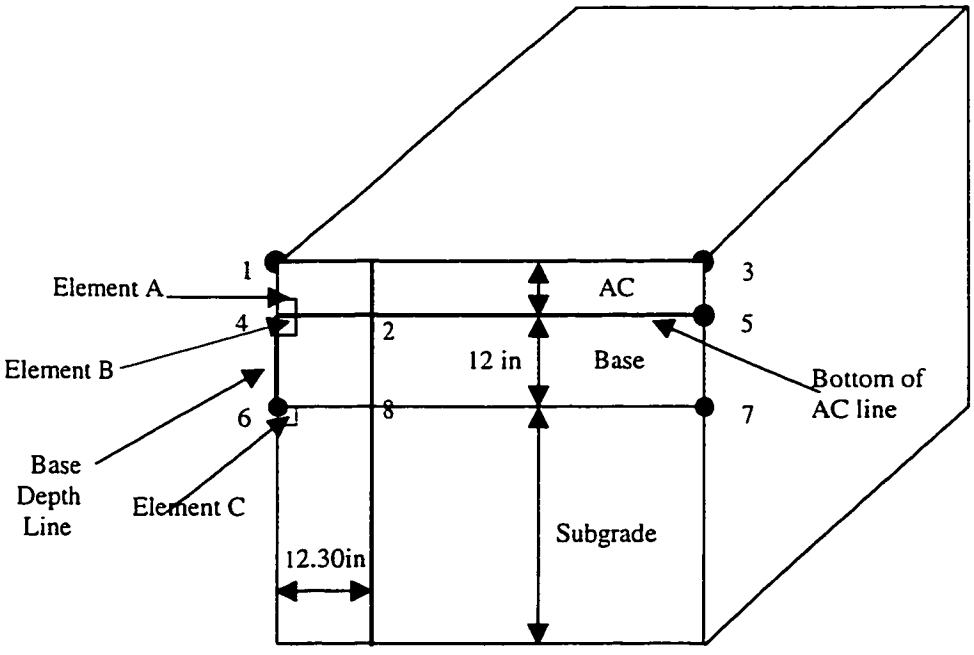

Figure (6.1) Element locations which are to be observed throughout the FE analyses

6.2 Preliminary Analyses

Based on the literature concerning the mesh size, reviewed previously, the length of the mesh and the depth of the subgrade are decided as shown in Figure (6.2). A single wheel of a single axle is considered. An equivalent 80 kN (18,000 lb) single axle load with single wheel is used; selected to be 1.8m The load on one tire is 40 kN =9000 lb . As the effect of the tire wall is neglected, the contact pressure is assumed to equal the tire pressure which could be taken as 550 kPa or 80 psi,

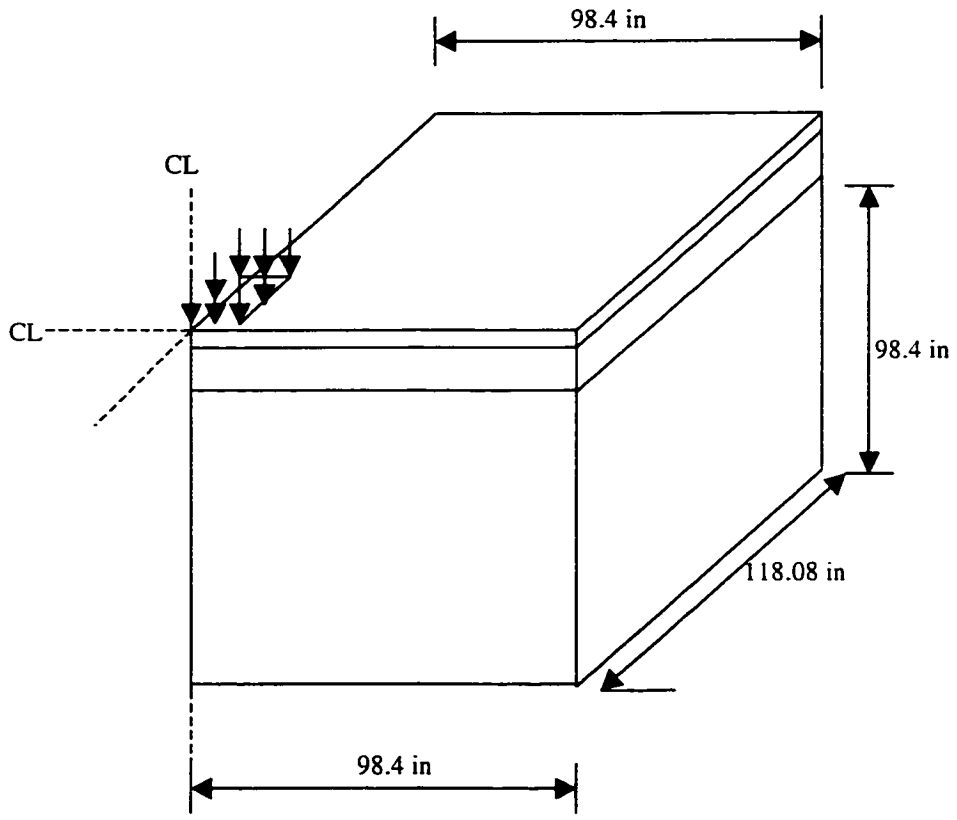

Figure (6.2)Dimensions of the FE mesh (a quarter of the system is analyzed due to double symmetry)

Then the contact area of $\frac{9000}{80} = 112.5 \text{ in}^2$ (725.85 cm^2) is considered. This area agrees with the recommendations of Center of Transportation Research, USA . After considering the relation (5.1) is applicable to a pure rectangular area, the contact area is converted into an equivalent rectangular area with a length of L=14.67 in (37.26 cm) and B=7.667 in (19.47 cm). For numerical modeling, theses dimensions can be taken as L=16 in (40.64 cm) and B=7 in (17.78 cm)

The layout of the contact area is shown in Figure(6.3).

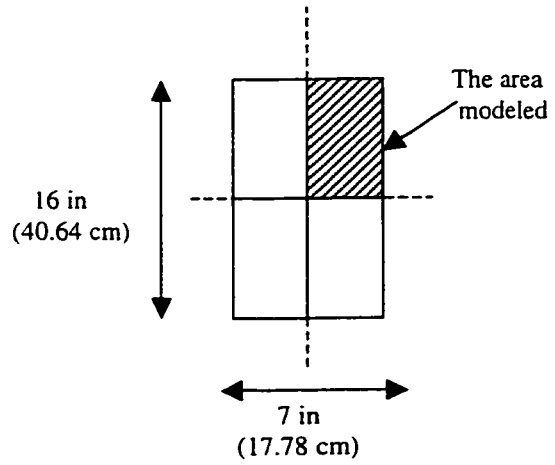

Figure (6.3) Tire contact area adopted

Referring to the dimensions in section 5.4.1 a triangualr wave shape of 0.1s time duration is adopted. The load duration is obtained, for a speed of 15 mph from the graph shown in Figure (5.3). Such speed is selected to be low because low speed leads to more damaging effect (Sam et al,1998) and consequently leads to a more conservative design. Alternatively, applying the relation (5.1) to a rectangular contact area and the specified speed is a reasonable approximation to get the time duration of the traffic load. The repeated load is considered either by calculating the total accumulated loading time of

one time function using the speed and the number of load repetitions which reduces the computation time and provides reasonable results, or by calculating the distresses, $\varepsilon_t, \varepsilon_c$, for one loading cycle and its rest period, and then using the empirical relations (2.1) and (2.3) to obtain the distresses $\varepsilon_t, \varepsilon_c$ for any number of loading cycles, provided the load-time function used in FE simulations reflects as much as possible the loading situation of the repeated test for which the empirical formula are obtained.

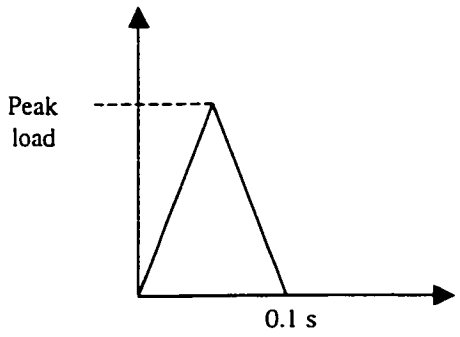

Figure (6.4) Time function used to reflect the cyclic traffic load

Each exterior boundary is fixed in the direction perpendicular to this boundary (roller support) except the base of the model which is fixed in all directions (fixed support). Each plane of symmetry is also roller-supported in the direction perpendicular to this face

6.2.1 Selection of the mesh and other related issues

A three dimensional analysis with 3D solid element of 8 nodes is used. The elastic material properties shown in Table (6.1) are used for testing the mesh grading and the refinement level

As shown in Table (6.2), three levels of refinements are tested for the purpose of selecting a convenient mesh.

Table (6.1) The elastic system used in the prime analyses for testing mesh grading and refinement

Layer	Thickness	Properties		
		E (kPa)	ν	ρ (g/cm^3)
Asphalt concrete (AC)	4 in (10.16 cm)	4134693	0.30	2.49
Base	12 in (30.48 cm)	206734	0.30	2.21
Subgrade	_	50581	0.30	1.38

Table (6.2) Maximum surface deflections for different size meshes

Mesh	Number of elements				Notes	Maximum Δ_z (in) at node 1 shown in Figure(6.1) (1 in = 2.54 cm)
	AC	Base	Subrgrade	Total		
1	300	600	1500	2400	Maximum aspect ratio less than 10	-2.01900E-02
2	960	1600	3200	5760	Maximum aspect ratio less than 10	-2.10726E-02
3	540	900	1800	3240	Maximum aspect ratio less than 16	-2.07834E-02
4	720	1080	2160	3960	Maximum aspect ratio less than 16	-2.08324E-02

The mesh is developed from a sequence of meshes, each of which contains improvement suggested by the results provided by previous meshes. Such sequence was terminated when the surface deflection differed very little from one mesh to another one. In mesh 4 Table (6.2) the number of the courses representing AC (asphalt concrete) layer and the base layer is increased. This led to better convergence in ε_t and ε_c.

It is noted that mesh 4 has a surface deflection close to the deflection of mesh 2 with remarkably fewer number of elements. Moreover, mesh 4 gave faster and better convergence in ε_t and ε_c than the meshes 2 and 3, This is because the number of courses representing the AC and the base has been increased. The disadvantage of mesh 4 is the large aspect ratio, almost 16, in areas far from the load applications area. As a result of these considerations, the mesh 4 Table (6.2), illustrated in Figure (6.5) is selected

6.2.2 Dynamic response of the selected mesh and testing performances of the implicit method

The selected mesh will be tested for suitability for dynamic analysis. This is usually done by assigning a number of time steps for the analysis time period, and checking how the results are improving after increasing this number. The same elastic system shown in Table(6.2) used in the mesh refinement and grading analyses is considered to test the dynamic reliability of the mesh; the Rayleigh damping proportionals, β and α are assigned in accordance with the discussion in section 5.5.1

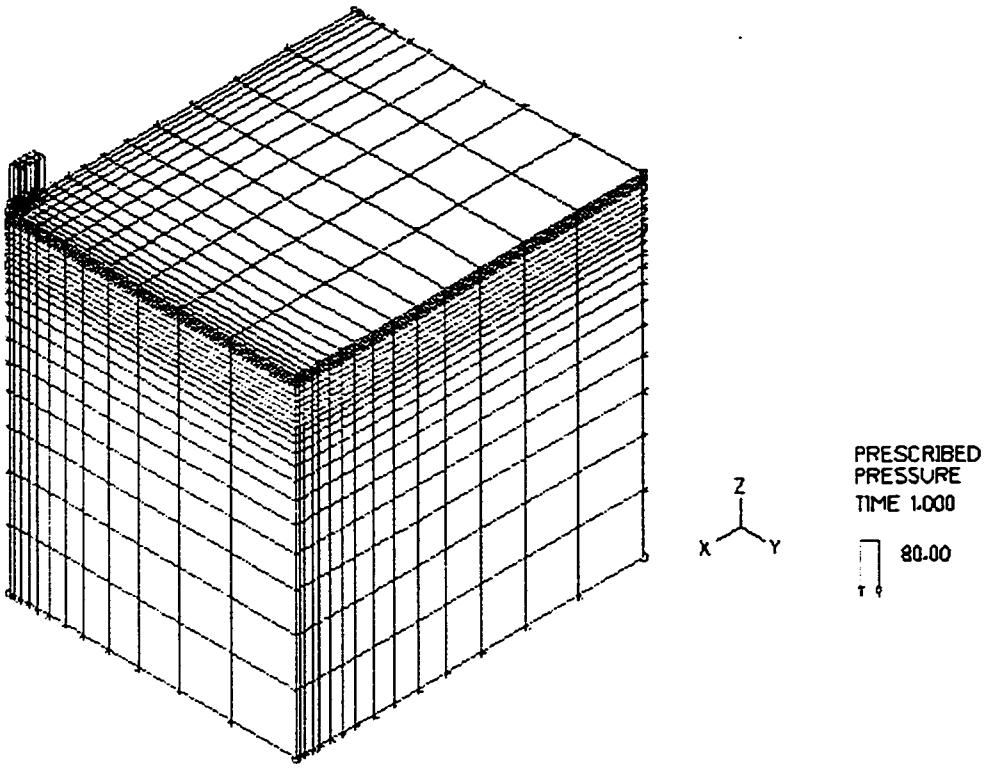

Figure (6.5) The configuration of the mesh adopted

Assuming ξ holds constant, independent of the frequency, $\xi = 5\ \%$. This is valid assumption for geologic materials .As mentioned earlier, the frequency of the input wave (loading frequency) would be an acceptable estimation for w_{min} (the frequency of interest).

$$\alpha = \xi_{min} w_{min} \quad = 0.05 \times \frac{2\pi}{0.1} = 0.05 \times 62.83 = 3.1416$$

$$\beta = \frac{\xi_{min}}{w_{min}} = \frac{0.05}{62.83} = 7.95 \times 10^{-4}$$

The higher frequencies are not important physically, and they are damped leaving the lower frequencies without damping, $\alpha = 0$

Testing the dynamic reliability of the mesh is done through the implicit mode. The implicit method was chosen because the rise time and duration of the load is only a few times greater than the time required for a sound wave to travel through the structure, and the problem is most probably of the structural dynamics type (Cook et al,1989), and implicit analysis is convenient in this case. In addition, the loading shape is triangular with not a very short time duration, which means that the load is not a shock loading.

The time step for the implicit mode is assigned according to the equations (5.12 to 5.14) as $\Delta t = 1.25\times10^{-3}$. This means that we need 80 time steps to reflect all the mode shapes and their corresponding frequencies for an analysis period equal to the duration of load 0.1s. Larger time steps are assigned for the time span following the load application, as tracing the time history beyond the traffic load application is not of interest. If the interest is only the low frequencies, not the high frequencies, inertial (mass) forces, are important., then $w_{co} = w_u$ should be adequate condition for giving good accuracy.. In such a case, $\Delta t = 0.005$. This means that 20 time steps are needed for quite accurate results for an analysis period equal to the duration of load 0.1.

The data in Table (6.3) are used to test the dynamic reliability of the selected mesh.

The analysis is repeated for smaller time step to assure that reasonable accuracy The results of the implicit method are compared with the static results .

As shown in Table (6.3), the computed results of analyses 2 and 4 differ only slightly, thus the larger time step in analysis 2 is sufficient and economical to give good accuracy for the linear system. The damping effect is also checked at this stage by comparing the time history of the vertical maximum surface deflection of the node 1 Figure(6.6)

Table(6.3) Results of the dynamic analyses of the linear system specified in Table (6.1) according to the adopted comparison criteria at the locations highlighted in Figure (6.1) for different time step sizes

Analysis	Number of time steps (step size) α, β :Proportional damping constants	**Maximum ε_t at element A**	**Maximum ε_c at element C**	**Maximum $\Delta_z(in)$ at node 1 (1 in =2.54 cm)**
2	$40(2.5\times10^{-3})+$ $90(0.01)$ $\alpha=0, \beta=0.0008$	2.36151E-04	-6.54705E-04	-1.05457E-02
3	$80(1.25\times10^{-3})+$ $180(5\times10^{-3})$ $\alpha=0, \beta=0.0008$	2.35645E-04	-6.54232E-04	-1.05466E-02
4	$80(1.25\times10^{-3})+$ $180(5\times10^{-3})$ $\alpha=0, \beta=0$	2.38245E-04	-6.83886E-04	-1.05645E-02

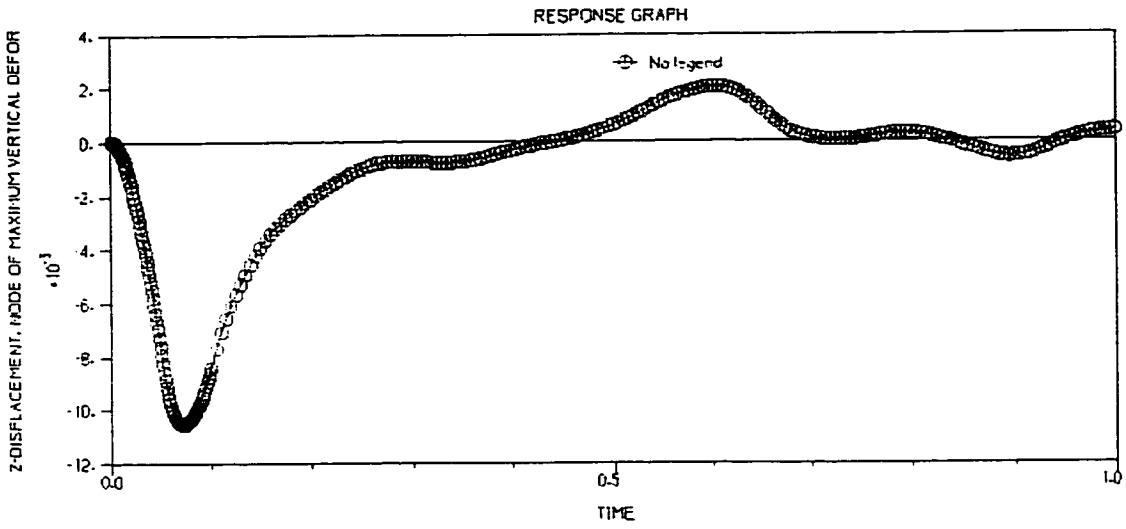

(a) Analysis 3 of inputs shown in Table(6.4)

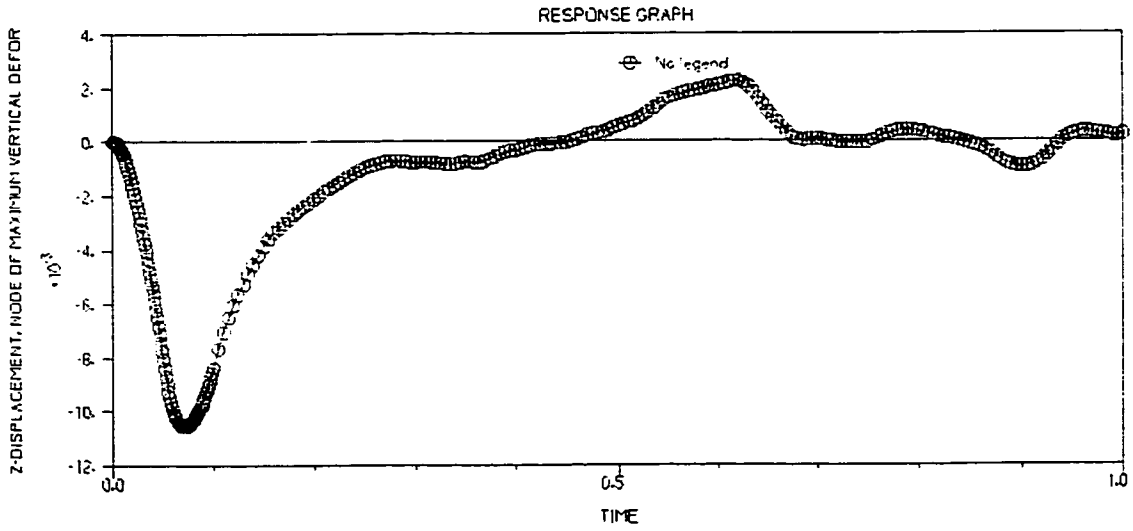

(b) Analysis 4 of inputs shown in Table (6.4)

Figure(6.6) Dynamic response graph for node 1, shown in Figure (6.1) of the elastic system, Table (6.3), in terms of surface deflection

6.2.3 Investigating the behavior of the pavement layers according to the selected constitutive laws

The following mechanical behavior of the pavement layers with the associated constitutive laws are investigated .

-Viscoelastic behavior of AC

-Linear elastic- cross anisotropic response of the base

-The elastic- perfectly plastic behavior of the base (Drucker-Parger)

-The elastoplastic strain hardening behavior of the subgrade (Cam Clay).

Table(6.4) shows the input parameters for the layers used in these analyses. The system geometry configuration shown in Figure (6.2) along with the thicknesses stated in Table (6.1) with the adopted mesh # 4 in Table (6.2) will be used throughout these analyses

The viscoelastic properties of the AC are assumed considering the points below:

-The long term shearing modulus and bulk modulus are considered to give the same elastic modulus of the AC (long term relaxation modulus)

-The viscoelastic volumetric strain is assumed to be zero that is reflected by assigning constant bulk modulus with time .

-The Prony series of the shearing modulus is assumed to have one term. Because the load is like duration time of the load is relatively short, the long term shearing modulus is assumed to be 0.8 times initial shearing modulus. This is also reflected by assuming high decay coefficient $\beta_i = \frac{E_{G_i}}{\eta_{G_i}} = 0.8$ 1/s which means that the modulus of the material reaches its constant value, elastic value , after short time elapses.

Table (6.4) Constitutive model input parameters of pavement layers investigating the choice of constitutive model on mechanical behavior of pavement system

Asphalt Concrete (AC) data

Viscoelastic	**Linear Elastic**
$G_0 = 576922$ psi (3975659 kPa) $G_\infty = 461538$ psi (3180530 kPa) $\beta_G = 0.8$ 1/s $K_0 = 500000$ psi (3445578 kPa) $K_\infty = 500000$ psi (3445578 kPa) $\beta_K = 0$ $T = 57^0$ $\rho = 0.09$ pci (2.49 g/cm^3)	$E = E_\infty = 600000$ psi (413 4693 kPa) $\nu = 0.3$ $\rho = 0.09$ pci (2.49 g/cm^3)

Base data

Linear Elastic	**Linear elastic cross anisotropic**	**Elastic perfect Plastic (Drucker- Prager)**
E= 60000 psi (413469 kPa) $\nu = 0.3$ $\rho = 0.08$ pci (2.21 g/cm^3)	$E_x = E_y = 30000$ psi (206734 kPa) $\nu_{xy} = 0.1$ $E_Z = 60000$ psi (413469 kPa) $\nu_{zx} = \nu_{zy} = 0.3$ $G_{xy} = G_{zy} = G_{Zx} = 23077$ psi (159027 kPa) $\rho = 0.08$ pci (2.21 g/cm^3)	E = 60000 psi (413469 kPa) $\nu = 0.3$ $\left.\begin{cases} C = 0 \text{ psi} \\ \phi = 38^\circ \end{cases}\right\} \Rightarrow \alpha = 0.298$ $\rho = 0.08$ psi (2.21 g/cm^3)

Subgrade data

Elastic	Elastoplastic: Cam Clay
E = 7340 psi (50581 kPa) ν = 0.3 ρ = 0.05 pci (1.38 g/cm^3)	E=7340 psi (50581 kPa) ν =0.28 M=1.24 Γ=1.347 k=0.0024 λ=0.014 ρ=0.05 pci (1.38 g/cm^3) OCR=1 e_0 =0.34 P_0 =10 psi (68.9 kPa) K_0=0.485 ϕ = 31° C = 8 psi (55.13 kPa)

Because simulating the nonlinear response under dynamic excitation requires more time steps, the number of time steps is increased to 80 steps of 0.1 s each. The results of the analyses testing the suggested mechanical behavior of the pavement system layers are summarized in the Table (6.5).

Table (6.5) Results of the analyses investigating the effects of the selected constitutive models on the dynamic behavior of pavement layers according to the adopted comparison criteria at the locations highlighted in Figure (6.1)

Analysis	**Constitutive model**			**Maximum ε_t at element A**	**Maximum ε_c at element C**	**Maximum $\Delta_z(in)$ at node 1 1 in= 2.54 cm**
	AC	**Base**	**Subgrade**			
6	LE	LE	LE	1.70879E-04	-5.04810E-04	-7.96261E-03
7	LV	LE	LE	1.11043E-04	-4.11632E-04	-6.41201E-03
8	LE	LEC	LE	1.78296E-04	-5.92834E-04	-8.18297E-03
9	LE	EPP (DP)	LE	2.18370E-04	-7.37514E-04	-1.03201E-02
10	LE	LE	EPSH(CC)	1.72379E-04	-3.02363E-03	-8.77804E-03

LE: Linear Elastic; **LVE**: Linear Viscoelastic; **LEC**: Elastic Cross-anisotropic, **EPP:** Elastic perfectly plastic, **DP**: Drucker-Prager, **EPSH**: Elastoplastic StrainHardening **CC:** Cam Clay

6.2.4 Conclusions of preliminary analyses

1-The preliminary FE (mesh number 4) shown in Figure(6.5) appears to give good accuracy and convergence, and is reliable for both static and dynamic analyses. No rigid body motion, nor artificial wave reflection were detected .

2- The implicit method is suitable to handle the dynamic equilibrium equations of the linear system under a traffic load represented by the triangular load shape shown in Figure(6.4) .Such method gives stable response and accurate results with reasonably no small number of time steps, and it handles the excited linear pavement system without any numerical trouble in computations and memory

3- The dynamic response of the pavement system under the traffic loading is remarkably different from the static response analysis. The maximum surface deflection of the

pavement system under the dynamic condition is almost 50 percent less than the corresponding static analysis. This agrees with the conclusions of (Yoder and Witczak, 1975; Sameh and White, 1993)

4- The linear system of viscoelastic AC gives the least strains ε_t and ε_c and least surface deflection Δ_z, followed by the linear elastic analysis. This is expected as the viscoelastic AC will react to the load by its relaxation modulus $E(t)$ which is initially higher than elasticity modulus E of the corresponding elastic AC,(long term modulus). Such difference will decrease with progress of time until it attains its final value or $E(t)=E(\infty)=E$

5-Analysis 9 shows that the elastic limit of the base is exceeded; i.e, plastic strain exists, under the specified loading system and the analyzed materials inputs. Inelastic analysis of the base is required for a more realistic representation of this layer.

6-Analysis 10 shows that the subgrade under the specified parameters in Table (6.4) and the assigned dynamic system also exceeds its elastic limit. Thus the elastic analysis of this layer is not realistic

7-The elastoplastic behavior of the base leads to shorter fatigue and rutting lives of the pavement system than the cross anisotropic behavior and elastic behavior and adopting it in the design leads to a more conservative results than the elastic and cross anisotrpic behaviors.

8-Similarly, the CamClay of subgrade results in shorter rutting and fatigue lives for the pavement system and adopting it in the design leads to more reserved conditions than the elastic behavior

9- As shown in Figure(6.6), the dynamic response of the damped vertical deflection of the node 1 tends to be smoother and more stable than the dynamic response of the undamped vertical deflection of this point. Such difference in the dynamic response would be more obvious if the analysis period were extended beyond 1 s.

6.3 Major Analyses

These analyses are made to achieve the main objectives of the parametric study, namely

1-Studying the effects of the (i) subgrade quality (ii) granular base quality(iii)granular base thickness on the fatigue and rutting of a pavement system (sensitivity analyses)

2-Studying the performance of a geosynthetically-reinforced pavement system and its variation with the geosynthetic location.

A linear AC layer under non-linear foundation, elastic-perfectly plastic base underlined by elastoplastic strain hardening subgrade, and the implicit dynamic analysis of the traffic load are considered in these analyses. It is assumed that no slippage occurs between the geosynthetic and the surrounding layers and between the layers themselves. The full bonding of the geosynthetic with the surrounding media is an acceptable assumption for the geogrid which has better frictional characteristics than the geotextile particularly with well graded and angular granular materials (Berg et al, 2000; Sarsby, 1985). This assumption is also made because poor literature is reported about deciding the interface parameters which are dependent on so many variables that need complicated and very precise tests facilities, and intensive investigations to examine these variables Milligan and Palmeira (1989) stated that misleading results of pull-out tests have often been reported and so many variables are involved in controlling the correct results.

As previously discussed in Chapter Two and Three the beneficial effects of the geogid depend on many factors such as the base quality, base thickness, subgrade quality, loading system, initial conditions like prerutting or prestressing of the geosynthetic , physical and mechanical characteristics of the geosynthetics

Three parameters are considered in this study , They are

1-Subgrade quality

2-Granular base quality

3-Granular base thickness

To study the effects of the base thickness, two thicknesses are considered, these are

6 in (15.24) and 12 in (30.48) see Figure (6.7)

To study the effect of granular base quality, two types of bases are considered, weak base (WB), and strong base (SB), See Table(6.6)

To study the effect of the subgrade quality, two types of soils are considered, clayey soil and silty sand soil, See Table(6.6) .

The asphalt concrete (AC) layer is kept constant in terms of its quality and thickness

As table (6.6) shows one type of geosynthetic is adopted in the analyses.

Three locations of geosynthetic reinforcement are studied as shown in Figure(6.8)

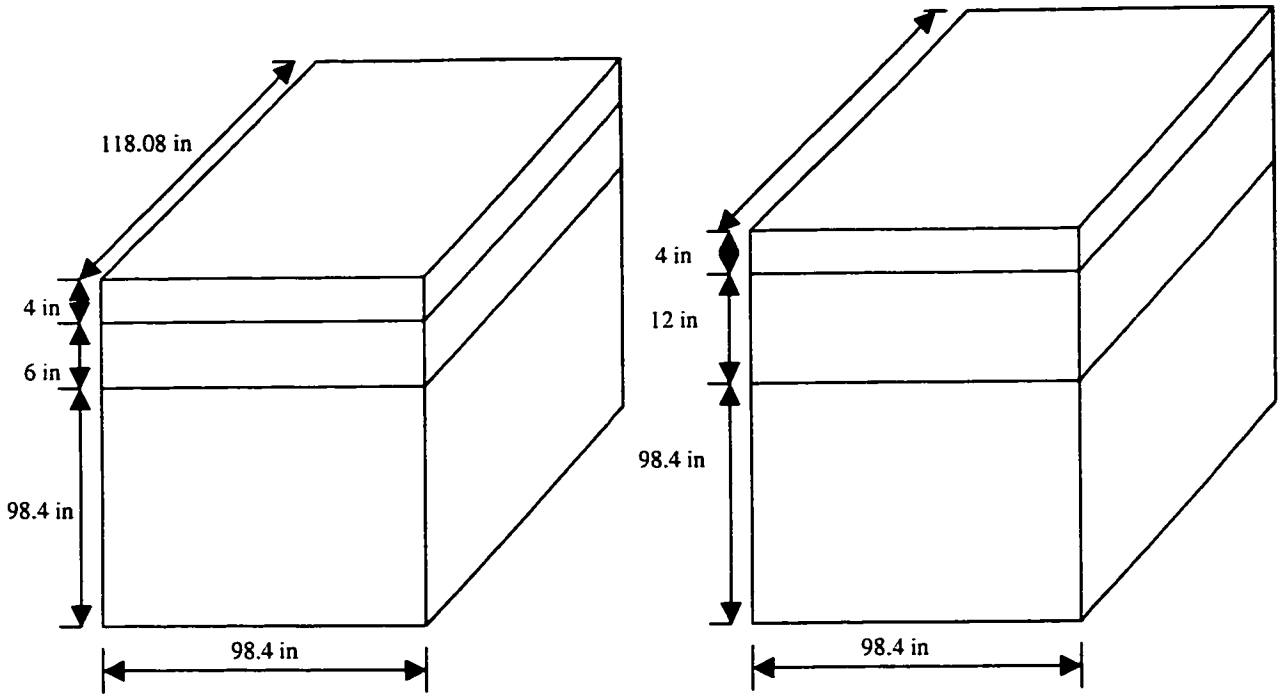

(a) Thin system (b) Thick system

Figure(6.7) Base thickness studied

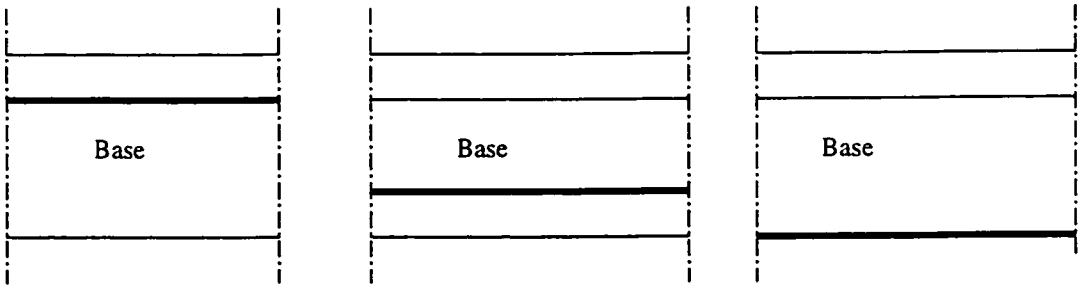

(a)AC-Base interface (b) Lower third of the base (c) Base-subgrade interface

Figure(6.8) Locations of the geogrid adopted in the parametric study

Two sets of analyses are constructed, the first set concerns pavement systems of thin bases (thin systems), and the second set concerns pavement systems of thick bases (thick systems) as defined in Figure(6.7)

Each set has four systems as shown bellow in Figure(6.9), They are:

System #1: CS(Clay Subgrade) WB (Weak Base) SAC (Standard Asphalt Concrete)

System #2 : CS(Clay Subgrade) SB (Strong Base) SAC (Standard Asphalt Concrete)

System #3 SSS(Silty Sand Subgrade) WB(Weak Base) SAC (Standard Asphalt Concrete)

System #4: SSS(Silty Sand Subgrade) SB (Strong Base) SAC (Standard Asphalt Concrete)

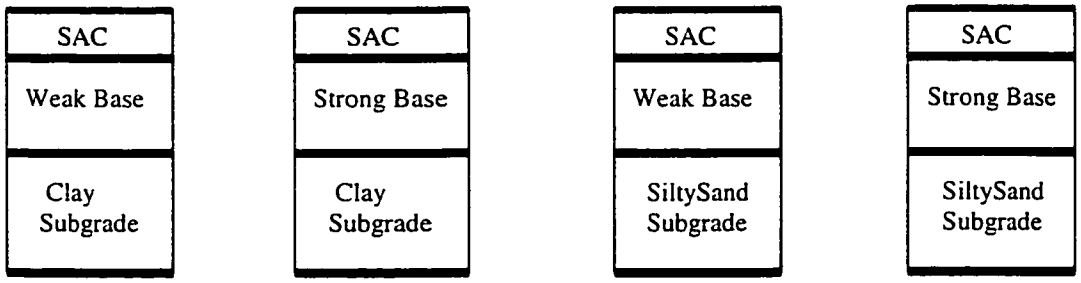

(a)System #1 (b) System #2 (c) System #3 (d) System #4

Figure (6.9) Pavement system used in the finite element analyses

Each system is further analyzed for four cases as follows:

Case #1 Unreinforced

Case #2 Geosynthetic is placed at the base-subgrade interface, Figure(6.8.a)

Case #3 Geosynthetic is placed at the lower third of the base layer, Figure(6.8.b)

Case #4 Geosynthetic is placed at AC-base interface, Figure(6.8.c)

The constitutive model data assigned for each layer of the pavement system are listed in Table (6.6) [(1 psi =6.89 kPa , 1 pci = 27.67 g/cm^3)] .

Table (6.6) Constitutive model input parameters for each of the pavement system layers

Layer	**Subgrade**		**Base**		**AC**	**Geogrid**
Model	**Cam Clay**		**Elastic-Perfectly plastic (Drucker-Parger)**		**Elastic**	**Linear elastic**
Quality	**Clay (CS)**	**Silty sand (SS)**	**Weak Base (WB)**	**Strong Base (SB)**	**Standard**	**Stiff**
Inputs	E=1200 psi ν =0.25 M=1 Γ=2.1 k=0.026 λ=0.147 ρ=0.04 pci OCR=1 e_0=1.08 P_0 =10 psi K_0=0.571 ϕ = 25° C = 4 psi	E=7340 psi ν =0.28 M=1.24 Γ=1.347 k=0.0024 λ=0.014 ρ=0.05 pci OCR=1 e_0 =0.34 P_0 =10 psi K_0=0.485 psi ϕ = 31° C = 8 psi	E = 14028 psi ν_z = 0.3 ρ = 0.06 pci $\left\{\begin{matrix}\phi = 25^\circ \\ C = 0\end{matrix}\right\} \Rightarrow$ $\left\{\begin{matrix}\alpha = 0.189 \\ k = 0\end{matrix}\right\}$	E = 60000 psi ν = 0.3 ρ = 0.07 pci $\left\{\begin{matrix}\phi = 38^\circ \\ C = 0\end{matrix}\right\} \Rightarrow$ $\left\{\begin{matrix}\alpha = 0.298 \\ k = 0\end{matrix}\right\}$	E = 600000 psi ν = 0.3 ρ = 0.09 pci	E=613044 psi ν =0.35 ρ=0.001 pci Strength At ε=5% = 3069
Source	(Desai and Siriwardane, 1984)	(Desai and Siriwarda-ne,1984)	(Liu et al, 1998) +Authors assumptions	(Sameh and White,1993) +Authors assumptions	(Sameh and White,1993) + Authors assumptions	(Andrew and Hans, 2001)

6.3.1 Model results

The results of maximum ε_c (at element C shown in Figure (6.1)) and maximum ε_t (at element A, shown in Figure (6.1)) are summarized in Table (6.7) below for each system analyzed. They lead to the following observations and conclusions

About the subgrade quality

The subgrade quality (strength) has small effect on ε_t regardless of the base quality or thickness. This agrees with the conclusion of Yang (1993). The largest decrease in ε_t was found when replacing the clay by silty sand for the thin system of weak base, which led to a decrease of 7% ε_t. On the other hand the subgrade quality (strength) has remarkable effect on the rutting of the pavement or ε_c (Yang, 1993). Such inversely proportional relationship is almost independent of the base quality or thickness.

The pavement system having the thick and weak base with the clay subgrade has maximum ε_c 60% higher than ε_c for the corresponding system with a silty sand subgrade. In the case of the strong base, the decrease in ε_c was around 55%.

The pavement of thin and weak base shows a decrease of 56% in ε_c as a result of changing the clay subgrade by a silty sand subgrade.

About the base quality

The results also show that the base quality has a considerable influence on the fatigue of the pavements. This influence is more pronounced when the base thickness increases and it is slightly affected by the subgrade quality. The system having thick and weak base

resting on clay subgrade has ε_t 30% less than its correspondence system of the strong base. Corresponding decrease in ε_t is 13 % when the base is thin. Almost the same

Table(6.7) Results of the sensitivity study conducted for testing base quality, base thickness, and subgade quality on the fatigue and rutting of a pavement system of materials shown in Table(6-6)

System	Base	Maximum ε_c (at element C)	Maximum ε_t (at element A)
AC / Weak Base / Clay Subgrade — System 1	Thick	-3.13130E-03	3.35053E-04,
	Thin	-3.88448E-03	3.73396E-04
AC / Strong Base / Clay Subgrade — System 2	Thick	-2.17556E-03	2.31817E-04,
	Thin	-3.25559E-03	3.21225E-04
AC / Weak Base / SiltySand Subgrade — System 3	Thick	-1.24254E-03	3.33554E-04
	Thin	-1.67257E-03	3.45984E-04,
AC / Strong Base / SiltySand Subgrade — System 4	Thick	-9.66172E-04	2.20848E-04,
	Thin	-1.03052E-02	3.04889E-04

Percentages decrease are noticed in the case of the siltysand subgrade

ε_c is also affected by the base quality. The results of the thin system of clay subgrade indicates that ε_c decreases by 30 % when the stronger base is used; that difference drops to 16% in the case of thin base and it becomes 22 % when keeping the thick base but on siltysand subgrade. This means that ε_c decreases with a stronger base and that decrease is more noticeable in the case of the thick base and in the case of founding on weak subgrade.

About base thickness

A decrease of 30% in the ε_t in the case of the system having strong base on clay soil ,is found as a result of increasing the base thickness from 6in (15.24 cm) to 12in (30.48 cm). Under the same conditions that decrease in ε_t drops to 10% when using the weak base.

ε_t declines by 27% in the case of the system having strong base on siltysand subgrade, as a consequence of increasing the base depth from 6in (15.24 cm) to 12in (30.48 cm) .Such decline becomes 3% when using the weak base. This means that increasing the thickness of the base leads to a longer life of a pavement system against fatigue. This proportional relationship between the base thickness and the fatigue life of a pavement system becomes more pronounced when using a stronger base. In addition, the quality of the subgrade has very small impact on this relationship.

Increasing the base thickness also leads to a smaller ε_c, longer rutting life. ε_c will decrease more in the case of the system with strong base .

6-3-2 Results of the geogrid reinforced pavement systems

The graphical results shown in Fgures (6.10) to (6.52) show the following :

The vertical surface deflection across the line 1-3 [Figure(6.1)] taken at the peak load when t=0.05s; see illustration of time function of the load [Figure(6.4)]

The envelope of the vertical surface deflection across the line 1-3 [Figure(6.1)].That is the line connecting the maximum vertical surface deflections which the nodes of line 1-3 attain during the duration of loading =0.1s

The horizontal strain across line 4-5; [Figure(6.1)] taken at the peak load when t=0.05s;

The envelope of horizontal tensile strain across line 4-5.That is the line connecting the maximum tensile strains which the nodes of line 4-5 attain during the duration of loading =0.1s.

The vertical compression plastic strain across base depth line 2-8 at peak load, in addition to its envelope are also considered in some analyses to show how the geosynthetic presence changes the stress-strain state induced within the base layer

The tables of the results, Tables (6.8) and table (6.9) concerns the following

The maximum surface deflection at node 1 [Figure(6.1)].

The maximum vertical strain transmitted to subgrade, that is at element C [Figure(6.1)]

The maximum tensile strain transmitted to AC, that is at element A[Figure(6.1)]

Table(6.8) Results of the sensitivity analyses for geogrid–reinforced pavement systems of the thick base systems.

System	Location of the geogrid	max ε_t (at element A)	max Δ_z (in) (at node 1) [1in =2.54 cm]	max ε_c (at element C)	max ε_t Decrease %	max Δ_z Decrease %	max ε_c Decrease %
AC / Weak Base / Clay Subgrade System 1	N/A	3.35053E-04	-1.76113E-02	-3.13130E-03	–	–	–
	Bottom of base	3.34510E-04	-1.71799E-02	-3.00678E-03	0.2	2	4
	Lower third of base	3.28163E-04	-1.60121E-02	-3.24874E-03	2	10	-3
	Top of base	1.74850E-04	-1.48088E-02	-2.77359E-03	48	16	11
AC / Strong Base / Clay Subgrade System 2	N/A	2.31817E-04	-1.31331E-02	-2.17556E-03	-	-	-
	Bottom of base	2.19993E-04	-1.13831E-02	-1.86111E-03	4	13	14
	Lower third of base	2.14780E-04	-1.11825E-02	-1.99669E-03	7	15	8
	Top of base	1.28100E-04	-1.16216E-02	-1.99730E-03	44	12	8
AC / Weak Base / Siltysand Subgrade System 3	N/A	3.33554E-04	-1.61290E-02	-1.24254E-03	-	-	-
	Bottom of base	3.33254E-04	-1.59243E-02	-1.22214E-03	0.09	1	1
	Lower third of base	3.27332E-04	-1.50017E-02	-1.32693E-03	1.8	7	-6
	Top of base	1.74178E-04	-1.36250E-02	-1.10665E-03	47	15	11
AC / Strong Base / Siltysand Subgrade System 4	N/A	2.20848E-04	-1.08274E-02	-9.66172E-04	-	-	-
	Bottom of base	2.12791E-04	-9.55733E-03	-8.19221E-04	3.6	11	15
	Lower third of base	2.06939E-04	-9.47098E-03	-8.97786E-04	6.3	12	7
	Top of base	1.22325E-04	-9.73416E-03	-8.92864E-04	44	10	8

Table(6.9) Results of the sensitivity analyses for geogrid–reinforced pavement systems of the thin base systems.

System	Geosynthetic location	max ε_t (at element A)	max Δ_z (in) (at node 1) [1in =2.54 cm]	max ε_c (at element C)	max ε_t Decrease %	max Δ_z Decrease %	max ε_c Decrease %
AC / Weak Base / Clay Subgrade — System 1	N/A	3.73396E-04	-2.35642E-02	-3.88448E-03	-	-	-
	Bottom of base	3.61294E-04	-2.22567E-02	-3.77611E-03	3.2	5.5	3
	Lower third of base	2.89116E-04	-1.27950E-02	-2.93175E-03	22	46	24
	Top of base	1.93475E-04	-1.96364E-02	-3.33623E-03	48	16	14
AC / Strong Base / Clay Subgrade — System 2	N/A	3.21225E-04	-2.02625E-02	-3.25559E-03	-	-	-
	Bottom of base	2.64835E-04	-1.69056E-02	-2.76090E-03	17	16	15
	Lower third of base	2.14590E-04	-1.11555E-02	-2.12967E-03	33	44	34
	Top of base	1.71060E-04	-1.74734E-02,	-2.88423E-03	46	13	11
AC / Weak Base / Siltysand Subgrade — System 3	N/A	3.45984E-04	-1.83408E-02	-1.67257E-03	-	-	-
	Bottom of base	3.39732E-04	-1.78900E-02	-1.63924E-03	2	3	2
	Lower third of base	2.86046E-04	-1.18620E-02	-1.39133E-03	17	36	16
	Top of base	1.80304E-04	-1.55317E-02	-1.45474E-03	47	15	13
AC / Strong Base / Siltysand Subgrade — System 4	N/A	3.04889E-04	-1.67186E-02	-1.03052E-02	-	-	-
	Bottom of base	2.51775E-04	-1.40587E-02	-9.91531E-03	17	16	32
	Lower third of base	2.04021E-04	-1.00010E-02	-1.07248E-03	33	40	83
	Top of base	1.61873E-04	-1.44446E-02	-9.04235E-03	47	13	12

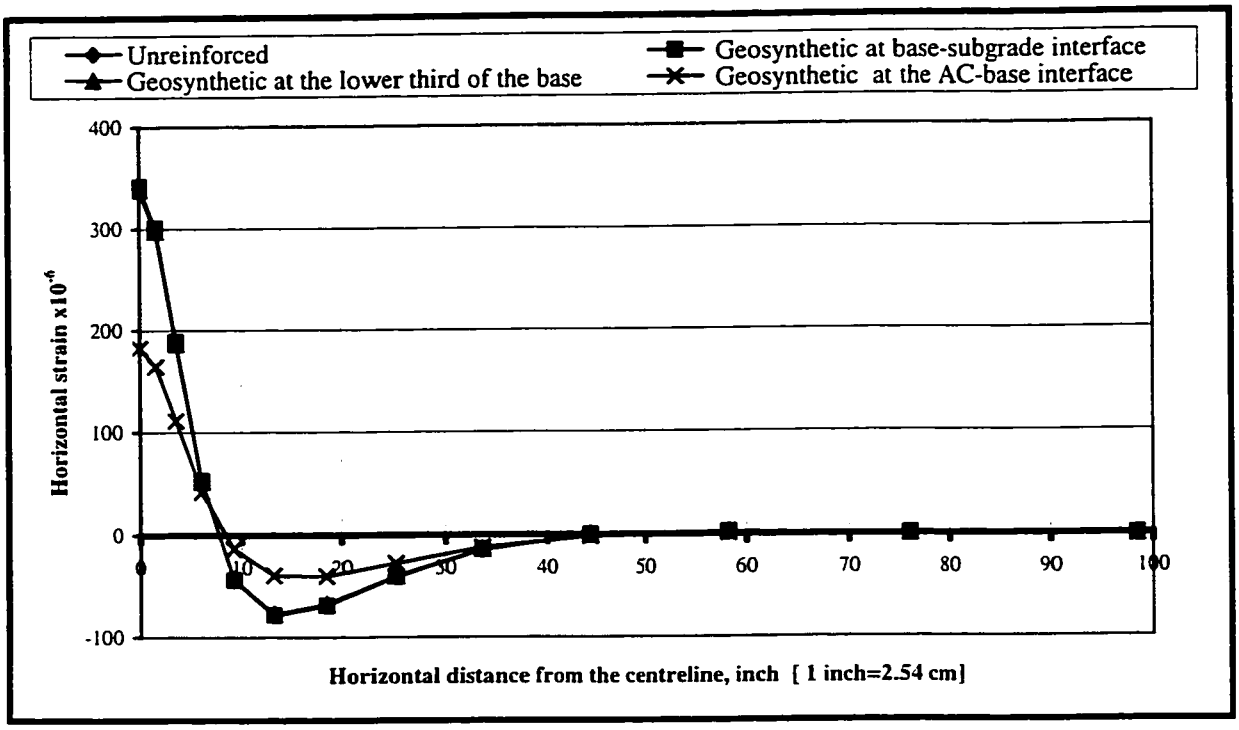

Figure (6.10) Horizontal strain at the bottom of AC layer at the peak load t=0.05s (Thick base system #1)

Table (6.10) The horizontal strain at the bottom of AC layer at peak load t=0.05s

Thick base system # 1				
Horizontal distance from the centreline (in) [1inch =2.54 cm]	Horizontal strain			
	Unreinforced	Geosynthetic at base-subgrade interface	Geosynthetic at the lower third of the base	Geosynthetic at the AC-base interface
98.40	-5.74745E-07	-5.74752E-07	-5.75525E-07	-3.97194E-07
75.89	2.74746E-07	2.74747E-07	2.73061E-07	3.42152E-07
58.26	2.17513E-06	2.17515E-06	2.13935E-06	0.000001252
44.44	6.34547E-08	6.11656E-08	-2.53004E-08	-1.63619E-06
33.62	-1.39427E-05	-1.39487E-05	-1.38597E-05	-1.17639E-05
25.14	-4.04021E-05	-4.03916E-05	-3.97403E-05	-2.71186E-05
18.49	-6.86129E-05	-6.85544E-05	-0.000067338	-3.99284E-05
13.28	-7.82832E-05	-7.81975E-05	-7.70504E-05	-0.000039029
9.20	-4.35288E-05	-4.34948E-05	-0.000043283	-1.30804E-05
6.01	5.32952E-05	5.32307E-05	5.20018E-05	4.23332E-05
3.50	0.000189091	0.000188958	0.000186422	0.000111569
1.54	0.000300974	0.000300819	0.0002975	0.000164345
0.00	0.000342056	0.000341896	0.000338333	0.000182774

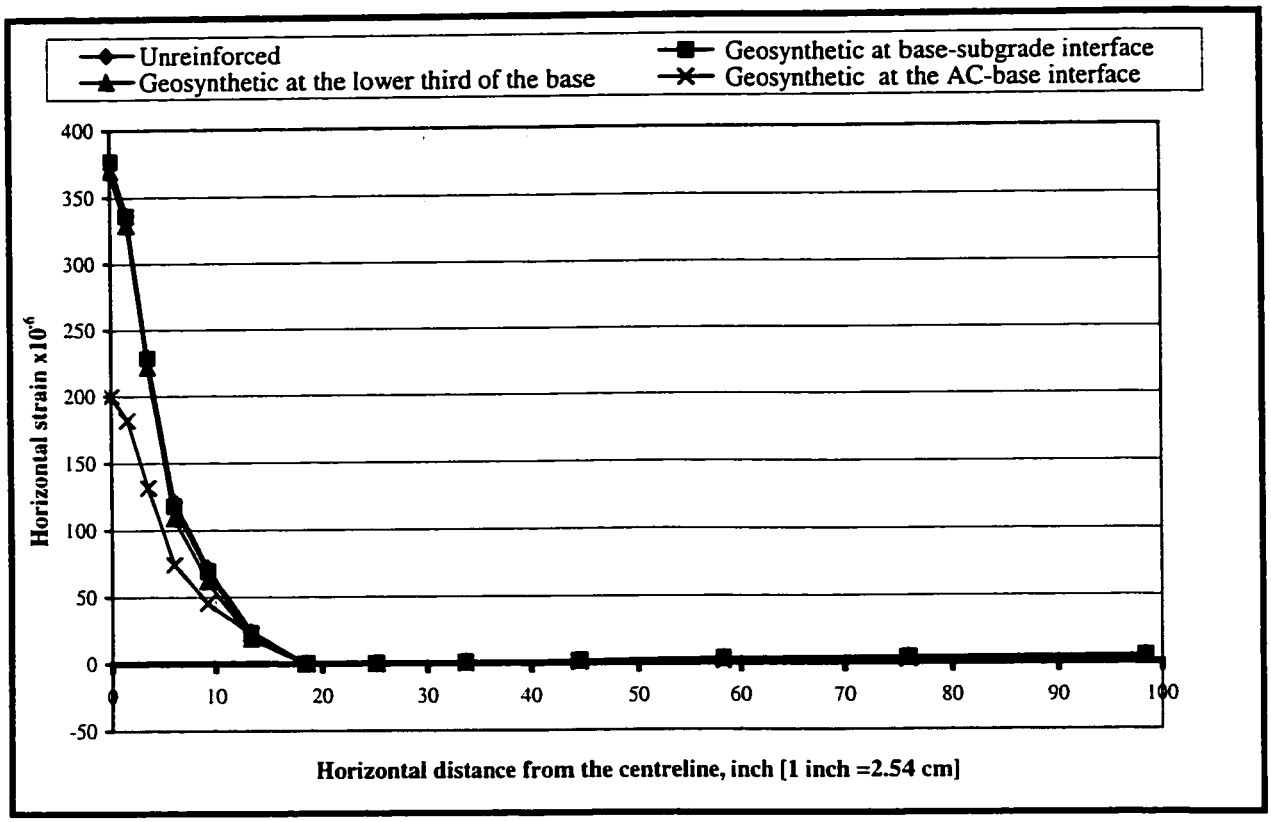

h

Figure (6.11) Envelope of the tensile strain at the bottom of AC layer
(Thick base system #1)

Table (6.11) Envelope of the tensile strain at the bottom of AC layer

Thick base system # 1				
Horizontal distance from the centreline (in) [1inch =2.54 cm]	Tensile strain			
	Unreinforced	Geosynthetic at base-subgrade interface	Geosynthetic at the lower third of the base	Geosynthetic at the AC-base interface
98.40	4.74604E-06	4.70673E-06	4.7749E-06	3.81451E-06
75.89	3.78558E-06	3.6669E-06	3.56571E-06	2.15127E-06
58.26	3.11866E-06	3.07942E-06	2.91037E-06	1.31248E-06
44.44	1.79134E-06	1.79134E-06	1.78674E-06	7.05824E-07
33.62	8.27464E-07	8.27464E-07	8.27464E-07	1.49692E-07
25.14	9.17309E-08	9.17309E-08	9.17309E-08	-1.39925E-11
18.49	9.81683E-10	9.81683E-10	9.81683E-10	-5.58867E-10
13.28	2.41207E-05	2.26817E-05	0.000018598	2.23506E-05
9.20	7.20421E-05	6.91751E-05	6.19965E-05	4.53429E-05
6.01	0.000121444	0.000117857	0.000108832	7.43312E-05
3.50	0.000229884	0.000228573	0.000221534	0.000131852
1.54	0.000336731	0.000335965	0.000328936	0.000182026
0.00	0.000377417	0.000376787	0.000369497	0.000200115

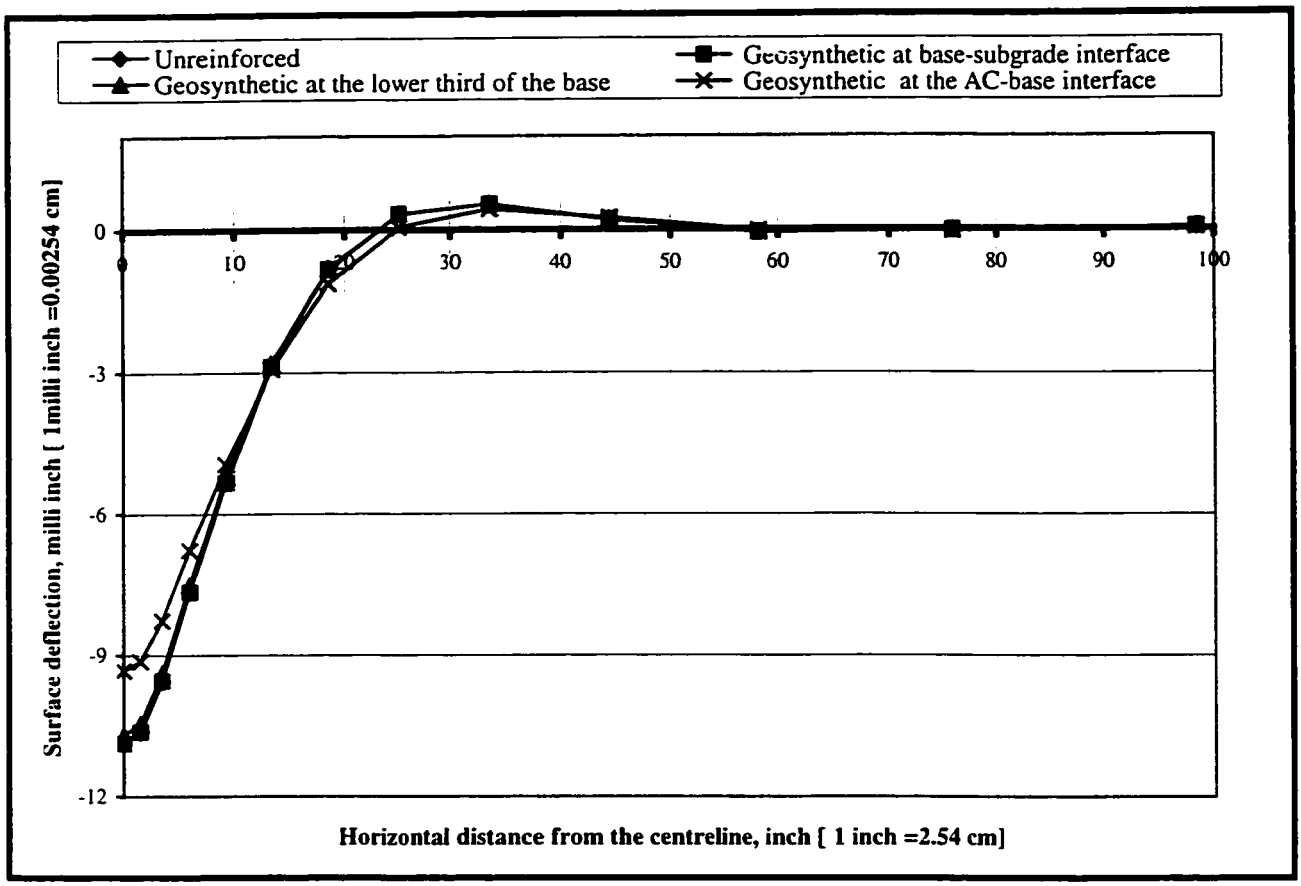

Figure (6.12) The vertical surface deflection across line 1-3 at the peak load t=0.05s (Thick base system #1)

Table (6.12) The vertical surface deflection across line 1-3 at the peak load t=0.05 s

Thick base system # 1				
Horizontal distance from the centreline (in) [1inch=2.54cm]	Surface Deflection (inch) [1 inch =2.54 cm]			
	Unreinforced	Geosynthetic at base-subgrade interface	Geosynthetic at the lower third of the base	Geosynthetic at the AC-base interface
0.00	-0.0108797	-0.0108702	-0.0106872	-0.0093185
1.54	-0.0106368	-0.0106275	-0.0104475	-0.00913269
3.50	-0.00955725	-0.00954875	-0.00938073	-0.0082665
6.01	-0.00767003	-0.00766317	-0.00751996	-0.00677303
9.20	-0.00534012	-0.00533579	-0.00523076	-0.00494462
13.28	-0.00287115	-0.00286949	-0.00281004	-0.00292417
18.49	-0.000830922	-0.000830871	-0.000811823	-0.00112407
25.14	0.000333594	0.000333433	0.000331017	0.000056966
33.62	0.000545789	0.000545796	0.000542113	0.000445653
44.44	0.000209435	0.000209446	0.000210069	0.00025435
58.26	-6.23626E-05	-6.23657E-05	-6.20067E-05	-2.39605E-05
75.89	-2.66581E-05	-2.66572E-05	-2.68092E-05	-3.73482E-05
98.40	0.000049501	4.95006E-05	4.95979E-05	4.40869E-05

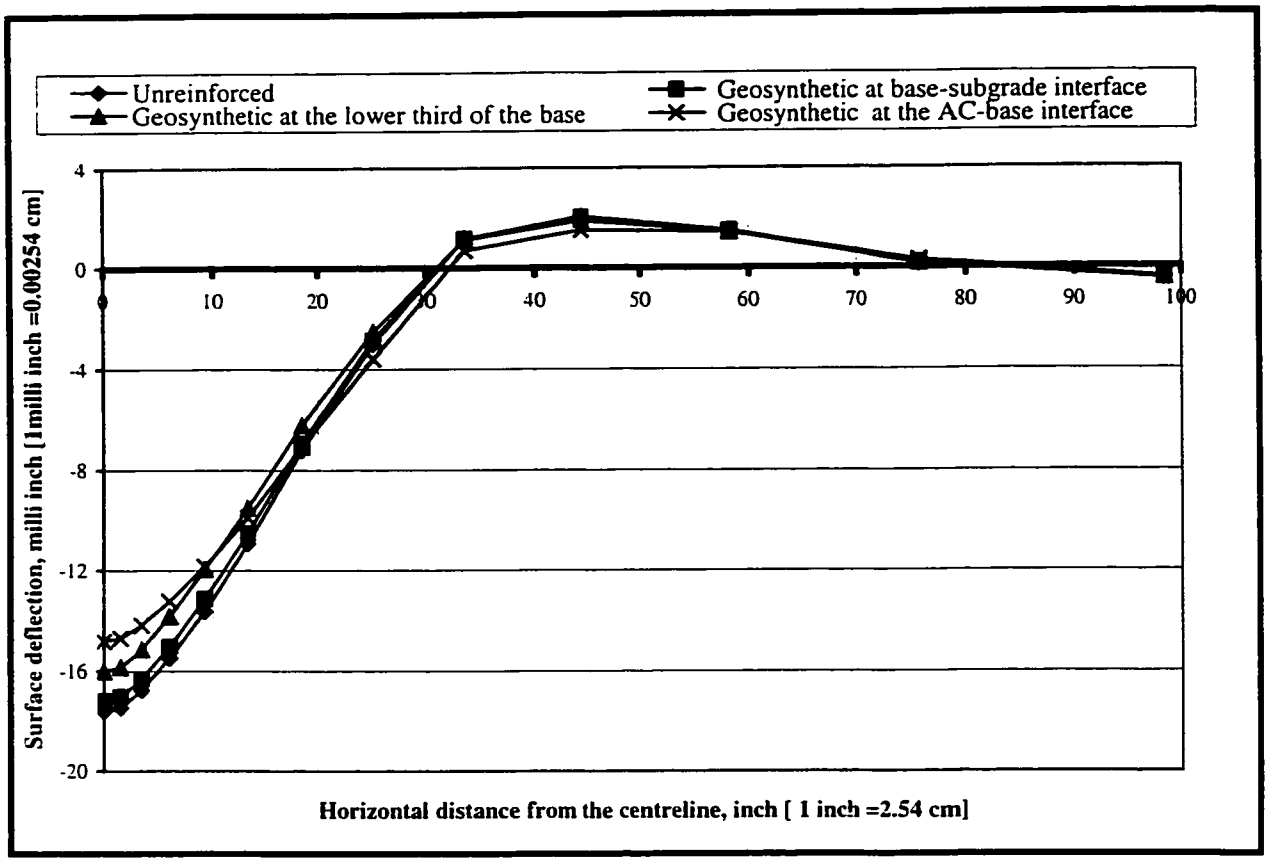

Figure (6.13) Envelope of the vertical surface deflection across line 1-3
(Thick base system #1)

Table (6.13) The envelope of vertical surface deflection across line 1-3

Thick base system # 1				
Horizontal distance from the centreline (in)	Surface Deflection (inch) [1inch =2.54 cm]			
	Unreinforced	Geosynthetic at base-subgrade interface	Geosynthetic at the lower third of the base	Geosynthetic at the AC-base interface
0.00	-0.0176113	-0.0171799	-0.0160121	-0.0148088
1.54	-0.0174427	-0.0170085	-0.0158433	-0.0146846
3.50	-0.0167598	-0.0163166	-0.0151415	-0.0141707
6.01	-0.0154775	-0.015014	-0.0138314	-0.0132195
9.20	-0.0136227	-0.0131344	-0.0119552	-0.0118374
13.28	-0.0109307	-0.0105249	-0.00950734	-0.00988959
18.49	-0.00720725	-0.0069318	-0.00621761	-0.00706177
25.14	-0.00298065	-0.00286305	-0.00252466	-0.00358718
33.62	0.00116795	0.0011581	0.00112889	0.000698891
44.44	0.00206112	0.0020212	0.00189946	0.00150725
58.26	0.00148003	0.00147437	0.00141859	0.00142661
75.89	0.000142888	0.000150976	0.000164638	0.000278627
98.40	-0.000440348	-0.000439009	-0.000417786	-0.000403107

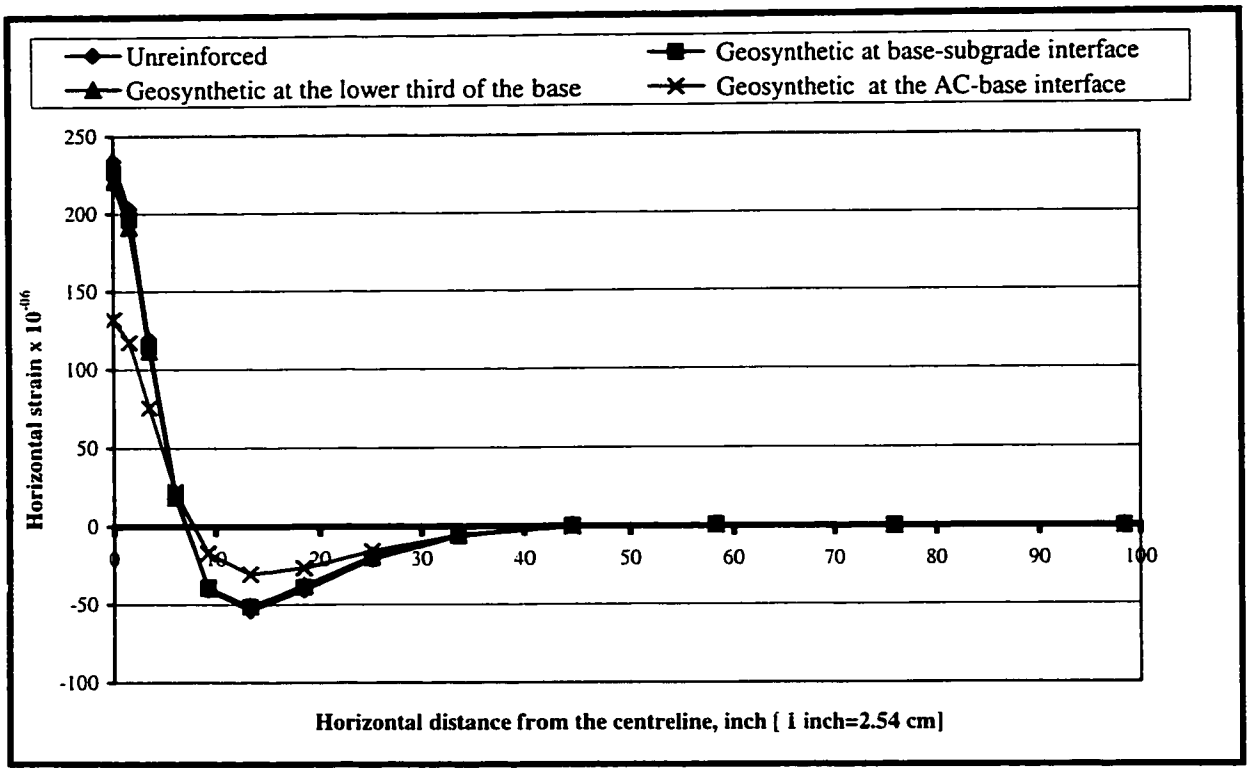

Figure (6.14) Horizontal strain at the bottom of AC layer at the peak load t=0.05s (Thick base system #2)

Table(6.14) The horizontal strain at the bottom of AC layer at peak load t=0.05s

Thick base system # 2				
Horizontal distance from the centreline (in) 1 inch =2.54 cm	Horizontal strain			
	Unreinforced	Geosynthetic at base-subgrade interface	Geosynthetic at the lower third of the base	Geosynthetic at the AC-base interface
98.40	-2.68269E-07	-2.71388E-07	-2.77747E-07	-2.05496E-07
75.89	-1.13232E-08	-2.44253E-08	-2.40735E-08	7.23373E-08
58.26	8.26817E-07	7.89092E-07	7.64038E-07	6.36476E-07
44.44	2.46974E-07	1.79951E-07	3.31727E-07	-3.85577E-07
33.62	-6.19199E-06	-6.15957E-06	-5.36561E-06	-5.68844E-06
25.14	-0.000020882	-2.02521E-05	-1.89031E-05	-1.56058E-05
18.49	-4.05485E-05	-0.000038815	-3.77228E-05	-2.64825E-05
13.28	-5.39924E-05	-5.15517E-05	-5.13426E-05	-3.05303E-05
9.20	-4.05014E-05	-3.89284E-05	-3.95872E-05	-1.68058E-05
6.01	2.13664E-05	2.01586E-05	1.86215E-05	2.22305E-05
3.50	0.000119457	0.000114851	0.00011175	7.56552E-05
1.54	0.000203166	0.000196377	0.000191298	0.000117543
0.00	0.000233973	0.000226572	0.000220565	0.000132225

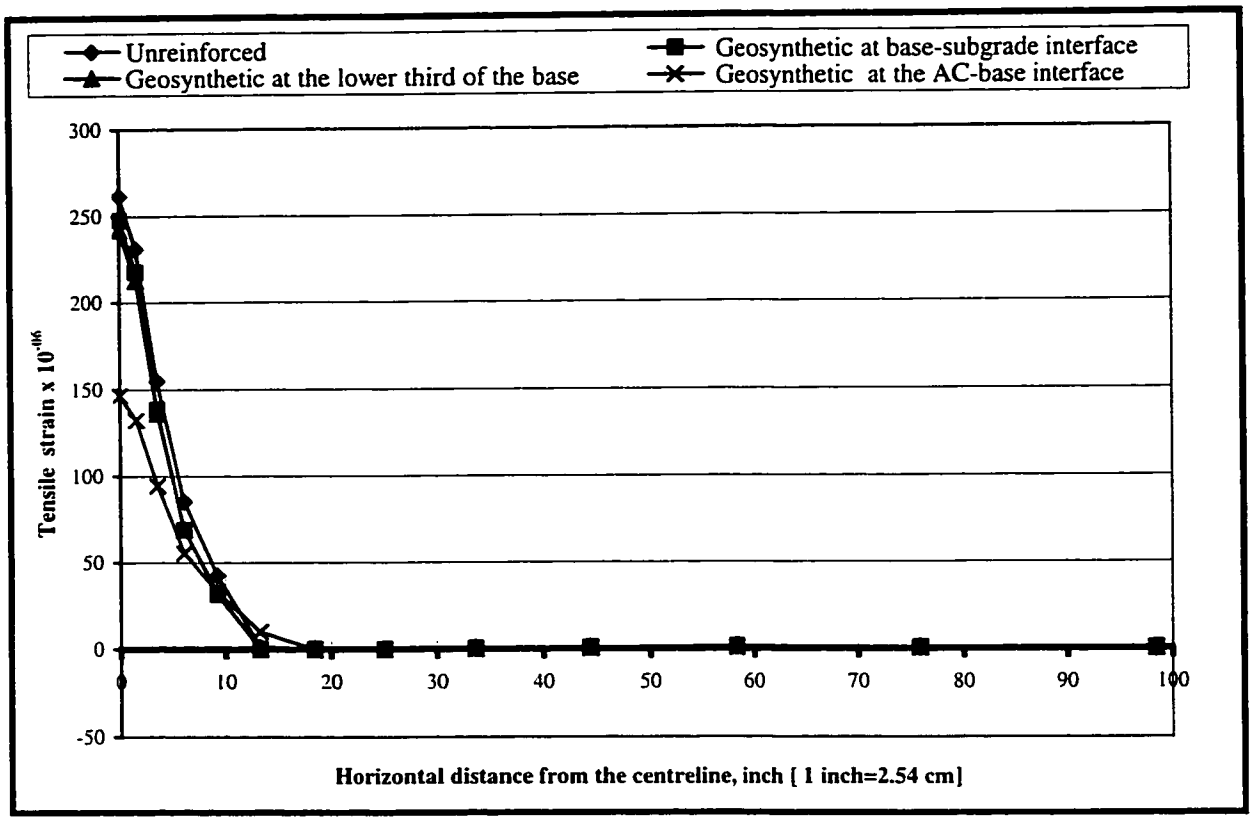

Figure (6.15) Envelope of the tensile strain at the bottom of AC layer
(Thick base system #2)

Table (6.15) Envelope of the tensile strain at the bottom of AC layer

Thick base system # 2				
Horizontal distance from the centreline (in) [1inch =2.54 cm]	Tensile strain			
	Unreinforced	Geosynthetic at base-subgrade interface	Geosynthetic at the lower third of the base	Geosynthetic at the AC-base interface
98.40	1.73186E-08	3.73587E-07	3.48324E-07	2.05211E-07
75.89	3.9506E-07	7.11893E-07	8.37992E-07	3.87615E-07
58.26	1.11526E-06	1.29131E-06	1.44781E-06	7.23043E-07
44.44	8.50707E-07	8.43922E-07	7.89544E-07	4.31473E-07
33.62	5.00209E-07	5.0019E-07	4.96853E-07	1.13153E-07
25.14	5.81535E-08	5.81535E-08	5.81444E-08	-8.62722E-12
18.49	1.0408E-09	1.0408E-09	1.0408E-09	-3.96854E-10
13.28	1.32704E-06	-5.07865E-09	-5.07865E-09	1.00548E-05
9.20	4.25659E-05	3.23921E-05	3.18337E-05	3.30875E-05
6.01	8.52527E-05	6.88733E-05	6.88818E-05	5.55865E-05
3.50	0.000154714	0.000138602	0.000136127	9.44823E-05
1.54	0.000231024	0.000217433	0.00021263	0.000132379
0.00	0.000261478	0.000247718	0.000241846	0.000146683

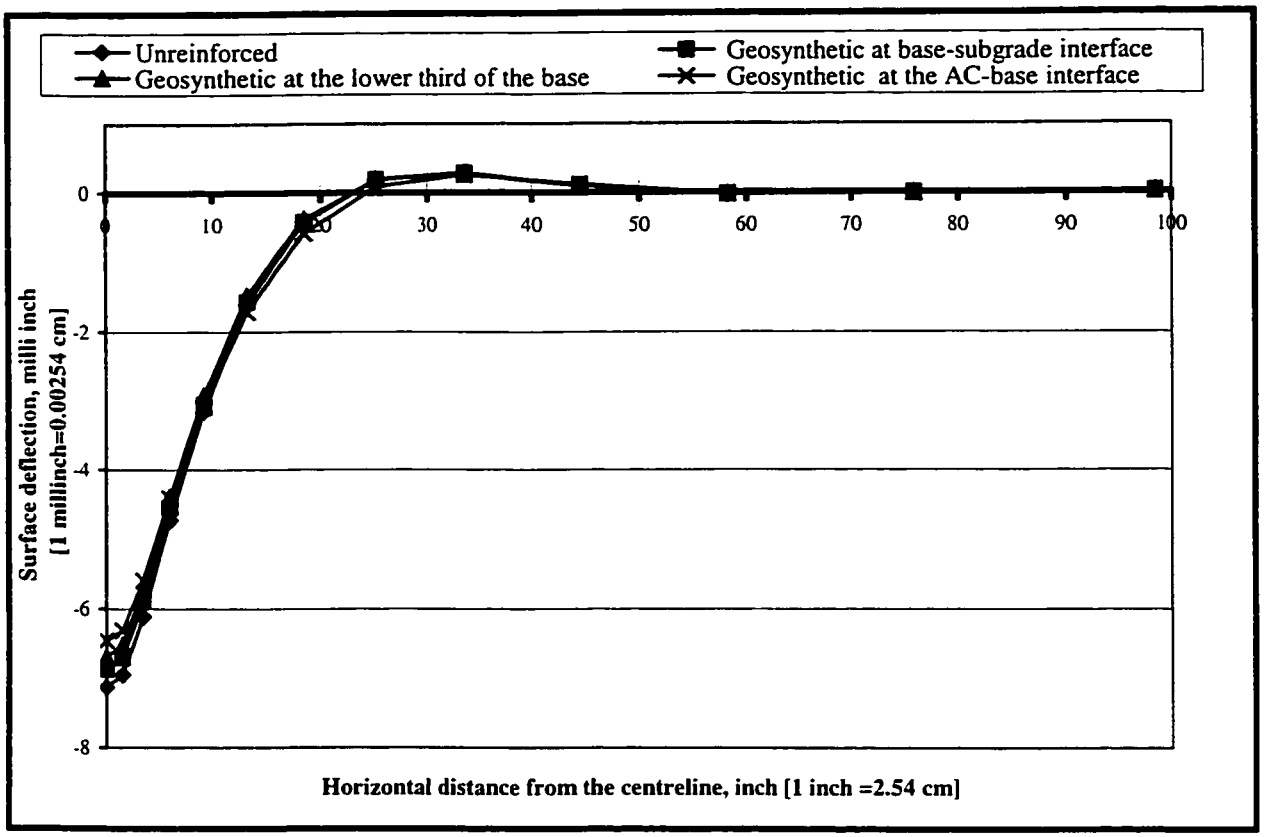

Figure (6.16) The vertical surface deflection across line 1-3 at the peak load t=0.05s (Thick base system #2)

Table (6.16) The vertical surface deflection across line 1-3 at the peak load t=0.05 s

Thick base system # 2				
Horizontal distance from the centreline (in) [1 inch =2.54 cm]	Surface deflection (inch) [1inch =2.54 cm]			
	Unreinforced	Geosynthetic at base-subgrade interface	Geosynthetic at the lower third of the base	Geosynthetic at the AC-base interface
0.00	-0.00712615	-0.00687366	-0.00668918	-0.00645062
1.54	-0.00694565	-0.00669971	-0.00651802	-0.00630318
3.50	-0.00610968	-0.00588895	-0.0057174	-0.00558816
6.01	-0.0047206	-0.00454867	-0.00439545	-0.00441044
9.20	-0.00315418	-0.00304802	-0.00292167	-0.00308491
13.28	-0.00160704	-0.0015646	-0.00147632	-0.0017127
18.49	-0.000420636	-0.000419724	-0.000379634	-0.000580129
25.14	0.000202125	0.000191186	0.000189133	9.22314E-05
33.62	0.000287561	0.000283432	0.000268943	0.000262639
44.44	9.99434E-05	0.000102447	0.000100862	0.000121823
58.26	-2.56702E-05	-2.41746E-05	-2.12955E-05	-1.63746E-05
75.89	-4.96654E-06	-5.27237E-06	-6.16274E-06	-1.02825E-05
98.40	1.60783E-05	1.61375E-05	1.63419E-05	1.67992E-05

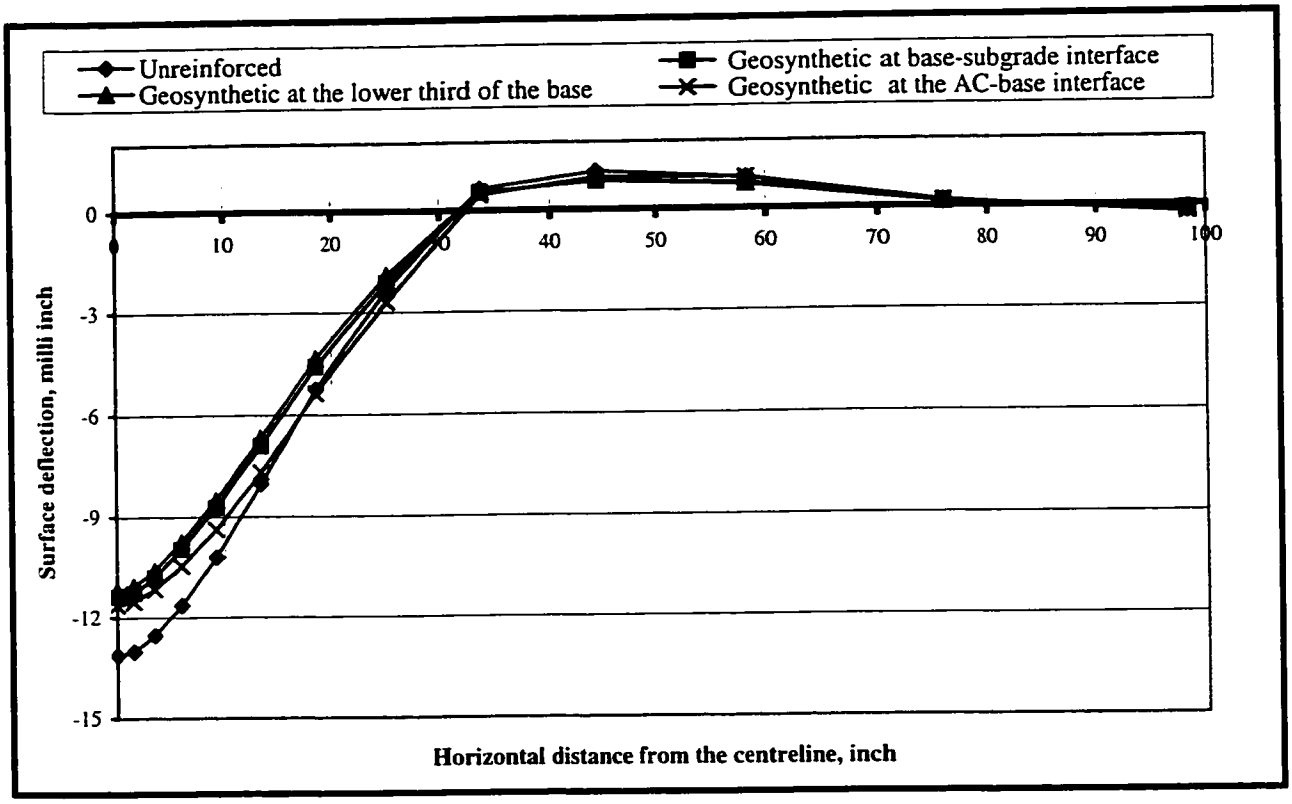

Figure (6.17) Envelope of the vertical surface deflection across line 1-3
(Thick base system #2)

Table (6.17) The envelope of the vertical surface deflection across line 1-3

Thick base system # 2				
Horizontal distance from the centreline (in)	Surface deflection (inch)			
	Unreinforced	Geosynthetic at base-subgrade interface	Geosynthetic at the lower third of the base	Geosynthetic at the AC-base interface
0.00	-1.31331E-02	-1.13831E-02	-1.11825E-02	-0.0116216
1.54	-1.30137E-02	-1.12701E-02	-1.10686E-02	-0.0115305
3.50	-1.25353E-02	-1.08087E-02	-1.06047E-02	-0.0111558
6.01	-1.16439E-02	-9.96164E-03	-9.75567E-03	-0.0104642
9.20	-1.02011E-02	-8.71889E-03	-8.50652E-03	-0.00938467
13.28	-8.02766E-03	-6.90061E-03	-6.67394E-03	-0.00768454
18.49	-5.25104E-03	-4.58033E-03	-4.34620E-03	-0.00535913
25.14	-2.33071E-03	-2.13012E-03	-1.91940E-03	-0.00270746
33.62	6.30986E-04	5.38805E-04	5.34335E-04	0.000465456
44.44	1.13115E-03	8.52892E-04	8.50605E-04	0.000952318
58.26	9.05561E-04	7.65113E-04	7.16603E-04	0.000921215
75.89	1.19570E-04	1.48884E-04	1.30245E-04	0.000167802
98.40	-2.03899E-04	-1.43697E-04	-1.37630E-04	-0.000219772

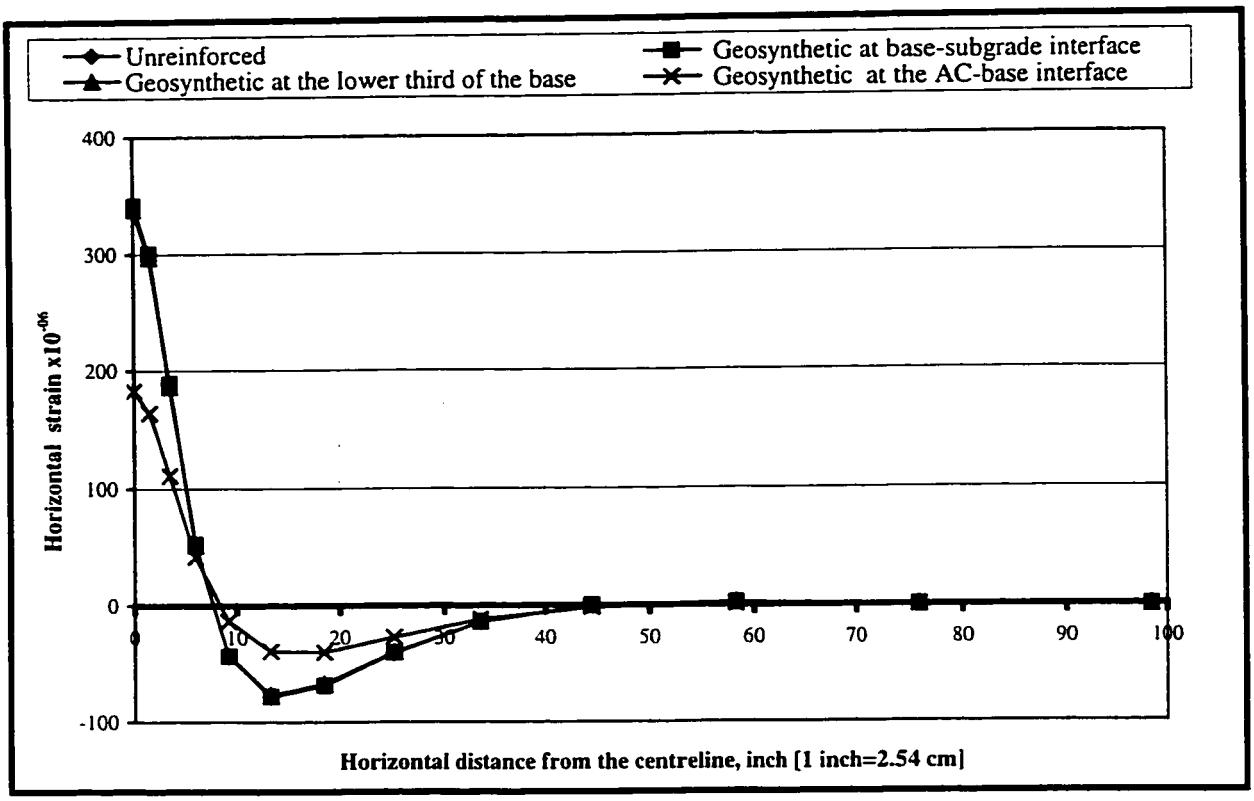

Figure (6.18) Horizontal strain at the bottom of AC layer at the peak load t=0.05s (Thick base system #3)

Table (6.18) The horizontal strain at the bottom of AC layer at peak load t=0.05s

Thick base system # 3				
Horizontal distance from the centreline (in) [1 inch =2.54 cm]	Horizontal strain			
	Unreinforced	Geosynthetic at base-subgrade interface	Geosynthetic at the lower third of the base	Geosynthetic at the AC-base interface
98.40	-5.74765E-07	-5.74771E-07	-5.75532E-07	-3.97211E-07
75.89	2.74769E-07	2.74771E-07	2.73065E-07	3.42184E-07
58.26	2.17516E-06	2.17517E-06	2.13941E-06	1.25164E-06
44.44	5.81308E-08	5.65257E-08	-2.77179E-08	-1.64089E-06
33.62	-1.39556E-05	-1.39594E-05	-1.38673E-05	-0.00001177
25.14	-4.03743E-05	-4.03667E-05	-3.97301E-05	-2.70914E-05
18.49	-6.84761E-05	-6.84374E-05	-6.72682E-05	-0.000039839
13.28	-7.80962E-05	-0.000078042	-7.69437E-05	-3.89298E-05
9.20	-4.34659E-05	-4.34468E-05	-4.32383E-05	-1.30632E-05
6.01	5.31497E-05	5.31066E-05	5.19291E-05	4.22398E-05
3.50	0.000188801	0.000188716	0.000186265	0.000111402
1.54	0.000300623	0.000300526	0.000297303	0.000164144
0.00	0.000341689	0.000341589	0.000338123	0.000182564

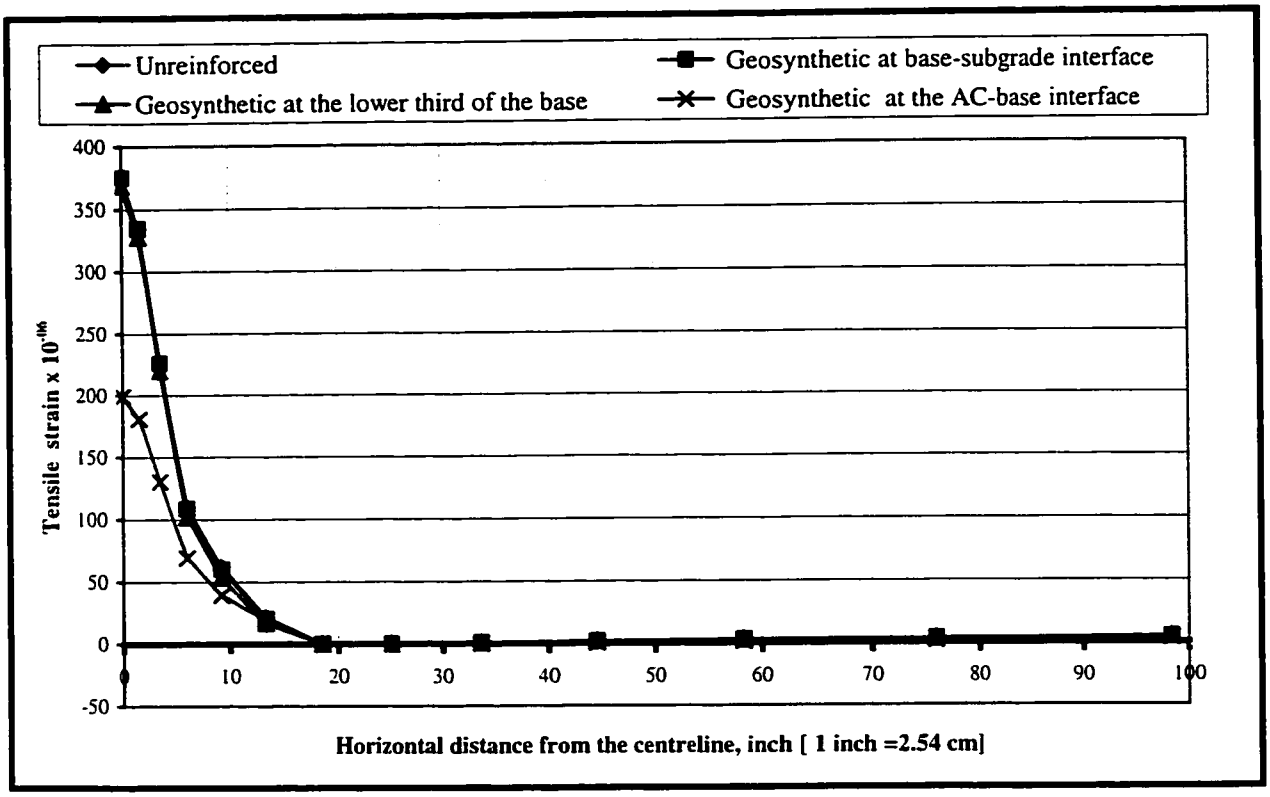

Figure (6.19) Envelope of the tensile strain at the bottom of AC layer
(Thick base system #3)

Table (6.19) Envelope of the tensile strain at the bottom of AC layer

Thick base system # 3				
Horizontal distance from the centreline (in) [1inch=2.54cm]	Tensile strain			
	Unreinforced	Geosynthetic at base-subgrade interface	Geosynthetic at the lower third of the base	Geosynthetic at the AC-base interface
98.40	4.58511E-06	4.53008E-06	4.6925E-06	3.67053E-06
75.89	3.41659E-06	3.3324E-06	3.32278E-06	1.93847E-06
58.26	2.99467E-06	2.97208E-06	2.82855E-06	1.30867E-06
44.44	1.79134E-06	1.79134E-06	1.78674E-06	7.05824E-07
33.62	8.27464E-07	8.27464E-07	8.27464E-07	1.49692E-07
25.14	9.17309E-08	9.17309E-08	9.17309E-08	-1.39925E-11
18.49	9.81683E-10	9.81683E-10	9.81683E-10	-5.58867E-10
13.28	2.16368E-05	2.04683E-05	1.68975E-05	1.96902E-05
9.20	6.22292E-05	6.01632E-05	5.33437E-05	3.93665E-05
6.01	0.000109926	0.000108578	0.000101764	6.95454E-05
3.50	0.00022666	0.000226036	0.000219623	0.000130317
1.54	0.000334695	0.000334341	0.00032775	0.000181076
0.00	0.000375677	0.000375327	0.000368522	0.00019919

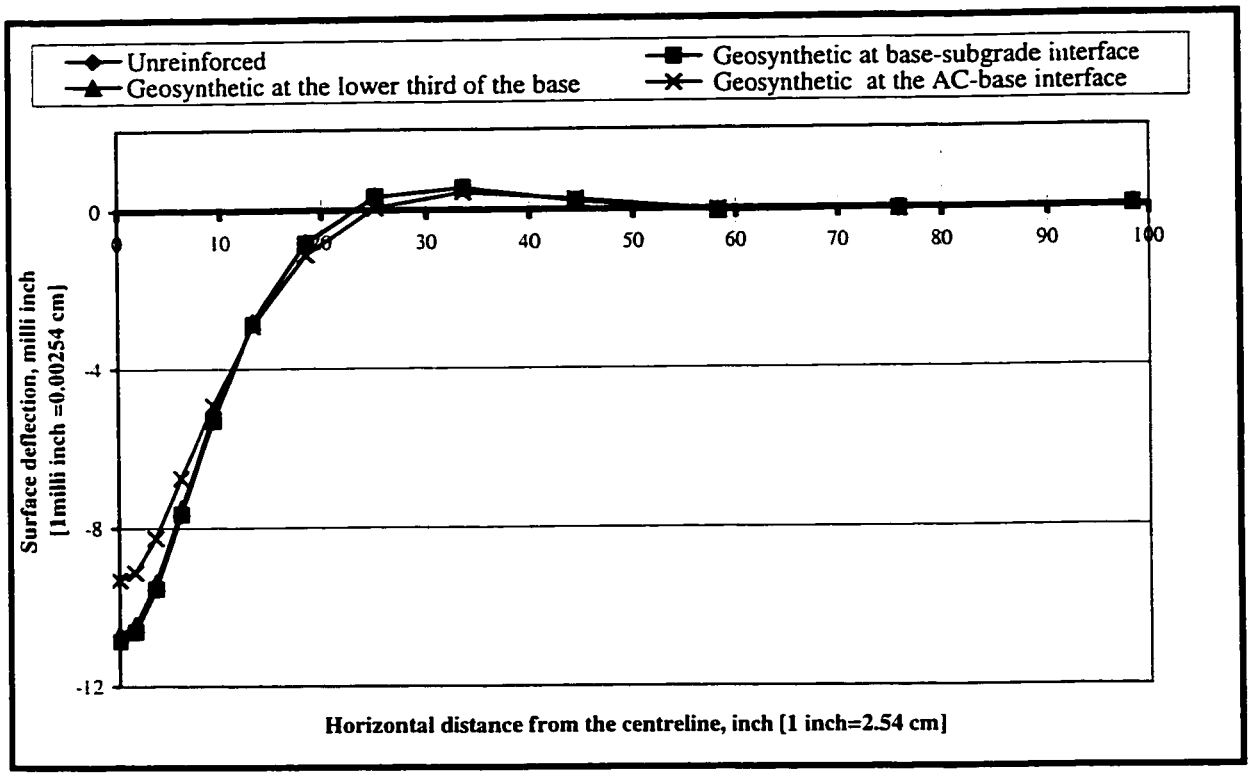

Figure (6.20) The vertical surface deflection across line 1-3 at the peak load t=0.05s (Thick base system #3)

Table (6.20) The vertical surface deflection across line 1-3 at the peak load t=0.05 s

Thick base system # 3				
Horizontal distance from the centreline (in) [1in= 2.54 cm]	Surface deflection (inch) [1 inch=2.54 cm]			
	Unreinforced	Geosynthetic at base-subgrade interface	Geosynthetic at the lower third of the base	Geosynthetic at the AC-base interface
0.00	-0.0108572	-0.0108511	-0.0106742	-0.00929808
1.54	-0.0106147	-0.0106087	-0.0104348	-0.0091126
3.50	-0.00953679	-0.00953127	-0.00936902	-0.00824776
6.01	-0.00765312	-0.00764864	-0.00751046	-0.00675728
9.20	-0.00532899	-0.00532612	-0.00522475	-0.00493384
13.28	-0.00286652	-0.00286537	-0.00280772	-0.00291925
18.49	-0.000830444	-0.000830388	-0.000811644	-0.00112329
25.14	0.000333276	0.000333167	0.000330868	5.66803E-05
33.62	0.00054579	0.000545793	0.000542121	0.00044562
44.44	0.000209458	0.000209466	0.000210077	0.000254377
58.26	-6.23695E-05	-6.23719E-05	-6.20097E-05	-2.39662E-05
75.89	-2.66567E-05	-2.66561E-05	-2.68086E-05	-3.73476E-05
98.40	4.95005E-05	4.95003E-05	4.95976E-05	4.40869E-05

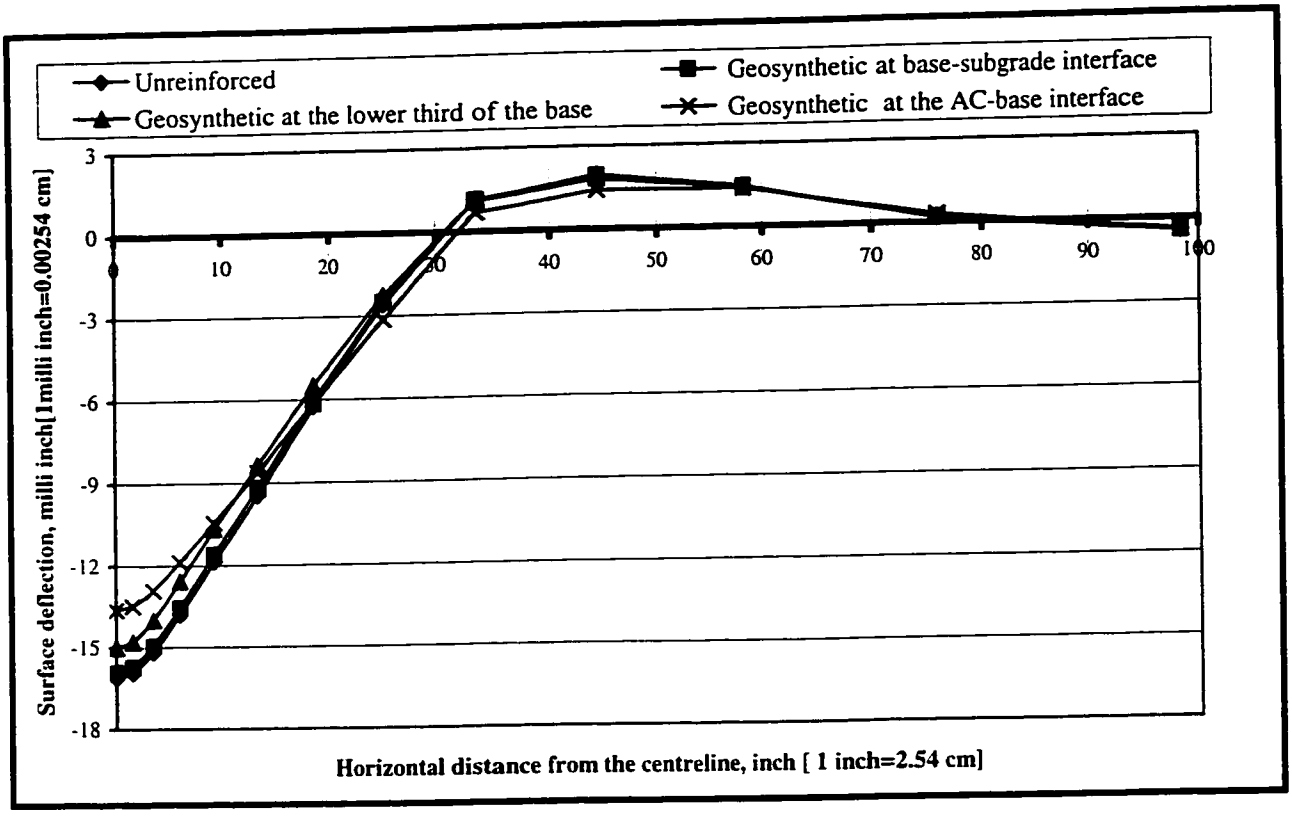

Figure (6.21) Envelope of the vertical surface deflection across line 1-3
(Thick base system #3)

Table (6.21) Envelope of the vertical surface deflection across line 1-3

Thick base system # 3				
Horizontal distance from the centreline (in) 1 inch=2.54 cm	Surface deflection (inch)[1inch =2.54 cm]			
	Unreinforced	Geosynthetic at base-subgrade interface	Geosynthetic at the lower third of the base	Geosynthetic at the AC-base interface
0.00	-0.016129	-0.0159243	-0.0150017	-0.013625
1.54	-0.0159445	-0.0157338	-0.0148103	-0.0134879
3.50	-0.0151846	-0.0149532	-0.0140082	-0.0129113
6.01	-0.0137986	-0.0135418	-0.0125838	-0.0118747
9.20	-0.0118712	-0.0115902	-0.0106676	-0.0104322
13.28	-0.00945824	-0.00917611	-0.00836093	-0.00860098
18.49	-0.0062565	-0.00605631	-0.00551751	-0.00615757
25.14	-0.0025894	-0.00249355	-0.00227598	-0.00314082
33.62	0.00114263	0.00113767	0.0011104	0.000687317
44.44	0.00195362	0.00193254	0.00182134	0.00141326
58.26	0.00145688	0.00145063	0.00140762	0.00138544
75.89	0.00016193	0.000166208	0.000179429	0.000293098
98.40	-0.00043981	-0.000438479	-0.000418364	-0.000396516

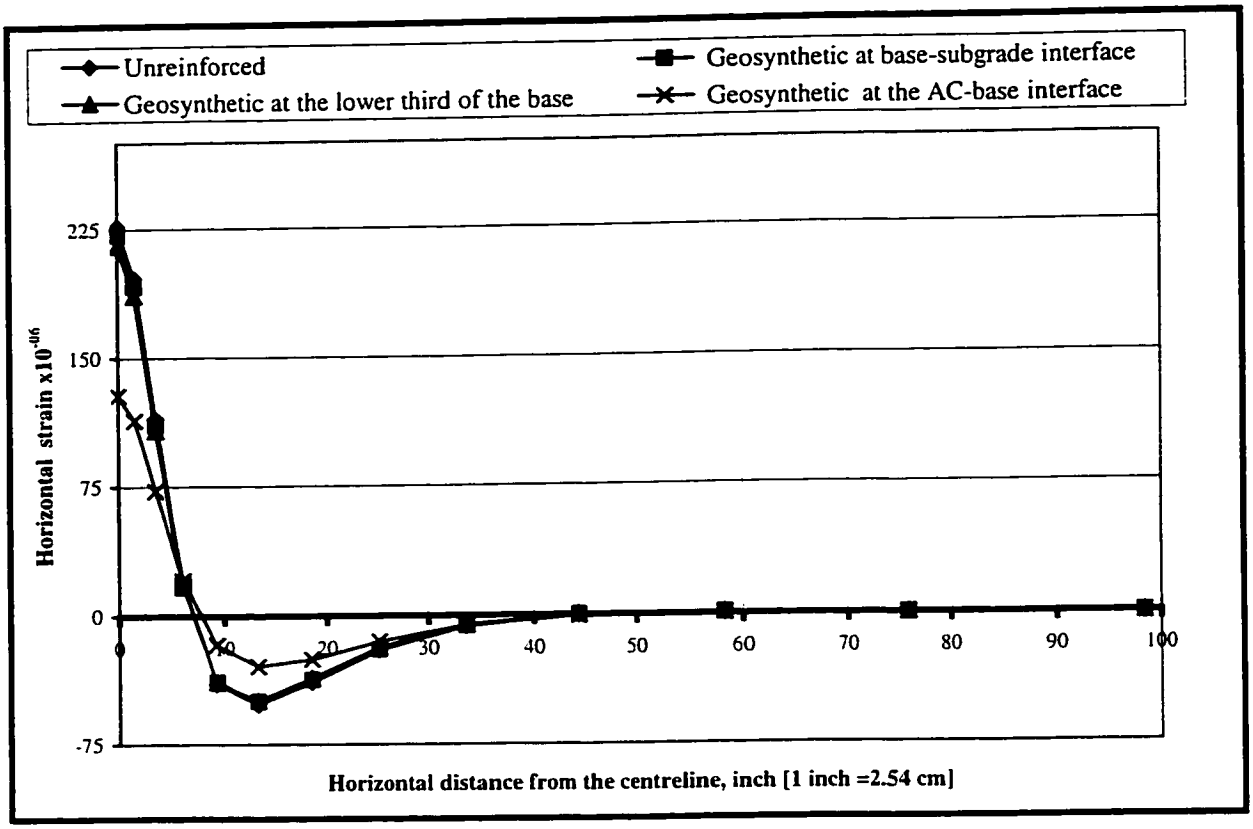

Figure (6.22) Horizontal strain at the bottom of AC layer at the peak load t=0.05s (Thick base system #4)

Table(6.22)The horizontal strain at the bottom of AC layer at peak load t=0.05s

Thick base system # 4				
Horizontal distance from the centreline (in) [1 inch=2.54 cm]	Horizontal strain			
	Unreinforced	Geosynthetic at base-subgrade interface	Geosynthetic at the lower third of the base	Geosynthetic at the AC-base interface
98.40	-2.69959E-07	-2.7221E-07	-2.79155E-07	-2.07992E-07
75.89	-1.51704E-08	-2.47539E-08	-2.71567E-08	6.72113E-08
58.26	7.93219E-07	7.58692E-07	7.37609E-07	6.05771E-07
44.44	1.52992E-07	8.77311E-08	2.50851E-07	-4.41039E-07
33.62	-6.11454E-06	-6.08329E-06	-5.31793E-06	-5.55422E-06
25.14	-1.99963E-05	-1.94666E-05	-0.0000182	-1.48876E-05
18.49	-3.84829E-05	-3.71198E-05	-3.60433E-05	-2.51322E-05
13.28	-5.15428E-05	-0.000049728	-4.93238E-05	-2.92229E-05
9.20	-3.94784E-05	-3.83999E-05	-3.87487E-05	-1.65756E-05
6.01	1.94126E-05	1.84082E-05	1.69673E-05	2.07451E-05
3.50	0.000114523	0.000111062	0.000107716	7.26563E-05
1.54	0.000196553	0.000191519	0.000186064	0.000113741
0.00	0.000226919	0.000221428	0.000215055	0.000128212

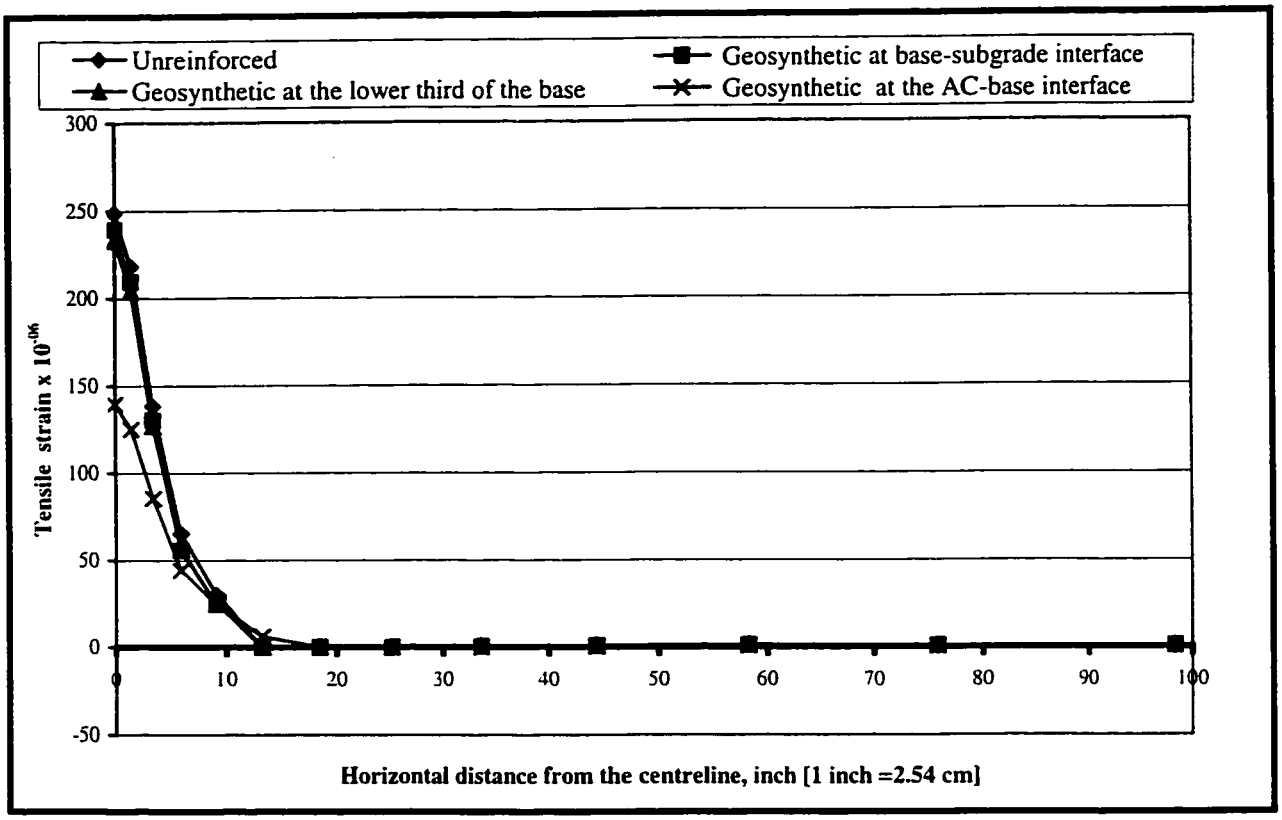

Figure (6.23)Envelope of the tensile strain at the bottom of AC layer
(Thick base system #4)

Table (6.23) Envelope of the tensile strain at the bottom of AC layer

Thick base system # 4				
Horizontal distance from the centreline (in)[1inch =2.54 cm]	Tensile strain			
	Unreinforced	Geosynthetic at base-subgrade interface	Geosynthetic at the lower third of the base	Geosynthetic at the AC-base interface
98.40	3.61309E-07	6.6504E-07	7.54767E-07	6.74371E-07
75.89	5.54867E-07	7.3921E-07	9.36163E-07	4.89321E-07
58.26	1.05353E-06	1.14007E-06	1.36791E-06	6.78691E-07
44.44	8.4026E-07	8.35224E-07	7.82376E-07	4.28753E-07
33.62	5.00173E-07	5.00157E-07	4.96833E-07	1.13148E-07
25.14	5.81535E-08	5.81535E-08	5.81444E-08	-8.62722E-12
18.49	1.0408E-09	1.0408E-09	1.0408E-09	-3.96854E-10
13.28	-5.07865E-09	-5.07865E-09	-5.07865E-09	6.26842E-06
9.20	3.00922E-05	2.47088E-05	2.50253E-05	2.46067E-05
6.01	6.56008E-05	5.56936E-05	5.61856E-05	4.44103E-05
3.50	0.000138385	0.000130295	0.000126917	8.55867E-05
1.54	0.000218234	0.000209341	0.000203701	0.00012527
0.00	0.000248761	0.000239407	0.000232797	0.000139701

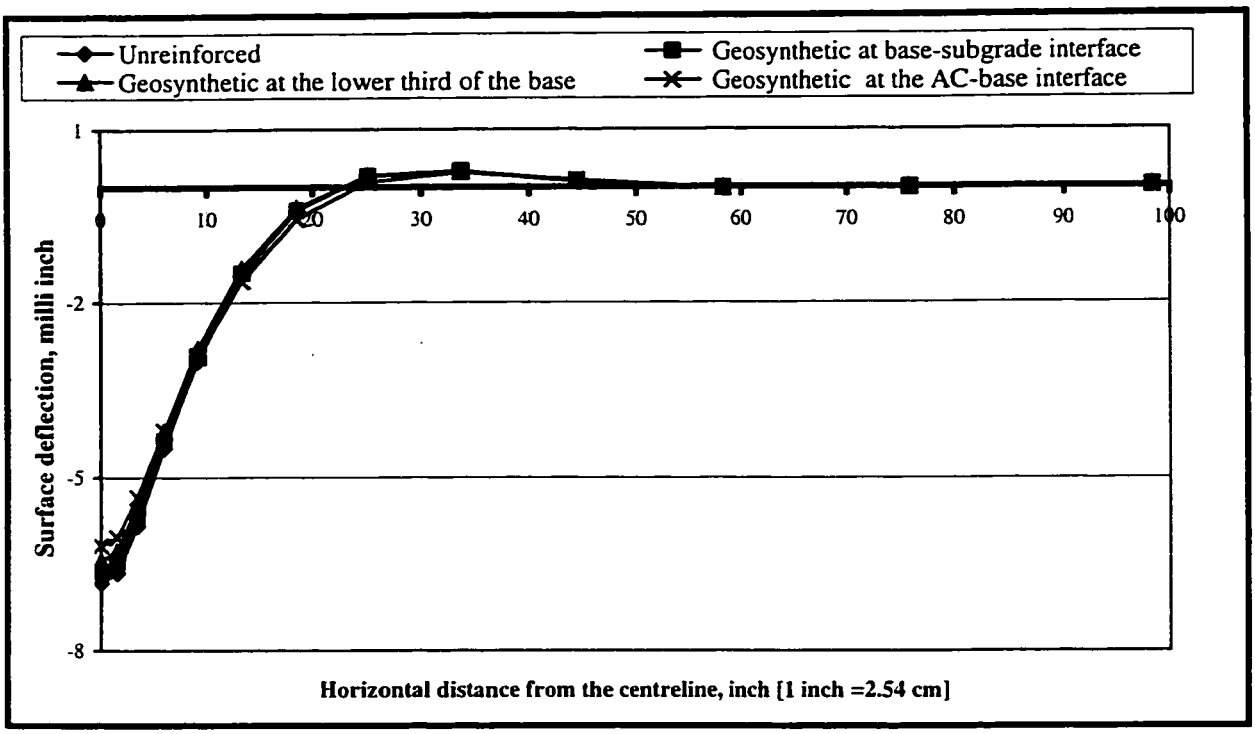

Figure (6.24)The vertical surface deflection across line 1-3 at the peak load t=0.05s (Thick base system #4)

Table (6.24) The vertical surface deflection across line 1-3 at the peak load t=0.05 s

Thick base system # 4				
Horizontal distance from the centreline (in) [1inch=2.54 cm]	Surface deflection (inch) [1inch =2.54 cm]			
	Unreinforced	Geosynthetic at base-subgrade interface	Geosynthetic at the lower third of the base	Geosynthetic at the AC-base interface
0.00	-0.00682017	-0.0066288	-0.00644311	-0.0061746
1.54	-0.00664561	-0.00645903	-0.00627661	-0.00603191
3.50	-0.00583307	-0.00566493	-0.00549452	-0.00533572
6.01	-0.004492	-0.00435978	-0.00421127	-0.00419727
9.20	-0.0029967	-0.00291346	-0.0027955	-0.0029318
13.28	-0.00152738	-0.0014926	-0.00141346	-0.00162901
18.49	-0.000400388	-0.000398494	-0.000364301	-0.000554307
25.14	0.000197008	0.000188737	0.000184968	8.90877E-05
33.62	0.000283036	0.000279996	0.000265716	0.000257397
44.44	0.000100427	0.000102555	0.000101324	0.00012192
58.26	-2.53153E-05	-0.000024222	-2.10578E-05	-0.000015872
75.89	-5.09928E-06	-5.3908E-06	-6.2449E-06	-1.04246E-05
98.40	1.61501E-05	1.62297E-05	1.63944E-05	1.68536E-05

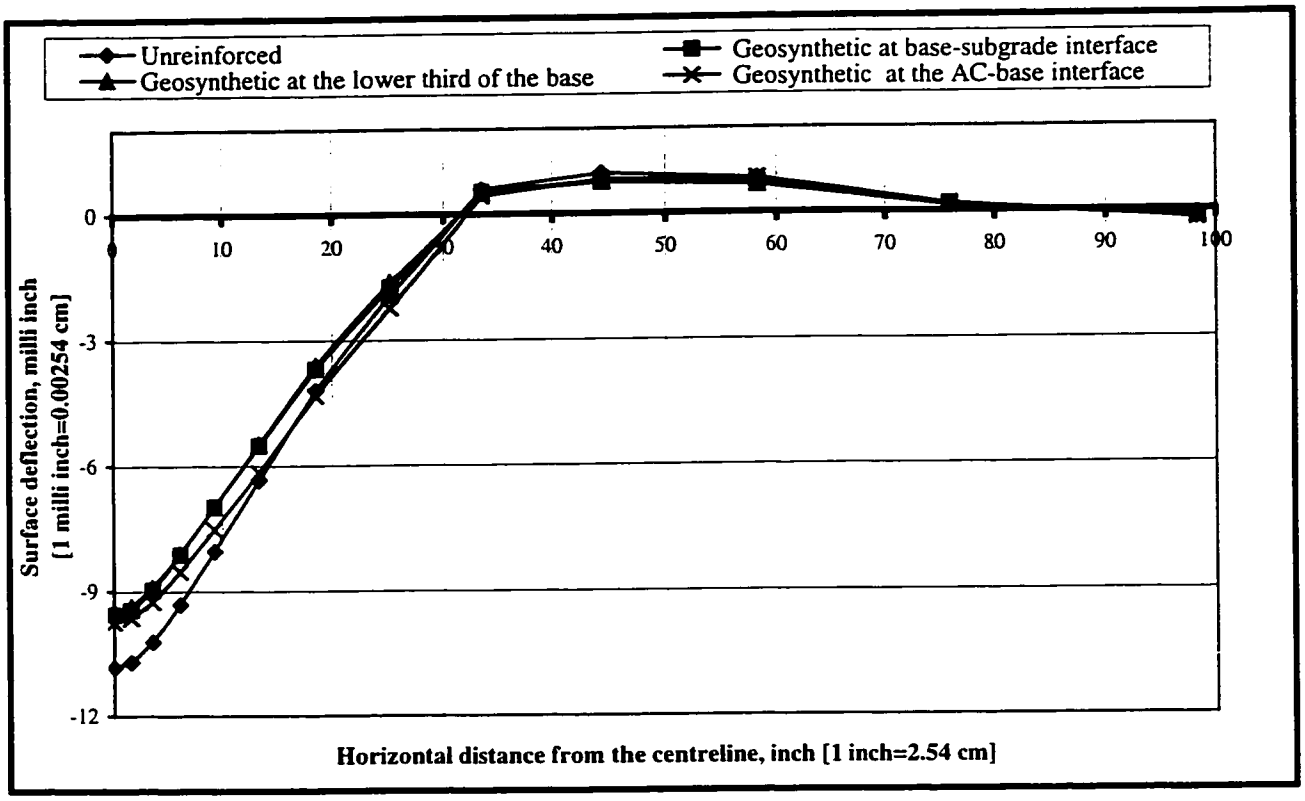

Figure (6.25)Envelope of the vertical surface deflection across line 1-3
(Thick base system #4)

Table (6.25) The envelope of vertical surface deflection across line 1-3

Thick base system # 4				
Horizontal distance from the centreline (in) [1inch= 2.54 cm]	Surface deflection (inch) [1inch =2.54 cm]			
	Unreinforced	Geosynthetic at base-subgrade interface	Geosynthetic at the lower third of the base	Geosynthetic at the AC-base interface
0.00	-0.0108274	-0.00955733	-0.00947098	-0.00973416
1.54	-0.0107062	-0.00944225	-0.00936078	-0.00963956
3.50	-0.0102101	-0.00896119	-0.00890499	-0.00924274
6.01	-0.00930432	-0.00811888	-0.00809313	-0.00852609
9.20	-0.0080298	-0.00697179	-0.00697069	-0.0075125
13.28	-0.00633589	-0.00551401	-0.00548448	-0.00614889
18.49	-0.00419108	-0.00368199	-0.00359533	-0.00431825
25.14	-0.00190484	-0.00172196	-0.00160614	-0.00221909
33.62	0.000575668	0.000514164	0.000498039	0.000426294
44.44	0.000942065	0.000776466	0.000742504	0.000794231
58.26	0.00079836	0.000705248	0.000649179	0.00080491
75.89	0.000119041	0.000141173	0.000125771	0.000163394
98.40	-0.000182384	-0.000139541	-0.00012917	-0.000193045

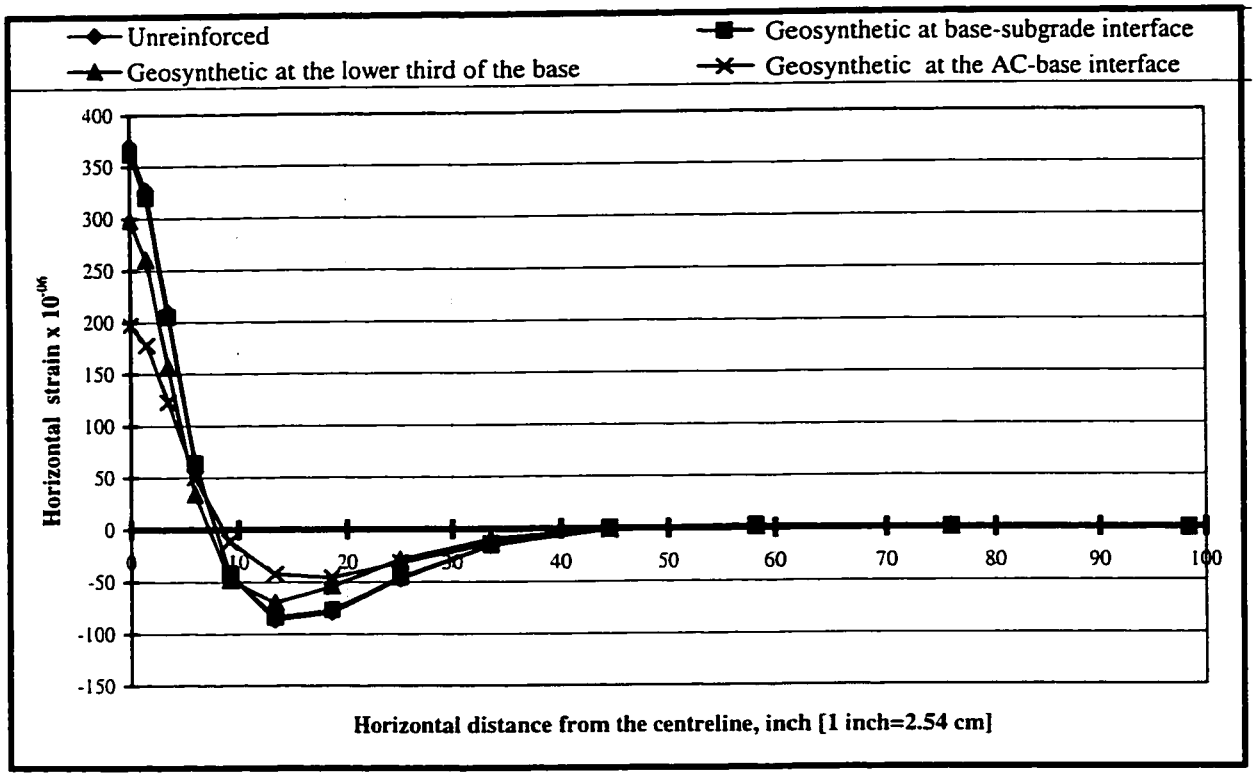

Figure (6.26) Horizontal strain at the bottom of AC layer at the peak load t=0.05s (Thin base system #1)

Table (6.26)The tensile strain at the bottom of AC layer at peak load t=0.05s

Thin base system # 1				
Horizontal distance from the centreline (in) [1inch =2.54 cm]	Horizontal strain			
	Unreinforced	Geosynthetic at base-subgrade interface	Geosynthetic at the lower third of the base	Geosynthetic at the AC-base interface
8.40	-5.61E-07	-5.66E-07	-6.08E-07	-3.82E-07
75.89	3.03E-07	2.96E-07	1.74E-07	3.85E-07
58.26	2.49E-06	2.45E-06	1.57E-06	1.52E-06
44.44	6.36E-07	5.27E-07	2.80E-08	-1.41E-06
33.62	-1.53E-05	-1.52E-05	-9.31E-06	-1.32E-05
25.14	-4.69E-05	-4.58E-05	-2.86E-05	-3.16E-05
18.49	-7.91E-05	-7.70E-05	-5.40E-05	-4.57E-05
13.28	-8.63E-05	-8.41E-05	-6.98E-05	-4.23E-05
9.20	-4.26E-05	-4.17E-05	-4.81E-05	-1.10E-05
6.01	6.52E-05	6.36E-05	3.37E-05	4.99E-05
3.50	2.10E-04	2.05E-04	1.57E-04	1.23E-04
1.54	3.27E-04	3.20E-04	2.60E-04	1.78E-04
0.00	3.70E-04	3.62E-04	2.98E-04	1.97E-04

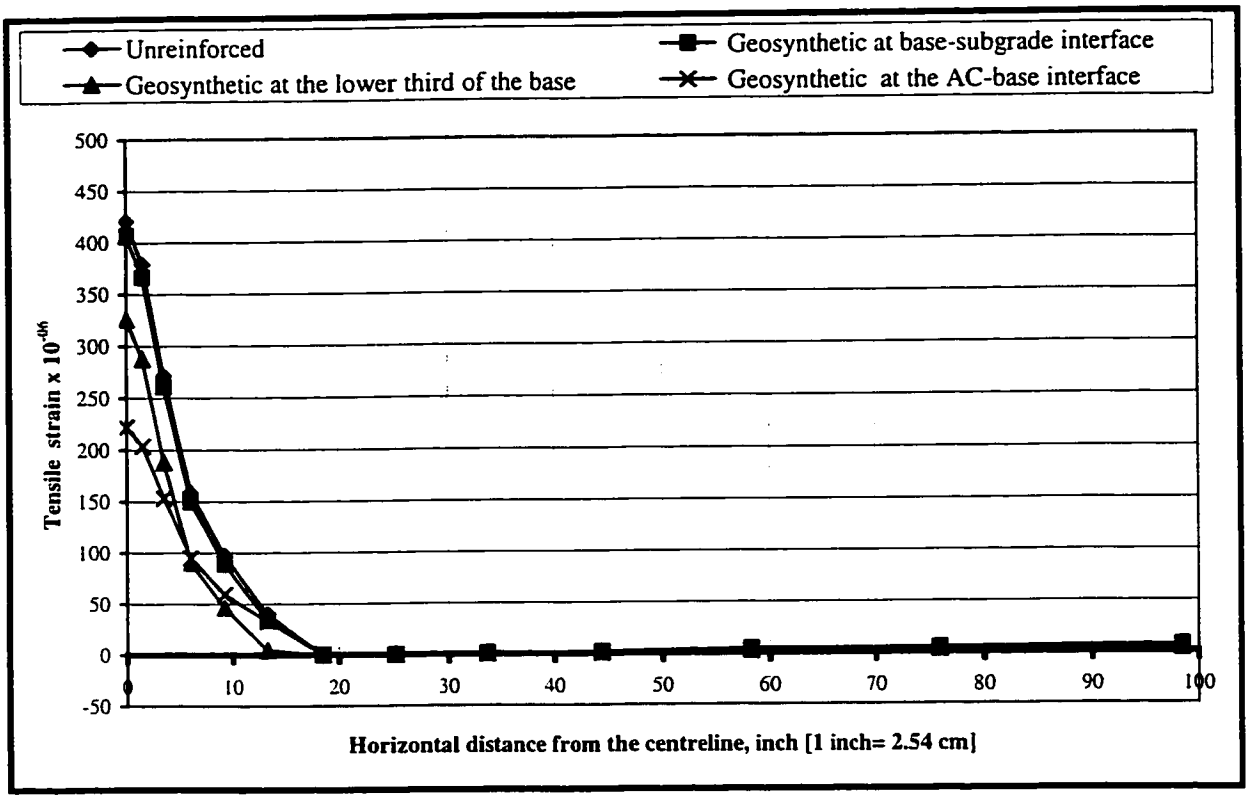

Figure (6.27)Envelope of the tensile strain at the bottom of AC layer
(Thin base system #1)

Table (6.27)Envelope of the tensile strain at the bottom of AC layer

The Thin base System # 1				
Horizontal distance from the centreline (in) [1inch =2.54 cm]	Tensile strain			
	Unreinforced	Geosynthetic at base-subgrade interface	Geosynthetic at the lower third of the base	Geosynthetic at the AC-base interface
98.40	6.47933E-06	6.49159E-06	3.28163E-06	5.30591E-06
75.89	4.77697E-06	4.66548E-06	3.06486E-06	2.67807E-06
58.26	4.13637E-06	4.02267E-06	2.63857E-06	1.78145E-06
44.44	1.91575E-06	1.88671E-06	1.40101E-06	7.21055E-07
33.62	8.26344E-07	8.26277E-07	8.03335E-07	1.49538E-07
25.14	9.08292E-08	9.08292E-08	9.17181E-08	-1.50355E-11
18.49	9.32503E-10	9.32503E-10	9.81702E-10	7.31928E-07
13.28	3.97719E-05	3.38345E-05	4.40385E-06	3.27655E-05
9.20	9.71187E-05	8.89294E-05	4.64126E-05	5.94506E-05
6.01	0.000158771	0.000149253	9.01082E-05	0.000094909
3.50	0.000271545	0.000260891	0.000188011	0.00015339
1.54	0.000379333	0.000366439	0.000287716	0.0002037
0.00	0.000420905	0.00040706	0.000325618	0.000221974

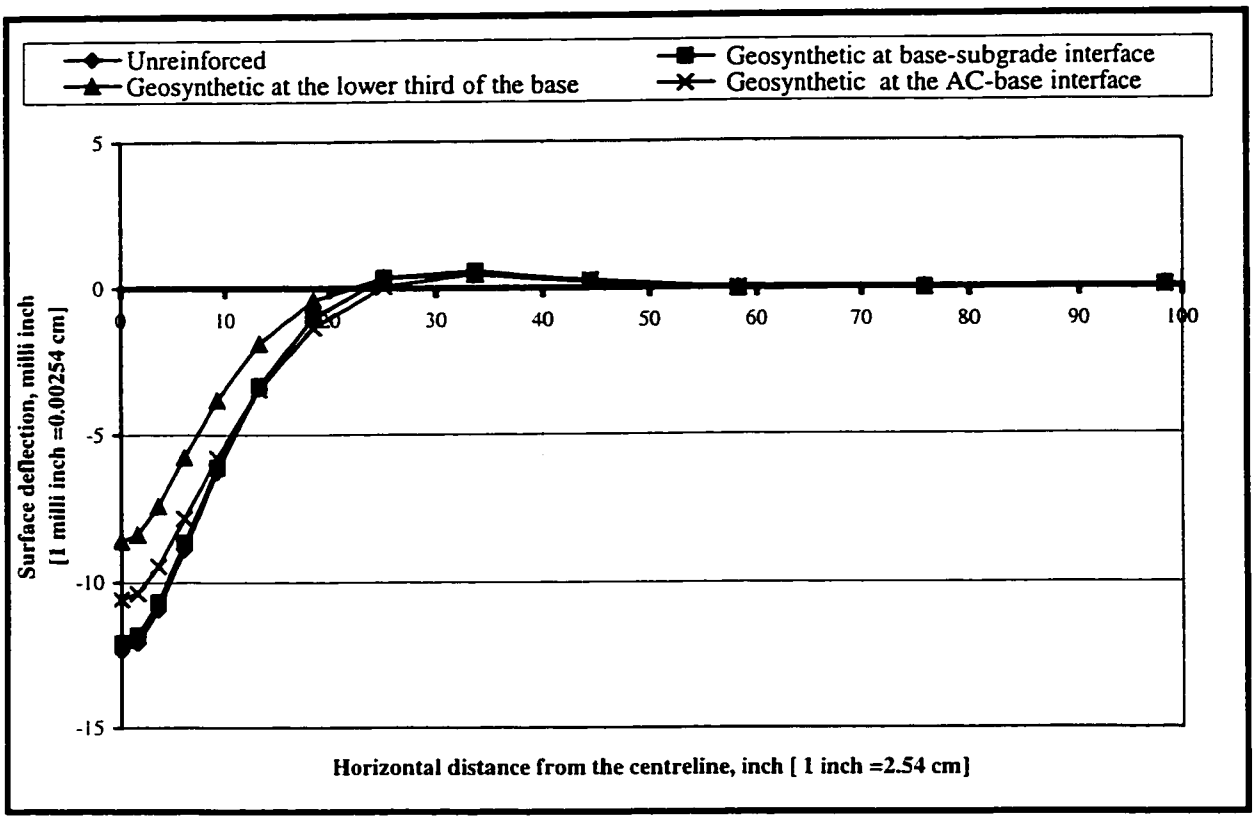

Figure (6.28)The vertical surface deflection across line 1-3 at the peak load t=0.05s (Thin base system #1)

Table (6.28) The vertical surface deflection across line 1-3 at the peak load t=0.05 s

The Thin base System # 1				
Horizontal distance from the centreline (in) [1 inch =2.54 cm]	Surface deflection (inch) [1 inch =2.54 cm]			
	Unreinforced	Geosynthetic at base-subgrade interface	Geosynthetic at the lower third of the base	Geosynthetic at the AC-base interface
0.00	-0.0123473	-0.0120693	-0.00860185	-0.0105735
1.54	-0.0120843	-0.0118125	-0.00838667	-0.0103732
3.50	-0.0109243	-0.0106759	-0.00741759	-0.00944859
6.01	-0.00886404	-0.00865978	-0.00576778	-0.00782721
9.20	-0.00624943	-0.00610586	-0.00383376	-0.00578128
13.28	-0.00341098	-0.00333418	-0.0019007	-0.00346219
18.49	-0.00101667	-0.000996863	-0.000424001	-0.00134749
25.14	0.000351113	0.000342477	0.000343631	4.79063E-05
33.62	0.000584032	0.000577605	0.00045159	0.000484708
44.44	0.000206676	0.000208079	0.000190562	0.00025774
58.26	-0.00006749	-6.64348E-05	-3.81446E-05	-3.00978E-05
75.89	-2.50762E-05	-2.52317E-05	-2.78336E-05	-3.61211E-05
98.40	4.86495E-05	0.000048752	4.73568E-05	4.36932E-05

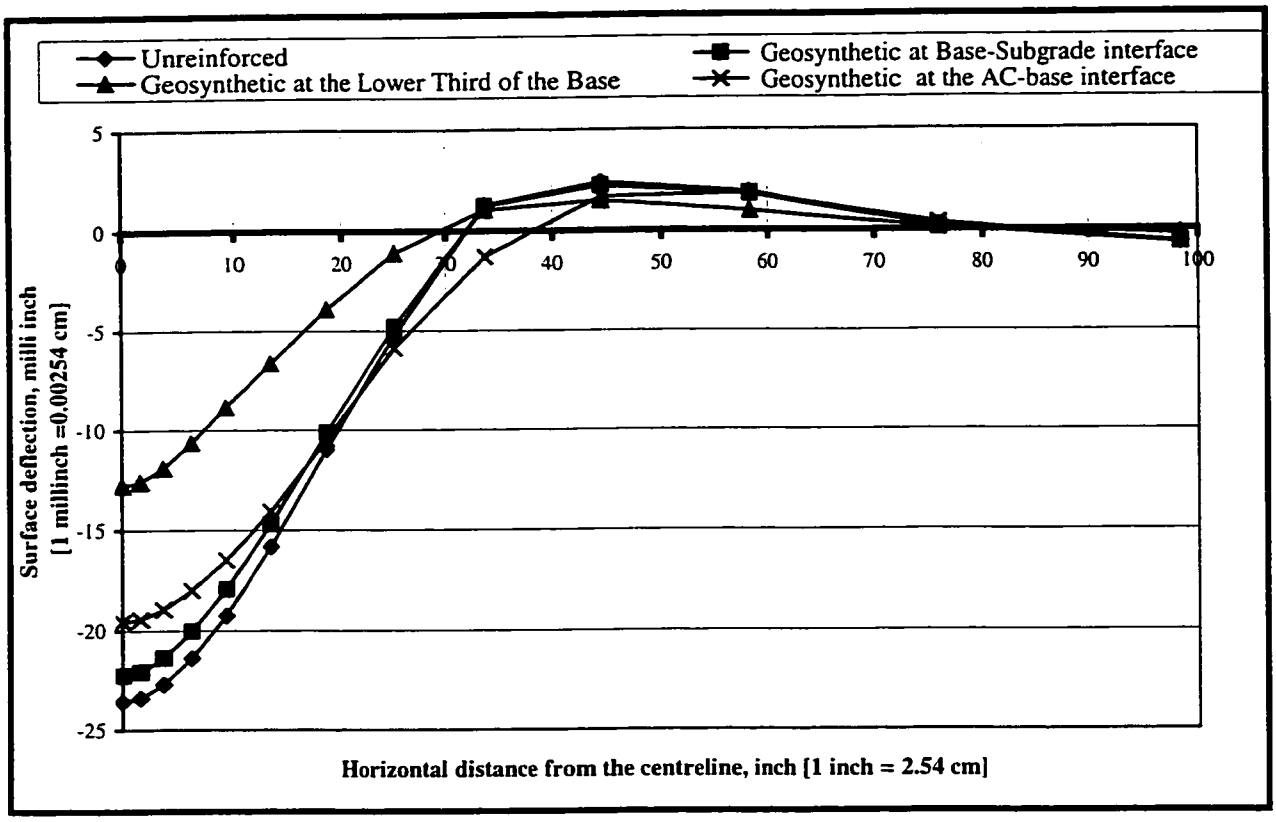

Figure (6.29)Envelope of the vertical surface deflection across line 1-3
(Thin base system #1)

Table (6.29)The envelope of vertical surface deflection across line 1-3

The Thin base System # 1				
Horizontal distance from the centreline (in) [1 inch = 2.54 cm]	Surface Deflection (in) [1 in = 2.54 cm]			
	Unreinforced	Geosynthetic at Base-Subgrade interface	Geosynthetic at the Lower Third of the Base	Geosynthetic at the AC-Base interface
0.00	-0.0235642	-0.0222567	-0.012795	-0.0195645
1.54	-0.0233945	-0.0220799	-0.0126261	-0.0194439
3.50	-0.0227088	-0.0213804	-0.011934	-0.0189469
6.01	-0.0213733	-0.0200181	-0.0106563	-0.0179925
9.20	-0.0192469	-0.01793	-0.00886153	-0.0164998
13.28	-0.0158264	-0.0146894	-0.00664338	-0.0140826
18.49	-0.0109771	-0.0101311	-0.00390222	-0.0104759
25.14	-0.00524529	-0.00479847	-0.00109496	-0.0058739
33.62	0.00126076	0.00120697	0.00103332	-0.00126929
44.44	0.00238635	0.00221922	0.00149159	0.00167922
58.26	0.00188332	0.00179234	0.000962845	0.0018423
75.89	0.000162918	0.000181674	0.000117239	0.000347185
98.40	-0.000658692	-0.000624703	-0.000238477	-0.000631092

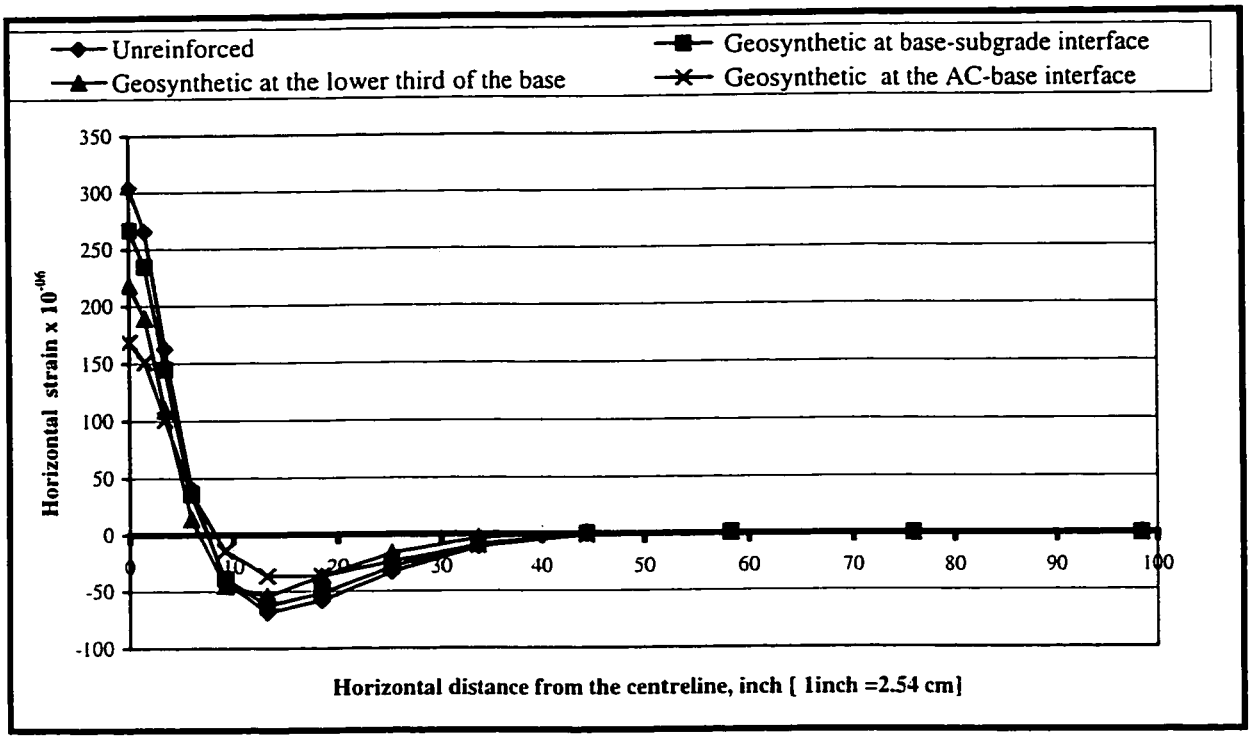

Figure (6.30)Horizontal strain at the bottom of AC layer at the peak load t=0.05s (Thin base system #2)

Table (6.30) The horizontal strain at the bottom of AC layer at peak load t=0.05s

The Thin base System # 2				
Horizontal distance from the centreline (in) [1inch = 2.54 cm]	Horizontal strain			
	Unreinforced	Geosynthetic at base-subgrade interface	Geosynthetic at the lower third of the base	Geosynthetic at the AC-base interface
98.40	-2.65139E-07	-3.91711E-07	-1.0767E-07	-2.40167E-07
75.89	-5.37879E-08	-9.71503E-08	3.1836E-08	5.92444E-08
58.26	1.19915E-06	1.2595E-06	7.77883E-07	8.8057E-07
44.44	1.08945E-07	6.69421E-07	1.16164E-06	-9.23886E-07
33.62	-1.09641E-05	-8.7096E-06	-3.15311E-06	-9.73059E-06
25.14	-3.31643E-05	-2.87028E-05	-1.62704E-05	-2.39846E-05
18.49	-5.78311E-05	-0.0000518	-3.68458E-05	-3.62551E-05
13.28	-6.84847E-05	-0.000062322	-5.42901E-05	-3.65128E-05
9.20	-4.19364E-05	-0.000038989	-4.53105E-05	-1.40024E-05
6.01	4.10428E-05	3.57467E-05	1.37147E-05	3.65675E-05
3.50	0.000162761	0.000144655	0.000109084	0.000101179
1.54	0.00026577	0.000234419	0.000189074	0.000151026
0.00	0.000304246	0.000266986	0.000217846	0.000168561

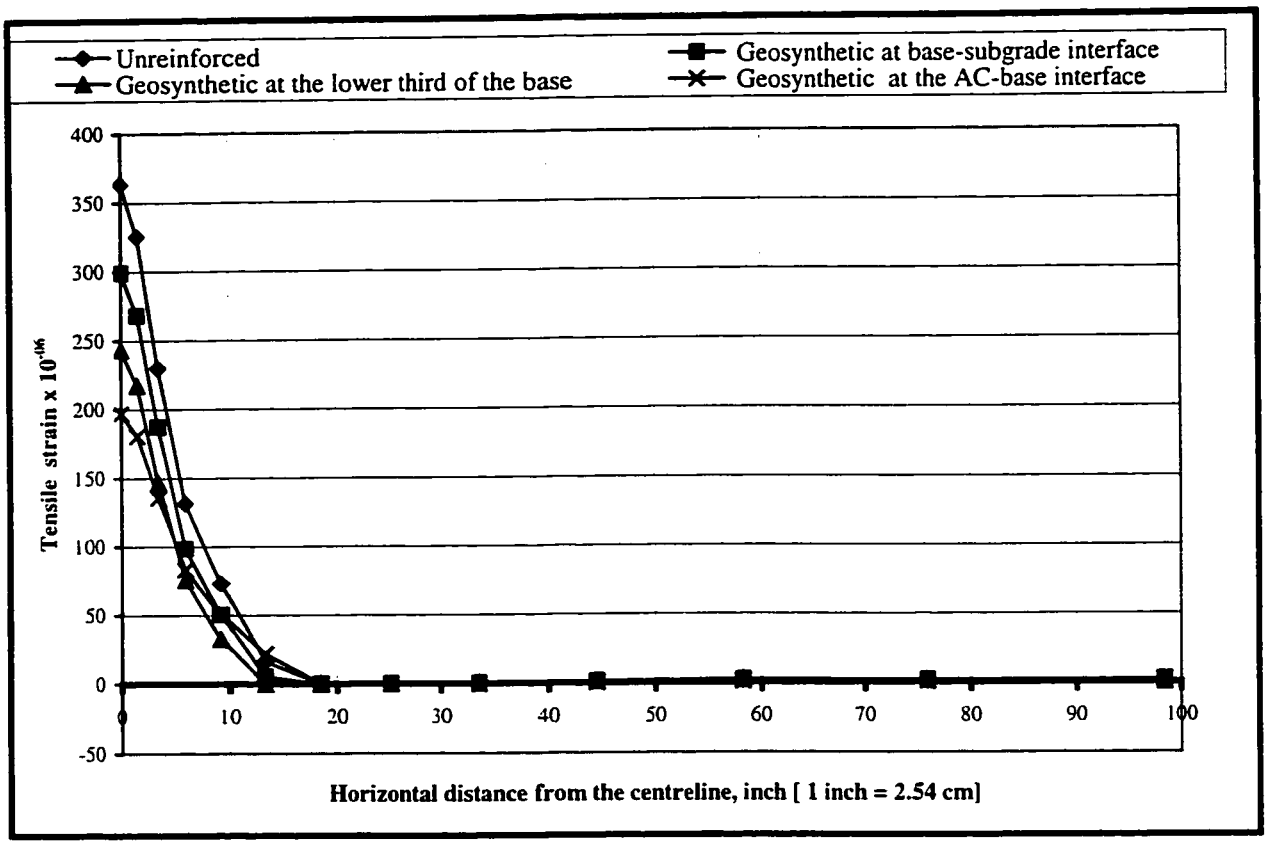

Figure (6.31)Envelope of the tensile strain at the bottom of AC layer
(Thin base system #2)

Table (6.31) Envelope of the tensile strain at the bottom of AC layer

Thin base system # 2				
Horizontal distance from the centreline (in) [1inch = 2.54 cm]	Tensile strain			
	Unreinforced	Geosynthetic at base-subgrade interface	Geosynthetic at the lower third of the base	Geosynthetic at the AC-base interface
98.40	1.29913E-06	2.02384E-06	3.80686E-07	1.85598E-06
75.89	1.21344E-06	1.79022E-06	1.5119E-06	8.91045E-07
58.26	1.83862E-06	0.000002186	2.37326E-06	1.05998E-06
44.44	1.31745E-06	1.29642E-06	1.16164E-06	6.65771E-07
33.62	5.95511E-07	5.73484E-07	3.46635E-07	1.40227E-07
25.14	5.89812E-08	5.8926E-08	5.16648E-08	-9.11414E-12
18.49	1.02494E-09	1.02483E-09	1.04024E-09	-4.07661E-10
13.28	1.63352E-05	5.15052E-06	-5.07879E-09	0.000021628
9.20	0.000073271	5.03477E-05	3.22771E-05	0.000050595
6.01	0.000131383	9.84275E-05	7.55903E-05	8.31228E-05
3.50	0.000230066	0.000187319	0.000146575	0.000135501
1.54	0.00032537	0.000268245	0.00021732	0.000180497
0.00	0.000363333	0.00029899	0.000243273	0.000197085

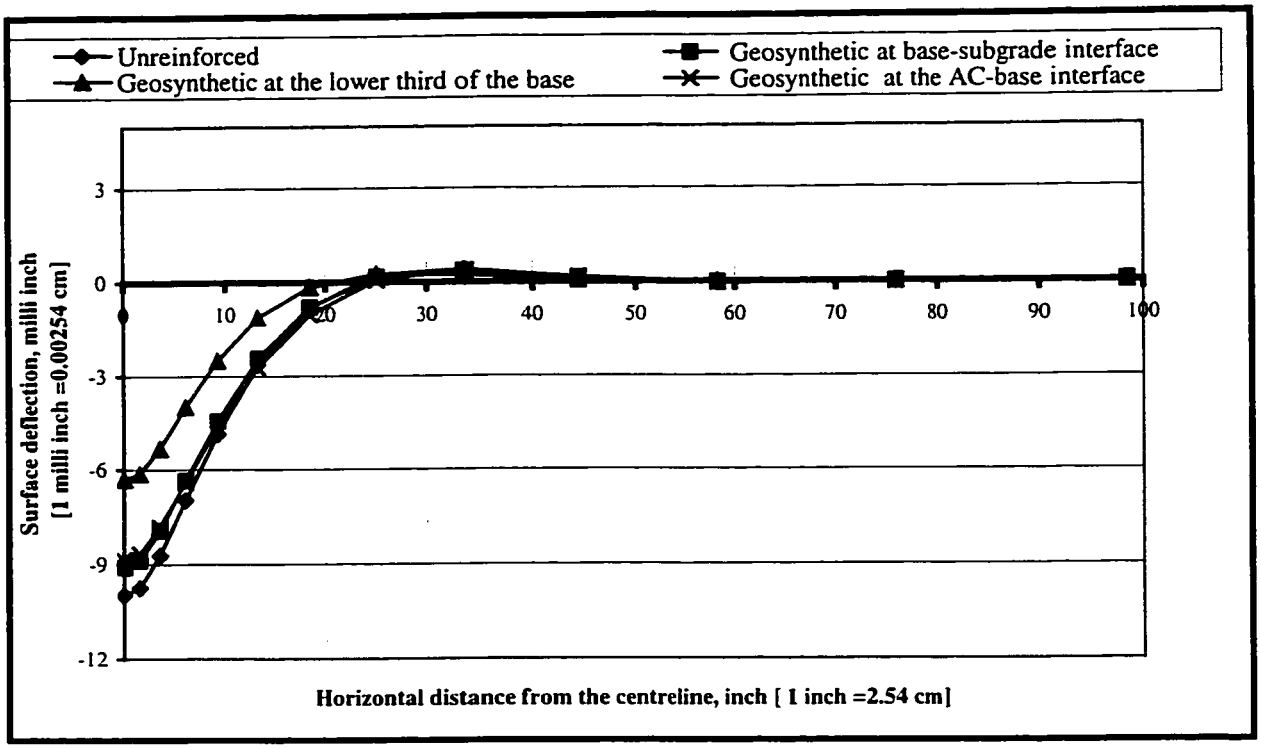

Figure (6.32)The vertical surface deflection across line 1-3 at the peak load t=0.05s (Thin base system #2)

Table (6.32)The vertical surface deflection across line 1-3 at the peak load t=0.05 s

Thin base system # 2				
Horizontal distance from the centreline (in) [1inch = 2.54 cm]	Surface deflection (in) [1 inch = 2.54 cm]			
	Unreinforced	Geosynthetic at base-subgrade interface	Geosynthetic at the lower third of the base	Geosynthetic at the AC-base interface
0.00	-0.00996278	-0.00907807	-0.00631383	-0.00885649
1.54	-0.0097356	-0.00887394	-0.00613906	-0.00867618
3.50	-0.00871894	-0.00794286	-0.00532513	-0.00783229
6.01	-0.00696549	-0.00634668	-0.00398283	-0.00638767
9.20	-0.00484563	-0.00443569	-0.00250519	-0.00463921
13.28	-0.00262582	-0.0024333	-0.00111479	-0.00272047
18.49	-0.000801105	-0.000784886	-0.000152577	-0.0010227
25.14	0.000236186	0.0001604	0.000251505	0.000067476
33.62	0.000412163	0.000351832	0.000222017	0.000376769
44.44	0.000119808	0.000125806	5.26764E-05	0.000158009
58.26	-5.02752E-05	-3.54995E-05	-1.48123E-05	-3.95833E-05
75.89	-6.79692E-07	-3.39382E-06	-2.4061E-07	-9.3391E-06
98.40	1.63639E-05	1.67936E-05	8.72305E-06	1.97258E-05

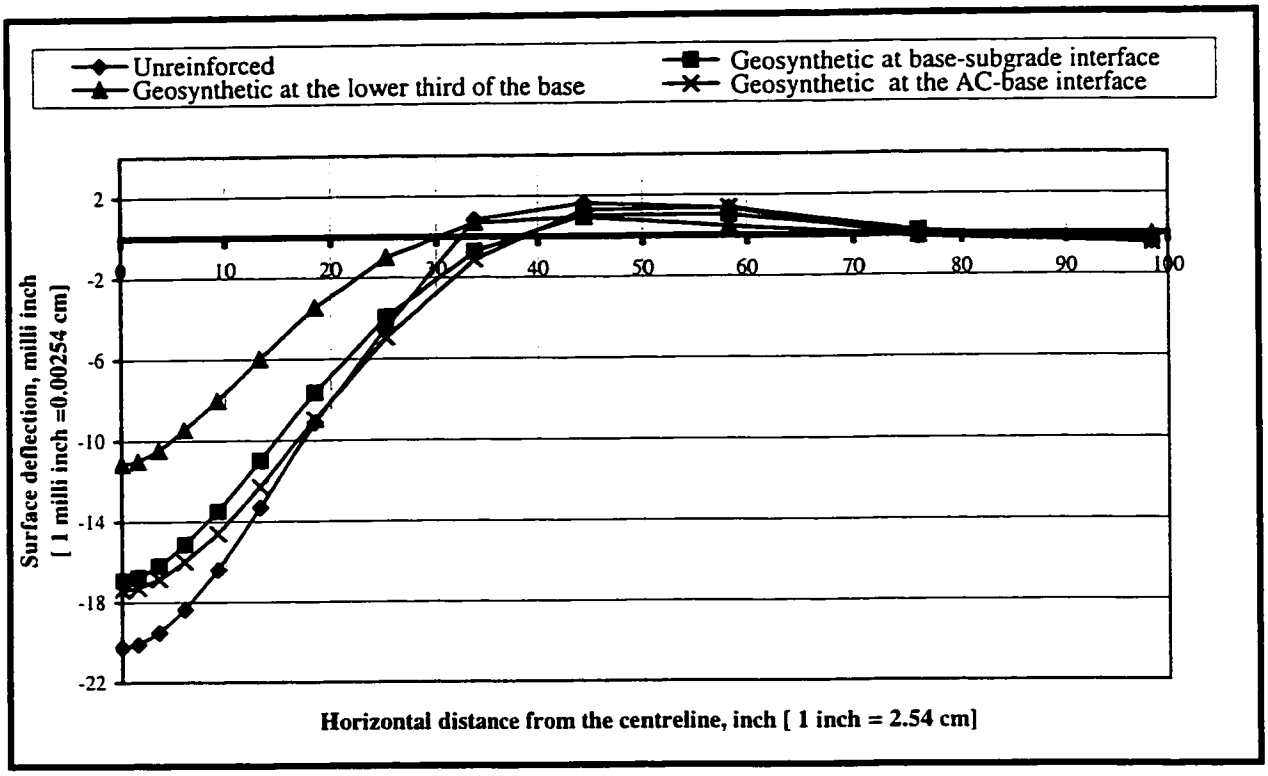

Figure (6.33) Envelope of the vertical surface deflection across line 1-3
(Thin base system #2)

Table (6.33) The envelope of vertical surface deflection across line 1-3

Thin base system # 2				
Horizontal distance from the centreline (in) [1inch = 2.54 cm]	Surface deflection (inch) [1inch = 2.54 cm]			
	Unreinforced	Geosynthetic at base-subgrade interface	Geosynthetic at the lower third of the base	Geosynthetic at the AC-base interface
0.00	-0.0202625	-0.0169057	-0.0111555	-0.0173985
1.54	-0.0201105	-0.0167651	-0.0110186	-0.0172876
3.50	-0.019517	-0.0162042	-0.0104729	-0.0168433
6.01	-0.0183629	-0.0151407	-0.00946914	-0.0159874
9.20	-0.016384	-0.01349	-0.00803512	-0.0145751
13.28	-0.0132885	-0.0109807	-0.00599119	-0.0122685
18.49	-0.0091216	-0.00765966	-0.00346614	-0.00896123
25.14	-0.00446554	-0.0039458	-0.00101488	-0.00495145
33.62	0.000842915	-0.000720338	0.000703603	-0.00111875
44.44	0.00163489	0.00105165	0.000958621	0.00130252
58.26	0.00135894	0.00103785	0.000465657	0.00139114
75.89	-0.000108569	0.000177768	-4.58728E-05	0.000194368
98.40	-0.000427319	-0.000277828	-0.000057803	-0.000458843

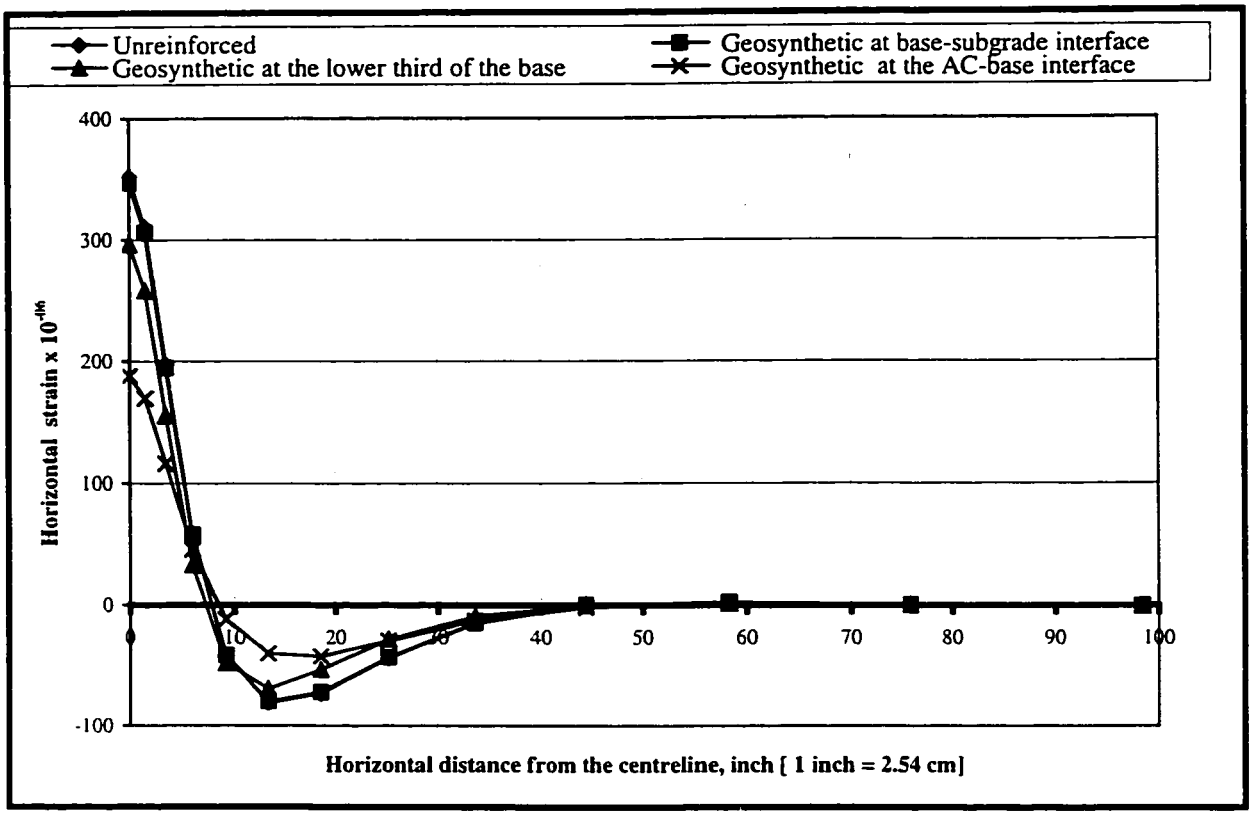

Figure (6.34) Horizontal strain at the bottom of AC layer at the peak load t=0.05s (Thin base system #3)

Table (6.34) The horizontal strain at the bottom of AC layer at peak load t=0.05s

Thin base system # 3				
Horizontal distance from the centreline (in) [1 inch = 2.54 cm]	Horizontal strain			
	Unreinforced	Geosynthetic at base-subgrade interface	Geosynthetic at the lower third of the base	Geosynthetic at the AC-base interface
98.40	-5.68943E-07	-5.72142E-07	-6.08536E-07	-3.8937E-07
75.89	2.93122E-07	2.87633E-07	1.73639E-07	3.68729E-07
58.26	2.35975E-06	2.32564E-06	1.56371E-06	1.40163E-06
44.44	3.2899E-07	2.77669E-07	-6.04613E-09	-1.5476E-06
33.62	-1.48027E-05	-1.46291E-05	-9.30986E-06	-1.25858E-05
25.14	-4.36557E-05	-4.29405E-05	-2.83971E-05	-2.92938E-05
18.49	-7.30766E-05	-7.19287E-05	-5.34382E-05	-4.22895E-05
13.28	-8.07496E-05	-7.96414E-05	-6.91121E-05	-3.98201E-05
9.20	-4.18585E-05	-4.13339E-05	-4.79224E-05	-1.15858E-05
6.01	5.89172E-05	5.81123E-05	3.30431E-05	4.57323E-05
3.50	0.000197328	0.000194585	0.000155283	0.000116138
1.54	0.000310581	0.00030616	0.000258367	0.000169488
0.00	0.000352098	0.000347046	0.000296393	0.000188086

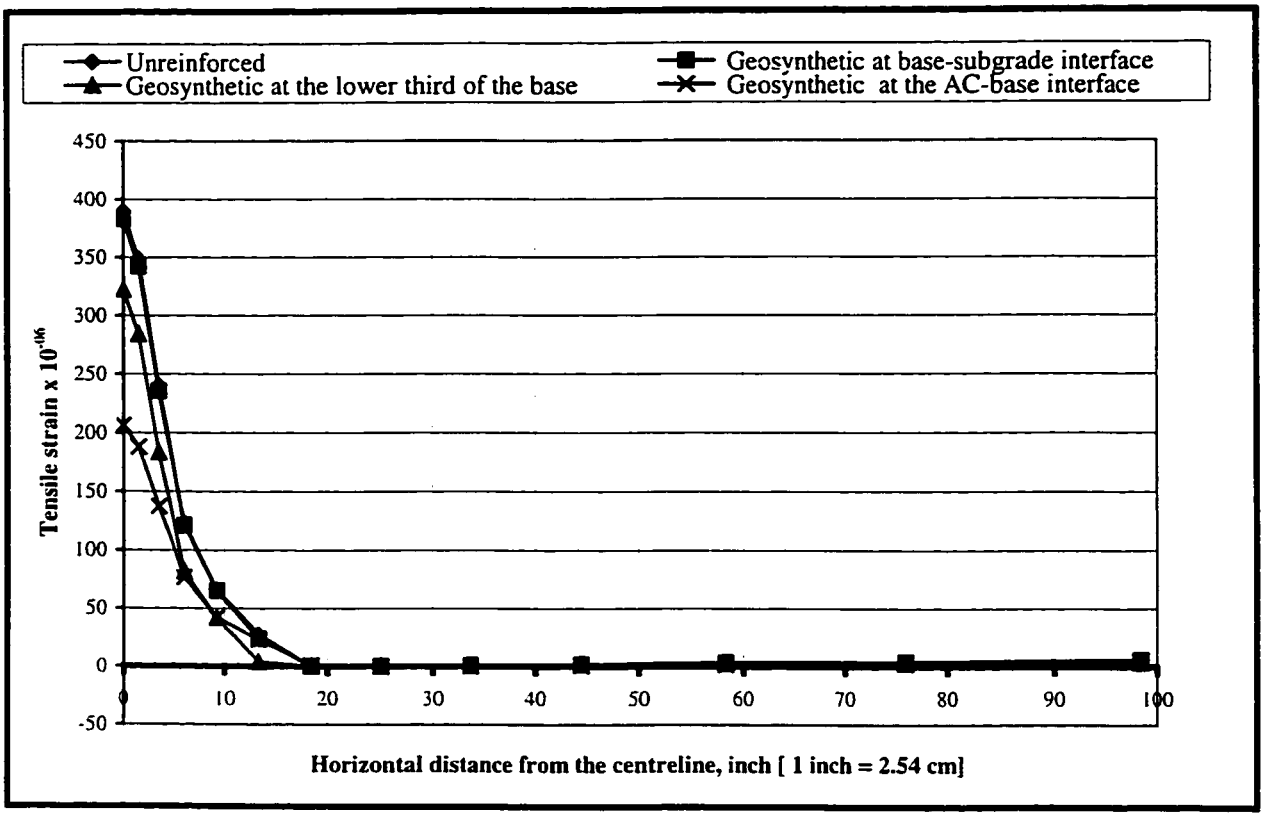

Figure (6.35) Envelope of the tensile strain at the bottom of AC layer
(Thin base system #3)

Table (6.35) Envelope of the tensile strain at the bottom of AC layer

Thin base system # 3				
Horizontal distance from the centreline (in) [1 inch = 2.54 cm]	Tensile strain			
	Unreinforced	Geosynthetic at base-subgrade interface	Geosynthetic at the lower third of the base	Geosynthetic at the AC-base interface
98.40	6.0003E-06	5.88901E-06	3.28822E-06	4.73136E-06
75.89	4.00165E-06	3.99479E-06	2.91054E-06	2.30031E-06
58.26	3.49428E-06	3.46784E-06	2.49774E-06	1.55259E-06
44.44	1.85259E-06	1.83734E-06	1.40063E-06	7.11796E-07
33.62	8.26236E-07	8.26186E-07	8.03334E-07	1.49535E-07
25.14	9.08292E-08	9.08292E-08	9.17181E-08	-1.50355E-11
18.49	9.32503E-10	9.32503E-10	9.81702E-10	8.2503E-07
13.28	2.73242E-05	2.37614E-05	3.57282E-06	2.29728E-05
9.20	6.61457E-05	6.49969E-05	4.18599E-05	4.20018E-05
6.01	0.000122839	0.000120824	8.16341E-05	7.66744E-05
3.50	0.000240135	0.000235501	0.000183324	0.000137444
1.54	0.000348649	0.000342119	0.00028385	0.000188219
0.00	0.000389741	0.000382599	0.0003221	0.00020647

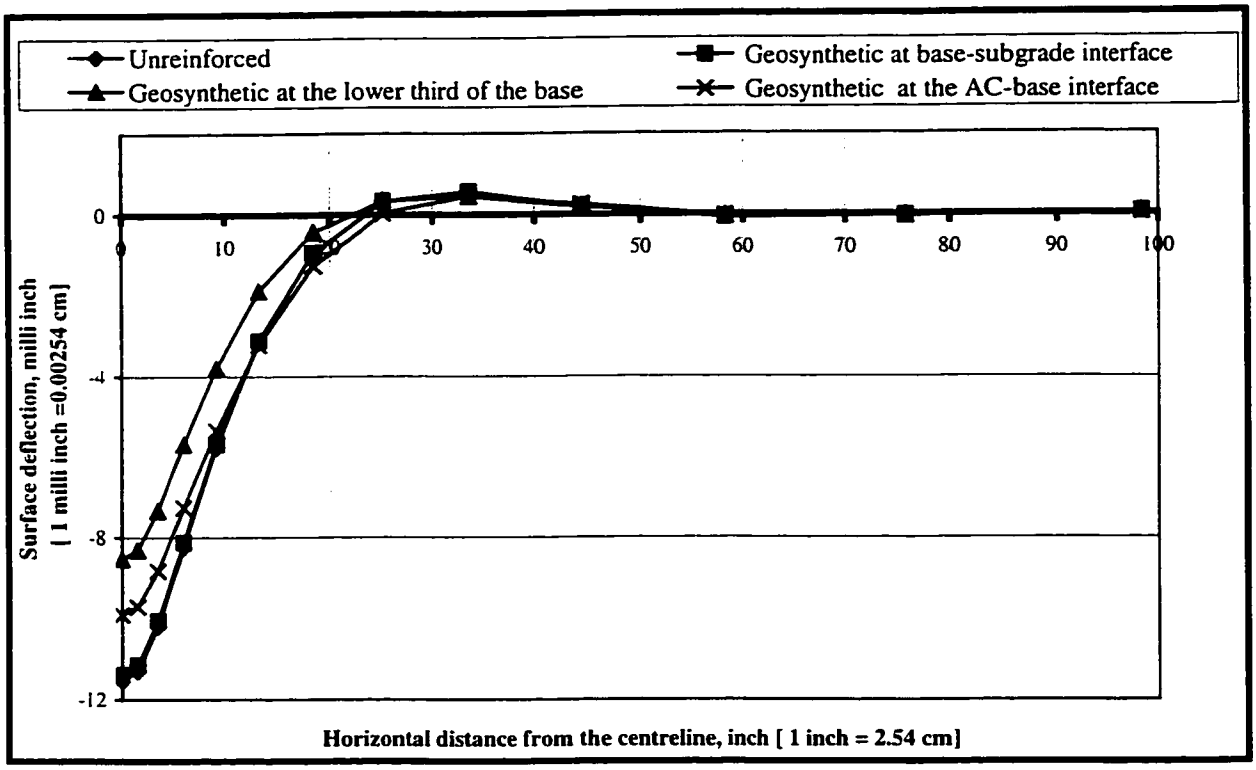

Figure (6.36) The vertical surface deflection across line 1-3 at the peak load t=0.05s (Thin base system #3)

Table (6.36) The vertical surface deflection across line 1-3 at the peak load t=0.05 s

Thin base system # 3				
Horizontal distance from the centreline (in) [1inch = 2.54 cm]	Surface deflection (inch) [1 inch = 2.54 cm]			
	Unreinforced	Geosynthetic at base-subgrade interface	Geosynthetic at the lower third of the base	Geosynthetic at the AC-base interface
0.00	-0.0115379	-0.0113815	-0.00852013	-0.00988742
1.54	-0.0112881	-0.0111351	-0.0083064	-0.00969662
3.50	-0.0101804	-0.0100402	-0.00734316	-0.00880998
6.01	-0.0082296	-0.00811329	-0.00570577	-0.00726971
9.20	-0.00578694	-0.00570226	-0.00379108	-0.00535572
13.28	-0.00315651	-0.00310647	-0.00187993	-0.003206
18.49	-0.000943297	-0.000925726	-0.000419671	-0.00125419
25.14	0.000334516	0.00033187	0.000341914	4.33611E-05
33.62	0.000566575	0.000562297	0.000450699	0.000465879
44.44	0.000209086	0.000209597	0.000190824	0.000257337
58.26	-6.54288E-05	-6.46347E-05	-3.81048E-05	-2.74219E-05
75.89	-2.58202E-05	-2.59648E-05	-2.78625E-05	-3.67522E-05
98.40	0.000049068	4.91422E-05	4.73781E-05	4.39209E-05

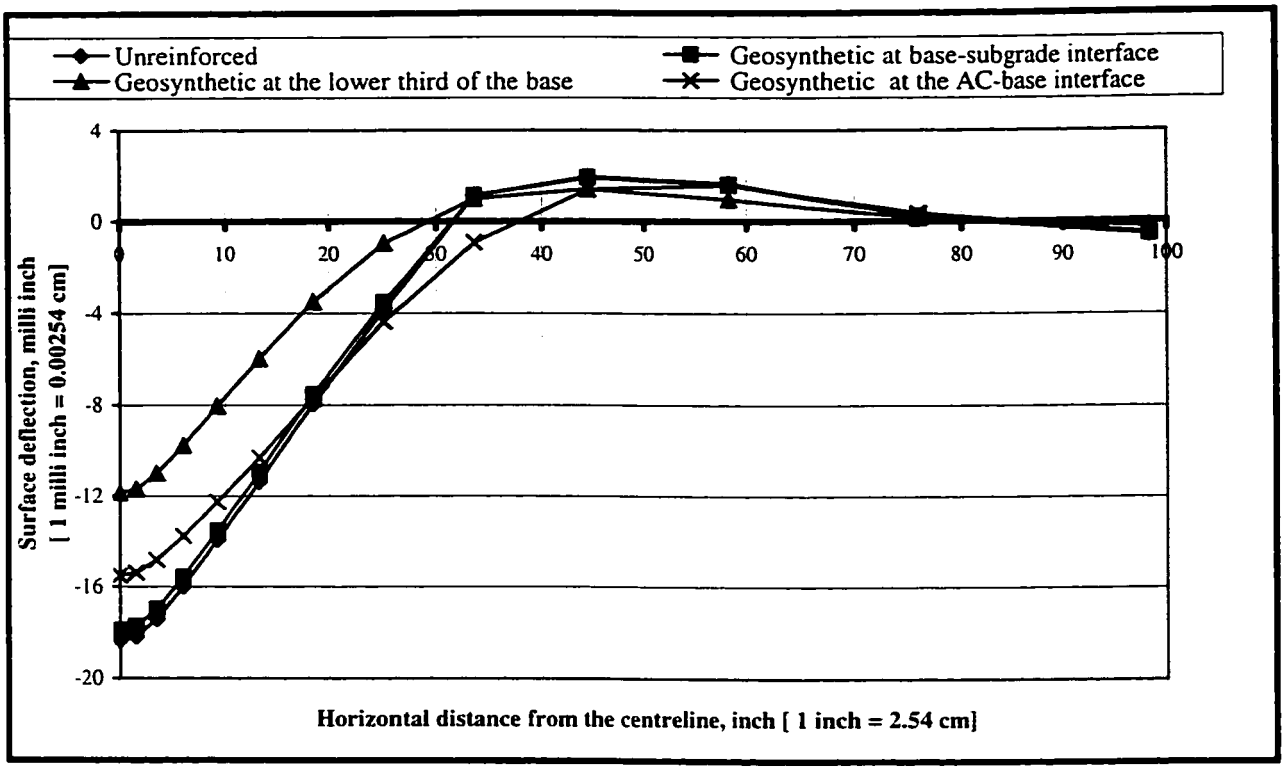

Figure (6.37) Envelope of the vertical surface deflection across line 1-3
(Thin base system #3)

Table (6.37) The envelope of vertical surface deflection across line 1-3

Thin base system # 3				
Horizontal distance from the centreline (in) [1 inch = 2.54 cm]	Surface deflection (inch) [1 inch = 2.54 cm]			
	Unreinforced	Geosynthetic at base-subgrade interface	Geosynthetic at the lower third of the base	Geosynthetic at the AC-base interface
0.00	-0.0183408	-0.01789	-0.011862	-0.01551
1.54	-0.0181558	-0.0177088	-0.011697	-0.0153765
3.50	-0.0173981	-0.0169645	-0.0110104	-0.0148085
6.01	-0.0159767	-0.0155632	-0.00976382	-0.01376
9.20	-0.0139353	-0.0135303	-0.00804418	-0.0122559
13.28	-0.0113605	-0.0109418	-0.00597181	-0.0103095
18.49	-0.00793952	-0.0075345	-0.00349801	-0.00769915
25.14	-0.00383061	-0.00352602	-0.000963956	-0.00434332
33.62	0.00113118	0.00111915	0.000998699	-0.000918954
44.44	0.00196295	0.00192062	0.00141256	0.00140054
58.26	0.00165755	0.00159995	0.000944934	0.00157687
75.89	0.000205147	0.000201679	0.000130013	0.000353436
98.40	-0.00056417	-0.000539717	-0.000234983	-0.000512232

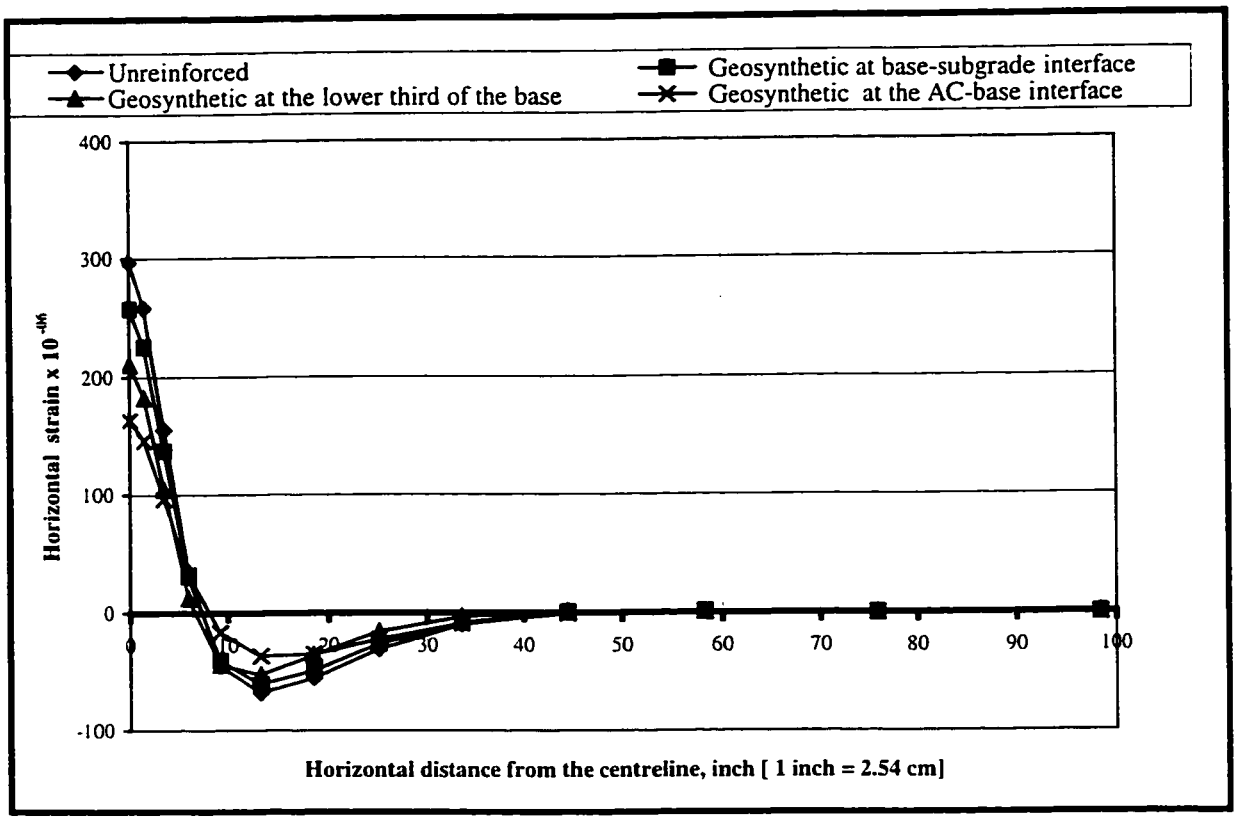

Figure (6.38)Horizontal strain at the bottom of AC layer at the peak load t=0.05s (Thin base system #4)

Table (6.38)The horizontal strain at the bottom of AC layer at peak load t=0.05s

Thin base system # 4				
Horizontal distance from the centreline (in) [1in = 2.54 cm]	Horizontal strain			
	Unreinforced	Geosynthetic at base-subgrade interface	Geosynthetic at the lower third of the base	Geosynthetic at the AC-base interface
98.40	-2.43915E-07	-3.31269E-07	-1.10325E-07	-2.07419E-07
75.89	-3.32971E-10	-4.08911E-08	3.39275E-08	1.06506E-07
58.26	1.23683E-06	1.20512E-06	7.60297E-07	9.26512E-07
44.44	3.97385E-07	6.77231E-07	1.10558E-06	-6.15199E-07
33.62	-9.60108E-06	-7.78275E-06	-3.04618E-06	-8.59547E-06
25.14	-3.04129E-05	-2.61465E-05	-1.55466E-05	-2.20336E-05
18.49	-5.47728E-05	-4.83674E-05	-0.000035193	-3.45138E-05
13.28	-6.73618E-05	-6.02725E-05	-0.000052104	-3.64008E-05
9.20	-4.46855E-05	-4.04769E-05	-4.40037E-05	-1.62346E-05
6.01	0.000034891	0.000030541	1.24113E-05	3.25449E-05
3.50	0.000155236	0.000137144	0.000104575	9.63917E-05
1.54	0.000258159	0.000225475	0.000182476	0.00014604
0.00	0.000296761	0.000257354	0.000210679	0.000163542

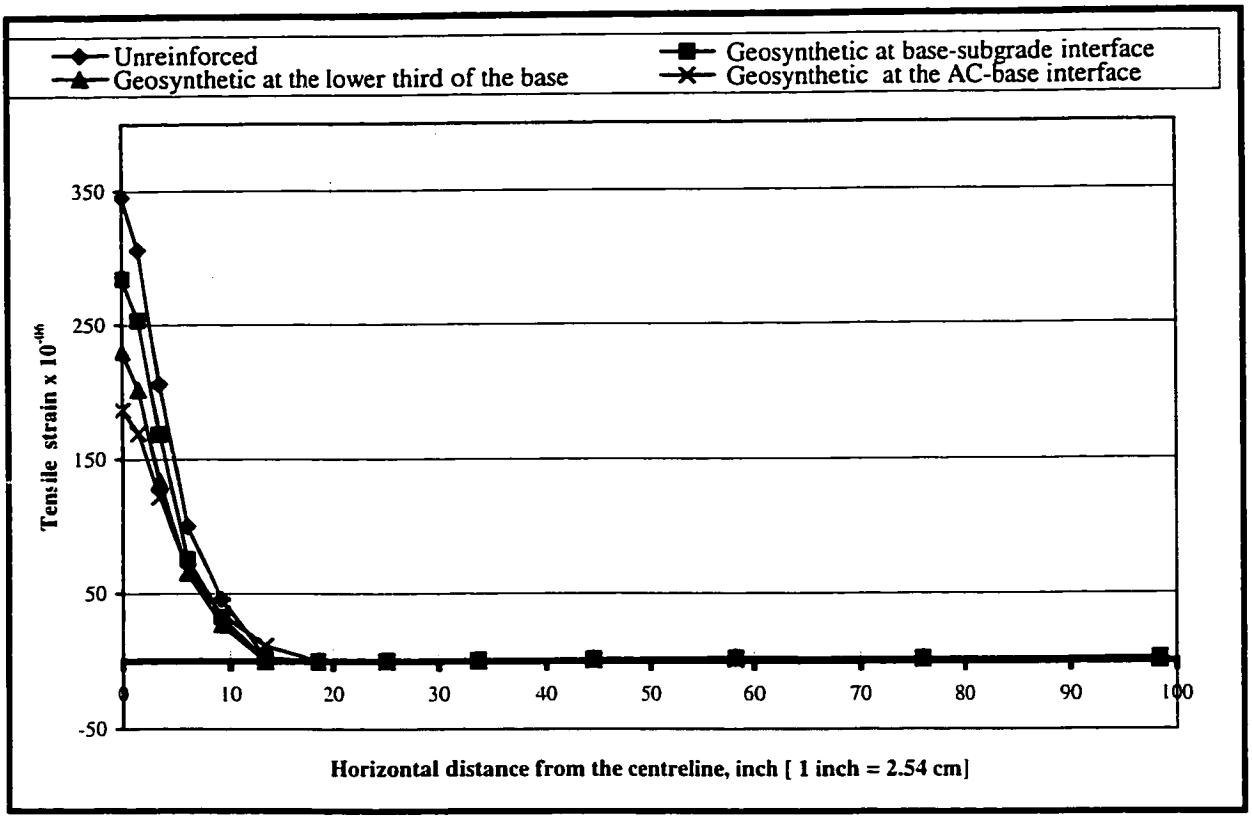

Figure (6.39)Envelope of the tensile strain at the bottom of AC layer
(Thin base system #4)

Table (6.39) Envelope of the tensile strain at the bottom of AC layer

Thin base system # 4				
Horizontal distance from the centreline (in) [1inch = 2.54 cm]	Tensile strain			
	Unreinforced	Geosynthetic at base-subgrade interface	Geosynthetic at the lower third of the base	Geosynthetic at the AC-base interface
98.40	1.97956E-06	2.11834E-06	6.21683E-07	2.21459E-06
75.89	1.67054E-06	1.83621E-06	1.55103E-06	1.21908E-06
58.26	1.97779E-06	2.08408E-06	2.27257E-06	1.1471E-06
44.44	1.31292E-06	1.22936E-06	1.10641E-06	6.58142E-07
33.62	5.79104E-07	5.58824E-07	3.45597E-07	1.35402E-07
25.14	5.88987E-08	5.88559E-08	5.16617E-08	-9.11415E-12
18.49	1.02494E-09	1.02494E-09	1.04024E-09	-4.07661E-10
13.28	2.58072E-06	3.32977E-07	-5.07879E-09	1.13625E-05
9.20	4.59307E-05	0.000032458	2.66882E-05	3.48003E-05
6.01	0.0001005	7.56965E-05	6.52475E-05	6.67486E-05
3.50	0.000205953	0.000168905	0.000133342	0.000122286
1.54	0.000306231	0.00025331	0.00020189	0.000169596
0.00	0.000345684	0.000284519	0.000229997	0.000186875

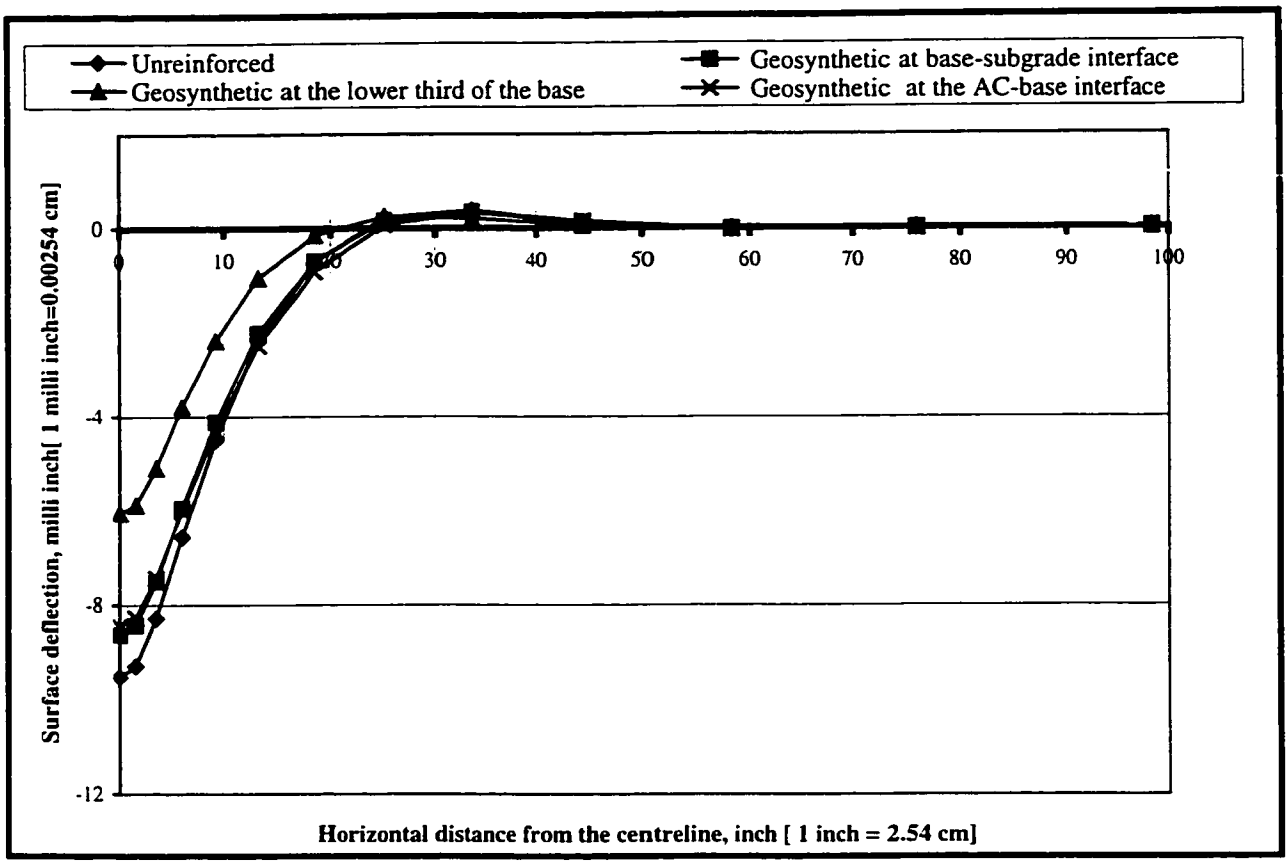

Figure (6.40)The vertical surface deflection across line 1-3 at the peak load t=0.05s (Thin base system #4)

Table (6.40) The vertical surface deflection across line 1-3 at the peak load t=0.05 s

Thin base system # 4				
Horizontal distance from the centreline (in) [1 inch = 2.54 cm]	Surface Deflection (inch) [1 inch = 2.54 cm]			
	Unreinforced	Geosynthetic at base-subgrade interface	Geosynthetic at the lower third of the base	Geosynthetic at the AC-base interface
0.00	-0.0095151	-0.00862628	-0.00605134	-0.00844805
1.54	-0.00928911	-0.00842551	-0.00588268	-0.00826837
3.50	-0.00827929	-0.00750885	-0.00509237	-0.00742877
6.01	-0.00655087	-0.00594937	-0.00379662	-0.00600211
9.20	-0.00449667	-0.00411328	-0.00238377	-0.00430533
13.28	-0.0023946	-0.00222611	-0.00105927	-0.00248637
18.49	-0.00070748	-0.000701751	-0.000143423	-0.000915013
25.14	0.000228916	0.000158734	0.000242708	7.21497E-05
33.62	0.00037796	0.000328912	0.000215997	0.000344956
44.44	0.000111688	0.000119529	5.31125E-05	0.000147035
58.26	-4.43772E-05	-3.21384E-05	-1.41517E-05	-3.38981E-05
75.89	-1.76478E-06	-4.60159E-06	-4.74515E-07	-9.76075E-06
98.40	1.61747E-05	1.66915E-05	8.82296E-06	1.90027E-05

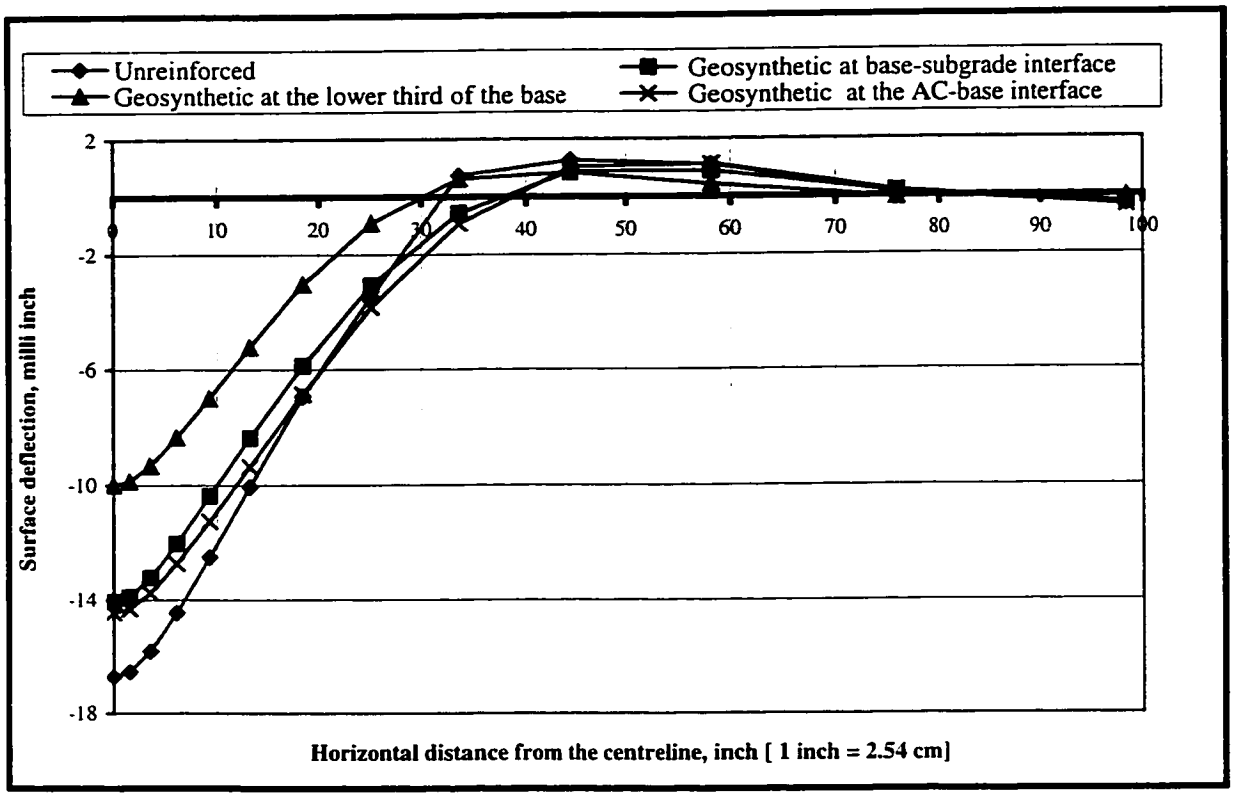

Figure (6.41)Envelope of the vertical surface deflection across line 1-3
(Thin base system #4)

Table (6.41)The envelope of vertical surface deflection across line 1-3

Thin base system # 4				
Horizontal distance from the centreline (in) [1inch = 2.54 cm]	Surface Deflection (inch) [1 inch = 2.54 cm]			
	Unreinforced	Geosynthetic at base-subgrade interface	Geosynthetic at the lower third of the base	Geosynthetic at the AC-base interface
0.00	-0.0167186	-0.0140587	-0.010001	-0.0144446
1.54	-0.0165383	-0.013896	-0.00986889	-0.0143125
3.50	-0.0158086	-0.0132333	-0.00932861	-0.0137536
6.01	-0.0144438	-0.0120281	-0.00835039	-0.0127221
9.20	-0.0125056	-0.0103703	-0.00699929	-0.0112485
13.28	-0.0100456	-0.00835983	-0.00522878	-0.00935485
18.49	-0.00692565	-0.00588	-0.00304052	-0.00684418
25.14	-0.00346382	-0.00307154	-0.000903635	-0.00383688
33.62	0.000740995	-0.000554425	0.000625566	-0.000912875
44.44	0.00127635	0.000894451	0.000845598	0.00104364
58.26	0.00110903	0.000880376	0.000427358	0.00112901
75.89	0.000100458	0.000160698	-4.05829E-05	0.000184371
98.40	-0.000328363	-0.00022921	-5.60985E-05	-0.000350419

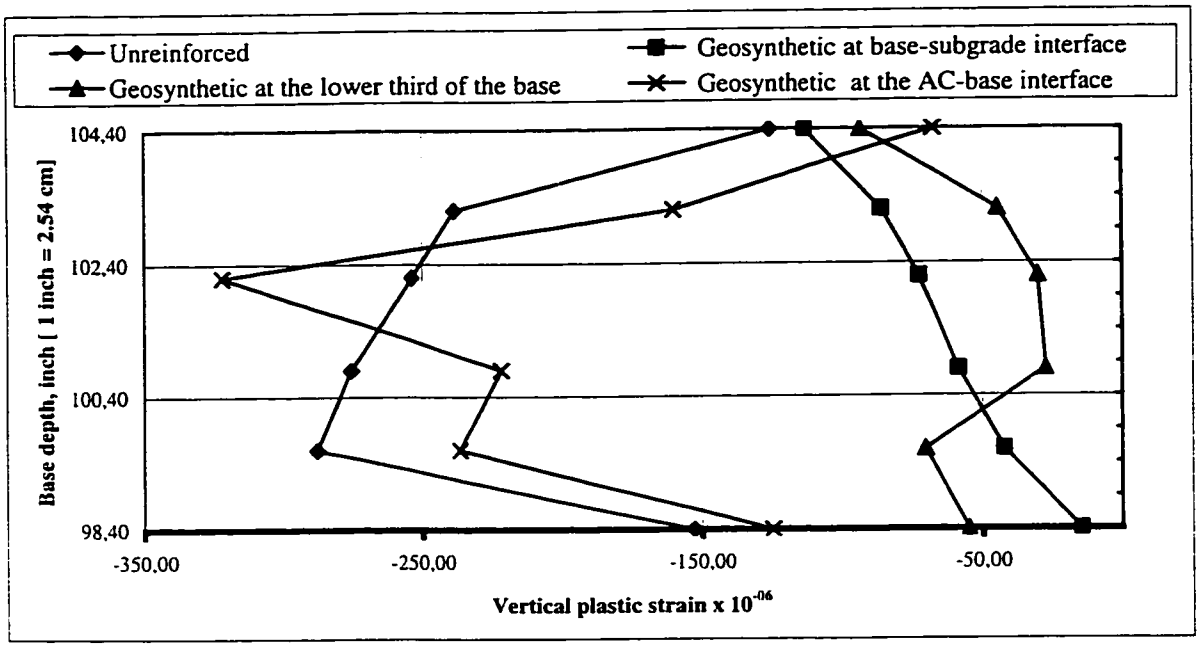

Figure (6.42) Vertical plastic micro strain across the base depth line 4-6 shown in Figure(6.1) taken at peak load t=0.05s
(Thin base system #2)

Table (6 .42) The vertical plastic strain across the base depth line 4-6 shown in Figure(6.1) taken at peak load t=0.05s

Thin base system # 2				
Z coordinate(in) of the nodes of base depth line 2-8 shown in Figure (6.1) [1 inch = 2.54 cm]	Vertical plastic strain			
	Unreinforced	Geosynthetic at base-subgrade interface	Geosynthetic at the lower third of the base	Geosynthetic at the AC-base interface
104.40	-1.24929E-04	-1.12216E-04	-9.25110E-05	-6.71326E-05
103.20	-2.38175E-04	-8.52496E-05	-4.47214E-05	-1.59859E-04
102.20	-2.54001E-04	-7.22285E-05	-3.03804E-05	-3.21580E-04
100.80	-2.75696E-04	-5.86400E-05	-2.76231E-05	-2.21293E-04
99.60	-2.87362E-04	-4.24912E-05	-7.02299E-05	-2.36020E-04
98.40	-1.52708E-04	-1.47240E-05	-5.49221E-05	-1.24260E-04

About the lateral confinement function of the geosynthetic grid to the base particles

In the following analyses, the lateral restraining function of the geosynthetic grid is tested for one system only.

This function of the geosynthetic which restrains the particles of the base from laterally spreading or moving a way is simulated to give the maximum effect. The maximum effect of the geosynthetic for preventing the lateral movement was simulated by preventing all the lateral motions of the base course aggregate at the level where would be in contact with the geosynthetic (Perkins, 2001). This is done by restraining the motion in x and y directions at that level

In other words, the geosynthetic is being assigned an infinite stiffness in these directions

The thick base system 2 is chosen, because, as reported in the literature, the confinement effect may be more predominant than the membrane effect in the case of thick base system. The results are reported in Tables (6.43) to (6.49) and plotted in Figures (6.43) to (6.48)

Table(6.43) Results of analyses testing the perfect lateral confinement of the thick system 2 base particles at the level of the geosynthetic grid with respect to the adopted comparison criteria at the locations highlighted in Figure (6.1)

System	Geosynthetic location	Maximum ε_t (at element A)	Maximum Δ_z (at node 1) (1 in = 2.54 cm)	Maximum ε_c (at element C)	Max ε_t Decrease %	Max Δ_z Decrease %	Max ε_c Decrease %
AC	N/A	2.31817E-04	-1.31331E-02	-2.17556E-03	-	-	-
Strong Base	Bottom of base	2.18330e-04	-1.09942E-02	-1.84296E-03	6	16	15
Clay Subgrade	Lower third of base	2.14780E-04	-1.11825E-02	-1.99669E-03	10	20	13

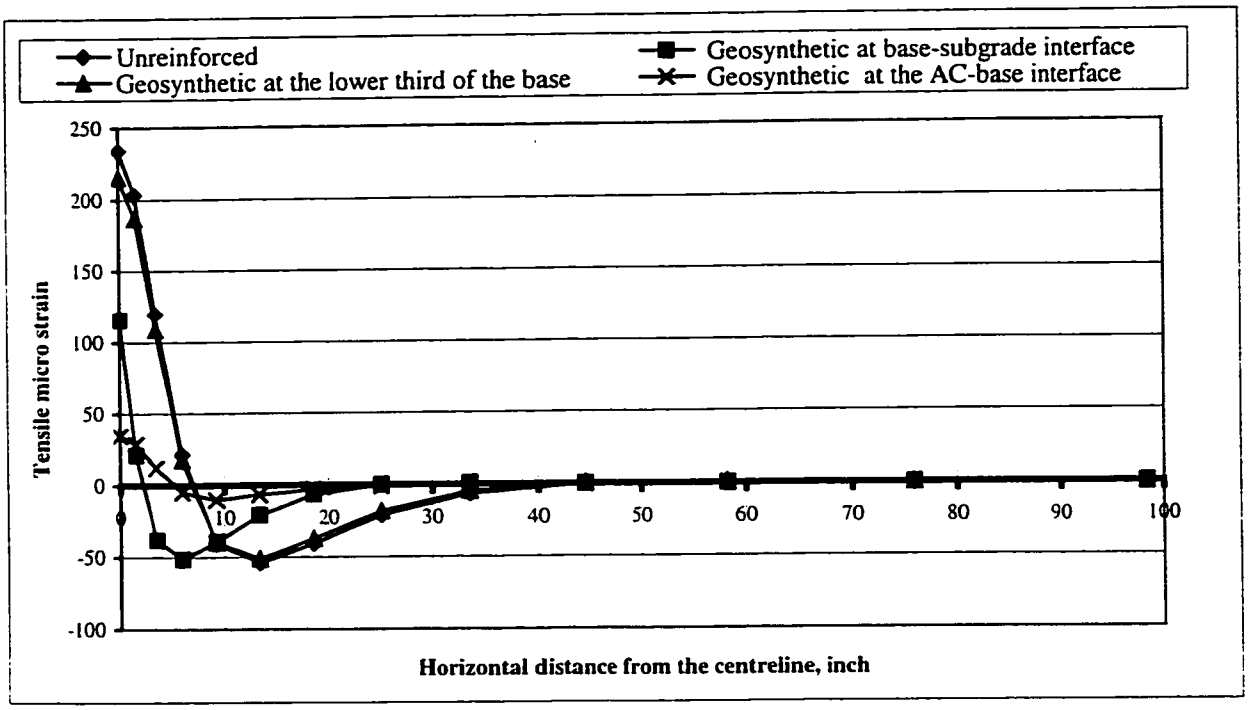

Figure(6.43) Horizontal strain at the bottom of AC layer at the peak load t=0.05s with perfect lateral confinement of the base particles at the level of the geosynthetic (Thick base system #2)

Table (6.44) The horizontal strain at the bottom of AC layer at peak load t=0.05s with perfect lateral confinement of the base particles at the level of the geosynthetic

Thick base system # 2				
Horizontal distance from the centreline (in) (1 in = 2.54 cm)	Horizontal strain			
	Unreinforced	Geosynthetic at base-subgrade interface	Geosynthetic at the lower third of the base	Geosynthetic at the AC-base interface
98.40	-2.68269E-07	-1.47E-09	-2.59E-07	-1.32E-08
75.89	-1.13232E-08	-1.47E-09	4.51E-08	4.77E-09
58.26	8.26817E-07	-3.04E-07	9.46E-07	8.98E-08
44.44	2.46974E-07	1.03E-08	6.94E-07	1.62E-07
33.62	-6.19199E-06	8.84E-07	-4.74E-06	-4.18E-08
25.14	-2.08820E-05	1.34E-07	-1.82E-05	-8.87E-07
18.49	-4.05485E-05	-6.47E-06	-3.73E-05	-2.88E-06
13.28	-5.39924E-05	-2.07E-05	-5.12E-05	-6.54E-06
9.20	-4.05014E-05	-3.92E-05	-3.99E-05	-9.97E-06
6.01	2.13664E-05	-5.14E-05	1.73E-05	-4.96E-06
3.50	1.19457E-04	-3.81E-05	1.09E-04	1.22E-05
1.54	2.03166E-04	2.11E-05	1.87E-04	2.89E-05
0.00	2.33973E-04	1.15E-04	2.15E-04	3.47E-05

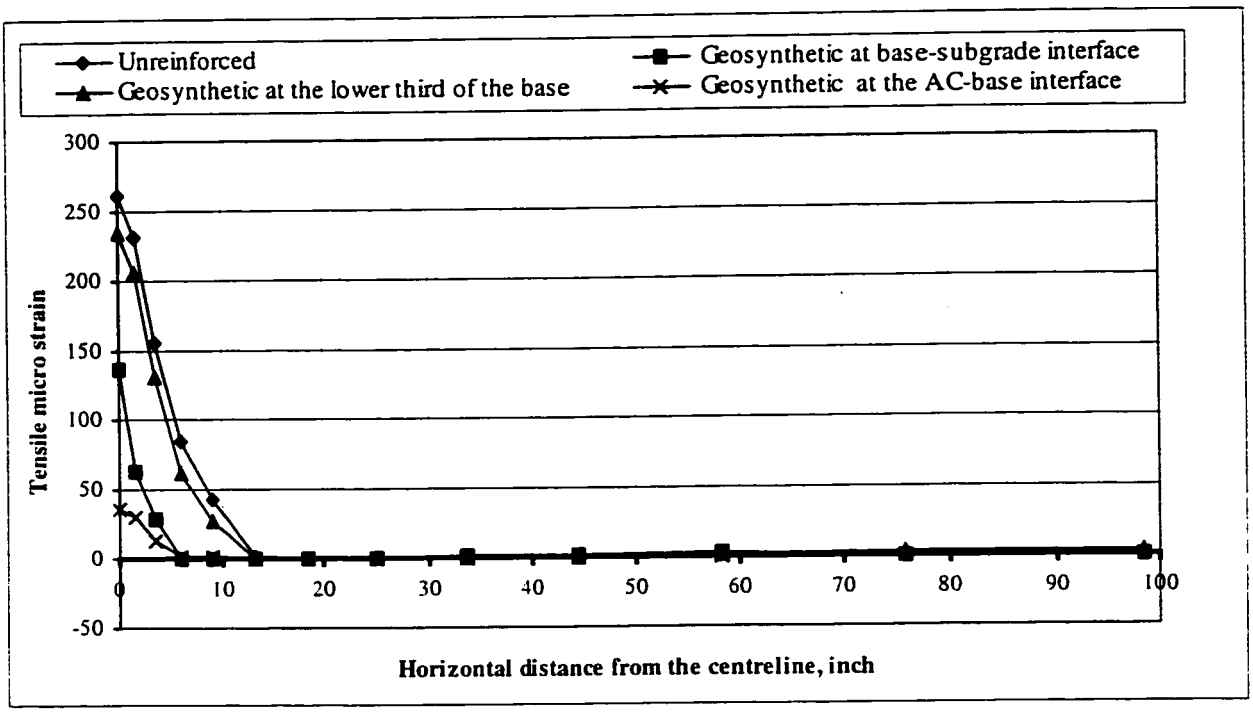

Figure(6.44) Envelope of the tensile strain at the bottom of AC layer with perfect lateral confinement of the base particles at the level of the geosynthetic
(Thick base system #2)

Table (6.45) Envelope of the tensile strain at the bottom of AC layer with perfect lateral confinement of the base particles at the level of the geosynthetic

Thick base system # 2				
Horizontal distance from the centreline (in) (1 in = 2.54 cm)	Tensile strain			
	Unreinforced	Geosynthetic at base-subgrade interface	Geosynthetic at the lower third of the base	Geosynthetic at the AC-base interface
98.40	1.73186E-08	8.32E-11	2.36E-06	6.82E-08
75.89	3.95060E-07	8.32E-11	2.56E-06	9.82E-08
58.26	1.11526E-06	2.37E-06	2.33E-06	1.78E-07
44.44	8.50707E-07	1.87E-06	8.27E-07	1.65E-07
33.62	5.00209E-07	1.61E-06	4.97E-07	1.49E-07
25.14	5.81535E-08	8.25E-07	5.81E-08	1.13E-07
18.49	1.04080E-09	4.90E-07	1.04E-09	1.87E-08
13.28	1.32704E-06	5.44E-08	-5.08E-09	4.95E-08
9.20	4.25659E-05	9.46E-10	2.69E-05	1.09E-06
6.01	8.52527E-05	-5.27E-09	6.22E-05	2.22E-06
3.50	1.54714E-04	2.86E-05	1.30E-04	1.35E-05
1.54	2.31024E-04	6.32E-05	2.06E-04	3.02E-05
0.00	2.61478E-04	1.37E-04	2.35E-04	3.60E-05

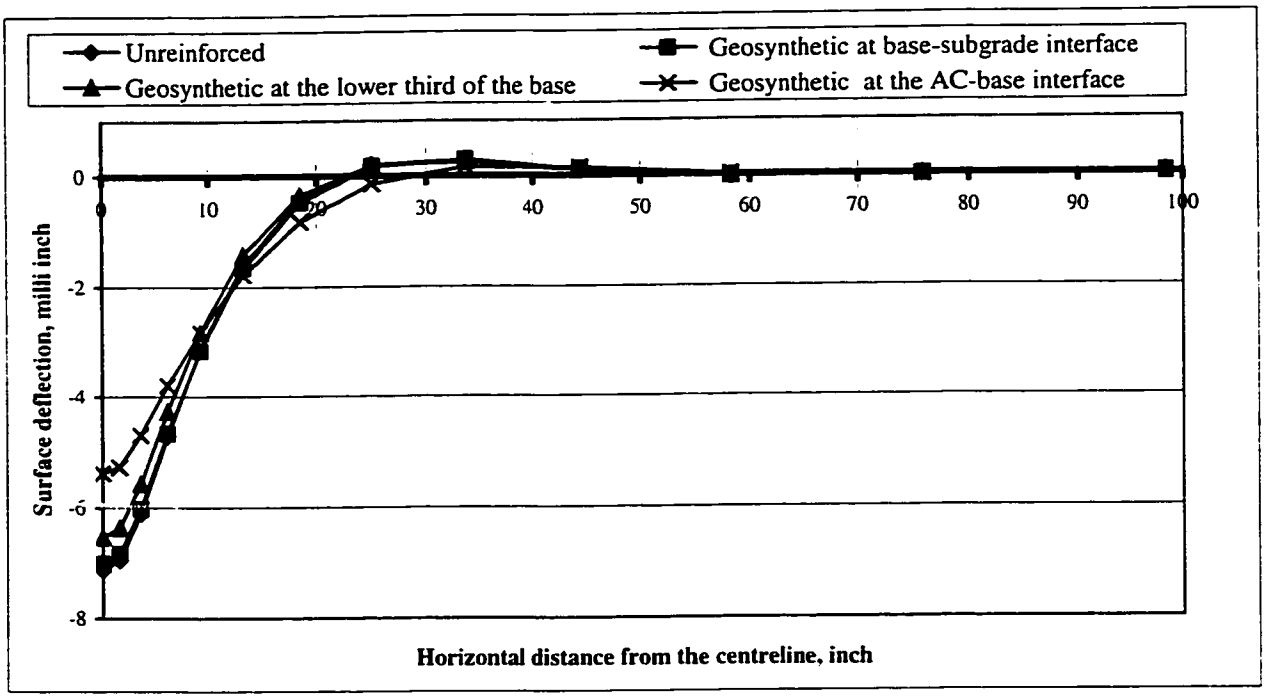

Figure(6.45) The vertical surface deflection at the bottom of AC layer at the peak load t=0.05s with perfect lateral confinement of the base particles at the level of the geosynthetic
(Thick base system #2)

Table (6.46) The vertical surface deflection across line 1-1 at the peak load t=0.05 s with perfect lateral confinement of the base particles at the level of the geosynthetic

Thick base system # 2				
Horizontal distance from the centreline (in) [1 inch = 2.54 cm]	Surface deflection (inch) [1 inch = 2.54 cm]			
	Unreinforced	Geosynthetic at base-subgrade interface	Geosynthetic at the lower third of the base	Geosynthetic at the AC-base interface
0.00	-7.12615E-03	-7.01E-03	-6.54E-03	-5.39E-03
1.54	-6.94565E-03	-6.84E-03	-6.37E-03	-5.28E-03
3.50	-6.10968E-03	-6.02E-03	-5.58E-03	-4.70E-03
6.01	-4.72060E-03	-4.68E-03	-4.28E-03	-3.80E-03
9.20	-3.15418E-03	-3.17E-03	-2.83E-03	-2.83E-03
13.28	-1.60704E-03	-1.66E-03	-1.41E-03	-1.78E-03
18.49	-4.20636E-04	-4.75E-04	-3.48E-04	-8.24E-04
25.14	2.02125E-04	1.73E-04	1.92E-04	-1.39E-04
33.62	2.87561E-04	2.90E-04	2.56E-04	1.64E-04
44.44	9.99434E-05	1.13E-04	9.23E-05	1.40E-04
58.26	-2.56702E-05	-2.48E-05	-2.16E-05	1.38E-05
75.89	-4.96654E-06	-7.90E-06	-5.85E-06	-1.37E-05
98.40	1.60783E-05	1.88E-05	1.60E-05	1.10E-05

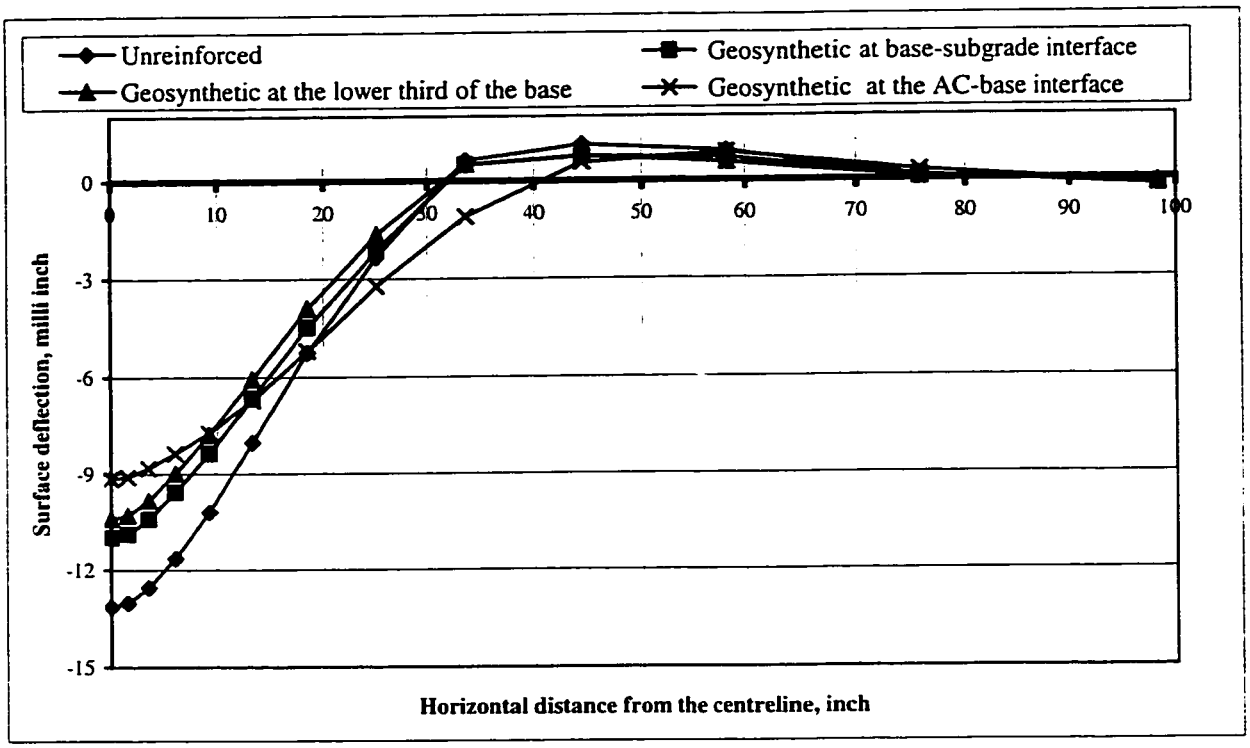

Figure(6.46) Envelope of vertical surface deflection at the bottom of AC layer with perfect lateral confinement of the base particles at the level of the geosynthetic (Thick base system #2)

Table (6.47) The envelope of vertical surface deflection across line 1-1 with perfect lateral confinement of the base particles at the level of the geosynthetic

Thick base system # 2				
Horizontal distance from the centreline (in) [1 inch = 2.54 cm]	Surface deflection (inch) [1 inch = 2.54 cm]			
	Unreinforced	Geosynthetic at base-subgrade interface	Geosynthetic at the lower third of the base	Geosynthetic at the AC-base interface
0.00	-1.31331E-02	-1.10E-02	-1.04E-02	-9.15E-03
1.54	-1.30137E-02	-1.09E-02	-1.03E-02	-9.09E-03
3.50	-1.25353E-02	-1.04E-02	-9.84E-03	-8.82E-03
6.01	-1.16439E-02	-9.57E-03	-8.99E-03	-8.36E-03
9.20	-1.02011E-02	-8.36E-03	-7.79E-03	-7.72E-03
13.28	-8.02766E-03	-6.66E-03	-6.07E-03	-6.72E-03
18.49	-5.25104E-03	-4.47E-03	-3.90E-03	-5.20E-03
25.14	-2.33071E-03	-2.15E-03	-1.65E-03	-3.22E-03
33.62	6.30986E-04	5.02E-04	5.16E-04	-1.11E-03
44.44	1.13115E-03	7.65E-04	7.69E-04	5.72E-04
58.26	9.05561E-04	7.06E-04	5.66E-04	8.67E-04
75.89	1.19570E-04	1.17E-04	5.77E-05	2.78E-04
98.40	-2.03899E-04	-1.89E-04	-1.33E-04	-1.95E-04

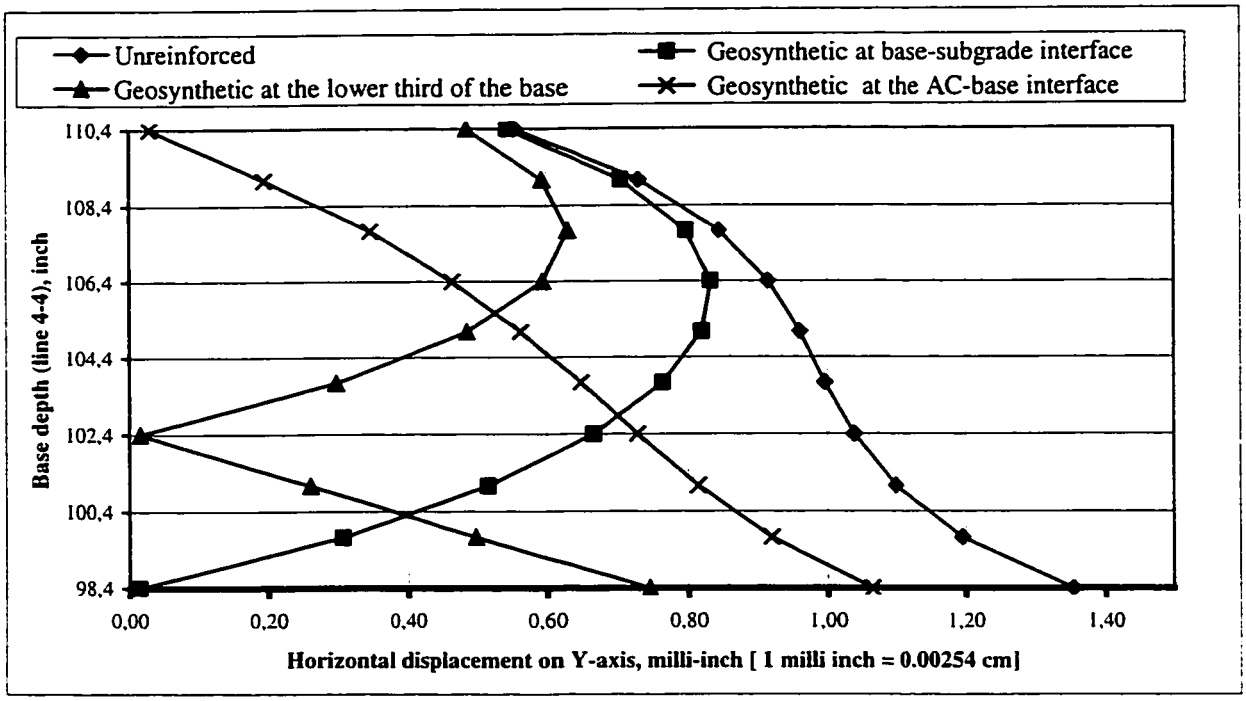

Figure (6.47) The horizontal displacement on Y axis across the base depth line 2-8 at the peak load t=0.05s with perfect lateral confinement of the base particles at the level of the geosynthetic
(Thick base system #2)

Table (6.48) The horizontal displacement on Y axis across the Base depth line 2-8 at the peak load t=0.05s with perfect lateral confinement of the base particles at the level of the geosynthetic

Thick base system # 2				
Z co-ordinates of Base depth line 4-4(in)) [1 inch = 2.54 cm]	Horizontal displacement (inch) [1 inch = 2.54 cm]			
	Unreinforced	Geosynthetic at base-subgrade interface	Geosynthetic at the lower third of the base	Geosynthetic at the AC-base interface
110.40	5.55E-04	5.45E-04	4.86E-04	3.02E-05
109.07	7.30E-04	7.04E-04	5.93E-04	1.95E-04
107.73	8.44E-04	7.97E-04	6.29E-04	3.45E-04
106.40	9.15E-04	8.32E-04	5.94E-04	4.65E-04
105.07	9.61E-04	8.19E-04	4.87E-04	5.63E-04
103.73	9.96E-04	7.63E-04	2.97E-04	6.47E-04
102.40	1.04E-03	6.65E-04	1.61E-05	7.27E-04
101.07	1.10E-03	5.17E-04	2.60E-04	8.14E-04
99.73	1.20E-03	3.05E-04	4.99E-04	9.20E-04
98.40	1.35E-03	1.50E-05	7.44E-04	1.06E-03

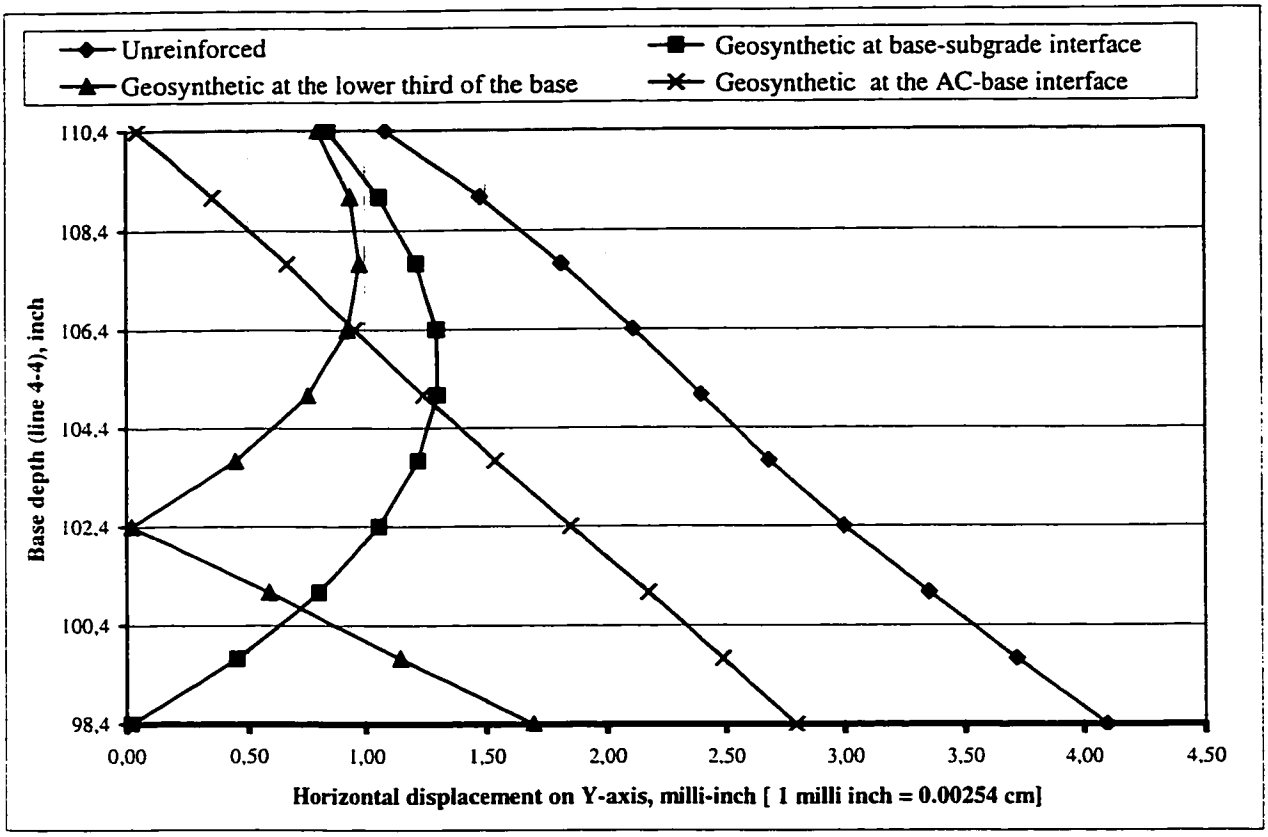

Figure (6.48) Envelope of The horizontal displacement on Y axis across the Base depth line 2-8 with perfect lateral confinement of the base particles at the level of the geosynthetic
(Thick base system #2)

Table (6.49) The envelope The horizontal displacement on Y axis across the Base depth line 2-8 with perfect lateral confinement of the base particles at the level of the geosynthetic

Thick base system # 2				
Z co-ordinates of Base depth line 4-4(in)	Horizontal displacement (inch) [1 inch = 2.54 cm]			
	Unreinforced	Geosynthetic at base-subgrade interface	Geosynthetic at the lower third of the base	Geosynthetic at the AC-base interface
110.40	1.09E-03	8.41E-04	7.96E-04	4.58E-05
109.07	1.48E-03	1.06E-03	9.36E-04	3.54E-04
107.73	1.81E-03	1.22E-03	9.75E-04	6.63E-04
106.40	2.11E-03	1.30E-03	9.23E-04	9.56E-04
105.07	2.40E-03	1.30E-03	7.52E-04	1.24E-03
103.73	2.68E-03	1.22E-03	4.47E-04	1.54E-03
102.40	3.00E-03	1.06E-03	2.13E-05	1.85E-03
101.07	3.35E-03	8.00E-04	5.85E-04	2.17E-03
99.73	3.72E-03	4.52E-04	1.15E-03	2.49E-03
98.40	4.10E-03	1.91E-05	1.70E-03	2.80E-03

Investigating the effect of the elastic behavior of the foundation on the performance of the reinforcement

Whether the elastic behavior of the foundation (base and subgrade) is influenced by effective location of the geosynthetic or not, is tested in following analyses. The thick base system # 2 is also chosen for this purpose, which is achieved through comparing the results of nonlinear foundation with the results of linear foundation The tables and the graphs below show the results obtained from the linear analyses.

Table(6.50) Results of analyses conducted on linear system to explore if the pavement foundation materials linearity affects choosing the geosynthetic best location with respect to the adopted comparison criteria at the locations highlighted in Figure (6.1)

System	Geosynthetic location	Maximum ε_t (at element A)	Maximum Δ_z (in) (at node 1) [1 in =2.54 cm]	Maximum ε_c (at element C)	Max ε_t Decrease %	Max Δ_z Decrease %	Max ε_c Decrease %
AC	N/A	1.73882E-04	-1.05767E-03	-9.20375E-03	-	-	-
Strong Base	Bottom of base	1.68499E-04	-8.57299E-04	-8.13125E-03	3	11	19
	Lower third of base	1.69587E-04	-1.01909E-03	-8.60370E-03	3	6	3
Clay Subgrade	Top of the base	1.02009E-04	-1.03235E-03	-8.84137E-03	40	4	2

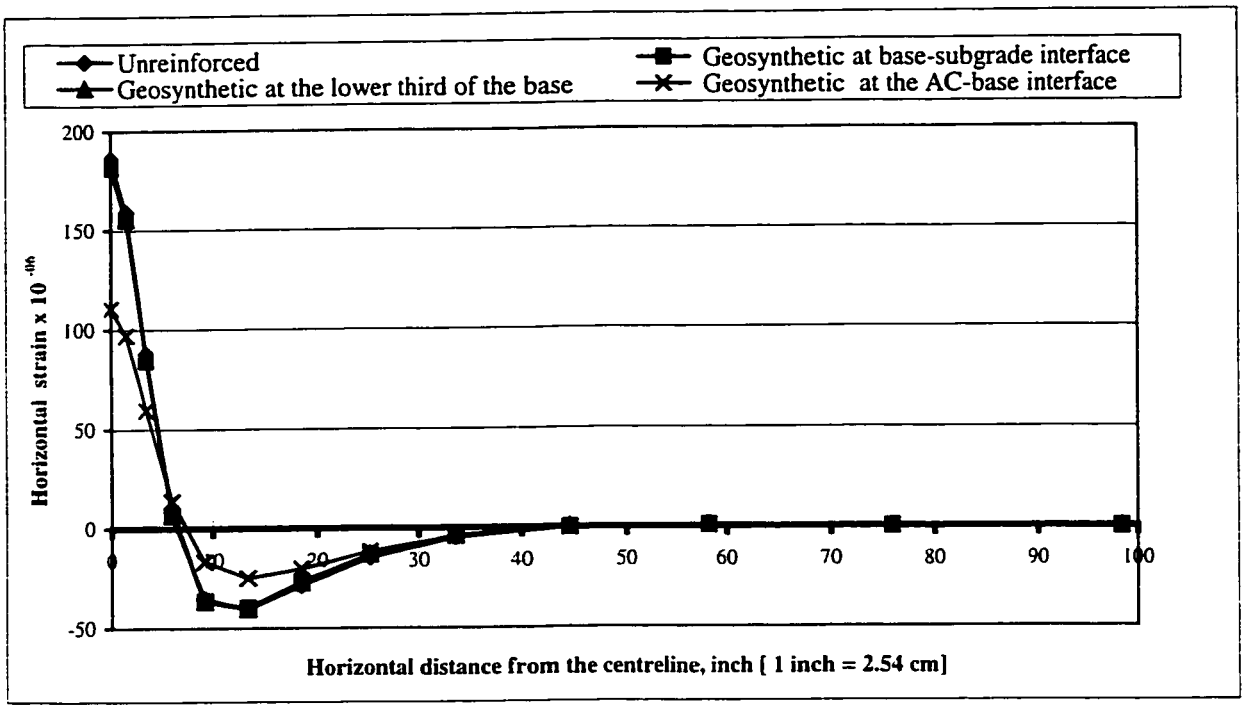

Figure (6.49) Horizontal strain at the bottom of AC layer at the peak load t=0.05s (Thick base system 2 with the elastic analysis)

Table (6.51)The horizontal strain at the bottom of AC layer at peak load t=0.05s with the elastic foundation

Thick base system # 2				
Horizontal distance from the centreline (in) [1in = 2.54 cm]	horizontal strain			
	Unreinforced	Geosynthetic at base-subgrade interface	Geosynthetic at the lower third of the base	Geosynthetic at the AC-base interface
98.40	-1.62E-07	-1.78E-07	-1.65E-07	-1.12E-07
75.89	1.74E-07	1.78E-07	1.22E-07	1.60E-07
58.26	8.62E-07	7.82E-07	7.42E-07	6.38E-07
44.44	1.08E-07	-9.69E-10	3.74E-07	-1.92E-07
33.62	-4.80E-06	-4.22E-06	-3.66E-06	-4.29E-06
25.14	-1.49E-05	-1.31E-05	-1.32E-05	-1.18E-05
18.49	-2.86E-05	-2.66E-05	-2.74E-05	-2.03E-05
13.28	-4.05E-05	-3.97E-05	-4.06E-05	-2.50E-05
9.20	-3.54E-05	-3.64E-05	-3.69E-05	-1.68E-05
6.01	8.92E-06	6.17E-06	6.25E-06	1.37E-05
3.50	8.82E-05	8.43E-05	8.47E-05	5.96E-05
1.54	1.59E-04	1.55E-04	1.55E-04	9.72E-05
0.00	1.86E-04	1.81E-04	1.82E-04	1.11E-04

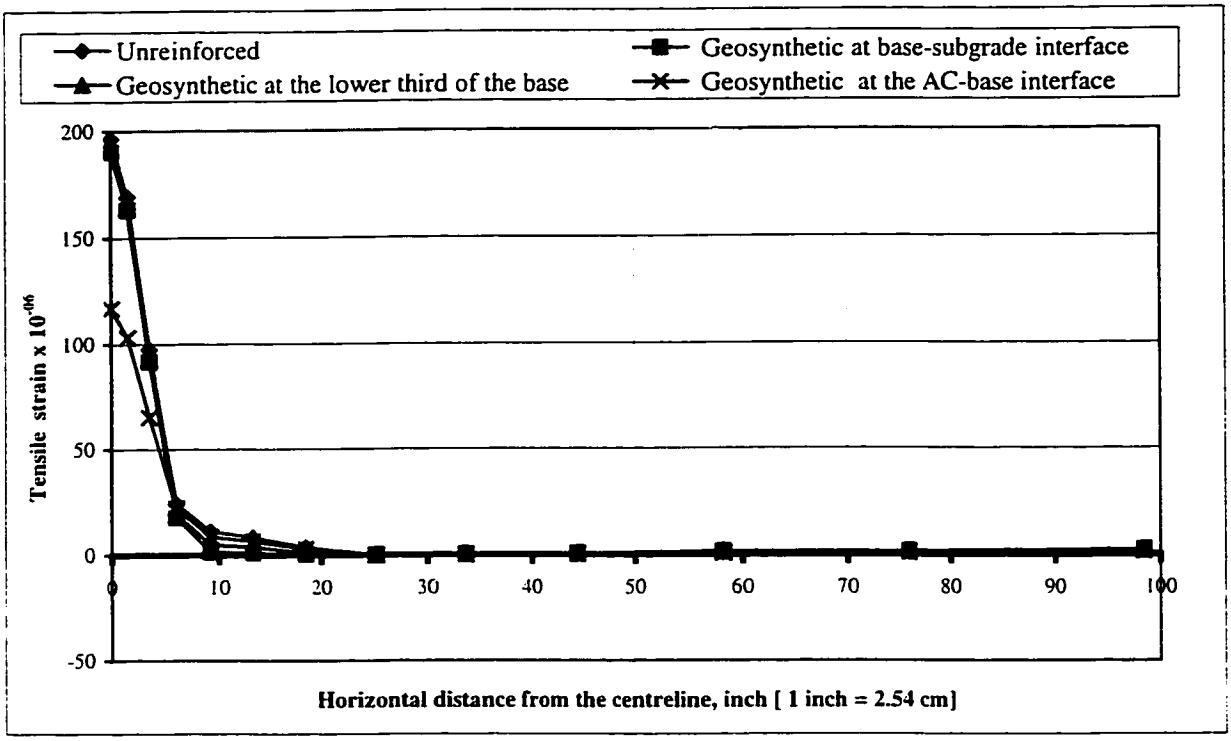

Figure (6.50) Envelope of the tensile strain at the bottom of AC layer
(Thick base system #2 with the elastic analysis)

Table (6.52)Envelope of the tensile strain at the bottom of AC layer with the elastic foundation

Thick base system # 2				
Horizontal distance from the centreline (in) [1 in = 2.54 cm]	Tensile strain			
	Unreinforced	Geosynthetic at base-subgrade interface	Geosynthetic at the lower third of the base	Geosynthetic at the AC-base interface
98.40	1.97E-06	2.26E-06	1.95E-06	1.55E-06
75.89	1.20E-06	1.52E-06	1.41E-06	9.16E-07
58.26	1.00E-06	1.32E-06	1.47E-06	7.03E-07
44.44	5.87E-07	5.80E-07	5.20E-07	2.90E-07
33.62	3.52E-07	3.52E-07	3.51E-07	6.75E-08
25.14	4.72E-08	4.72E-08	4.72E-08	9.80E-12
18.49	3.63E-06	3.40E-07	1.19E-06	2.93E-06
13.28	8.32E-06	1.11E-06	3.75E-06	6.50E-06
9.20	1.13E-05	1.55E-06	5.01E-06	8.82E-06
6.01	2.40E-05	1.78E-05	1.92E-05	2.22E-05
3.50	9.76E-05	9.17E-05	9.31E-05	6.54E-05
1.54	1.69E-04	1.63E-04	1.65E-04	1.03E-04
0.00	1.97E-04	1.90E-04	1.92E-04	1.17E-04

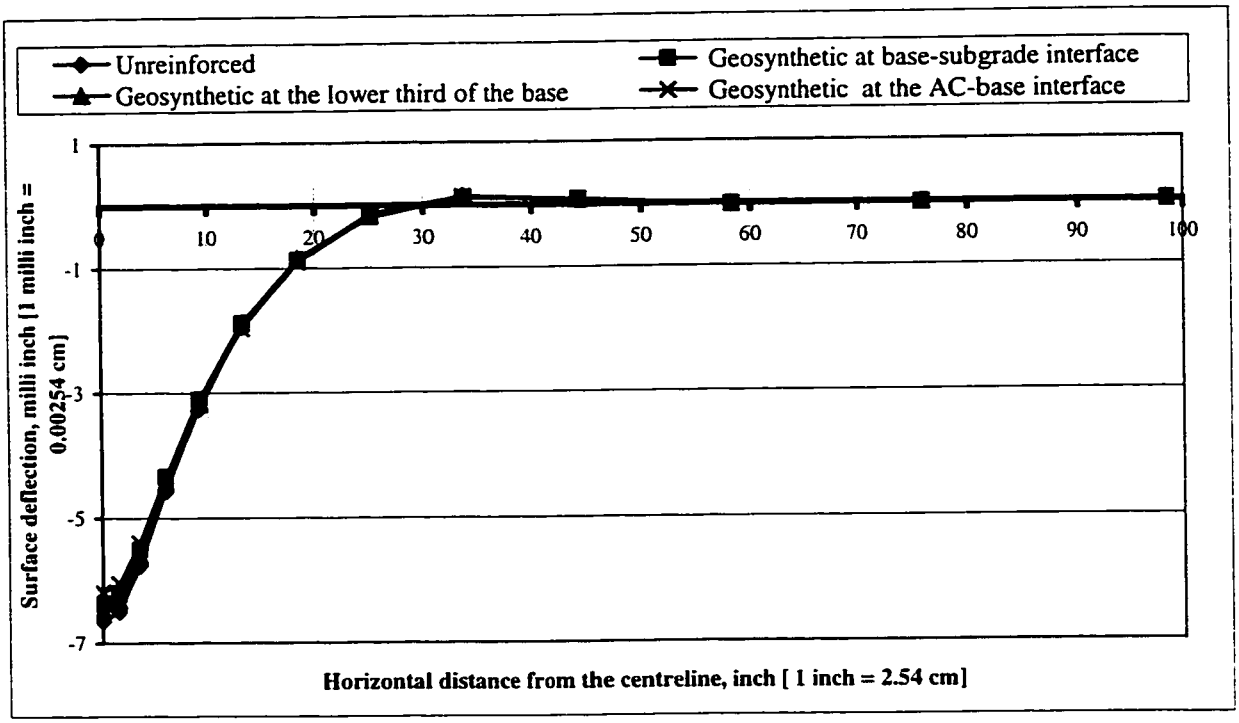

Figure (6.51) The vertical surface deflection at the bottom of AC layer at the peak load t=0.05s (Thick base system 2 with the elastic analysis)

Table (6.53) The surface deflection across line 1-1 at the peak load t=0.05 s with the elastic foundation

Thick base system # 2				
Horizontal distance from the centreline (in) [1 in = 2.54 cm]	Surface deflection (inch) [1 in = 2.54 cm]			
	Unreinforced	Geosynthetic at base-subgrade interface	Geosynthetic at the lower third of the base	Geosynthetic at the AC-base interface
0.00	-6.65E-03	-6.37E-03	-6.48E-03	-6.18E-03
1.54	-6.49E-03	-6.22E-03	-6.32E-03	-6.05E-03
3.50	-5.76E-03	-5.50E-03	-5.60E-03	-5.39E-03
6.01	-4.56E-03	-4.34E-03	-4.42E-03	-4.34E-03
9.20	-3.26E-03	-3.10E-03	-3.15E-03	-3.19E-03
13.28	-1.95E-03	-1.88E-03	-1.89E-03	-1.97E-03
18.49	-8.49E-04	-8.64E-04	-8.42E-04	-9.04E-04
25.14	-1.25E-04	-1.85E-04	-1.55E-04	-1.64E-04
33.62	1.45E-04	1.07E-04	1.14E-04	1.36E-04
44.44	7.92E-05	8.51E-05	7.52E-05	8.72E-05
58.26	-2.22E-05	-1.50E-05	-1.30E-05	-1.73E-05
75.89	-8.71E-06	-1.04E-05	-9.63E-06	-1.05E-05
98.40	1.16E-05	1.23E-05	1.09E-05	1.13E-05

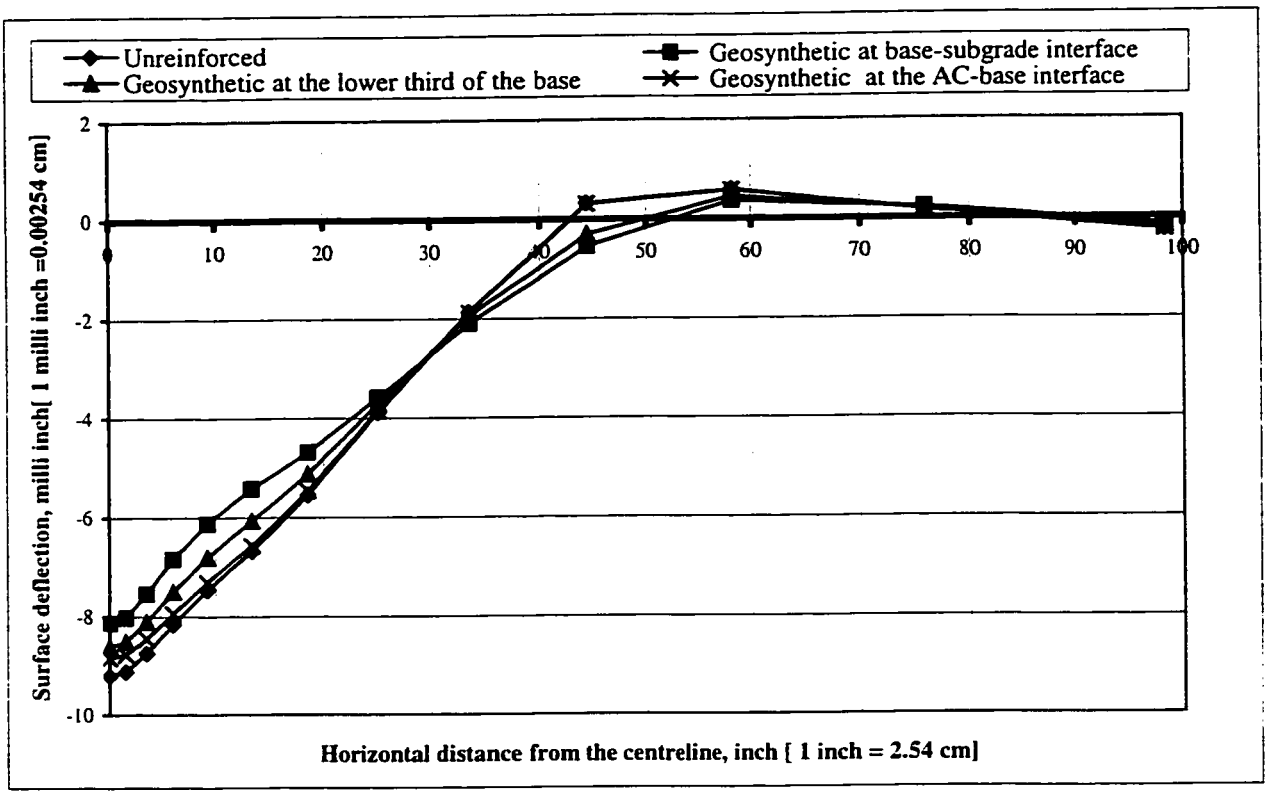

Figure (6.52) Envelope of the vertical surface deflection at the bottom of AC layer (Thick system 2 with the elastic analysis)

Table (6.54) The envelope of vertical surface deflection across line 1-1

Thick base system # 2				
Horizontal distance from the centreline (in) [1 in = 2.54 cm]	Surface deflection (inch) [1 in = 2.54 cm]			
	Unreinforced	Geosynthetic at base-subgrade interface	Geosynthetic at the lower third of the base	Geosynthetic at the AC-base interface
0.00	-9.20E-03	-8.13E-03	-8.60E-03	-8.84E-03
1.54	-9.12E-03	-8.02E-03	-8.51E-03	-8.77E-03
3.50	-8.74E-03	-7.54E-03	-8.11E-03	-8.45E-03
6.01	-8.15E-03	-6.84E-03	-7.50E-03	-7.93E-03
9.20	-7.45E-03	-6.13E-03	-6.81E-03	-7.30E-03
13.28	-6.68E-03	-5.43E-03	-6.07E-03	-6.56E-03
18.49	-5.54E-03	-4.69E-03	-5.13E-03	-5.47E-03
25.14	-3.88E-03	-3.59E-03	-3.71E-03	-3.86E-03
33.62	-1.86E-03	-2.09E-03	-1.93E-03	-1.88E-03
44.44	3.28E-04	-5.41E-04	-2.98E-04	3.14E-04
58.26	5.89E-04	3.69E-04	4.54E-04	5.81E-04
75.89	1.72E-04	2.24E-04	1.93E-04	1.82E-04
98.40	-2.41E-04	-1.27E-04	-1.72E-04	-2.40E-04

Figure (6.10) shows the horizontal strain plotted along the bottom of the AC layer starting from the centre of the wheel load [line 1-3 shown in Figure (6.1)] at the peak load for the thick base pavement system having weak base and weak subgrade. It is noticed from Figure (6.10) that the geosynthetic placed at the bottom of the AC layer leads to the largest reduction in the horizontal strain transmitted to the bottom of the AC layer. This reduction is more pronounced near the wheel load center and reaches its greatest value directly under the wheel load centre (almost 40 %) where the tensile stress is maximum in the control (unreinforced) system. The geosynthetic placed at the lower third of the base and the geosynthetic placed at the base-subgrade interface lead to insignificant reduction in the horizontal strain transmitted to the bottom of the AC layer for such system. The results of thin base system having weak base and weak subgrade show the same trend with respect to the horizontal strain transmitted to the bottom of the AC [Figure (6.26)]. However, the geosynthetic placed at the lower third of the base results in a tangible decrease in this strain. That reduction is more pronounced under the centre of the wheel load.

For the same system, which has weak subgrade and weak base, Figure (6.12) shows the surface deflection considered at the peak load and plotted at various horizontal distances from the wheel load centre for the case of the thick base. From this Figure, it is noticed that the surface deflection does not change significantly as a result of reinforcing the system. The highest reduction in the surface deflection occurs when placing the geosynthetic at the bottom of the AC. Such reduction reaches its peak under the wheel load center. The difference in the surface deflection (taken as an absolute value) between the reinforced and unreinforced systems tends to decrease by moving away from the

wheel load center until it disappears at a distance of almost 60 in (152.4 cm) from the wheel load center. The geosynthetic placed at the subgrade-base interface and at the lower third of the base give less reduction in the vertical surface deflection than the geosynthetic placed at the bottom of the AC as shown in Figure (6.10). On the other hand, the geosynthetic placed at the lower third of the thin base of the pavement having the same foundation results in a remarkable reduction in the surface deflection as shown in Figure (6.28). The stiffness of the pavement system increases almost by 30 % as a result of placing the geosynthetic at such location.

From Figure (6.28) it is also noticed that the reinforced systems have flatter profile of vertical surface deflection than the unreinforced system. The greatest reduction in the vertical surface deflection occurs when placing the geosynthetic at the lower third of the base. Based on the results of the sensitivity analysis for the reinforced systems, the following observations can be made:

1-In both thick and thin base systems analyses it is seen that the maximum decrease in the tensile strain occurs when placing the geosynthetic at the bottom of the AC layer and such decrease tends to be independent of the base quality, subgrade quality, and base thickness. The geosynthetic in this case significantly participates in absorbing the horizontal tensile strain induced at the bottom of AC which would be otherwise carried by the AC alone.

After conducting some further analyses, testing the influence of increasing E of AC on the ε_c and ε_t it is found that placing the geosynthtic at the bottom of AC and assuming strong bonding between them, one gets improvement in the performance of a pavement system against fatigue and rutting almost similar to that which is obtained by increasing the AC modulus of elasticity .

In other words, by placing the geosynthetic at the bottom of AC, effectiveness of the AC is enhanced and as a result the overall performance of the asphalt pavement is improved if the effective bonding is maintained between the geogrid and AC. This agrees well with the conclusion of Liu and Zheng (2001)

2-The results also show that the geosynthetic potential in decreasing the vertical strain is more pronounced when using it in the systems of thin bases. This agrees with the conclusion of Berg et al (2000) who showed in their state of art report that for a moderate load the geosynthetic appears to be more beneficial when the base depth is less than 250 mm.

3- It is noticed that the geosynthetic placed within the thin base remarkably changes the stress-strain state in the pavement system. For example, the vertical strain induced throughout the base decreases considerably particularly when placing the geosynthetic at the lower third of the base . Such decrease is more noticeable in the neighboring areas of the geosynthetic. In addition, this decrease becomes more pronounced when the vertical strain induced in the unreinforced base is high. This can also be seen from the table which shows that the maximum ε_c decrease taken as a percentage has higher value when the Max ε_c transmitted to the subgrade increases. Also Figure (6.42) shows the

significant decrease in the vertical plastic strain through the base as the result of using the geosynthetic

Changing the horizontal displacement measured at line 2-8 shown in Figure (6.1) is also a proof of the change in the stress-strain state as a consequence of placing the geosynthetic. The improvement which the geosynthetic offers in this case exists through its confinement effect (vertical and horizontal components taken by the geosynthetic) as was illustrated for an unpaved system by Nishigata and Yamaoka (1990) who found also that the geosynthetic benefit decreases by increasing the base thickness.

5-In the case of thin base systems the supports of the vertical and horizontal components appear to be higher when placing the geosynthetic at the lower third of the base. In other words, out of the three locations illustrated in the Figure (6.8), the geosynthetic placed at the lower third of the base tends to give the highest decrease in ε_c transmitted to the subgrade and leads to the longest rutting life for a pavement system of thin base.

6-The placement of the geosynthetic within the base at such location is equivalent to increasing the base thickness by a specific ratio, e.g., the consequences of placing the geosynthetic at this location on a pavement system are similar to the consequences of a specific increase of the base thickness on the performance of such system, which are discussed in the last section. For example, geosynthetically reinforcing the base at this location leads to a tangible decrease in ε_t , this decrease is more pronounced in the case of using a stronger base. Moreover, when reinforcing weak base the decrease in ε_t becomes more pronounced in case of founding on clay subgrade.

7-As Table (6.9) shows, the higher is the total (elastic and plastic) vertical strain transmitted to the subgrade, the higher is the ε_c decrease occurred as a result of using the

reinforcement. The highest decrease in ε_c is noticed in the case of using strong foundations (strong base and siltysand subgrade). The unreinforced system of this case shows the highest and completely pure elastic strain.

8-For a thick base system the range of the decrease in ε_c is 11 to 15 %. The results show small effects of the base quality and subgrade quality (particularly the subgrade quality) on the ε_c decreases obtained through using the reinforcement. ε_t improves only slightly when placing the geosynthetic at the bottom or at the lower third of the base.

9-For a system resting on a weak foundation (weak base and clay subgrade) the geogrid located at the bottom of AC gives best improvement against rutting . The same results are obtained with a weak base over siltysand subgrade , where the geosynthetic placed at the top of the base results in highest decrease in ε_c, 11%, and when using strong base underlined by clay subgrade as a foundation of the AC, the geosynthetic placed at the bottom of the base results in higher decrease in ε_c, almost 14%, but the decrease in ε_t, 4%, was insignificant. The results of strong foundations (strong base over siltysand subgrade) gives almost the same conclusions.

10-After comparing the unconfined thick base system #2 results obtained in the previous section with the results obtained from these analyses, it is concluded that adding the lateral restraining function, even with an exaggerated manner giving maximum effect and completely preventing the lateral movement of the base particles, the decreases in ε_t and ε_c are small. The results also show that when placing the geosynthetic at the lower third of the base, the confinement effect is more utilized than when placing it at the bottom of the base for the analyzed thick base system. This would justify that the geogrid in the

case of a thick system having weak base resting on weak subgrade is mainly supporting the system through its membrane function and not through the lateral restraining function resulting from base particles confinement by geosynthetic grids. However, for this system, if it is tended to operate the geogrid by its lateral confinement function within a thick base it is more beneficial to place it at the lower third or middle of the base. Other investigations are required to explore whether the confinement function is beneficial or not in other pavement systems.

11-Comparing the thick base system # 2 results shown in Table(6.8) with the results obtained from linear analyses, pure elastic reinforced system analyses, it is noticed, for the this thick base system which has a strong base and clay subgrade, that the results of linear analyses are slightly different from the results of the nonlinear analysis. Such difference becomes more evident when the geosynthetic is located at the lower third of the base. At that location, the nonlinear analyses shows more benefit in terms of decreasing the surface deflection

In terms of the best location for the geosynthetic, the linear analyses show that the best location for decreasing ε_c is still at the bottom of the base, and the best location for decreasing ε_t is also still at the bottom of AC for the thick base system #2.

Chapter 7

CONCLUSIONS AND RECOMMENDATIONS

7-1 Conclusions

Preliminary and major numerical analyses have been conducted to help examine the structural performance of a pavement system with and without geosynthetic reinforcement. In the preliminary analyses, different models were developed to test the numerical performance and convergence of the results of the proposed pavement system finite element analysis with its boundary conditions, selected constitutive laws of the materials, and the response to dynamic loads.

The following conclusions are drawn from the preliminary analyses;

1. Under static and dynamic loading effects, and for linear and nonlinear pavement systems the suggested mesh with its boundary conditions successfully converges and meet the required criteria of a successful finite element mesh with an acceptable number of elements, and reasonable computation time and computer memory.
2. For a linear pavement system, and taking the surface deflection as a comparison criterion the static response of the pavement system represented by mesh # 4 [[Table (6.2)] is more damaging than the dynamic response [Table (6.3)], which is numerically handled by the implicit dynamic method.
3. The elastoplastic (Drucker-Prager) base and elastoplastic strain hardening (CamClay) subgrade show higher strains than the linear elastic base and linear elastic subgrade, respectively. Considering this and considering the appearance of

plastic zone in the nonlinear models leads to adopting these models for more realistic and conservative simulations. On the other hand, the linear elastic model for the AC layer gives similar results for the viscoelastic model. However, the latter requires much higher computation time. For that reason the AC is considered linear elastic.

4. The damping effect considered through Ralyeigh viscous damping coefficients has little impact on the dynamic response of the nonlinear pavement system. This may be due to the energy dissipated through the plastic deformation which helps the response to decay and makes assigning the proportional damping coefficients less critical than in the case of linear elastic system.

The models of major analyses have been constructed to investigate the effects of the subgrade quality, base quality, and base thickness parameters on the fatigue and rutting of the pavement system as a first objective. The second objective of these models was to study the performance of a geogrid reinforced pavement system, and how this performance changes with the previous parameters. The focus in these analyses was where to place the geosynthetic to make it more beneficial against rutting and fatigue of the pavement system.

The following results are obtained from the major analyses.

1. The subgrade quality (strength) has insignficant effect on fatigue of the pavement system regardless of the base quality or thickness. This conclusions agrees well with the KENLAYER multilayer elastic sensitivity study conducted by (Yang, 1993).

2. The subgrade quality (strength) has a remarkable effect on the rutting of the pavement or the value of vertical strain transmitted to the subgrade, ε_c. Such inversely proportional relation is not dependent on the base quality or thickness.
3. The base quality has a considerable influence on the fatigue characteristics of the pavements. This influence is more pronounced when the base thickness increases and it is affected slightly by the subgrade quality.
4. Rutting of the pavement system decreases by using stronger base and that decrease is more noticeable in the case of a thick base and in the case of founding on a weak subgrade.
5. Increasing the thickness of the base leads to longer life of the pavement system against fatigue. This proportional relationship becomes more pronounced when using a stronger base. In addition, the quality of the subgrade has very little impact on this relationship
6. Increasing the base thickness leads to less rutting for the pavement system. The rutting decreases more in the case of the system with a strong base.

The major analyses of the reinforced pavement systems led to the following results

1. The maximum decrease in the tensile strain at the bottom of AC (fatigue failure criterion) occurs when the geosynthetic is placed at the bottom of the AC layer. .Such decrease tends to be very slightly dependent on the base quality, subgrade quality, and base thickness. The geosynthetic in this case participates significantly in absorbing the horizontal tensile strain induced at the bottom of AC which

would be otherwise carried by the AC alone. After conducting some analyses testing the influence of increasing E of AC on the ε_c and ε_t, it is noted that placing the geosynthtic at the bottom of AC and assuming strong bonding between them, the improvement in the performance of a pavement system against fatigue and rutting is almost similar to that which is obtained by increasing the modulus of elasticity of the AC by a specific ratio. In other words, by placing the geosynthetic at the bottom of AC, its quality is effectively improved, and as a result the overall performance of the asphalt pavement system is improved, if the effective bonding is maintained between the geogrid and AC .This agrees well with the conclusion from the experimental investigations of Liu and Zheng (2001)

2. The geosynthetic potential in decreasing the vertical strain transmitted to subgrade is more pronounced when using it in the systems of thin bases. This agrees with the conclusion of Berg et al. (2000) who showed in their state-of- the art review that for a moderate load, the geosynthetic appears to be more beneficial when the base depth is less than 250 mm.

3. Out of the three locations analyzed, the base-subgrade interface, location at the AC-base interface and at the lower third close to the middle of the base, the geosynthetic placed at the lower third close to the middle of the base thickness tends to give the highest decrease in ε_c transmitted to the subgrade and leads to the longest rutting life for a pavement system of thin base. This location also leads

to a tangible decrease in ε_t and it is more pronounced in the case of using a stronger base. It is also seen that placing the geosynthetic at this effective location is equivalent to increasing the depth by a specific ratio.

4. For pavement with a thick base with weak foundation (weak base and clay subgrade), the geosynthetic located at the bottom of AC gives the best improvement against rutting. The same results are found when having weak base over siltysand subgrade, where the geosynthetic placed at the bottom of AC results in the largest decrease in ε_c, 11% and when using strong base underlined by a clay subgrade as a foundation of the AC, the geosynthetic placed at the bottom of the base results in a larger decrease in ε_c (almost 14%) but the decrease in ε_t (4%) was insignificant. The results for a strong foundations (strong base over siltysand subgrade) gives almost the same trends.

5. The lateral restraint idealized to give complete restriction against lateral movement is tested for a thick base system having a clay subgrade and a strong base and it is found that adding this reinforcement slightly improves the response of this system. Such improvement is more pronounced the geogrid is at the lower third of the base thickness to the middle. This conclusion implies that the geosynthetic supports the system mainly by its horizontal and vertical confinement of the membrane confinement

7-2 Recommendations for further research work

1. Investigations considering the possibility of the geosyntheic slippage at its upper and lower interfaces with the surrounding media .
2. Validation of the numerical model results by laboratory tests.
3. More model parametric study concerning the geosynthetic stiffness and other physical properties, stiffness and thickness of the AC layer, loading value and configuration, prerutting and prestressing of the geosynthetic effects on the performance of the geosynthetic is recommended
4. Further studies may be conducted regarding the benefits/cost issues regarding the geosynthetic reinforcement.

References

Alfreds.R.Jumiks, 1962, Soil Mechanics, D.Van Nostrand Company Inc.

ADINA, 2001, " Finite Element Computer Program, Theory and Modeling Guide Volume 1,Report ARD 01-7

Barksdale, R., Francis Chan. & Stephen F.Brown,1989, " Aggregate Base Reinforcement of Surfaced Pavement " , Geotextiles and Geomembranes 8, pp.165-189.

Barksdale, R., Francis Chan. & Stephen F.Brown,1989, " Potential Benefits of Geosynthetics in Flexible Pavement Systems ", NCHRP. Report 315,TRB, National Research Council, Washington, D.C.,

Barksdale,R., Robnett, Q.,Lai,J.& Zeevaert-Wolff,A.," Experimental and Theoretical Behavior of Geotextile Reinforced Aggregate Soil System",In of The Mechanics of International Conference on Geotextiles, Vol II, Las Vegas, Nevada, USA, pp. 375-386.

Bathe,K.J,1996," Finite Element Procedures", 2nd ed., Prentice-Hall,Inc., New Jersey

Bearden, J. and Labuz, J., 1998, " Fabric For Reinforcement and Separation in Unpaved Roads", Final Report, Minnesota Department of Transportation ,pp.52-64

Berg R.R., Christopher,B.R.,and Perkins,S.W.,2000, " Geosynthetic Reinforcement of Aggregate Base Course of Flexible Pavement Structures", GMA White Paper II,Geosynthetic Materials Association .

S.F.Borg,1990, Fundamentals of Engineering Elasticity, Second Edition, World Scientific, pp.248-257.

Braja.M.Das, Kim.H.Khing, & Eun.C.Shin, 1998, " Stabilization of Weak Clay with Strong Sand and Geogrid at Sand Clay Interface " , , In Transportation Research Record 1611, TRB, National Research Council, Washington, D.C., pp.55-62.

H.J.Burd& C.J.Brocklehurst,1990, " Finite Elements Studies of The Mechanics of Reinforced Unpaved Roads", In 4th International Conference on Geotextiles,Geomembranes, and Related Products, Vol 1, The Hauge, Netherlands, pp.217-221.

Chandan Ghosh, & M.R.Madhav, 1994, " Reinforced Granular Fill-Soft Soil System : Confinement Effect " , Geotextiles and Geomembranes 13, pp.727-741.

Chandan Ghosh, & M.R.Madhav, 1994, " Reinforced Granular Fill-Soft Soil System : Membrane Effect " , Geotextiles and Geomembranes 13, pp.743-759.

Chen-Ming Kuo, Kathleen T.Hall, and Michael I.Darter,1995, In Transportation Research Record 1505, TRB, National Research Council, Washington, D.C., pp.119-127

W.F.Chen and G.Y. Baladi, 1985, "Soil Plasticity :Theory and Implementation" Elsevier.

Constantine.A.Vokas & Robert.D.Stoll, 1988, " Reinforced Elastic Layered Systems " ,In Transportation Research Record 1188, TRB, National Research Council, Washington, D.C., pp.1-7.

Dafalias,Y.F. and Hermann,L.R,1982," Bounding Surface Formulation of Soil Plasticity" Soil Mechanics-Transient and Cyclic Loads,Chapter 10, Jhon Wiley and Sons, pp.253-282.

Dave Ta-The Chang, Nuan-Hsuan Ho,Horng-YI Chang & Harn-Sheng Yeh., 1988, " Laboratory and Case Study for Geogrid-Reinforced Flexible Pavement Overlay " , In Transportation Research Record 1687, TRB, National Research Council, Washington, D.C., pp.125-130.

R.David Espinoza, 1994, " Soil-Geotextile Interaction : Evaluation of Membrane Support ", Geotextiles and Geomembranes 13, pp.281-293.

David Croney, & Paul Croney, 1991, Design And Performance of Road Pavements , Third Edition, McGraw-Hill.

De Bondt,A.,1995, "Properties of Antireflective Cracking System", Report No7-95-203-22, Faculty of Civil Engineering, Delft University of Technology, The Netherlands.

C.S.Desai and, H.J.Siriwardane,1984,"Constitutive Laws For Engineering Material",Prentice-Hall, Inc., Englewood Cliffs.

G.Dondi, 1996," Laboratory Test on Bituminous Mixes Reinforced By Geosynthetic", In Proceeding of The Third International RILEM Conference on Reflective Cracking In Pavements, Delft University, Maastricht, The Netherlands, pp.221-230.

G.Dondi, 1994,"Three_dimensional Finite Element Analysis of a Reinforced Paved Road",In Fifth International Conference on Geotextiles, Geomembranes and Related Products,vol No.1, Singapore,pp.95-100

Dong-Yeob Park, Hee-Ku Lee, Sik Youn In ,and Young-Chan Suh, 2002, " Impact of Geosynthetic Placement Location on Viscoelastic Responses of Reinforced Flexible Pavements" Submitted for Presentation and Publication at the 2002 TRB Annual Meeting of the Transportation Research Board, Washington,D.C.

Erol Tutumluer and Marshall R.Thompson,1997, " Anisotropic Modeling of Granular **Error! Hyperlink reference not valid.**Bases in Flexible Pavements" In Transportation Research Record 1577, TRB, National Research Council, Washington, D.C., pp.18-26

Fereidoon Moghaddas-Nejad, & John C. Small, 1996, " Effect of Geogrid Reinforcement in Model Track Tests on Pavement " , Journal of Transportation Engineering, ASCE, Vol.122, No.6, pp.468-474.

J.P.Giroud, & R.Bonaparte, 1984, " Design of Unpaved Roads and Trafficked Areas with Geogrids " In Proceeding of Polymer Grid Reinforcement Conference, Thomas Telford, London, pp.116-127.

Gryczmanski.M, & SekowskiJ, 1986," A Composite Theory Application for Analysis of Stress in A Subsoil Rinforced By Geotextile " , Third International Conference on Geotextiles , Vol.1, Vienna, Austria, pp.181-186.

Guy.T.Houlsby, & Richard.A. Jewell, 1990, " Design of Reinforced Unpaved Roads for Small Rut Depths, In Fourth International Conference on Geotextiles, Vol.1, The Hauge, Netherlands, pp.171-176.

Hans Erickson and Andrew Drescher, 2001," The use of Geosynthetics to Reinforce Low Volume Roads" University of Minnesota , Mannisota Department of Transportation,Report No MN/RC-2001-15

Harold L.Von Quintus, 1994," Performance Prediction Models In the Superpave Mix Design System", Strategic Highway Research Program, National Research Council, SHRP-A-699,Washington, D.C,

Hicks.R.G and C.L.Monismith, 1971," Factors Influencing The Resilient Response of Granular Material ", Highway Research Record 345, TBR, National Research Council, Washington, D.C, pp.15-31.

Hidetoshi Ochiai, Shigenori Hayashi, Eiji Ogisako & Akirasakai,1988," Analysis of Polymer Grid- Reinforced Soil Retaining Walls ", In Proceeding of The Sixth International Conference on Numerical Methods In Geomechanics, Balkema, Rotterdam, Vol.2, pp.1449-1453.

Hoe I.Ling, &Zheng Liu," Performance of Geosynthetic-Reinforced Asphalt Pavement" Journal of Geotechnical and Geoenvironmental Engineering, ASCE, Vol.127, No.2, 2001, pp.177-184.

T.S.Ingold, 1994, Geotextiles And Geomembranes Manual, Elsevier Advanced Technology,.

Irwin,L.H. and B.M.Gallaway, 1974,"Influence of Laboratory Test Method on Fatigue Test Results For Asphalt Concrete . Fatigue of Dynamic tests of bitumenous Mixture" Technical Paper 561, ASTM, pp. 12-46.

Jewell, R.A., Milligan,G.W.E., Sarsby,R.W., and Dubois, D.,1984, " Interaction Between Soil and Geogrids'' Polymer Grid Reinforcement, Thomas Telford.pp.18-29

Jiwon Kim and William G.Buttlar, 2002, " Analysis of Reflective Crack Control System Involving Reinforced Grid Over Base-Isolating Interlayer Mixture",Journal of Transportation Engineering,Vol.128,No. 4, ASCE.

C.Joel Sprague, Sam Allen, & William Tribbett, 1998, " Tensile Properties of Asphalt Overlay Geothenthetic Reinforcement " , In Transportation Research Record 1611, TRB, National Research Council, Washington, D.C., pp.65-69.

Hjelmstad, K.D., J. Kim, and Q.H.Zuo,1997 , " Finite Element Procedures for Three Diminsional Pavement Analysis", Proceeding, Aircraft/Pavement Technology: In the Midst of Change, ASCE, Seattle, Washington,pp.125-137

Kaliakin,V.N, Dafalias,Y.F. and Hermann,L.R., 1987, Notes For A Short Course Held in Conjuction With Second International Conference on Constitutive Laws for Engineering Materials, Tucson, AZ, January.

Koerner.R.M.,1990,Designing with Geosynthetics, Third edition, Prentice-Hall Inc, New Jersey.

X.Liu, A.Scarbas, J.Blaauwendraad, & D.D.Genske, 1998, "Geogrid Reinforcing of Recycled Aggregate Materials for Road Construction : Finite Element Investigation " , In Transportation Research Record 1611, TRB, National Research Council, Washington, D.C., pp.78-85.

Mordechai Perl, Jacob Uzan, and Arieh Sides, 1983, " Visco-Elastic-Plastic Constitutive Law for a Bituminous Mixture Under Repeated Loading" , In Transportation Research Record 911, TRB, National Research Council, Washington, D.C., pp.78-85.

N.Miura, A.Sakai, Y.Taesiri, K.Mouri, & Ohtsubo., 1988, " Model and Field Tests of Reinforced Pavement on Soft Clay Ground " , International Geotechnical Symposium on Theory and Practice of Earth Reinforcement, Vol.2, Fukuoka, Japan, pp.227-232.

Naic.Yang, 1972, Design of Functional Pavements, McGraw-Hill.

T.Nishigata, & I.Yamaoka, 1990, " Bearing Capacity of Unpaved Road Reinforced By Geotextile " , fourth International Conference on Geotextiles , Vol.1, The Hauge, Netherlands, pp.249.

J.Otani, H.Ochiai, & Hayashi,1992, "Restraining Effect of Geogrid Reinforced Soil In Finite Element Analysis" International Geotechnical Symposium on Theory and Practice of Earth Reinforcement, Vol.2, Balkema, Rotterdam, pp.147-150.

Pagan,C.A.,1965, Highway Research Record,No.67,1965,p.1

Perkins,S.W., 2001," Mechanistic-Empirical Modeling and Design Model Development of Geosynthetic Reinforced Flexible Pavements" , Final Report, Montana Department of Transportation, Helena, Montana, Report No FHWA/MT-01/002/99160-1.

Perkins,S.W., 2001," Numerical Modeling of Geosynthetic Reinforced Flexible Pavements of " , Final Report, Montana Department of Transportation, Helena, Montana, Report No FHWA/MT-01/003/99160-2 .

Per Ullidtz, 1987,Pavement Analysis, Elsevier.

Ragui.F, Wilson-Fahmy, & Robert.M.Koerner, 1993, " Finite Element Modeling of Soil-Geogrid Interaction With Application To The Behavior of Geogrids In A Pullout Loading Condition " Geotextiles And Geomembranes 12, pp.479-501.

Ralph Haas, Jamie Walls, &R.G.Carroll., 1988, " Geogrid Reinforcement of Granular Bases in Flexible Pavements " , In Transportation Research Record 1188, TRB, National Research Council, Washington, D.C., pp.19-27.

Ralph Haas,1984," Structural Behaviour of Tensar Reinforced Pavement and Some Field Application", In Proceeding of Polymer Grid Reinforcement Conference, Thomas Telford, London, pp.166-170.

Robert.D.Cook, David.S.Makus, & Michael.E.Plasha, 1989, Concept And Applications of Finite Element Analysis, Third Addition, John Wiley and Sons

G.P.Saha, & M.H.Kabir, 1988, " Design of Geotextiles and Geogrid Reinforced Unpaved Roads " , International Geotechnical Symposium on Theory and Practice of Earth Reinforcement, Vol.2, Fukuoka, Japan, pp.233-238.

Sam Helwany, Jhon Dyer, and Joe Leidy, 1999, Journal of Transportation Engineering, Vol.124,No.5, ASCE, pp.491-499.

Sameh M. Zaghloul, Thomas D. White, 1993,"Use of a Three-Dimensional, Dynamic Finite Element Programe for Analysis of Flexible Pavement" In Transportation Research Record. 1388, TRB, National Research Council, Washington, D.C., pp.60-69.

Saraby,R.W., 1985, "The Influence of AperatureSize/Particle Size on The Efficiency of Grid Reinforcement ",Proc.2nd Canadian Symp. On Geotextiles and Geomembranes, Edmonton, Albertapp.7-12

Saraf, C.L. and Majidzadeh, Kamran, 1974," Dynamic Response and Fatigue Characteristics of Asphaltic Mixtures "Fatigue and Dynamic Testing of Bituminous Mixtures, ASTM STP 561, American Society for Testing and Materials, pp. 95-114.

Saxena,S.K., and Budiman,J.S.,1985, "Interface Response of Geotextile ",Proc., Eleventh International Conference on Soil Mechanics and Foundation Engineering,vol.3, San Francisco.pp.1801-1804.

A.Scarpas, A.H.De Bondt, And G.Gaark-Euken, 1996, " Reflective Cracking Control Via Reinforcing Systems : Finite Element Modelling of Reinforced Overlays ", In Proceeding of The Third International RILEM Conference on Reflective Cracking In Pavements, Delft University, Maastricht, The Netherlands, pp.344-353.

A.Scarbas, A.H.Debondt, A.A.A.Molenaar, & G.Gaarkeuken, 1996, " Finite Element Modelling of Cracking In Pavements " , In Proceeding of The Third International RILEM Conference on Reflective Cracking In Pavements, Delft University, Maastricht, The Netherlands, pp.82-91.

A.Scarbas, A.H.Debondt, and M.P.Steenvoorden, 1996, " Effect of Reinforcement on Crack Response " , In Proceeding of The Third International RILEM Conference on Reflective Cracking In Pavements, Delft University, Maastricht, The Netherlands, pp.221-230.

A.N. Schofield,1993, " Original Cam-Clay " CUED/D-Soils/TR259, Prepared as a Keynote Lecture for the International Conference on Soft Soil Engineering, Guangzhou, 8-11 November.

Sellmeije.J.B, Kenter.C.J,& Van Den Bery.C., 1982, " Calculation Method for A Fabric Reinforced Roads" , In Second International Conference on Geotextiles, Vol.2, Las Vegas, Nevada, USA, pp.393-398.

Sweere,G.T.H,1990,"Unbound Granular Base For Roads" Ph.D,Dissertation, Delft Technical University, The Netherlands.

Terrel, R. L., Awad, I.S., and Foss, L.R., 1974, " Techniques for Characterizing Bituminous Materials Using a Versatile Triaxial Testing System", Fatigue and Dynamic Testing of Bituminous Mixtures, ASTM STP 561, American Society for Testing and Materials, pp. 47-66.

S.Timoshenko, & J.N.Goodier, 1951, Theory of Elasticity, Second Edition, McGrow-Hill.

Uzan,J., 1985, " Characterization of Granular Material" In Transportation Research Record 1022, TRB, National Research Council, Washington, D.C., pp.52-59.

R.veldhuijzen Van Zanten, 1986, Geotextiles and Geomembranes in Civil Engineering, A.A.Balkema. Rotterdam, Netherlands

Thomas D. White, Jhon E.Haddock, Adam J.T.Hand, Hongbing Fang, 2002," Contributions of Pavement Structural Layers to Rutting of Hot Mix Asphalt Pavements" NCHRP, Report 468 TRB, National Research Council, Washington, D.C., pp.52-59.

W Uddin, and Ricalde, " Nonliner Material Modeling and Dynamic Finite Element Simulation of Asphalt Pavements "

Wathugala,G.W,Huang,B. and,Pal,S,1996, " Numerical Simulation of Geogrid Reinforced Flexible Pavements" " In Transportation Research Record 1534, TRB, National Research Council, Washington, D.C., pp.58-65

T.D.White,S.M.Zahloul,G.L.Anderton, and D.M.Smith, 1995," Pavement Analysis For Moving Aircraft Load" In Journal of Transportation Engineering ASCE.,Vol, 123, No.6,pp.436-446

Witczak, M. W . and Root, R. E., 1974" Summary of Complex Modulus Laboratory Test Procedure and Results", ", Fatigue and Dynamic Testing of Bituminous Mixtures, ASTM STP 561, American Society for Testing and Materials, pp. 67-94.

Y.Lu,and P.J.Write, 1998, " Numerical approach of Visco-Elastoplastic Analysis for Asphalt Mixtures", In Computer and Structures, 69,pp.139-147.

Yang.H.Huang,1993, Pavement Analysis And Design, Prentice Hall.

Yoon-Ho Cho,B.Frank McCullough, and Jose Weissmann,1996, " Considerations on Finite Element Method Application in Pavement Structural Analysis" " In Transportation Research Record 1539, TRB, National Research Council, Washington, D.C,pp.96-101

E.J.Yoder, & M.W.Witczak, 1975, Principles of Pavement Design, Second Edition, John Wiley & Sons Inc.

Zienkiewicz,O.C and R.L.Taylor,1989, The Finite Element Method, Vol.1: Basic Formulations and Linear Problems, 4th ed, Mcgrow Hill